Towards tandem bio-chemo catalytic systems for the activation of alkanes and subsequent oxidation of alcohols to aldehydes using biofabricated Pd and Au catalysts

Prepared by

Mivashya Govender

In fulfilment of the requirements for the degree of Master of Chemical Engineering

Main Supervisor: **Athanasios Kotsiopoulos**
Co-Supervisor: **Susan T.L. Harrison**

Department of Chemical Engineering
Faculty of Engineering and the Built Environment
University of Cape Town

March 2021

Plagiarism Declaration

1. I know that plagiarism is wrong. Plagiarism is to use another's work and to pretend that it is ones own.
2. I have used the Harvard system for citation and referencing. Each significant contribution to, and quotation in, this report from the work, or works, of other people has been attributed, and has been cited and referenced.
3. This report is my own unaided work, except for assistance received from the teaching staff.
4. I have not allowed, and will not allow, anyone to copy my work with the intention of passing it off as his or her own work.

Signed by candidate

Signature

Abstract

Alkane activation is known to be difficult due to the stable, saturated nature of the C-H bonds. Typical C-H bond activation techniques use harsh conditions, toxic solvents and excessive amounts of energy to produce low-value fuels and solvents. To develop value from the alkane feedstock and promote sustainable chemical manufacture, bio-catalysts are considered for terminal bond activation. This has been successfully demonstrated for the conversion of n-octane to 1-octanol using cytochrome P450 enzymes (Gudiminchi et al., 2012; Julsing et al., 2008; Meissner, 2013; Olaofe, 2013; Pennec et al., 2014). However, due to the low conversion and lower-value of the alcohol product (Olaofe, 2013), the generation of higher value chemicals is needed to achieve a techno-economically feasible operation. A tandem catalytic process is proposed to valorize alkane activation using a cascade of bio-chemo reactions. Typically, chemical catalysts are synthesized using synthetic supports such as titanium dioxide or activated carbon. However, certain biological supports have a natural affinity for metal ions and have the ability to generate uniform, mono-dispersed nanoparticles, without the use of stabilizers or capping agents. The bacterial cell can be used as a support for chemo-catalysts that are easily accessible and cultivated. In this study, three different strains of *Escherichia coli* (*E. coli*) bacteria were considered as catalyst supports; namely *E. coli* DH5α, *E. coli* ATCC25922, *E. coli* BL21DE3. *E. coli* BL21DE3 was previously used as the host cell for the biocatalytic activation of alkanes. However, due to the known deficiency in hydrogenase for this strain, alternative *E. coli* strains (*E. coli* DH5α and *E. coli* ATCC25922) that could potentially also be used for the expression of this enzyme, were also considered. Reduction on these microbial supports required an electron donor (hydrogen and sodium formate) for manufacture of monometallic Palladium (Pd) and Gold (Au) nanocatalysts.

Biosorption studies showed rapid adsorption of Pd and Au ions onto all microbial strains within 1-5 minutes of cell exposure that was best described by the chemisorption of the metals onto amine, hydroxyl or thiol functional groups. Near-complete adsorption of Pd(II) occurred on all microbial strains, with *E. coli* ATCC25922 achieving the greatest capacity (ca. 94.4% mol/mol) at 5% (w/w) Pd loading. The adsorption efficiency declined to 27.9% (mol/mol) when the metal loading was increased to 25% (w/w) Pd. Reduction timeframes were dictated by the electron donor, with a hydrogen induced colour change noted within 20 minutes compared to 24 hours using sodium formate. Showing characteristics of ideal nanocatalysts, hydrogen-generated Pd(0) nanoparticles ranging from 3.0-3.5 nm and 3.9-9.3 nm in size were formed across all microbial strains at either 5% (w/w) or 25% (w/w) metal loadings. These nanoparticles were uniform and well-distributed within the cytoplasm. Clustering was most prevalent for the hydrogen-generated 25% (w/w) Pd loaded catalysts on *E. coli* ATCC25922 and *E. coli* BL21DE3. Minimal agglomeration and loss of Pd was observed on *E. coli* DH5α. In comparison to Pd(II), Au(III) was poorly adsorbed on all microbial strains with ca. 45.6% (mol/mol) and 33.7% (mol/mol) adsorbed on *E. coli* ATCC25922 at the 5% (w/w) and 25% (w/w) loadings. Bioreduction for this metal was only observed with hydrogen as the electron donor on *E. coli* ATCC25922 with irregularly-shaped Au(0) nanoparticles between 20 nm and 40 nm being formed. Catalyst activity was assessed using the oxidation of benzyl alcohol to benzaldehyde as a control reaction. No notable activity was detected for any of the Au catalysts. The greatest activity was observed by hydrogen-generated Pd catalysts at 25% (w/w) loading with conversions of up to 32.8$\pm$2.7% (mol/mol) and selectivity of 94.1$\pm$2.8% (mol/mol) across all microbial strains. For 1-octanol, hydrogen-generated 25% (w/w) Pd loaded *E. coli* ATCC25922 nanocatalysts achieved the highest activity to reach a conversion of 2.4% (mol/mol) with a selectivity of 82.7% (mol/mol) towards octanal. The addition of water limited byproduct poisoning to improve the conversion of 1-octanol to 9.6% (mol/mol) and 99.4% (mol/mol) selectivity to the aldehyde. The successful activity of the biofabricated catalyst on aromatic and aliphatic alcohols shows promise for tandem catalysis to valorize the alcohol product from bio-

catalytic activated alkanes. Consequently, this approach can be used to improve the value of n-octane via a bio-chemo catalytic cascade reaction where higher selectivity to the aldehyde can be reached.

Acknowledgements

Firstly, I would like to express my gratitude to c*change DST-NRF Centre of Excellence in Catalysis and the Centre for Bioprocess Engineering Research (CeBER) for providing the essential funding for my project.

Secondly, I would like to acknowledge my supervisor, Dr. Athanasios Kotsiopoulos, for his guidance and patience over the course of my project and always having an open-door policy to discuss any problems encountered. From his vast wealth of knowledge and experience, I have learnt the value of the scientific process and project management. The skills I have gained during this journey will guide me in the research space and this experience has only reinforced my passion for bioprocessing and biotechnology. To my co-supervisor, Professor Susan Harrison, I thank you for sharing your knowledge and giving invaluable advice whenever possible.

I am grateful to Dr. Derik Wilbers and Miss Deborah Chikukwa, my postgraduate colleagues within CeBER, for often taking the time to discuss any experimental issues and lend a helping hand when I was not able to be on campus. Without your assistance, I would not have reached this final chapter of my project. A special acknowledgment to Mr. Mohamed Jaffer, from the UCT Electron Microscope Unit, who gave his valuable time to work with me to establish the best protocols for imaging as it pertained to my study.

I would like to thank my family for their patience and support throughout my studies, without which I would have been truly lost. Lastly, I wish to express my deepest gratitude to the Almighty for removing all obstacles faced, for giving me the opportunity to further my studies and giving me the strength to persevere during difficult times.

Table of Contents

List of Figures

List of Tables

Glossary of Terms

a_t/A_T	Temkin isotherm constant
b	Langmuir constant relating to the energy of adsorption
b_t	Temkin model constant
B_T	relates to the heat of adsorption
c	constant that provides insight into boundary layer
Ce	concentration of the adsorbate at equilibrium
f	intraparticle diffusion rate constant
k_1	pseudo-first order rate constant
k_2	pseudo-second order rate constant
k_f	relates to factors that affect adsorption capacity and extent of adsorption
kFG	The Fowler-Guggenheim model equilibrium constant (L/mg)
n	relates to adsorption intensity and degree of heterogeneity of the support
q_D	maximum adsorption capacity
$q_{e\ (exp)}$	experimentally determined metal ion capacity at equilibrium
q_{max}	monolayer adsorption capacity
q_t	amount of metal ion adsorbed at a point in time
R	universal gas constant (kJ/mol.K)
S	Selectivity
T	Temperature (K)
w	interaction energy between adsorbed molecules (kJ/mol)
$X_{Product}$	Conversion based on product formed
$X_{Substrate}$	Conversion based on substrate
Y	Yield
Y_{exp}	Dependent variable in the equation obtained experimentally
Y_{model}	Dependent variable in the model equation
α	initial adsorption rate
β	desorption constant that relates the extent of surface coverage and the activation energy of adsorption
β_{D-R}	isotherm coefficient used to determine adsorption energy
θ	A dimensionless parameter, defined as coverage

Aerobic	In the presence of oxygen
Agglomeration/clustering	A heap or cluster of components (in this case metal nanoparticles)
Aliphatic alcohol	Straight-chained, branched or cyclic alcohols
Anaerobic	A state that requires an absence of oxygen
Anoxic	A condition in the absence of oxygen
Apoptosis	Cell death that occurs naturally during the cell's life cycle
Aromatic alcohol	An alcohol that consists of a conjugated structure
Assimilatory adsorption	The uptake of metal ions for use within the cell

Autocatalytic	The use of a product from a reaction to catalyze a second reaction
Autoclave	The method of using high temperature and pressurized steam to sterilize
Bimetallic	The use of two different metals
Bio-catalysis	The use of natural compounds derived from biological materials, like enzymes, that speed up a reaction
Bioaccumulation	The accumulation of substances (metals, pollutants etc) by a microorganism over time
Biofabrication	Using biological components and or processes for the production of compounds or complexs
Bioreduction	The reduction in electronic state of a positively charged compound or metal through mechanisms within a biological organism (fungi, bacteria (etc.)
Bioremediation	The use of microorganisms for the targeted removal of pollutants
Biosorption	The accumulation of metal ions or pollutents by a biological component
Chemisorption	Adsorption and binding on a surface as a result of chemical bonds
Chemo-catalyst	The use of chemical catalysts to speed up a reaction
Circumneutral	Defined as a near-neutral pH of a solution (pH between 6.5-7.5)
Cytoplasm	A viscous solution that fills cells and is encased within a membrane
Deactivation	The loss of catalytic activity over time
Dehydrogenase	An enzyme that aids in the removal of hydrogen
Denature	Modification the nature of a protein such that it loses its ability to perform its function
Dissimilatory adsorption	Metal interactions are independent of the cell
Electron donor	A chemical component that provides an electron to another compound
Facultative anaerobe	A microorganism that is able to survive in the presence as well as the absence of oxygen
Gram negative/positiive	A staining technique used to classify bacteria denotates that cells that retain the violet dye within the cell wall are gram-negative and the cells that do not as gram-positive
Inoculation	Introduce a smaller volume of cells into fresh growth medium
Ligands	Ion or functional group where a metal may bind
Lysis	The rupturing of the cell wall or membrane
Metalloenzyme	Enzymes that contain metal ions within their structure
Monometallic	The use of one metal
Nitrogenase	An enzyme that catalyzes the reduction of nitrogen and ammonia
Oxidant	The oxidizing agent in a reaction
Oxidation	The chemical process of adding oxygen to a compound
Peptidoglycan	A polymer that is found within cell walls
Periplasm	The space within the cell that is between the cell wall and cell membrane
Physisorption	The physical bonding of a molecule to a surface
Pre-cultures	A smaller volume cell culture prepared before the main culture. Often used to boost cell growth in larger volumes of media
Scaffold	A base biological structure that creates a structure for the active component to form on
Starter culture	Preparation of a smaller volume of cells made to assist the start of growth in a larger volume
Stock culture	A culture of microorganisms made and maintained in large batches to ensure viable cells and consistency in growth across experiments

Turgid	In the context of bacterial cells, turgidity is a result of water moving into the cell via osmosis and exerting pressure on the external cell wall
Vacuole	A small space within the cell cytoplasm that contains fluid

Acronyms and Abbreviations

AARD	Average absolute relative deviation
BSE	Backscattering of electrons
CTL	Coal-to-Liquid
CYP	Cytochrome
D-R	Dubinin-Radushkevich
DCW	Dry cell weight
DMSO	Activated dimethyl sulfoxide
EDS	Energy Dispersive Spectrometry
EDTA	Ethylenediaminetetraacetic acid
EDX	Energy dispersive X-ray
FHL	Formate hydrogenlyse
FID	Flame ionization detector
FT	Fischer-Tropsch
FTIR	Fourier Transform Infrared Radiation
GC	Gas chromatography
ICP-OES	Inductively Coupled Plasma-Optical Emission Spectrophotometer
IPD	Intraparticle diffusion
LB	Luria Bertani
M-H	Metal hydride
MC	Methylcellulose
MOPS	3-N-(morpholino)propanesulfonic acid
NADH	Nicotinamide adenine dinucleotide + Hydrogen
NADPH	Nicotinamide adenine dinucleotide Phosphate + Hydrogen
OD	Optical density
OMV	Outer membrane vesicle
PBS	Phosphate-buffered saline
PGM	Platinum group metals
R^2	Co-efficient of determination
ROS	Reactive oxygen species
SEM	Scanning Electron Microscopy
SRB	Sulfur-reducing bacteria
SSE	Sum of square errors
Syngas	Synthesis gas
TEM	Transition Electron Microscopy
TEMPO	2,2,6,6-tetramethylpiperidin-1-oxidenyl

Chapter 1

1 Introduction

1.1 Project background

Poor waste and emission management in industrial sectors has led to the promotion of stringent environmental regulations by various governments to limit the impact on climate change. In light of these regulations the chemical industry, known for their poor resource efficiency and waste management, has shifted towards more sustainable processing practices.

Traditional transition metal extraction and catalyst manufacturing techniques are labour intensive, expensive, and make use of harsh solvents or reaction conditions (Ciriminna and Pagliaro, 2013). Alternate technologies for chemical and catalyst manufacture are required to maintain sustainable yet effective processes. Transition metals namely the Platinum Group Metals (PGM) and precious metals are rare earth elements that are essential to electronic devices, automotive, jewellery, medicine and medical devices, as well as for promoting effective chemical manufacture. The unique catalytic, electrical and optical properties of transition metals present an opportunity for these metals to be recovered and re-used in the automotive, fine and bulk chemical industry.

1.2 Context

The chemical industry is mostly composed of bulk and fine chemicals, pharmaceuticals and petrochemicals. Waste management is a common concern in this industry. An example in the petrochemical sector is the Coal-to-liquid (CTL) processing in which liquid fuels are produced. One of the major concerns within this process is the generation of by-products, such as linear alkanes, that often have limited value. Alkanes are extremely stable molecules because of their unsaturated bonds and are traditionally used to produce low value fuels and solvents. The activation of alkanes is commonly achieved using chemical reagents. However, these approaches are often unselective and lead to poor conversion to the desired product (Latham et al., 2016).

Green chemistry considers the minimization of hazardous material outputs throughout the lifecycle of the chemical and is governed by twelve major guidelines. These guidelines encompass resource efficiency, waste prevention and the use of green technology to ensure a sustainable chemical process. Catalysts are a form of green technology that reduces reaction time and the amount of solvent required as compared to stoichiometric reactions (Anastas and Eghbali, 2009). Typical chemo-catalytic alkane activation brings about poor selectivity requiring the use of toxic, expensive chemicals and intense reaction conditions (Hosseinkhani et al., 2012; Sobjerg et al., 2011; Wells et al., 2014). To maintain sustainable

practices and achieve better activity, bio-catalysis is considered as an alternative. Bio-catalysts, such as cytochrome P450 enzymes, are highly selective towards the terminal C-H bond during the activation of alkanes. Recent investigations have focused on using these enzymes for the successful activation of n-octane to the primary alcohol (Ayala and Torres, 2004; Gudiminchi et al., 2012; Meissner, 2013; Olaofe et al., 2013; Pennec et al., 2014). However, the 1-octanol product is generated in low volumes and is of a lower value than the alkane feed. Dehydrogenase enzymes are known to assist in further oxidation of alcohols, but they often require the use of expensive co-factors and often achieve poor selectivity towards the desired aldehyde product (Bühler et al., 2003; Dong et al., 2018; Gandolfi et al., 2001). Chemical catalysts are known to exhibit better conversion of alcohols and have moderate selectivity to the aldehyde, and are therefore better suited for further valorization of the cheap alkane feedstock (Enache et al., 2006).

Valorisation of the alkane feed may be achieved by incorporating both bio- and chemo catalysis to achieve efficient, cost-effective production of higher value aldehydes, carboxylic acids or ketones. A combination of individual stepwise catalytic reactions that rely on one another are said to operate in tandem. Tandem catalytic processes try to mimic rapid enzymatic cascading reactions observed in living metabolic systems. This area in catalysis results in efficient processes that reduce the need for purification, limit downstream processing, reduce yield losses and work up time. However, one major consideration when operating a tandem process with multiple catalytic cycles is the challenge of catalyst compatibility (Gröger and Hummel, 2014).

In this study the chemo-catalytic oxidation of alcohols using a transition metal catalyst is considered subsequent to the bio-catalytic activation of alkanes. Typically, these metal catalysts are supported on synthetically manufactured supports like activated carbon or titanium dioxide (Enache et al., 2006; Sun et al., 2017; Wang et al., 2015). The deposition of metal nanoparticles onto these supports requires the use of harsh chemicals such as stabilizers and capping agents to maintain an adequate size and to prevent the leaching of nanoparticles. Microorganisms such as bacteria, yeast and fungi have shown a natural affinity for metal adsorption and nanoparticle formation (Lesmana et al., 2009; Lovley, 1993; Pantidos and Horsfall, 2014). Such microorganisms possess the unique ability of generating uniform, mono-dispersed metal nanoparticles with minimal expense or energy input.

Biological supports are considered a sustainable method of catalyst manufacture and may be effectively produced following the recovery of precious metals during bioremediation. Rare metals like Palladium (Pd), with unique catalytic properties, are predominantly obtained from primary sources that involve the extraction of minerals from the earth. The increased stress on global primary sources has promoted the need to recover these metals from secondary streams. The effectiveness of bacteria for the recovery of precious metals from waste streams, such as jewellery waste and automotive catalyst leachates has been demonstrated (Deplanche et al., 2011b; Mabbett et al., 2006; Yong et al., 2003). These microorganisms have the potential to be used as a low cost, resource efficient substrates for the bioremediation of metal rich effluents. Following reduction using an appropriate electron donor, the resulting

metal-microorganism complexes may be exploited as chemo-catalysts that may be use for the further oxidation of the alcohol product obtained from alkane activation.

1.3 Problem definition

Chemical and catalyst manufacture is hampered by waste generation and the use of toxic solvents, such as capping agents, base reagents and stabilisers. Regulations have promoted the shift in industrial chemical production to greener alternatives, promoting sustainable chemical processing and value from waste streams.

Alkanes, a petrochemical processing by-product that is undervalued and under-utilised, may be used as a cheap feedstock to the fine chemical industry. The bio-catalytic activation of alkanes is effective. However, the low volume and value of the alcohol product hinders process viability. To ensure an economically feasible process, higher value products like aldehydes or carboxylic acids are desired. A tandem bio-chemo catalytic approach may provide a means to achieve good conversion and selectivity to higher value chemicals. To support a resource efficient industry, biofabricated metal catalysts are considered as an alternative to the standard synthetic catalyst. Using such inexpensive catalysts can ensure improved selectivity to the desired aldehyde product, generating greater value for the activation of the alkanes (Deplanche et al., 2012).

1.4 Overall objective

In this investigation the valorization of activated alkanes through the generation of higher value aldehydes is considered. The study is centred on demonstrating comparable activity of biofabricated metal catalysts, supported on gram-negative bacteria such as *E. coli,* to their biological and synthetic counterparts. The objective is to consider the potential of three different *E. coli* strains (*E. coli* BL21DE3*, E. coli* DH5α and *E. coli* ATCC25922) to produce uniform, monodispersed nanoparticles that facilitate the oxidation of alcohol to the aldehyde under mild solvent and base free conditions. By comparison of catalyst activity, the most suitable support for the manufacture of biofabricated bimetallic catalysts can be determined.

E. coli BL21DE3*, E. coli* DH5α and *E. coli* ATCC25922 are commonly used as hosts for the expression of enzymes in biocatalysis. Presently, *E. coli* BL21DE3 is used as the host cell for the expression of P450 monoxygenases that promotes the activation of terminal C-H bonds in linear alkanes. With the eventual aim of upgrading the activated alkane products to more desirable aldehydes in a tandem reaction system, this microbial strain has the potential to be both a host in biocatalysis and a support for biofabricated nanoparticle catalysts. In this study, the suitability of the selected microbial strains *E. coli* DH5α and *E. coli* ATCC25922, including *E. coli* BL21DE3, to act as supports for the biofabrication of Pd and Au nanoparticle catalysts will be investigated.

Chapter 2

2 Literature review

2.1 Valorising alkane activation

The Fischer-Tropsch (FT) process is widely used for the conversion of syngas to liquid hydrocarbons. The process which typically occurs between 150-400^{o}C uses synthesis gas commonly derived from either coal or natural gas to produce these chemicals (De Klerk, 2008). The conversion of coal-to-liquids (CTL) proceeds via FT reactions at high temperatures varying between 300-350^{o}C (Maitlis and Klerk, 2013; Rushdi and Simoneit, 2001; Sudiro and Bertucco, 2009). Under these high temperature conditions saturated hydrocarbons, such as the straight chained alkanes or paraffins, are formed as a byproduct (Bergman, 2007; De Klerk, 2008). Alkanes are chemically inert under ambient conditions and require large amounts of energy to modify its thermodynamically stable structure. Such saturated hydrocarbons are commonly utilised to manufacture low value fuels or are converted to more reactive intermediates, namely unsaturated alkenes. These unsaturated compounds act as intermediates to higher value chemicals and are typically produced by either dehydrogenation or via the oxidation of the alkanes at temperatures between 200-600^{o}C. However, the conversion to the alkene brings about minimal financial returns and low resource efficiency (Ayala and Torres, 2004). Ideally the paraffin feedstock can be used to directly generate higher value products, promoting the use of alkanes as a cheaper base synthesis reagent.

The direct activation of the alkane to higher value products is achieved using super acids, free radicals, combustion or thermal dehydration. These methods for direct alkane activation are energy intensive processes that utilise costly and toxic chemicals (Labinger and Bercaw, 2002). For these reasons, bio-catalysts are considered as low-energy alternatives to standard chemo-catalysis. Enzyme bio-catalysts allow for the limitation of toxic solvents, such as stabilizers, alkaline reagents and strong acids. In the activation of alkanes these bio-catalysts advantageously achieve higher selectivity at physiological conditions (Ayala and Torres, 2004; Gudiminchi et al., 2012; Meissner,2013).

Enzymes are considered efficient bio-catalysts due to their ability to facilitate rapid, multi-step reactions in biological systems. Cytochrome P450 (CYP) monooxygenases are a family of enzymes that are able to naturally catalyze the oxidation of alkanes to primary alcohols. The CYP enzyme is able to reach a high degree of selectivity when heme is used as a cofactor (Gudiminchi et al., 2012; Koch and Arnold, 2013; Meissner, 2013; Olaofe, 2013; Pennec et al., 2014). However, the bio-catalytic activity is limited by the suitability of the reaction environment. Unlike chemo-catalysts that remain stable at high temperatures, high pressures and low pH environments, the bio-catalyst is less robust. Bio-catalysts usually operate under less extreme conditions, typically at near ambient temperature, atmospheric pressure and in

circumneutral solutions. This narrow operational range restricts bio-catalytically assisted reactions (Denard et al., 2013).

The production of the CYP bio-catalyst is done by a carrier bacterial cell in an aqueous media prior to being introduced to the alkane reaction environment. Due to the insoluble nature of the alkane in water, a two-phase liquid system results. This two-phase barrier limits the transport of the oxidant (typically oxygen or hydrogen peroxide) across the organic-aqueous boundary. As a consequence, mass transfer limitations impact the availability of the substrate and oxidant to the active cells reducing overall conversion to the desired alcohol product (Bergman, 2007; Meissner, 2013).

Bio-catalytic activation of alkanes to the primary alcohol, is highly selective but yields are less than 5% (Gandolfi et al., 2001). Economic feasibility at such conversions would require production of more valuable chemicals, like aldehydes or carboxylic acids. Bio-catalytic oxidation of the alcohol to higher value oxygenates is typically achieved by dehydrogenase enzymes. In the enzyme's isolated form, co-factors such as NADP+/NADPH are needed to sustain activity. A limitation of this approach is the expense associated with the co-factor (Brummund et al., 2015). Compared to the isolated form, production of the enzyme in a whole cell system is possible. Active whole cells can express the desired enzymes while simultaneously producing its own supply of co-factors (Dong et al., 2018). The elimination of the co-factor cost reduces raw material expenses significantly. However, whole cells also have alcohol and aldehyde dehydrogenase enzymes that are produced naturally in the cell (Bühler et al., 2003; Dong et al., 2018; Gandolfi et al., 2001). The use of these particular bio-catalysts promotes over-oxidation, thus lowering overall selectivity towards the desired product.

Having one catalyst to convert the alkane to higher value products such as the aldehyde would be ideal. However, the isolated and whole cell bio-catalytic systems are not effective for successive oxidation of alkanes (Bühler et al., 2003; Dong et al., 2018). High productivities and control of reaction cannot always be achieved by these bio-catalysts (Gandolfi et al., 2001). Chemically synthesized catalysts are considered as the alternative for the oxidation of alcohols due to the high selectivity achieved in these reactions. Metal catalysts, such as Pt, Pd and Au, have been successfully shown to be active under mild temperature and atmospheric pressure in aqueous systems (Besson and Gallezot, 2000; Enache et al., 2007). Under these less intense operating conditions, tandem bio-chemo catalytic systems are more compatible and may be more effective for the valorization of alkanes (Rudroff et al., 2018). This combination of catalytic systems results in a high selectivity with acceptable conversions to the desired product. As such, the possibility of low volume, high value, high purity chemicals tailors alkane activation towards the pharmaceutical and fine chemical manufacturing industries.

2.2 Tandem catalytic system

Tandem catalytic processes mimic natural enzymatic systems that co-ordinate multiple reactions as a series of well-timed and rapid cascade processes (Gröger and Hummel, 2014). Several tandem configurations are possible and are indicated in Figure 2-1 below.

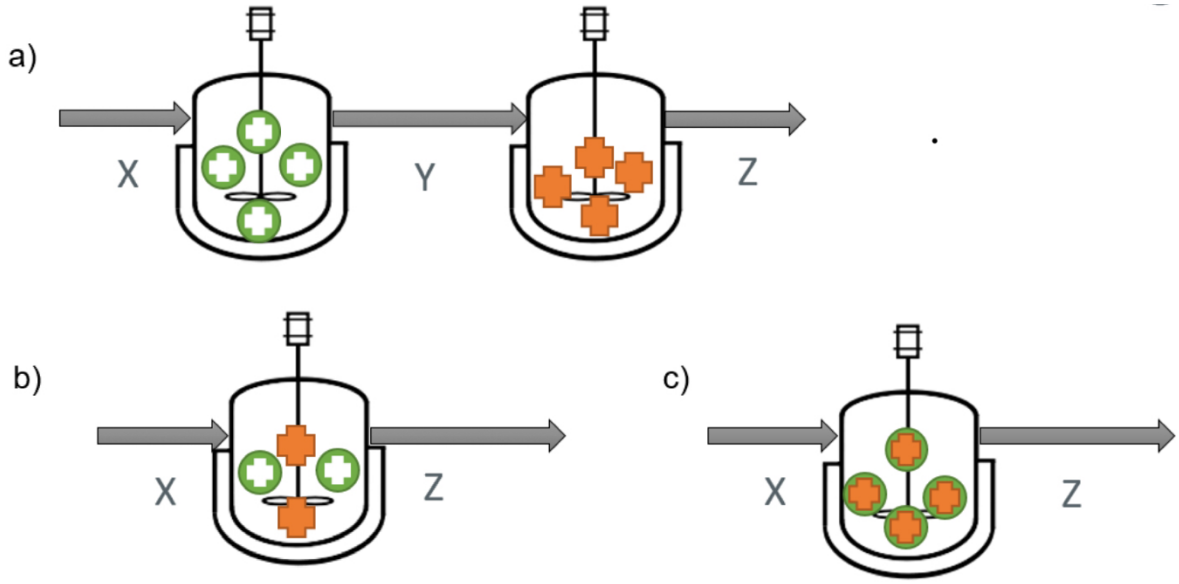

Figure 2-1 Diagram showing multiple possible tandem systems. Where a) is a sequential catalytic reaction b) one-pot with separate catalysts and c) one-pot with a combined catalyst

In these systems, catalytic reactions are performed in sequential reaction configurations. Such processes require intermediate purification stages to deliver the desired stream to the subsequent reaction vessel (Figure 2-1 a). In contrast to interstage separation, one-pot reaction systems, are also considered (Figure 2-1 b and c). In these systems catalysts and reagents are incorporated in a single reaction vessel, thereby reducing the number of down-stream processing units. This ultimately leads to lower energy demand, reduced waste production, reduced use of toxic intermediates, decreased losses in yield and improved work up time (Gröger and Hummel, 2014; Rudroff et al., 2018). A one-pot system can entail the incorporation of multiple, individual catalysts that are either added sequentially or concurrently to facilitate multiple individual reactions (Figure 2-1b). Alternatively, various active components of the catalysts may be combined to create a single catalyst that is then added to the single reaction vessel (Figure 2-1c). This effectively results in an efficient, single-stage catalytic reaction in which the desired product is produced in a single step.

In the case of alkane valorization, tandem one-pot, bio-chemo catalytic systems may experience practical limitations due to catalyst incompatibilities (Gröger and Hummel, 2014; Latham et al., 2016). These incompatibilities are usually a result of differing reaction conditions that are required to achieve optimal activity for each of the individual catalysts while simultaneously maintaining maximum conversion and selectivity. To counteract this and to achieve the required balance for optimal performance, strides have been made to alter both bio- and chemo- catalysts. Focus has been directed towards improving the robustness of

microbial bio-catalysts in the presence of organic substrates while simultaneously targeting efficient chemo-catalytic operations at near ambient conditions (De Vargas et al., 2004; Denard et al., 2013). Physical mechanisms such as the compartmentalization of reactions is considered as an alternative solution to catalyst incompatibility. This technique entails the separation of key reactions by a barrier. The isolated processes operate efficiently within each compartment of the vessel or reaction environment. Various compartmentalization techniques exist, namely biphasic systems, immobilization and size isolation membrane filtration (Table 2-1; Latham et al., 2016; Wang et al., 2018). In this respect (Figure 2-1), semi permeable microbial supports may simulate immobilization techniques by acting as both efficient bio-catalyst carriers while supporting fine metal nanoparticles to simultaneously exhibit characteristics of chemical catalysts.

Table 2-1 Description of compartmentalization techniques (Latham et al., 2016; Wang et al., 2018)

Technique	Description
Biphasic systems	This method uses the immiscibility of two liquid reagents to ensure a phase separation of reaction environments
Immobilization	Enzymes can be bound to the same solid as the chemo-catalysts. Creating a localized, seamless catalytic environment.
Size isolation membrane filtration	A semi-permeable membrane is used to select for particles of a particular size to be excluded. This can be used to isolate a catalyst yet still allow for free movement of reagents

Apart from ensuring catalyst compatibility, an optimal catalytic system also entails considering aspects of the catalyst itself, including the metal type, the support type and reaction conditions.

2.3 The metal catalyst

Metal catalysts are universally used in the chemical industry for hydrogenation, halogenation and oxidation / reduction reactions. Such catalysts are predominantly used for their ability to reduce the activation barrier of the reaction without undergoing any lasting change in structure or composition (Murzin, 2013). The catalyst selected should be viable for industry, highly effective in the reaction while ensuring continued activity if combined with other catalysts in tandem systems.

2.3.1 Heterogenous, homogenous and nanoparticle catalysis

Homogeneous or heterogeneous are the main subcategories of catalysts and are distinctive based on the chemical and physical characteristics of the material. Homogeneous catalysts assume the same phase properties as the reagents and are usually indistinguishable in the reaction vessel. This direct contact between the reagents and the homogeneous catalyst

allows reactivity to be maximized. However, these catalysts are not easily recoverable due to its miscibility with the reagents. This hampers its effectiveness as a catalyst, as reusability in the industrial context is limited (Miedziak et al., 2011b). Conversely, heterogeneous catalysts have physical or chemical properties that allow them to be easily separated from their reaction environment and may be reused. However, these heterogeneous systems are hindered by reduced contact between the catalyst surface area and the reagents, compromising selectivity to the desired product. To avoid this, the catalyst size can be minimized to maximise the specific surface area available for reaction. This reduced particle structure creates a pseudo-homogenous state, maximising contact between the catalyst active sites and the substrate while remaining recoverable from the solution (Astruc et al., 2005). The technique used for supported nanoparticle synthesis can dictate catalyst morphology and distribution of the catalytic material onto the support. Smaller, uniform particles that are equally distributed across the catalyst support are preferred as they directly improve catalyst activity (Creamer et al., 2007; Narayanan and Sakthivel, 2010).

Nanoparticles are manufactured by two general techniques, namely top-down and bottom-up synthesis. The top-down method entails the reduction of bulk material to the required size via mechanical or physical means (Narayanan and Sakthivel, 2010). Some of the techniques used include attrition or ball milling and are commonly used methods for reducing bulk materials to a fine powder. Alternate methods include mechanical crushing, pulverization or pyrolysis (Tavakoli et al., 2007; Thakkar et al., 2010). A limiting factor of these top-down techniques is the inability for precise control of the nanoparticle size (Tavakoli et al., 2007). As an alternative, bottom-up approaches allow particles to be built up from a single atom using chemical reagents (Narayanan and Sakthivel, 2010; Tavakoli et al., 2007; Thakkar et al., 2010). The methods used to build these nanoparticles are dependent on the organic or inorganic catalytic material, such as silica or metal. A few common methods to generate metal-based nanoparticles include reduction, precipitation or deposition of the metal precursor onto the support of choice (Gawande et al., 2015). For this type of bottom-up synthesis, transition metals are preferred due to their unique catalytic properties and applicability in various reactions.

2.3.2 Transition metals in chemo-catalysis

Transition metals are metals characterized by their valence electron or d-orbital shell. This electron orbital structure promotes the loss or gain of electrons and allows for numerous oxidation states of these metals (Flint, 2017). The d-orbital shell also shields the atom core from reaction, ensuring minimal change to the metal. In most cases making them ideal catalysts. Of these d-block transition metals, interest lies largely in the group 10 and group 11 elements as these metals possess unique catalytic characteristics when applied to the oxidation of alcohols (Peköz and Oymak, 2014).

Nickel

Given their proximity on the periodic table, the group 10 metals, nickel (Ni), palladium (Pd) and platinum (Pt) exhibit similar catalytic activation mechanisms and are therefore, frequently applied in similar reactions systems. Ni-based catalysts are cheaper alternatives as primary reserves of this metal exceed those of Pd and Pt (Lin et al., 2004; Lok, 2015; Tasker et al., 2014). Ni-based catalysts have been successfully applied in organic synthesis, such as cross-coupling reactions. Some examples of such reactions include the Suzuki, Tsuji-Trost and Mizoroki-Heck reactions (Bricout et al., 1998; Lam, 2011). When comparing the benefits of Pd over Ni-based catalysts, Lin et al. (2004) noted that oxidative addition in the Heck cross coupling system was quicker when using Ni. However, regenerating the Ni catalyst is difficult as the oxygen binds strongly to the surface generating multiple metal oxidation states. The unstable nature and multiple oxidation states of the metal can lead to the formation of unwanted, over-oxidized products that decrease process selectivity (Ananikov, 2015; Tasker et al., 2014). The unique ground state electronic configuration of the Pd metal with a full 4d orbital and an empty 5s orbital, allows only two possible oxidation states. The configuration allows for an energetically stable atom with unique catalytic, optical and conductive properties making this highly a desirable element across several industrial sectors (Hartings, 2012; Johnson and Matthey, 2017). Apart from improved stability, further benefits of both Pt and Pd are the reduced catalyst loading used to achieve the same activity as Ni (Lam, 2011; Lin et al., 2004). Although, Pd, and similarly Pt, are costly their unique catalytic properties make them more efficient catalysts. This is of particular importance in industry where achieving high activity and controlling selectivity can impact overall process economics.

Platinum and Palladium

The Platinum Group Metals (PGM) include platinum (Pt), palladium (Pd), iridium (Ir), rhodium (Rh), ruthenium (Ru) and osmium (Os). Pt is usually extracted from alluvial, copper/nickel ores or chromite in conjunction with the other PGM metals (U.S. Department of the Interior, 2017). A few countries dominate the global supply of these rare PGMs (Figure 2-2).

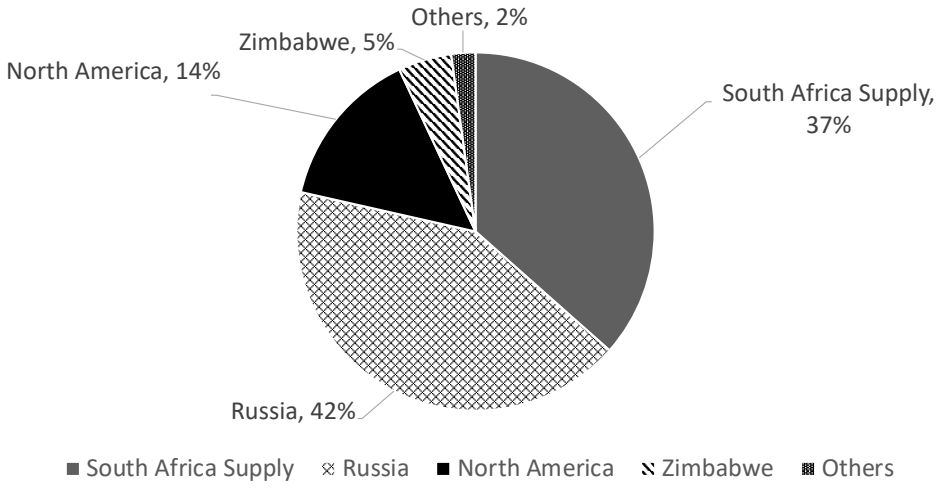

Figure 2-2 Supply breakdown for palladium per country (Johnson and Matthey, 2019)

South Africa and Russia are the largest suppliers of PGMs (U.S. Department of the Interior, 2017). South Africa contributes approximately 76% Pd and 30% Pt to the global supply (Bennett et al., 2016; Deplanche et al., 2011b). Due to increasing application of these metals, strain has been placed on a dwindling supply (Figure-2-3).

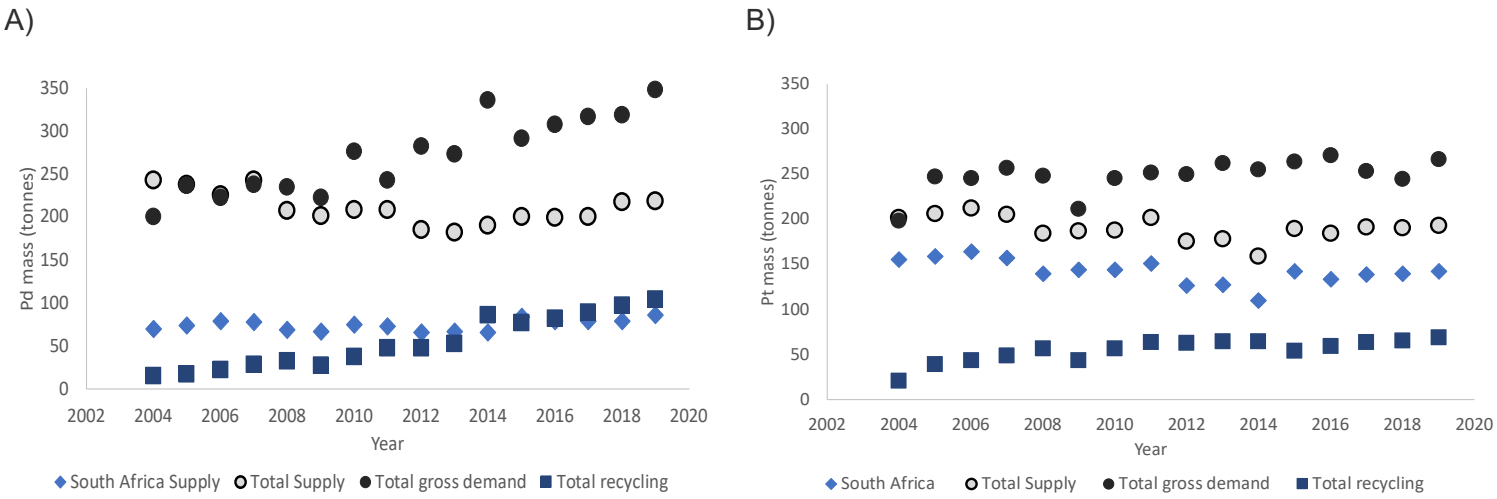

Figure-2-3 Supply and demand for A) Pd and B) Pt. (Johnson and Matthey, 2019)

One of the more prominent applications of these metals is their use in catalytic converters in cars (Figure 2-4). From as early as 2008 the autocatalyst, commonly used to reduce carbon dioxide (CO_2) emissions from motor exhausts, has become an important component in motor vehicle manufacture. The enforcement of stringent regulations on new motor vehicle emissions compounded the need for Pd and Pt. This has placed great strain on primary sources which have seen a declining over the past decade (Figure-2-3). The recycling of metals from waste or secondary streams, in comparison has been increasing since 2004 in an effort to supplement primary supply of the metals (Figure-2-3).

Apart from use as autocatalysts in motor vehicles, the unique structure and properties of Pt and Pd lends itself to be applied in organic chemistry, petrochemical refining and in electronic appliances. The metal is also known to be integrated in jewellery and in medical devices, as illustrated in Figure 2-4 (Deplanche et al., 2011a; Johnson and Matthey, 2019). Although these metals have similar attributes, from a catalytic standpoint there are differences in activity. Griffin et al. (2002) compared the catalytic properties of both metals for the oxidation of alcohols. The investigation determined that Pt is preferred for aliphatic alcohols and Pd for the conversion of aromatic alcohols. In these aromatic reaction environments, the Pt catalyst is able to achieve high conversion, but selectivity to the desired product was poor. Whereas, the Pd catalyst exhibited low conversion as well as moderate selectivity for the aldehyde (Griffin et al., 2002). This finding was supported by Enache et al. (2007) for the oxidation of benzyl alcohol. The study noted that a 50% selectivity to the aldehyde was achieved using a Pd-based catalyst with 50% of the benzyl alcohol being converted. For the oxidation of alcohols Pd is preferred over Pt, as over oxidation is more likely using the latter metal. Although, Pd

has limitations in terms of its susceptibly to sulfur poisoning, it is the cheaper alternative metal of the two and is able to achieve adequate activity.

Precious metals (Silver and Gold)

Silver (Ag), a valuable precious metal, has garnered wide interest for its applicability in water treatment as well as in targeted cancer treatments and opto-electric devices (He et al., 2003; Narayanan and Sakthivel, 2010). The applications of the metal nanocatalysts is a result of the antimicrobial, antifungal as well as anti-inflammatory properties of Ag nanoparticles. Similarly, gold (Au) also exhibits antibacterial properties and is inert in its bulk state limiting corrosion under oxygen (Meenakshisundaram et al., 2010; Okazaki et al., 2005). Due to its luster, non-corrosive qualities and inert nature in its bulk form, Au is prominently used in jewellery production. A smaller percentage is utilised in electronics and medicinal treatments (Kitco, 2015; World Gold Council, 2019).

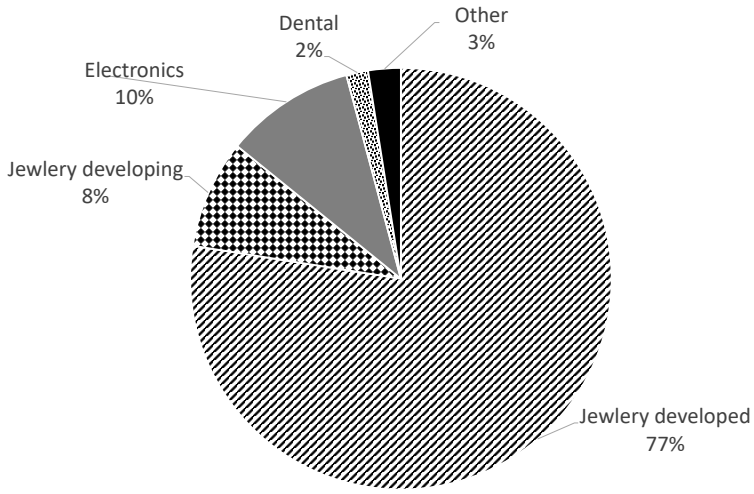

Figure 2-4 Application of Au demand in 2015 (Kitco, 2015)

The application of Au in chemo-catalysis is limited by the inactivity of the metal in the bulk state. This is considered to be due to the low ionization energy and near-noble metal electronic configuration of the Au atom. The Au nanoparticles allow easier loss and gain of electrons. This results in various optical, electronic and catalytic properties of the metal nanoparticles (Haruta, 2003). Following this, Au nanoparticles have shown great success over the past two decades in catalysis (Meenakshisundaram et al., 2010). The renewed interest in Au nanocatalysts has increased the demand for the metal, contributing to significant stress on primary sources. Consequently, secondary supply streams, such as recycled gold from waste leachates, used catalysts and electronic waste streams are being repurposed to supplement nearly a third of the global Au supply (Kitco, 2015). The usually dilute metal ion concentrations noted in secondary streams are not easily recoverable. The precipitation of the metal ion as Au particles from these streams presents an opportunity to exploit this as a more effective and inexpensive recovery process. This secondary stream is a cheaper source for the catalytic material. The resulting nanoparticles can then be easily and directly applied in electronics, biosensor development, drug-delivery and nanocatalysis (Hutchings, 2007).

Activity of oxidation reactions facilitated by Au nanoparticles is challenging. Hutchings (1985) and Haruta et al. (1989) were pioneers in the oxidation of CO using Au nanocatalysts. Rossi and Pratti (1998) also demonstrated the suitability of these catalysts for the oxidation of alcohols. In this case, to ensure activity, an alkaline solvent was required to promote the catalytic reduction of the metal ion (Hutchings and Haruta, 2005). Together with the Au nanoparticles newfound activity, the noble nature of this metal still ensures a resistance against catalyst poisoning and the prevention against over-oxidation (Mallat and Baiker, 2004; Prati and Rossi, 1998). These unique properties have thereby promoted interest in the application of gold in bimetallic systems to prevent catalyst deactivation.

2.3.3 The combination of group 10 and 11 metals

Monometallic catalysts are used extensively in industry and have shown to be highly effective at promoting oxidation and dehydrogenation reactions. Current monometallic catalysis using group 10 metals, face the challenge of over-oxidation and deactivation of the metal nanocatalysts resulting in poor selectivity. The addition of metals, such as Ag and Au, are proposed to improve the overall selectivity (Anderson et al., 2002; Astruc et al., 2005; Bernardotto et al., 2009; He et al., 2003; Zhu, 2014). Ferrando et al. (2008) reviewed various combinations of bimetallic catalysts, including interactions within the same periodic group (Cu-Ag, Cu-Au, Au-Ag and Ni-Pd, Ni-Pt, Pt-Pd) and across periodic groups 10 and 11 (Ni-Cu, Ni-Ag, Ni-Au, Cu-Pd, Cu-Pt, Pd-Ag, Pd-Au, Pt-Ag, Pt-Au) indicating unique interactions among these metals. Pd-Au interactions in particular, have garnered interest due to the unique synergy that exists between the metal atoms (Bhattarai et al., 2013). A fusion of atoms with a full 4d outer valance band, like those in the group 10, with group 11 atoms that have mostly empty outer valence orbitals allows for unique bonding. The electrons of both atoms are shared and the orbitals are filled to an extent that is not possible by the monometallic form (Rodriguez and Rodriguex, 1996; Sinfelt, 1977). The valence orbital interactions allow Au atoms to act as a promoter for active Pd. The charge transfer that occurs between the metals isolates the Pd sites. The increase of Pd selectivity is a result of the Au particles ability to inhibit oxygen deactivation of the metal (Chen et al., 2005; Gao and Goodman, 2012; Villa et al., 2015).

The method of catalyst formation and the ratio of these metals determine the structure of the nanoparticles and thus the type of interactions these metals experience. Chen et al (2005) showed that the location of Au atoms relative to Pd atoms, have an effect on catalytic performance. A large cohesive energy and smaller atomic radius implies the Pd will most likely form the core of the nanoparticle. Whereas, the Au atom has a smaller surface energy, implying that Au will preferentially form as the surface shell of the particle. The bimetallic system, Pd_{core}-Au_{shell} is thought to be the most thermodynamically stable form of the Au-Au nanocatalyst (Ding et al., 2010; Pittaway et al., 2009; Zhu, 2014). However, Ding et al. (2010) noted the preferred metal arrangement was dependent on the temperature used during nanoparticle synthesis. With lower reduction temperatures promoting the Au_{core}-Pd_{shell} structure (De Corte et al., 2011b; Deplanche et al., 2012; Enache et al., 2007; Solsona et al.,

2006). This Au_{core}-Pd_{shell} can be more effective as the Pd active sites are exposed to reagents while the Au core reduced deactivation, leading to a greater selectivity and activity being realized during reaction.

The optimal ratio of the metals in the bimetallic catalyst is dictated by the chemical reaction, and plays an important role in achieving optimal catalytic activity (Carter et al., 2016). A study performed by Enache et al. (2007b) examined the use of the mixed Au-Pd catalyst supported on titanium dioxide (TiO_2) for the oxidation reaction of benzyl alcohol. It was concluded from this study that an equivalent ratio of Pd to Au leads to the best catalytic activity. When investigating optimal activity for the oxidation of alcohol, Carter et al. (2016) further substantiated this claim. Optimal activity was reached at a 50 mol% Au content. Further addition of Au beyond this point resulted in over-oxidation of the aldehyde, decreasing selectivity and catalytic activity (Carter et al., 2016). Although, these metal interactions are essential for achieving optimal activity, the interactions between the metal and support are equally as important.

2.4 Supports and scaffolds

Heterogenous metal, nanocatalysts may form in free in solution or on a support medium. The nanoparticles that are free in solution have a greater tendency to clump due to attractive forces between the particles (Ashraf et al., 2018). The tendency for free particles to agglomerate limits the surface area to volume ratio of the nanoparticle, reducing the number of exposed active catalytic sites that negatively impacts activity (Ashraf et al., 2018). Nanoparticles bound to a support promote better control of the size, distribution, morphology and reusability of the particles. These properties are influenced by interactions amongst the metals as well as the metal and the support (Overbury et al., 2004).

2.4.1 The types of biological scaffold

Typically, the type of nanocatalyst support selected is based on availability, cost of catalyst, thermal and chemical stability and a high surface to volume ratio (Sakata et al., 2006). A strong metal-support interaction is crucial to prevent leaching of the metal into the reaction environment. This interaction depends on the catalytic material and support used (Mehrabadi et al., 2017). Catalyst supports are usually composed of synthetic materials like carbon, silicon, titanium, and alumina (Enache et al., 2006; Sun et al., 2017; Wang et al., 2015). The manufacture of these nanoparticles on such synthetic supports is usually energy intensive and makes use of hazardous capping agents and stabilizers (Hosseinkhani et al., 2012; Sobjerg et al., 2011; Wells et al., 2014). Conversely, the use of biological organisms as a support or scaffold is considered a green alternative to nanoparticle synthesis, with nanoparticles produced under ambient conditions with minimal energy input (Li et al., 2011). Various biological scaffolds, such as fungi, algae, bacteria, viruses, plants and plant extracts have been investigated (Ahmed et al., 2016; Nakajima, 2003; Narayanan and Sakthivel, 2010; Pantidos and Horsfall, 2014). Each with their own benefits and limitations, these bio-based

supports have been investigated due to their natural affinity for the adsorption of metals (Lesmana et al., 2009; Lovley, 1993; Pantidos and Horsfall, 2014).

An advantage of fungi is that it has a large surface area that allows for a greater number of active sites and is easy to recover from the reaction solution. This microbial support has the ability to secrete proteins into solution promoting nanoparticle production (Pantidos and Horsfall, 2014). Plants and plant extracts have also been considered as potential scaffolds. Chitosan, a plant extract, has shown remarkable capability for metal nanoparticle formation due to the high proportion of amino functional groups present on the support that act as metal binding sites (Fujiwara et al., 2007). Biological supports, like bacteria, are also considered as advantageous as a support, as these microorganisms are easily genetically modified, accessible, cheap and rapidly manufactured in bulk (Ahmed et al., 2016). These microorganisms form a stable matrix that prevents the aggregation of nanoparticles with certain strains stimulating efficient and rapid adsorption of metal ions (De Vargas et al., 2004).

2.4.2 Bacteria as a support

Various types of bacteria have been studied for their unique ability to adsorb metals. Bacteria such as *Geobacter metallireduces,* first discovered in 1993, was investigated for its ability to sequester metals such as of Fe (III) and MnO_2 during anaerobic growth (Coleman et al., 1993). Sulfur-reducing bacteria (SRB) were also originally considered for their exceptional metal reduction capabilities and are prominent in biofabrication studies (Lovley and Phillips, 1988). Interactions between such microorganisms and metals can occur via assimilatory or dissimilatory mechanisms.

Assimilatory adsorption mechanisms deal with the uptake of metal ions by the cell. Ordinarily, this uptake process occurs via three stages, namely bioaccumulation, energy generation or metal removal (Deplanche, 2008; Deplanche et al., 2011b; Torgeman, 2017). Typically, bioaccumulation in bacterial cells occurs in the presence of metals such as nickel (Ni), iron (Fe) and cobalt (Co). Such metals are used prominently for protein synthesis. It is thought that Pd can be adsorbed into the cell, in place of similar d-block metals like Ni (Torgeman, 2017). In the case of anaerobically grown microorganisms, the metal ion can be utilized as a terminal electron acceptor to generate energy to maintain the cellular metabolism (De Windt et al., 2005; Yong et al., 2002a). However, if the metal ion concentration becomes toxic to the cell, detoxification can occur. This detoxification proceeds via methods, such as precipitation, that convert the toxic ions to its non-toxic solid form (Iravani, 2014). Cellular metabolic products may also indirectly influence metal precipitation. Other detoxification methods include structural changes in membrane transport and efflux systems that aid the cell in removing undesirable components (Deplanche, 2008; Ehrlich, 1997; Iravani, 2014; Lovley and Phillips, 1988). Comparatively, dissimilatory metal reduction occurs independently of the cell activity. This dissimilatory reduction of the metal ion is a result of electrostatic forces near functional groups abundant on the cell wall that attract the metal cations (Bunge et al., 2010; Deplanche, 2008; Rotaru et al., 2012). The quantification of the type and extent of the various mechanisms

for adsorption on bacteria are not well established. Determining features of this mechanism can aid in assessing the optimal conditions required for biofabricated catalyst manufacture.

2.5 Adsorption of metals onto a bacterial support

Biologically manufactured Pd nanoparticles are considered to form within three areas of the cell in varying sizes. Particles greater than 40 nm have been detected on the extra-cellular surface, while particles between 10-40 nm have been noted within the periplasmic space. Nanoparticles less than 10 nm have also been found to form within the intracellular space of the cell (Torgeman, 2017). Knowledge of the size and the location of these particles provide an indication of why this adsorption would occur. Various theories exist that attempt to explain adsorption of metal ions onto bacteria (Lloyd et al., 1998; Rotaru et al., 2012).

2.5.1 Biosorption of the metal onto bacteria

Biosorption is the first stage of nanoparticle formation on the bacterial support, which may be divided into passive and active adsorption of metal ions (Torgeman, 2017; Yong et al., 2002b). Passive adsorption occurs near functional groups abundant in the organic matrix, such as hydroxyl, amine, thiol and carboxyl groups (De Vargas et al., 2004; Rotaru et al., 2012). Rotaru et al. (2012) investigated adsorption of Pd and Au onto various biological scaffolds. The study established a non-enzymatic, passive mechanism of adsorption of these metals onto functional groups. Complex cell wall and membrane structures, with their associated ligands, such as cysteine are abundant in hydroxyl and thiol groups (Ahmed et al., 2016; Deplanche et al., 2008). The Pd ions are known to coordinate well with the hydroxyl and amine groups, while Au ions readily associate with the thiols (De Vargas et al., 2004; Rotaru et al., 2012). A deficiency in key enzymes can impact the number of binding sites available on the cell. Apart from this passive adsorption, active biosorption of metal ions also occurs. Intracellular nanoparticle formation strongly indicates that an active cell is required for transport of the metal ion through the cell membrane into the cell cytoplasm (Deplanche et al., 2011; Torgeman, 2017). This supports the theory that the cells may mistake and accumulate alternative cations, such as Pd in place of Ni, Fe or Co necessary for protein synthesis. Both active and passive adsorption occurring on the cell can be modeled by three typical stages of mass transfer. This is shown by Figure 2-5.

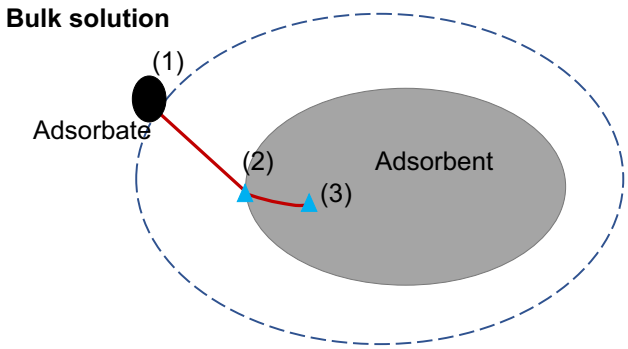

Figure 2-5 A schematic for adsorption of the adsorbate onto a support. (1) diffusion of the adsorbate from bulk to the support surface where adsorption onto active site (▲) can occur, (2) diffusion of the adsorbate into the pores of the adsorbent and (3) sorption of the adsorbate onto active sites

Figure 2-5 illustrates the process whereby the adsorbate (the metal ion) diffuses from the bulk solution to the external surface of the adsorbent (the bacterial cell). The adsorbate then undergoes internal diffusion to the active site. Adsorption occurs at the active site via physical or chemical interactions. Mathematically this process is described by Equation 2-1.

$$q_t = \frac{(C_i - C_t)V}{M} \qquad \text{Equation 2-1}$$

where q_t is the amount of metal ion adsorbed (mg/g) at time t (min), C_i is the initial metal ion concentration present in solution (mg/L), C_t is the metal ion concentration present in solution at time t (mg/L), M is the mass of the adsorbent (g) and V is the volume of metal ion solution (L). The stages of adsorption occur at different rates with the slowest stage considered rate limiting. This stage will have the greatest effect on the rate of adsorption. Most kinetic models are simplified based on the limiting stage and are effective for modelling adsorption (Qiu et al., 2009).

2.5.2 Adsorption kinetics

Determining the kinetics of adsorption onto a support provides basic knowledge of the mechanism that promotes this phenomenon. By modeling the rate of adsorption, the rate-limiting step can be deduced. A comparison of the adsorption kinetics of various absorbents, can provide insight into the effectiveness of a catalyst support (Inyinbor et al., 2016; Qiu et al., 2009). An effective support is defined by rapid adsorption and a large metal capacity. A faster rate reduces the time for adsorption, and improves the efficiency of the adsorbent (Aljeboree et al., 2017).

Various models, which are fundamentally based on the rate limiting step exist to describe the kinetics and rates of adsorption (Qiu et al., 2009). Of the many available options, four common models will be discussed in this study. These include the pseudo-first order model, the pseudo-second order model, the Elovich model and the intra-particle diffusion model. Many of these models are commonly used to describe the removal or adsorption of pollutants (Ho and McKay, 1998a; Qiu et al., 2009).

Pseudo-first order model

The pseudo-first order kinetic model was first proposed by Lagergren in 1898 to describe liquid-solid adsorption (Ho, 2006). Assuming physisorption of the adsorbate onto the support, the rate was expressed as a function of the adsorption capacity at equilibrium (q_e) and at a specific point in time, q_t (Equation 2-2).

$$\frac{dq_t}{dt} = k_1(q_e - q_t) \qquad \text{Equation 2-2}$$

where q_e is the amount of metal ion adsorbed at equilibrium (mg/g), and k_1 is the pseudo-first order rate constant (min^{-1}). The mathematical derivation depicting general adsorption of an adsorbate molecule (Equation 2-2) is only applicable when the initial metal concentration is high. This assumption is made such that the change in adsorbate concentration in the bulk solution is insignificant (Azizian, 2004). Equation 2-2 can be integrated at the boundary conditions (namely when t =0, q_t=0 and t=t, q_t= qt) and linearized to give Equation 2-3 (Inyinbor et al., 2016).

$$\log(q_e - q_t) = \log(q_e) - \frac{k_1}{2.303}t \qquad \text{Equation 2-3}$$

An assumption of pseudo-first order kinetic model is that the energy of adsorption is independent of the adsorption capacity of the support. It is further assumed that there are no interactions between adsorbed molecules on adjacent sites (Tan and Hameed, 2017).

Pseudo-second order model

The pseudo-second order model is another model that describes the kinetics of adsorption. In comparison to pseudo-first order, this model describes the chemisorption of the adsorbate onto the support (Qiu et al., 2009). The rate of this model is defined as a second order function in the difference between adsorption at equilibrium (q_e) and adsorption at a specific point in time, q_t (Equation 2-4).

$$\frac{dq_t}{dt} = k_2(q_e - q_t)^2 \qquad \text{Equation 2-4}$$

where k_2 is the pseudo-second order rate constant (g/mg.min). The pseudo-second order model assumes that chemisorption is rate limiting (Ho and McKay, 1998b; Senthil Kumar et al., 2010). In comparison to pseudo-first order, this model is independent of the equilibrium adsorption capacity in its linearized form. This is especially advantageous as this variable is not always easily determined experimentally (Qiu et al., 2009). From the general description of adsorption given by Azizian et al. (2004), this model is accurate when the change in the bulk metal ion concentration is considered significant.

Elovich model

The Elovich model was established in 1934 by Roginsky and Zeldowitsch for gas adsorption onto a solid (Roginsky and Zeldovich, 1934). Typically, this model is ideal for describing chemisorption onto a support (Ho, 2006; Inyinbor et al., 2016; Ramachandran et al., 2011). The rate of adsorption is defined as an exponential function of surface coverage β and the adsorption capacity at any time point (q_t) and is given below.

$$\frac{dq_t}{dt} = \alpha e^{-\beta q_t} \qquad \text{Equation 2-5}$$

By linearizing and integrating Equation 2-5 at the boundary conditions defined previously and assuming that $\alpha, \beta,$ t >> 1, the equation below is obtained (Qiu et al., 2009; Ramachandran et al., 2011).

$$q_t = \frac{1}{\beta}\ln(\alpha\beta) + \frac{1}{\beta}\ln(t) \qquad \text{Equation 2-6}$$

In Equation 2-5, β describes the desorption constant as well as defines a relationship with extent of surface coverage and the activation energy of chemisorption (g/mg), α is the initial adsorption rate mg/(g.min) and t the time (min). This model is based on the assumption that the energy of adsorption is linear with respect to surface coverage. The bulk adsorbate concentration is also assumed to be constant (Largitte and Pasquier, 2016). Unlike pseudo-first order, interaction amongst adjacent adsorption sites are assumed to occur using this model. Unrealistically, the model also suggests the support has an infinite adsorption capacity with time (Largitte and Pasquier, 2016; Tan and Hameed, 2017).

Intra-particle diffusion model

The intra-particle diffusion model is based on the three stages of adsorption. Namely, external diffusion, internal diffusion and the subsequent adsorption of the adsorbate (Qiu et al., 2009; Ramachandran et al., 2011). The model assumes adsorption capacity has a quadratic relation with time and is independent of equilibrium. Equation 2-7 below defines this model.

$$q_t = ft^{0.5} + c \qquad \text{Equation 2-7}$$

where f is the intra-particle diffusion rate constant (mg/g.min$^{0.5}$) and c provides insight into the thickness of the boundary layer. If c is large, there is a prominent film diffusion or boundary layer effect that is rate limiting. Upon analysis of experimental data, various regions of linearity may appear. In this case, if the data passes through the origin (c = 0) it suggests that two or more stages of adsorption prevail and intra-particle diffusion is likely to be the rate limiting step (Inyinbor et al., 2016; Osma et al., 2007; Özcan et al., 2005; Qiu et al., 2009; Ramachandran et al., 2011).

2.5.3 Adsorption isotherms

Adsorption and desorption occur simultaneously on any support. After a period of time and under specific temperature conditions, the rate of adsorption and desorption stabilize. This is known as the point of equilibrium between the metal concentration at the surface and the bulk solution (Allen et al., 2004). The Langmuir, Freundlich, Temkin and the Dubinin-Radushkevich model are four commonly used isotherms that describe adsorption at equilibrium. These adsorption isotherms are built on various assumptions that clarify aspects of the mechanism of adsorption as well as maximum capacity of the support and the affinity of the support for the metal.

The Langmuir model

The Langmuir model developed by Irving Langmuir in 1918 is used extensively to describe adsorption of components onto solid supports (Langmuir, 1918). The model describes ideal adsorption of the adsorbate onto the support, assuming monolayer coverage. All binding sites using this model have equivalent energies of adsorption with no interaction occurring between the adjacent adsorbate molecules (Inyinbor et al., 2016; Ng et al., 2002). The model is defined by Equation 2-8 and linearized further in Equation 2-9.

$$q_e = \frac{bq_{max}C_e}{1 + bC_e} \qquad \text{Equation 2-8}$$

$$\frac{C_e}{q_e} = \frac{1}{bq_{max}} + \frac{C_e}{q_{max}} \qquad \text{Equation 2-9}$$

where C_e is the metal ion concentration at equilibrium (mg/L), C_o the initial adsorbate concentration (mg/L) and q_{max} the maximum monolayer adsorption capacity of the adsorbent (mg/g) after which no further adsorption occurs (Allen et al., 2004). The Langmuir adsorption constant *b* relates the energy of adsorption on a volume to mass basis (L/mg) (Namasivayam and Kavitha, 2007; Ramachandran et al., 2011). These isotherm parameters once defined can be used to assess the R_L parameter in Equation 2-10.

$$R_L = \frac{1}{1 + bC_o} \qquad \text{Equation 2-10}$$

This is a dimensionless parameter known as the equilibrium or separation parameter. It is used to assess whether adsorption is favourable, unfavourable, irreversible or linear (Table 2-2).

Table 2-2 The table depicts the meaning of the R_L constant (Allen et al., 2004; Namasivayam and Kavitha, 2007; Padmesh et al., 2006)

Range	Adsorption type
$0 < R_L < 1$	Favourable adsorption
$R_L > 1$	Unfavourable adsorption
$R_L = 0$	Irreversible adsorption
$R_L = 1$	Linear adsorption

Favourable adsorption is expected when R_L lies between zero and one, which is also a strong indicator of physisorption. Unfavourable adsorption, or desorption, occurs when R_L is greater than one. Contrastingly, irreversible adsorption is defined when R_L is equal to zero. This irreversibility describes extremely strong adsorption of the adsorbate onto the support. Alternatively, if R_L is equal to unity then adsorption is considered to be linear (Ayawei et al., 2017; Namasivayam and Kavitha, 2007).

The Freundlich model

The Freundlich model was proposed by Herbert Freundlich in 1906 and is often used in comparison to the Langmuir isotherm. Unlike the Langmuir model, this model is empirical in nature. It assumes that surface adsorption is not rate limiting and that multi-layer adsorption of the adsorbate occurs onto heterogeneous surfaces (Allen et al., 2004; Ng et al., 2002). Consequently, an exponential number of active sites may exist on the support (Equation 2-11).

$$q_e = k_F C_e^{\frac{1}{n}} \qquad \text{Equation 2-11}$$

where k_f relates to factors that influence adsorption capacity and the extent of adsorption. The exponent *1/n* relates to adsorption intensity and the degree of heterogeneity of the catalyst (Dada et al., 2012; Inyinbor et al., 2016). The inverse of the factor *1/n* provides relevant information on the mechanism of metal adsorption. Like the Langmuir R_L factor, *n* may be used to describe the type of adsorption in the system. Özcan et al., (2005) classified *n* as a measure of the deviation from linear adsorption. When *n* is equal to one, linear adsorption is noted and typically suggests adsorption is independent of concentration of the adsorbate. When *n* is less than one, adsorption is dictated by chemisorption and if *n* is greater than one, adsorption is favourable and occurs via physisorption (Dada et al., 2012).

The Temkin model

The Temkin model considers that interactions between adsorbed molecules occur, and assumes a linear decrease in the heat of adsorption, B_T, in proportion to an increase in surface coverage (Tempkin and Pyzhev, 1940). The model is defined by Equation 2-12.

$$q_e = B_T(\ln A + \ln C_e)$$ Equation 2-12

where

$$B_T = \frac{RT}{b_t}; A = a_t$$ Equation 2-13

and A or a_t is the Temkin isotherm constant and B_T is the heat of adsorption constant (Inyinbor et al., 2016). This variable is related to the universal gas constant R (8.314 J/mol.K), the adsorption temperature T (K) and the Temkin constant b_t (J/mol) (Equation 2-13). If the sign associated with B_T is positive, then the process of adsorption is considered to be exothermic and vice versa (Inam et al., 2017).

The Dubinin-Radushkevich model

The Dubinin-Radushkevich model is based on the adsorption of gas onto a solid and is ideal for microporous materials (Chen et al., 2014). This model assumes a heterogeneous absorbent surface and a Gaussian distribution of adsorption energies on the surface (Inyinbor et al., 2016; Özcan et al., 2005). The model is defined by Equation 2-14 and Equation 2-15.

$$ln(q_e) = ln(q_D) - \beta\varepsilon^2$$ Equation 2-14

$$\varepsilon = RTln\left(1 + \frac{1}{C_e}\right)$$ Equation 2-15

$$E = \frac{1}{(2\beta)^{0.5}}$$ Equation 2-16

where q_D is the maximum adsorption capacity (mg/g), R the gas constant (8.314 J/mol.K) and T is the Temperature (K). β (mol^2/J^2) is the isotherm coefficient and used to define the mean sorption energy (kJ/mol) E in Equation 2-16. This constant, E, represents the energy required to desorb a molecule from the active site (Inyinbor et al., 2016). The Polyani potential, ε, is a function of the equilibrium concentration C_e and the environment temperature T as presented in Equation 2-16. The Polyani potential is used to indicate the adsorption potential and was defined by Michael Polyani for an adsorption mechanism where a gradient in chemical potential exists between the adsorbate and the support (Xu et al., 2008). If the mean sorption energy is less than 8 kJ/mol, physisorption is the prevalent mechanism. If E is between 8-16 kJ/mol adsorption occurs via ion exchange. Otherwise, if E > 16 kJ/mol then chemisorption is expected (Inam et al., 2017; Özcan et al., 2005; Ramachandran et al., 2011).

2.6 Bioreduction and nanoparticle morphology

Once the metal is absorbed onto the biological support an electron donor is added to promote bioreduction of the metal ion. Reduction ensures the conversion of the metal ions to its zerovalent form. The formation of zerovalent nanoparticles is usually indicated by a distinct colour change. For example, the reduction of Pd(II) to Pd(0) is noted by a solution colour

change from yellow to black/grey-black. In the case of Au(III) bioreduction, a colour change is noted from pale yellow to purple/red (Deplanche et al., 2008; Liz-Marzán, 2004; Lloyd et al., 1998). These visual indicators, dictated by the size and shape of the particles, are a result of optical and quantum effects usually experienced when electrons are confined to the atomic scale (Liz-Marzán, 2004; Mulvaney, 1996).

The bioreduction or detoxification process is mediated by metabolic proteins associated with the electron shuttle pathways in the cell (Brayner et al., 2007; Torgeman, 2017). These include enzymes such as nitrogenase and hydrogenase, which are prevalent under anoxic conditions (Pinske et al., 2011b). Both enzymes catalyse reactions to ensure a sufficient electron pool within the cell to be used for bioreduction (Deplanche et al., 2010; Lloyd et al., 1998; Mikheenko et al., 2008). Lloyd et al. (1998) utilized this natural cellular process to establish a successful protocol for Pd nanoparticle formation on *E. coli.* In this study, Lloyd et al. (1998) suggested that hydrogenase acts primarily as a site for Pd nanoparticle formation. The importance of these enzymes in bioreduction was further supported by Mikheenko et al. (2008). The study by Mikheenko et al. (2008) demonstrated the importance of specific types of hydrogenase in achieving uniform, monodispersed nanoparticles on the bacterial scaffold. The selective reduction of Au(III) in hydrogen indicated that enzymes, specifically hydrogenase, that catalyze hydrogen decomposition and generation of electrons are required for Au reduction (Deplanche and Macaskie, 2008; Kashefi et al., 2001; Konishi et al., 2006). Any deficiency of the hydrogenase should limit the formation of nanoparticles. However, Pd nanoparticle formation was evident when using both gaseous and chemical donors as well as on hydrogenase-deficient and denatured cells. In the absence of hydrogenase, agglomeration and non-uniformly distributed particles were observed (Bunge et al., 2010; Creamer et al., 2007; Lloyd et al., 1998; Mabbett et al., 2006; Torgeman, 2017; Yong et al., 2002a). This contradicted the importance of the hydrogenase in metal reduction, suggesting additional pathways and/or a passive mechanism was in part responsible for metal reduction (Rotaru et al., 2012). Upon further analysis of the reduction capability of heat killed cells, Torgeman (2017) postulated that at low concentrations of the metal ion, reduction via non-biological means was suppressed. This indicated that the metal ion concentration could dictate the prominence of select bioreduction mechanisms. In the case of hydrogenase deficient bacterial strains, the cells were still active such that alternate redox pathways within the cell could promote metal ion reduction (Torgeman, 2017). Creamer et al. (2007) and Deplanche et al. (2008) suggested a secondary enzymatic mechanism that was assisted by hydrogenase. Nitrogenase, a nitrogen fixing enzyme in the cell, is a reducing agent that facilitates electron transfer to the electron acceptor. This enzyme is known to promote the generation of Ag nanoparticles (Brayner et al., 2007).

Cytochrome c and NADPH are also considered to be key in assisting ion reduction (Ahmed et al., 2016; Chah et al., 2005). These components of the cell are commonly used to shuttle electrons within the cells. The pH of the surrounding solution influences folding and unfolding of the cytochrome c and the morphology of nanoparticles (Ahmed et al., 2016; Deplanche and Macaskie, 2008; Stoyanov and Browns, 2003). The effect of such conformational changes

were noted by Du et al. (2007) and Deplanche et al. (2008) resulting in Au nanoparticles that ranged in size from 20-50 nm on *E. coli* when solutions where at pH 6-7.

2.6.1 Bacterial strain and hydrogenase enzyme activity

Hydrogenase enzymes are metalloenzymes that are essential to certain cells during anaerobic and fermentative growth (Pinske et al., 2011b). Typically, the protein assists with the maintenance of cellular respiration and energy generation. The structure of the metalloenzyme usually consists of a transition metal center and complex, coordinating ligands. Common types of hydrogenases include [NiFe], [Fe], [FeFe] metal centered frameworks (Lloyd et al., 1998; Lukey et al., 2010). The type and abundance of each enzyme is dependent on the strain of bacteria. Particularly in *E. coli,* the [NiFe] type is abundant with four known sub-types of the [NiFe] centered hydrogenase (Lloyd et al., 1998; Lukey et al., 2010; Pinske et al., 2011b). Of these metal-centered enzymes only three have been well-studied, namely Hyd-1, Hyd-2 and Hyd-3. Each of these proteins are found in specific locations and have specialised functions within the cell (Deplanche et al., 2010; Lukey et al., 2010; Pinske et al., 2011b). Hyd-1 and Hyd-2 are ordinarily located on the cell membrane and typically face the periplasm. This unique position coincides with the location where Pd nanoparticles have been found in previous studies (Deplanche, 2008; Deplanche et al., 2010; Lukey et al., 2010; Mikheenko et al., 2008; Torgeman, 2017). These two enzyme subtypes, Hyd-1 and Hyd-2, account for approximately 10% of the total hydrogenase activity and catalytically promote the dissociation of hydrogen to generate electrons for transport. The Hyd-3 enzyme accounts for the remaining 90% of total hydrogenase activity (Pinske et al., 2011b). This [NiFe]-centered enzyme is also membrane-bound but is cytoplasm facing. The position of these enzymes correspond to the intracellular nanoparticles noted previously (Deplanche et al., 2010; Deplanche and Macaskie, 2008; Lukey et al., 2010; Omajali et al., 2017). The Hyd-3 protein forms a complex with formate hydrogenlyase (FHL) proteins. This is to aid in the production of hydrogen and carbon dioxide in fermentative and anaerobic systems (Lloyd et al., 1998; Peck and Gest, 1955; Pinske et al., 2011a). As not all microorganisms have the ability to survive under anoxic conditions, the variation of bacterial strain can easily dictate the degree of reduction and morphology of metal nanoparticles. De Vargas et al. (2004) investigated different *Desulfovibrio* strains for the production of biofabricated Pd nanoparticles and suggested that notable hydrogenase variation across different strains can impact support capacity and rate of adsorption.

The influence of bacterial strain on nanoparticle formation was initially considered insignificant (Deplanche et al., 2010). However, this was disregarded when the catalytic activity of various gram-negative and gram-positive bacterial supports were later investigated (De Vargas et al., 2004; Deplanche et al., 2014). In these studies, gram-negative strains were found to exhibit greater catalytic activity than gram-positive bacteria. The activity is associated with the structure of the gram-negative cell wall. The abundance of proteins on the complex double membrane and the thin peptidoglycan layer of the gram-negative strain, allows for ample nucleation sites and ease of metal ion transport into the cell (Bunge et al., 2010; De Vargas et al., 2004; Yong et al., 2002b). Of the five gram-negative strains studied by Deplanche et al.

(2014), *Desulfovibrio desulfuricans* (*D. desulfuricans*) and *Escherichia coli (E. coli)* displayed the best catalytic activity. Although both bacterial strains presented favourably as catalyst supports, *D. desulfuricans* are SRB capable of generating hydrogen sulphide, which is a known catalyst poison (Deplanche et al., 2014). On the other hand, *E. coli* does not generate harmful metabolic products that affect catalyst performance (Yong et al., 2002a). These bacteria are also more accessible than SRB and are easier to manipulate with uniform, mono-dispersed nanoparticles being formed on the cell surface, periplasmic space as well as within the cytoplasm (Deplanche et al., 2011a; Lloyd et al., 1998; Yong et al., 2002b).

Most studies to date have focused on the biofabrication of nanoparticle catalysts using *E. coli* MC4100 as the support (Deplanche, 2008; Deplanche et al., 2011a; Deplanche and Macaskie, 2008; Mabbett et al., 2006). Unlike Desulfovibrio *sp.*, limited investigations have considered different *E. coli* strains as potential catalyst supports. As previously suggested, these different bacterial strains respond in different ways to anoxic environments which could be inherently related to varying hydrogenase activities (Table 2-3).

Table 2-3 Hydrogenase activity of various strains of *E. coli* (Pinske et al., 2011)

Strain of *E. coli*	Specific hydrogenase activity (U/mg protein)
MC4100	3.01
BL21DE3	0.02

Varying degrees of hydrogenase activity are displayed by different *E. coli* strains (Table 2-3). Considering the role of hydrogenase in the bioreduction process, the activity of the enzyme can be an important factor in assessing the suitability of a microbial support for nanoparticle formation. *E. coli* BL21DE3, a common carrier used for the CYP P450 bio-catalyst that is utilised for alkane activation, has a low hydrogenase activity. In a tandem one-pot, single step process it would be ideal to use the same carrier bacteria as a scaffold for the subsequent oxidation reaction. This compartmentalizing technique isolates the reactions to different regions of the cell. With the bio-catalyst situated within the cell and the nano catalysts forming outside the cell, separated by a semi-permeable membrane.

2.6.2 The effect of the electron donor

Apart from the strain, the electron donor can also impact reduction efficiency and nanoparticle formation. Biofabrication studies have mainly focused on using electron donors such as formate and hydrogen gas for the formation of Pd and Au nanoparticles (Yong et al., 2002b, 2002a). These donors are naturally produced by the cell under anoxic conditions (Pinske et al., 2011a). For the production of nanoparticles, chemical electron donors are preferred. This is because reduction may be controlled by the addition of known concentrations into the system while maintaining acceptable mixing to achieve uniformly distributed particles. However, reduction using chemical electron donors is not always successful. This was noted for Au (III) reduction onto a gram-negative facultative anaerobe (Husseiny et al., 2007). For Au(III), hydrogen was the only donor that could induce reduction (Kashefi et al., 2001; Konishi et al., 2006). Yong et al. (2002a) indicated that hydrogen is the preferred electron donor due

to the higher degree of reduction activity noted under acidic conditions (pH 2). The acidic environment is similar to that experienced in waste leachates or other secondary streams used for the recovery of precious metals. However, hydrogen gas does face the problem of mass transfer limitations between the gas and liquid reagents used for reduction (Deplanche et al., 2010; Husseiny et al., 2007; Yong et al., 2002a).

2.7 Oxidation of alcohol

Oxidation reactions are common in chemical processing. In particular the oxidation of alcohols plays a crucial role in fine chemical and pharmaceutical manufacture (Ciriminna et al., 2015). These alcohols are of great interest as they are highly reactive and are cheap base reagents that are ideal for generating higher value products. Previous investigations on the bio-catalytic activation of alkanes used n-octane as a model compound to produce 1-octanol. Low conversion of the substrate was observed but high selectivity to the 1-octanol product was noted (Olaofe, 2013). To ensure an integrated tandem process for valorization of alkane activation it would be ideal to use 1-octanol oxidation to the aldehyde as the model reaction. However, the oxidation of aliphatic alcohols are often very difficult to achieve (Dimitratos et al., 2006).

In the area of alcohol oxidation reactions, benzyl alcohol is a widely studied compound specifically for the conversion to the higher value benzaldehyde product. Oxidation of benzyl alcohol is often used as a control reaction to monitor catalyst activity and serves as a good baseline for more complex reactions (Gavriilidis et al., 2016). The aldehyde is widely used as an intermediary compound for more complex chemical synthesis and is used prominently in cosmetics as well as in the flavour and fragrance industries (Nagy et al., 2019). A challenge faced in applying such oxidation reactions in the fine chemical industry is the need for sustainable oxidants, while still maintaining high selectivity to the desired product (Hoeldericht and Kollmer, 2000).

2.7.1 The alcohol oxidation reaction environment

Although oxidation of alcohols may occur naturally, reagents are usually added in stoichiometric quantities and are used to facilitate the reaction (Mobley and Crocker, 2015; Ten Brink et al., 2000). These reagents include chromium-based compounds such as potassium dichromate, activated dimethyl sulfoxide (DMSO) and 2,2,6,6 – tetramethylpiperidin-1-oxidenyl (TEMPO) (Mallat and Baiker, 2004; Miedziak et al., 2011b; Nagy et al., 2019). However, the use of stoichiometric quantities of these reagents results in poor resource efficiency and waste in the form of metal salts. Due to a shift towards more environmentally sustainable processing, the need for green synthesis routes that limit waste and resource inefficiency is preferred (Sheldon et al., 2007). Instead of reagents, catalytic systems make use of oxygen or hydrogen peroxide as oxidants. Hydrogen peroxide has been shown to be a green and cheap alternative oxidant (Bhati et al., 2008; Ciriminna et al., 2016; Sadri et al., 2014). It is an oxidant that can be well mixed in the liquid phase and allows operation at mild conditions. A disadvantage of this chemical oxidant is that, in excess, it poses

a challenge to biologically facilitated one-pot tandem systems, as it can be toxic to the cells (Imlay and Linn, 1987). To ensure success in the tandem system, the ideal case for a more sustainable processing route would be to promote the use of air as an oxidizing agent (Nagy et al., 2019). Gaseous air reduces the cost of purchasing purified oxygen and eliminates the dangers associated with using pure oxygen in the presence of highly flammable hydrocarbons (Gavriilidis et al., 2016).

Apart from the reagents, catalysts and oxidants, the reaction can also be performed in various reaction media and solvents. Such solvents generally promote interaction of the oxidant amongst itself and the catalyst as well as the other reagents in the system. In benzyl alcohol reaction systems, the generation of the carboxylic acid is promoted when water is used as the solvent. If an organic solvent, such as toluene, is used as the reaction medium the formation of the ester is favored (Dimitratos et al., 2006). Removing the dependency on either solvent is desired as milder less toxic conditions may be applied in processes where the catalyst can be easily separated and reused (Dimitratos et al., 2006; Nagy et al., 2019). In order to further facilitate operation at milder conditions, the effect of other system parameters need to be assessed. In addition to the solvent and base, parameters such as the temperature, catalyst loading, reaction time, oxidant concentration and pressure have also been investigated (Table 2-4)

Table 2-4 The effect of changing process parameters on the performance of the benzyl alcohol oxidation reaction (Ambili, 2011; De Corte et al., 2011a; Deplanche et al., 2011a; Enache et al., 2007, 2006). Where X is conversion and S is the selectivity

Parameter	Disturbance	Effect on X	Effect on S
Temperature	Increase	+	-
Catalyst loading	Increase	+	-
Reaction Time	Increase	+	-
Pressure	Increase	+	+
Concentration	Increase	+	-

From Table 2-4 it can be seen that a change in nearly all process parameters, apart from the pressure, impact the conversion and selectivity in a similar manner. The increase in these parameters cause an increase in conversion, while the selectivity to the aldehyde tends to decrease. The decrease in selectivity when increasing the temperature, catalyst loading, and the time of reaction can be attributed to over-oxidation (Deplanche et al., 2011a; Enache et al., 2007, 2006; Gavriilidis et al., 2016). Increasing the temperature provides sufficient energy to overcome the activation barrier for reaction to proceed unhindered. Similarly, in a system in which the reaction is allowed to proceed over longer periods, the likelihood of over-oxidized product being produced increases. The over-oxidation potential is also higher with increased chemical oxidant concentration as an excess of electron donors promotes the generation of other byproducts. Further, an increase in catalyst loading increases the number of active sites, which increases the likelihood of products binding to unoccupied sites. Contrastingly, if air or oxygen is used as an oxidant, a pressure increase improves both conversion and selectivity, as contact and mass transfer between the phases are improved. After evaluating the effect of these parameters on activity it can be stated that operating at milder reaction conditions such

as at low temperature, catalyst loading, reaction time and a reduced concentration of the oxidant can be beneficial to selectivity but detrimental to conversion (Ambili, 2011; De Corte et al., 2011a; Deplanche et al., 2011a; Enache et al., 2007, 2006). Using atmospheric pressure conditions can significantly impact the performance of the system especially when using air as the oxidant. This is the result of oxygen only occupying 21% (v/v) of air. This low oxygen delivery can impact mass transfer, imposing a limit to the contact between the reagents and oxidant resulting in a reduced yield of the desired product (Deplanche et al., 2012; Miedziak et al., 2011b).

2.7.2 Reaction and inhibitors for the oxidation of alcohols

Benzyl alcohol reaction pathway

Considering these reaction parameters and constraints, in the presence of either Pd, Au or Au/Pd catalysts the conversion of benzyl alcohol can proceed via the various reaction pathways (Figure 2-6 to Figure 2-8).

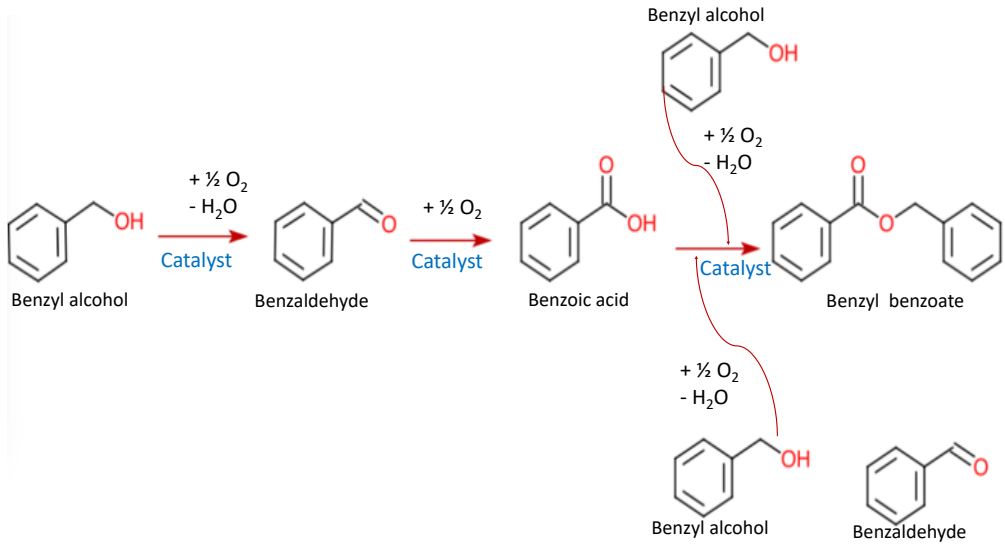

Figure 2-6 Reaction scheme 1 for the oxidation of benzyl alcohol

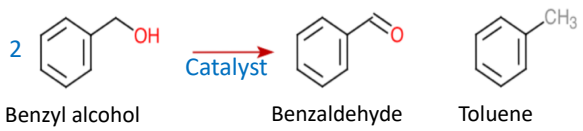

Figure 2-7 Side-reaction scheme 2 for the disproportionation of benzyl alcohol

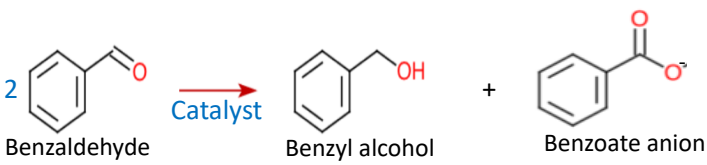

Figure 2-8 Side-Reaction scheme 3 for the Cannizarro reaction during benzyl alcohol oxidation in the he presence of a strong base

From Figure 2-6 to Figure 2-8, it can be seen that the reaction can proceed via 3 distinct pathways. The most plausible in the presence of oxygen being the main pathway for the oxidation of the alcohol to other oxygenates (Figure 2-6). Under specific conditions such as the absence of oxygen or addition of a strong base, disproportionation of the alcohol (Figure 2-7) or the Cannizarro reaction can result (Figure 2-8) (Nagy et al., 2019; Zhu, 2014).

Deactivation can occur as a result of byproduct contamination. For the oxidation of alcohols, the carboxylic acid readily occupies catalytic active sites. However, in the unique case of benzyl alcohol, this compound has a higher affinity for active catalytic sites. This hinders the binding of the byproducts to the catalyst, ensuring limited conversion of these byproducts to other unwanted chemicals (Sankar et al., 2014).

1-octanol reaction pathway

In comparison to aromatic compounds the conversion of the aliphatic alcohol proceeds via a similar pathway to reaction scheme 1 (Figure 2-9).

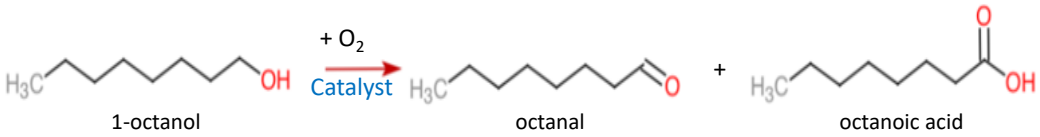

Figure 2-9 Reaction scheme 4 for the oxidation of 1-octanol

Over-oxidation of the primary alcohol is the main side reaction, with the formation of the ester possible after longer reaction periods (Figure 2-9). Unlike benzyl alcohol, limited studies consider the conversion of the aliphatic alcohols, such as 1-octanol (van der Pol and van Hooff, 1993; Villa et al., 2009). This aliphatic compound is considered to be difficult to activate (Dimitratos et al., 2006). Conversions of 1-octanol, in similar reaction conditions to benzyl alcohol, have been repeatedly shown to be low (< 12%) (Dimitratos et al., 2006; Zhang et al., 2015). This inactivity is largely thought to be a result of the octanoic acid being formed, occupying and deactivating active catalyst sites (Sankar et al., 2014). To counteract the observed deactivation, Sankar et al. (2014) added a base or a basic support material to bind the carboxylate. However, the addition of the base deviates from green process synthesis and limits the activity of the Pd metal in a bimetallic catalyst system (Dimitratos et al., 2006; Ishida et al., 2012). Knowledge of these reaction variables and resulting potential pathways assist in assessing appropriate conditions for aldehyde synthesis.

2.7.3 Stability and reusability of the catalyst

Apart from the catalyst being active, it should also be stable in the chosen reaction environment. The degree to which metal ions leach can cause catalyst deactivation and instability in reaction (Sádaba et al., 2015). This deactivation in solution determines the reusability of the catalyst. Such leaching of metals from the solid phase into the reaction solution is a continued challenge for current heterogeneous catalysis (Mallat and Baiker, 2004).

Bennett et al. (2013) investigated the effectiveness of recycling biologically supported Pd nanoparticles on *D. desulfuricans* relative to an industry standard (activated) carbon supported nanoparticle catalyst. The study indicated that the carbon supported catalysts deactivated faster after each successive run, while negligible amounts of Pd ion was noted in solution upon reuse of the biofabricated Pd catalyst. The catalyst in these investigations could be reused 3-4 times before leaching 10% of the metal. In comparison, nearly 50% of the metal leached out of the carbon supported catalyst within the second reaction run. Sobjerg et al. (2011) noted similar stability of the biofabricated catalyst with yields in reaction at 95% maintained up to the fourth reaction run. Further in these studies, Bennett et al. (2013) was able to show that metal leaching had a detrimental effect on the nanoparticles size, which impacted deactivation significantly (Table 2-5)

Table 2-5 The effect of reusing Pd catalysts on the nanoparticles size in oxidation reactions (Bennett et al., 2013)

Catalyst	Initial NP size [nm]	NP size [nm]
Pd/Carbon	2.3	23 *
Pd/*D. desulfuricans*	4	20 **

* the size of the nanoparticles was assessed after the reaction run 2

** the size of the nanoparticles was assessed after the reaction run 6

In their experiments, the authors noted that the Pd/C nanoparticle size increased 10-fold to 23 nm after the first run, whereas a similar particle size was only achieved after the sixth run for the biofabricated Pd system. These large particles hinder activity due to its reduced active surface area (Table 2-5). As opposed to the biological support, the larger nanoparticles evident on the activated carbon support was a result of excessive leaching and precipitation of the metal back into solution, promoting autocatalytic particle growth. Although the loss of active metal sites was minimal for the biofabricated catalyst, it was necessary to minimise leaching to further extend the life of the catalyst. Synthetic catalysts undergo calcining to ensure metal does not leach from the support. This technique does not extend to biological supports as the cell can disintegrate under typical calcination conditions (> 400^{o}C). Bennett et al. (2010) suggested that the leaching of metal from biological supports can be suppressed by adding ligands or using lower metal loadings (Ciriminna and Pagliaro, 2013).

2.8 Problem definition

Alkanes, a petrochemical processing by-product that is undervalued and under-utilised, may be used as a cheap feedstock to the fine chemical industry. The stable nature of the terminal C-H bond of alkanes necessitates the use of extreme temperature and pressures to promote activity. CYP450 enzymes have shown great success for the bio-catalytic activation of alkanes at mild conditions. However, the low volume and value of the alcohol product upon bio-catalytic activation hinders process viability. To ensure an economically feasible process, higher value products like aldehydes or carboxylic acids are desired. Further oxidation of the alcohol product via chemo-catalysis is necessary to produce such high value chemicals. To support a resource efficient industry, biofabricated transition metal catalysts are considered as an alternative to the standard synthetic catalyst. Manufacture of metal nanocatalysts on synthetic supports often requires stabilizers or capping agents. Biological supports in comparison to synthetic alternatives have shown a natural affinity for metal nanoparticle formation. Using such inexpensive catalysts can ensure improved selectivity to the desired aldehyde product, generating greater value for the activation of the alkanes (Deplanche et al., 2012). The strict anaerobe *D. Desulifuricans* is the only bacteria that has been extensively studied. However, gram-negative *E. coli*, which has been previously shown to be the most efficient at forming metal nanocatalysts, has not been as widely studied as its predecessor. This results in limited understanding on the mechanisms of adsorption on this microorganism. Bioreduction of nanoparticles onto the bacteria is mainly due to the presence of electron donors like hydrogen and sodium formate. Although the gaseous and chemical donors have their individual benefits and limitations, no study has shown the direct impact these donors have on nanoparticle formation or activity.

Valorization, following alkane activation, can potentially be achieved using a tandem bio-chemo catalytic approach by ensuring good conversion and selectivity to higher value chemicals. For maximum economic returns, this tandem approach would be best achieved as a one-pot process. To ensure catalyst compatibility, near ambient operating conditions are needed to remain within the limits of bio-catalytic activation. For the alcohol oxidation reaction air is proposed as an oxidant as it is a cheaper alternative; only generating water as the major byproduct.

Current work on bio-catalytic activation of alkanes is mainly centered on the conversion of n-octane to 1-octanol. As such, this study will focus on the chemo-catalytic oxidation of 1-octanol to the corresponding high-value aldehyde product. However, due to the extremely stable nature of long chained linear alcohols, the conversion of this substrate is poor at mild reaction conditions and often very difficult to achieve.

2.9 Objectives

It is clear from the literature that there is limited understanding of the potential to exploit tandem catalysis as a means to valorise the products of activated alkanes. Previous studies have successfully shown that nanoparticles may be effectively produced with *E. coli* when using

various electron donors. However, limited knowledge on the metal-microbe interactions and the kinetics of adsorption exists. Further, there is no clear evidence that indicates which combination of microbial support and electron donor would result in the most active biofabricated nanocatalyst. Although activity has been noted on benzyl alcohol, the application of these biofabricated catalysts to linear alcohol systems is unknown.

The objective of this study is to determine the efficacy of three different gram-negative *E. coli* strains, *E. coli* DH5α, *E. coli* ATCC25922 and *E. coli* BL21DE3, as well as the efficiency of two common electron donors, hydrogen and sodium formate, to biofabricate Pd and Au nanoparticles. The activity of the biofabricated catalysts will thereafter be determined via the oxidation of both aromatic and aliphatic alcohols. The scope of this investigation will include the production and characterisation of the newly synthesised catalysts on the aforementioned *E. coli* strains. The investigation will further include the hydrogenase deficient *E. coli* BL21DE3 strain, which is commonly used as a carrier for CYP153A6 enzymes that bio-catalytically facilitate the activation of linear alkanes. The objective is to determine the potential of recycling these cells as biological supports for Pd or Au nanoparticles that may be used in a combined one-pot bio-chemo tandem reaction. The overall aim of this proof of concept study will be to provide insight to the effectiveness of the biofabricated catalysts to convert alcohols to the desired aldehyde using air as the primary oxidant. Activity of the catalyst will be tested within fixed set of operating parameters with optimization being considered in a future study.

2.10 Hypothesis

Gram-negative *E. coli* with sufficient hydrogenase activity, such as *E. coli* MC4100, have previously been shown to be an effective support for the biofabrication of metal nanocatalysts. This type of bacteria is preferred over gram-positive bacteria due to the double-layered cell membrane, which introduce more available binding sites. In these investigations, hydrogen was shown to be an effective electron donor for metal reduction. This is a result of the electron donor being effective at lower pH, and is not limited by Cl^- ions that are typically associated with metal salt precursors. This gas is also known to reduce Au ions with greater efficiency than chemical reducing agents in the presence of biological cells.

It is therefore hypothesized that gram-negative *E. coli* DH5α and *E. coli* ATCC25922, without any known hydrogenase deficiency, will grow well under anoxic conditions as opposed to hydrogenase deficient *E. coli* BL21DE3. A deficiency in these enzymes will impact the uniformity, location and distribution of metal nanoparticles associated with the cells. This is because hydrogenase enzymes play an important role in maintaining the metabolic activity of the cells as well as in the transport and generation of electrons for reduction. In the case of palladium, the formation of these nanoparticles have generally been linked to similar locations as periplasmic and cytoplasmic hydrogenases. The use of hydrogen as the electron donor will therefore promote the activation of anaerobic pathways in the cell and will allow for rapid formation of uniform, mono-dispersed nanoparticles on the biological support. The effectiveness of hydrogen is likely linked to hydrogenase enzymes, which typically aid in the heterolytic cleavage and dissociation of hydrogen that promote the transport of electrons

within the cell. An excess supply of the donor will lead to a large pool of electrons that are available for reduction; ex-situ of the cell. Although sodium formate may be less efficient than hydrogen, the slower reduction will limit agglomeration. In this case, the metal ions biosorb over a longer period and will attach onto available binding sites rather than result in rapid reduction of the ion in solution that leads to the autocatalytic growth of nanoparticles.

The Pd and Au nanoparticles formed on an *E. coli* strain rich in hydrogenase enzymes in the presence of hydrogen will result in the feasible production of higher value aldehyde products. These nanoparticle catalysts will allow improved selectivity to the desired product compared to similar reactions on their synthetically produced counterparts.

2.11 Key questions

Therefore, it follows that the key questions of the study are:

- Which adsorption mechanism can be used to best describe Pd(II) and Au(III) ion adsorption onto the selected biological supports?
- Can Pd and Au ions be reduced using sodium formate and/or hydrogen as the electron donors?
- What is the impact of the electron donor on the physical characteristics of the nanoparticles that are formed?
- What characteristics, such as size and shape, result in the most active biofabricated nanocatalyst?
- Does the *E. Coli* strain type affect metal adsorption, reduction and the nanoparticles size and shape?
- Can the biofabricated catalysts be used to facilitate the oxidation of alcohols to aldehydes while achieving high selectivity?

Following these key questions, this thesis will firstly describe the materials and methods used during all experiments. This section will consider the anaerobic growth of the biomass in preparation for adsorption, the reduction of the metal ions onto the support and the subsequent characterization of these nanoparticles, and the approach to testing the catalysts activity for the oxidation of alcohols. Upon consideration of the methodology, the results and discussion is then divided into three sections namely the adsorption characteristics of Au and Pd onto the three selected *E. coli* strains, reduction and characterization of the nanoparticles and the structural change in supports, and the activity of these catalysts for the oxidation of alcohols. From these results, conclusions and recommendations are made on the most suitable microbial strain and electron donor for the conversion of 1-octanol to octanal and production of bimetallic catalysts.

Chapter 3

3 Methodology

This chapter seeks to investigate three main characteristics that influence catalyst synthesis and activity. These include examining the effectiveness of the support for adsorption, the effect of different electron donors and support strains on nanoparticle formation and the application of these catalysts to the oxidation of aromatic and aliphatic compounds. As such, an experimental approach was developed that considered the production of the biomass, the manufacture of Au and Pd catalysts under different conditions, the assessment of adsorption of the aforementioned metals onto the microorganisms, the characterization of the catalyst and analysing the activity of the catalyst.

3.1 The production of biomass as a scaffold

3.1.1 Strain selection for scaffolds

In this study, select *E. coli* bacteria were used as biological scaffolds for the manufacture of nanoparticles. Current studies investigating the synthesis of Au-Pd catalysts using biological scaffolds have focussed on the *E. coli* MC4100 strain as a support. Although not explicitly stated, its use was partly due to its known hydrogenase activity. This study will be considering various strains of *E. coli* as potential scaffolds due to their varied hydrogenase activity; these include *E. coli* BL21DE3*, E. coli* DH5α and *E. coli* ATCC25922. These bacterial cells are common strains that assist in the expression of enzymes and can also potentially be used as host cells for the cytochrome P450 bio-catalysts used for alkane activation to primary alcohols.

3.1.2 General growth procedure for the microorganisms

Growth of the *E. coli* was subdivided into three main sections: the preparation of the growth medium, the cultivation and maintenance of the starter culture and the bulk growth of biomass (Figure 3-1).

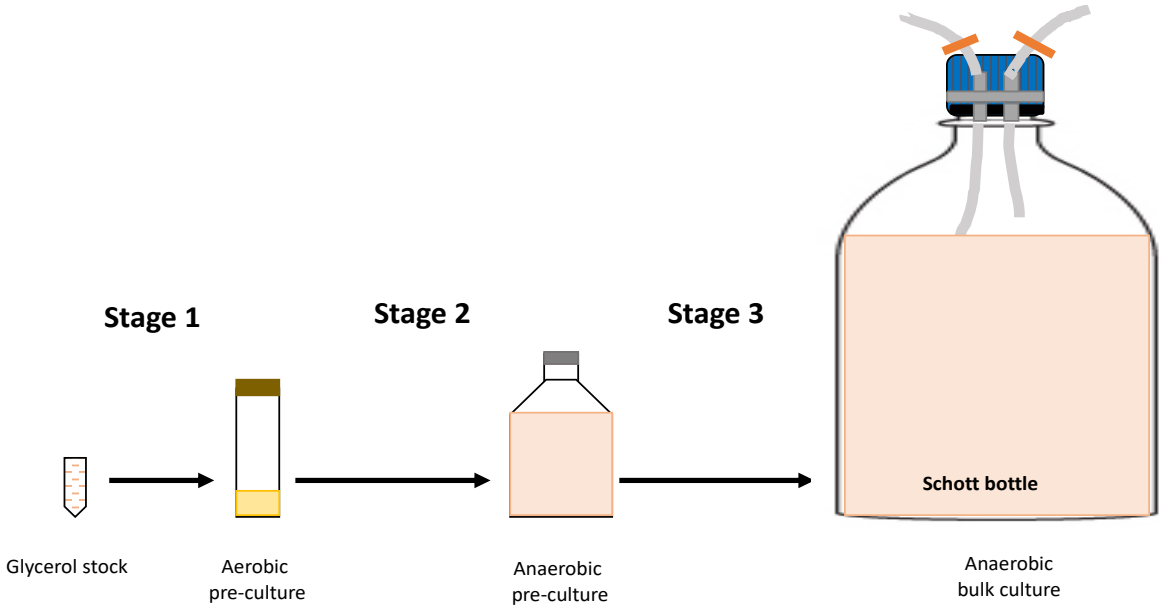

Figure 3-1 Flow diagram of the procedure for biomass growth. **Stage 1:** was the inoculation of the glycerol stock culture into the 5 ml aerobic preculture in LB media, the culture was incubated at 37°C overnight at 120 rpm. **Stage 2:** the aerobic culture was then use used to inoculate the anaerobic 100 ml supplemented LB preculture in the serum bottles. This preculture was incubated for 4-6 hours at 37°C at 120 rpm to ensure the cells are in the exponential phase. **Stage 3:** the exponential phase preculture was then used to inoculate the main 1L LB supplemented media in the modified Schott bottle. The main culture was incubated 37°C and left to stand over12-17 hours before harvesting

Figure 3-1 describes the multiple stages of pre-culture growth required to ensure maximum bulk cell growth under anaerobic conditions. Such pre-cultures were essential to ensure robust cell development during aerobic and anoxic growth conditions.

Preparation of the growth medium

To facilitate the growth of *E. coli,* Luria Bertani (LB) broth was used. This complex broth has sufficient nutrients to maintain good cell growth and is often used for this type of bacteria (Sezonov et al., 2007). All aerobically grown bacteria were grown in sterilised LB medium. In cultures grown anaerobically, the LB medium was first supplemented with 0.4% (w/v) sodium fumarate dibasic and 0.5% (v/v) of 100% (v/v) glycerol solution before sterilisation. These supplements were used as a terminal electron acceptor and an additional carbon source to assist cell cultivation under the anoxic environment (Appendix A.1).

The aerobic pre-culture was made in 20 ml McCartney bottles that contained 5 ml of sterile LB medium. To ensure an aerobic environment the headspace was four to five times the volume of the media (Will, 2015). In preparation for anaerobic pre-culture growth, 100 ml of the supplemented LB medium was added to 120 ml borosilicate-glass serum bottles and sealed with butyl rubber stoppers (Figure 3-1). The sealed media were autoclaved at high pressure and temperature (at 15 psi and 121°C for 20 min) to establish sterile, oxygen-free conditions, similarly achieved by sparging with nitrogen. For bulk anaerobic bacterial growth, large volume Schott bottles were modified to mimic the seals used in serum bottles (Figure 3-2).

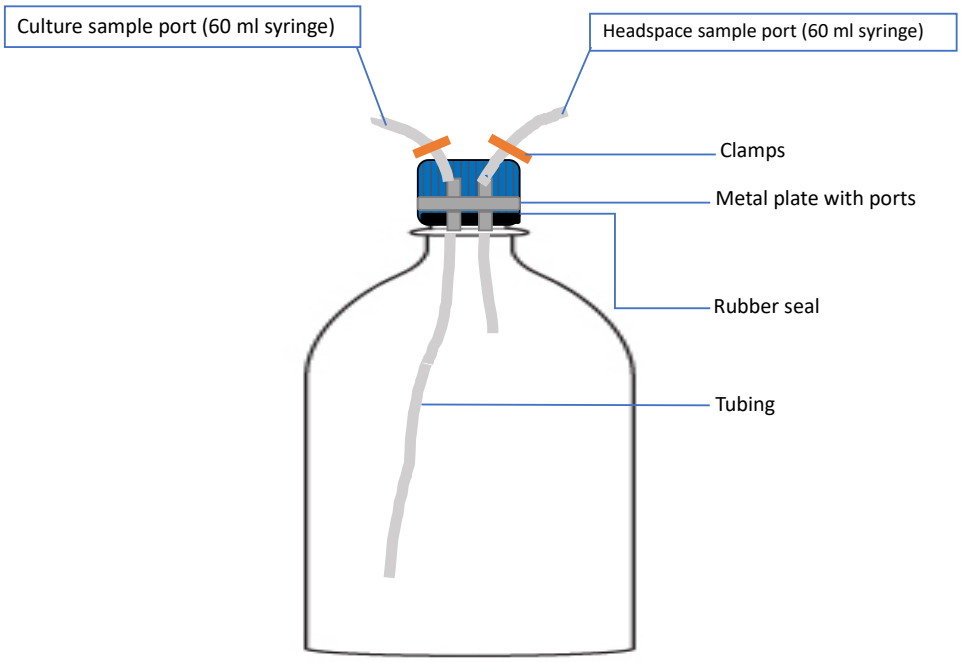

Figure 3-2 Schematic of the modified Schott bottle used for bulk biomass growth

The Schott bottle lids were cut to fit a metal plate that included two ports (Figure 3-2). One port was used for inoculation and sampling of the culture and the other for the release of any accumulated gas, such as carbon dioxide, hydrogen or methane, released during anaerobic respiration (Figure 3-2). A rubber seal was added around the rim of the metal cap to prevent any oxygen from entering the system. The Schott bottles, having a total volume of approximately 1.2 L, were filled with 1 L of supplemented LB medium. This minimised the head space in the vessel and reduced the likelihood of oxygen in the environment. To further ensure the absence of oxygen, the media was autoclaved under the same conditions as the pre-cultures.

Preparation of glycerol stock cultures

Glycerol stocks were used as starter cultures for the growth of biomass (Figure 3-1). These were prepared in bulk to minimise variation across experiments. Stock cultures were made by streaking a viable culture onto a LB agar plate. After incubation overnight at 37°C (an optimal growth temperature for the bacteria) a single colony from the plate was selected to inoculate into 5 ml of sterile LB medium within the McCartney bottle. This pre-culture was grown aerobically for 6-7 hours at 37°C on a platform shaker at 120 rpm and was thereafter used to inoculate 50 ml of sterile LB medium. The culture was then grown aerobically overnight at 37°C on the same shaker. After this final incubation, fresh stock cultures were prepared by adding 1 ml of the liquid biomass culture to 1 ml of sterilised 50% (v/v) glycerol solution. The 2 ml glycerol stocks were then stored at -60°C to preserve the cells for later use. This method made a maximum of 40-50 glycerol stocks and ensured sufficient seed cultures for large volume experiments.

Bulk E. coli culture growth

The bulk growth of biomass for nanoparticle production was initiated by inoculating the 5 ml aerobic medium with a pre-made glycerol stock (Figure 3-1, Stage 1). To achieve high cell densities, the seed culture was grown aerobically overnight at 37°C on a platform shaker at 120 rpm. The supplemented anoxic pre-culture medium in the serum bottle was thereafter inoculated with 5 ml of the aerobic pre-culture from the McCartney bottle and left at 37°C at 120 rpm for 4 to 6 hours (Figure 3-1, Stage 2). This reached optical densities between 0.5 to 0.7, which was indicative of exponential growth (Appendix A:). Under such anaerobic conditions the *E. coli* expresses hydrogenase enzymes that are known to assist in nanoparticle formation (Pinske et al., 2011a).

Approximately 50 ml of this anaerobic pre-culture was used to inoculate the 1 L anoxic medium within the modified Schott bottle (Figure 3-1, Stage 3). The 1 L stationary culture was then allowed to grow overnight at 37°C. Limiting the stirring of the culture inhibited any oxygen transfer within the system, maintaining an anaerobic environment. After incubation for 12 to 17 hours, the culture entered the stationary growth phase. The Gensys UV-Vis spectrophotometer was used to measure the optical density (OD) of the biomass at 600 nm. This reading was used to confirm the dry cell weight (DCW) of the biomass as predicted from previously obtained OD-DCW correlations (Appendix A.2 and B.3). The resting cells, of a 1 L total volume, were then harvested via centrifugation at 7000 rpm for 10 minutes at 4°C using a Beckman Avanti J-E or Avanti J-25 centrifuge with JA-10 rotor. Under such conditions the shear on the cells and enzyme deactivation was prevented.

Once the cells were separated from the supernatant, the cell pellet was washed three times in 20 mM of MOPS-NaOH buffer (pH 7) to ensure that remaining salts or other impurities were not attached to the pellet (Bunge et al., 2010; Deplanche et al., 2010; Lloyd et al., 1998; Torgeman, 2017). This MOPS-NaOH buffer was prepared beforehand and degassed via sonication while the cell pellet was being harvested (Appendix B.1). The cell pellet was then resuspended in a MOPS-NaOH buffer that was five times less than the growth culture volume (Torgeman, 2017). The cell pellet in MOPS buffer was mixed using a vortex to establish a pseudo-homogeneous solution. The mixture was stored on ice at 4°C to prevent denaturing of the enzymes and cell death. Biofabrication of the metal nanoparticles on the biological supports were performed on the day of harvesting to ensure maximum viability of the cells. (Deplanche et al., 2011a; Torgeman, 2017; Zhu, 2014)

3.2 Metal nanoparticle preparation

Nanoparticle catalysts were prepared following a series of steps tailored according to the selected metal (Figure 3-3).

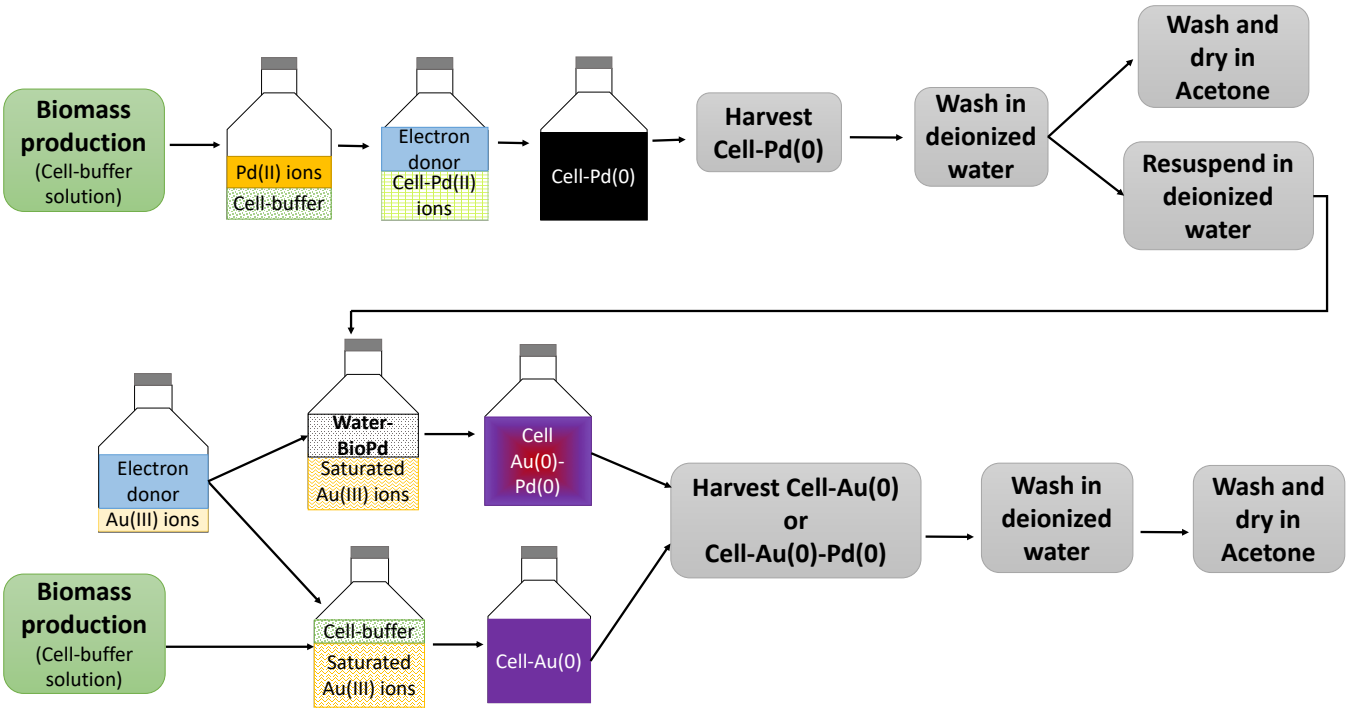

Figure 3-3 Flow diagram showing the process of forming biofabricated Pd, Au and Au-Pd nanoparticle catalysts

In synthesising the biofabricated catalysts a stepwise approach was followed. Initially the metal precursor was solubilised and then added to the microbial cells to facilitate biosorption. Depending on the metal, the electron donor was added either after the addition of the cells or before cell addition to ensure the saturation of the solubilised ion solution. The addition of the electron donor in either case promoted metal ion reduction before the resulting biofabricated catalysts were harvested (Figure 3-3).

3.2.1 Metal salt precursor preparation

The metal salt precursor used during nanoparticle formation was first dissolved in acidified water to promote the dissociation of the metal ions in solution. The acidified water was prepared in bulk (500 ml) by adjusting the pH of deionized water to 2.3 using 0.1 M nitric acid (HNO_3). An aqueous 2 mM Pd(II) ion solution was generated by dissolving sodium tetrachloropalladate (Na_2PdCl_4) in the required volume of acidified water. Similarly, 1 mM aqueous Au(III)-solution was prepared by dissolving gold(III) chloride trihydrate ($HAuCl_4.3H_2O$) in newly prepared acidified water. A sample calculation may be found in the Appendix B.2 (Deplanche et al., 2011a; Torgeman, 2017; Zhu, 2014)

3.3 Forming biofabricated nanoparticles: metal adsorption and reduction

3.3.1 Pd nanocatalysts

Once the metal precursor was prepared, a pre-determined volume of the cell/MOPS-NaOH buffer suspension and a corresponding volume of 2 mM Pd(II) precursor solution was added to 120 ml borosilicate, serum bottles. The amount of metal ion solution added to the buffer was determined by the ratio of the metal weight to the cell dry weight required to achieve the desired biofabricated catalyst metal loading (Table 3-1). An extended sample calculation is provided in Appendix B.4.

Table 3-1 Relationship of metal weight and cell mass to obtain the specified metal loading. The cell pellet is suspended in a 20 mM MOPS-NaOH buffer (at pH 7). The provided metal precursor volumes are based on the reduction of 2 mM Pd(II) and 1 mM Au(III) on 0.1 g of *E. coli* ATCC25922. In the case of a bimetallic catalyst, a 1:1 ratio of Pd to Au (by weight) was considered

Ratio	Metal loading % (w/w)	Volume of cell buffer (ml)	Volume of Pd(II) precursor (ml)	Volume of Au(III) precursor (ml)
1:38.5	2.5%	2.7	12.4	13.3
1:19	5%	2.7	25.0	26.9
1:9	10%	2.7	52.9	56.8
1:4	25%	2.7	118.9	127.9

To form the Pd nanocatalyst, the cell-Pd(II) ion suspension was sparged with nitrogen (N_2) for approximately 1 minute immediately after the cells were added to the serum bottle. Once sparged, the vessel was sealed with a butyl rubber stopper to maintain an anoxic environment. The sealed serum bottles were left to stand at 30^{o}C for 30 minutes during which time biosorption of the Pd(II) ions onto the microbial supports occurred. After biosorption, the residual metal ion concentration in solution was determined via the stannous chloride colourmetric assay (Section 3.4.1). Thereafter, a chemical (sodium formate) or gaseous (hydrogen) electron donor was introduced to the system.

When using the chemically based electron donor, 50 mM sodium formate solution was added to the adsorbed ion mixture so that a 20 mM final concentration of the chemical donor was achieved. Alternatively, a 10% (v/v) hydrogen (H_2) to argon mixture was used when introducing the gaseous electron donor. This electron donor was sparged into the metal ion solution at 200 ml/min to 300 ml/min for 20 minutes (Zhu, 2014). Any gas built up in the serum bottle was released into a water trap as illustrated in Figure 3-4.

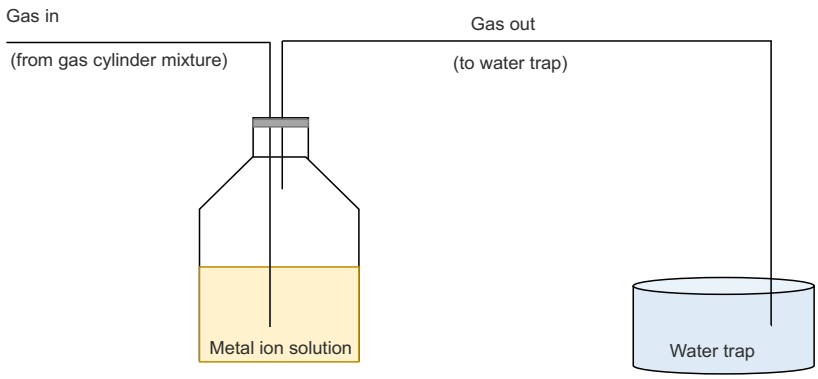

Figure 3-4 Schematic of the hydrogen electron donor sparging system. The gaseous electron donor was sparged in solution to allow for maximum contact between the gas and the metal ion precursor

In this system (Figure 3-4), access of air into the vessel was restricted once the gas cylinder was closed. After sparging, the metal-cell mixture was left to stand overnight at 30°C to allow for the solids to settle under gravity. During this period, a colour change of the solution from yellow to grey-black occurred indicating the reduction of Pd(II) to Pd(0). The Pd(0) nanoparticles bound to the cell were then harvested via centrifugation at 7000 rpm for 10 minutes at 4°C (Beckman Avanti J-E or Avanti J-25 centrifuges with JA-20 rotor). For the monometallic catalysts, the solid cell-Pd(0) pellet was then washed two to three times with deionised water and once with acetone to remove any excess reagents. The cell-Pd(0) pellets were then resuspended in 5 ml of acetone and left to dry overnight in air at atmospheric conditions (Deplanche et al., 2011a; Torgeman, 2017; Zhu, 2014).

3.3.2 Au nanocatalysts

To form Au nanocatalysts, the solubilised gold metal salt precursor volume, determined by the required metal loading in Table 3-1, was sealed in a clean serum bottle and sparged with nitrogen. Sparging of the serum bottles ensured anoxic conditions before adding 50 mM sodium formate to a final concentration of 20 mM. When hydrogen was used as the electron donor, the gold solution was sparged with the 10% (v/v) (H_2/Ar gas mixture at 200 ml/min to 300 ml/min for 60 minutes using the same configuration as illustrated in Figure 3-4. Sparging over this extended period ensured that the metal ion solution was saturated with hydrogen. The longer time required for hydrogen sparring is due to the fact that metals in group 10 of the periodic table (Cu, Au and Ag), unlike other transition metals, have weak interactions between the metal and hydrogen (Yu et al., 2013). Saturation with hydrogen ensures Au-H binding to some extent. After introducing the electron donor, the cell-buffer solution was transferred into the same serum bottle. Once the Au(III) ions adsorbed onto the biological support, the residual ion in solution could be assessed using the thiamine-nitrate assay (Section 3.4.2). During incubation at 30°C the serum bottles were agitated overnight at 120 rpm to promote the reduction of Au(III) to Au(0) on the bacteria. A colour change from pale yellow to an intense purple/dark-red confirmed Au(0) nanoparticle formation. The reduced nanoparticle catalysts were recovered via centrifugation at 7000 rpm for 10 minutes at 4°C. Similar to the Pd nanoparticle preparation, cell-Au(0) pellets were washed three times with deionised water, once in acetone and re-suspended in 5 ml of acetone and left to dry overnight in air.

3.4 Spectrophotometric assays

3.4.1 The stannous chloride ($SnCl_2$) assay for detecting residual Pd(II) ions

The $SnCl_2$ assay was used to detect the amount of residual Pd(II) ion in solution, in accordance to previous investigations for similarly prepared biofabricated catalysts (Ayres and Alsop, 1959; De Vargas et al., 2004; Deplanche et al., 2014). The required reagent was prepared by dissolving 1 g of $SnCl_2$ powder in 16.7 ml of 2 M HCl. In a plastic cuvette the assay was initiated by adding 0.2 ml of samples from either the reduction or adsorption supernatant to 0.8 ml of the $SnCl_2$ reagent. The 4 ml cuvettes were placed back into the cuvette box to prevent spillage and then incubated at 30°C for one hour at 120 rpm. During incubation, the chloride ions (Cl^-) from $SnCl_2$ binds to available Pd(II) ions creating a complex as described by the mechanism in Equation 3-1.

$$Sn^{2+} + 2Cl^- + Pd^{2+} \rightarrow Sn^{2+} + Pd^0Cl \qquad \text{Equation 3-1}$$

The formation of the Pd^0Cl complex in Equation 3-1 turned the solution green in colour. The intensity of the solution increased with increasing temperature and time. Absorbance was monitored after the recommended incubation period using the Gensys UV-Vis spectrophotometer at 463 nm. A calibration curve showing the relationship between absorbance and metal ion concentration is provided in the Appendix C.1.1. A blank was similarly prepared replacing the metal ion with acidified water. The assay accounted for the dilution of the residual metal ions as a result of biosorbent and buffer addition (see Appendix C.1.1) (Ayres and Alsop, 1959; Deplanche et al., 2014).

3.4.2 The thiamine-phloxine assay for detecting residual Au(III) ions

The thiamine-phloxine assay was used to determine residual Au(III) ion in solution. The assay was performed on 0.2 ml samples from either the reduction or adsorption supernatant. To this sample various reagents were added; namely 0.2 ml of 10 mM thiamine nitrate, 0.2 ml of 1 mM phloxine B solution, 0.9 ml of deionised water and 0.4 ml of an EDTA-citrate buffer. EDTA (in the form of the trisodium salt) and citric acid were combined to achieve 0.05 mM EDTA and 0.1 mM citric acid in the stock to achieve a final pH of 4.6. In addition to these chemical reagents, 0.1 ml of 0.5% (w/v) methylcellulose (MC 25) was added to the assay vessel. Methylcellulose was carefully prepared using a procedure outline in Appendix C.2 to ensure that the reagent remained in solution (Deplanche and Macaskie, 2008; Fujita et al., 1999). In preparation, the gold ion initially binds with the thiamine ligand. After the phloxine dye is added, a Au:thiamine:phloxine complex is produced at a molar ratio of 1:2:2, respectively. The formation of this complex brings about a colour change in solution that is detected by the spectrometer. The buffer in this assay is used to regulate pH, while the surfactant MC 25 prevents the precipitation of the complex (Fujita et al., 1999).

Once the solutions were prepared at the required pH and concentration, the relevant quantities were transferred into cuvettes and then incubated at 40°C for 20 minutes and 120 rpm. The

presence of Au(III) ions was indicated by the solution turning from a pale yellow to an intense purple/red colour. Absorbance of the aqueous gold samples was measured using the Gensys UV-Vis spectrometer at 570 nm; and was comparatively measured against a blank prepared in the same manner as the experimental sample replacing the ion solution with acidified water. The concentration of residual Au(III) in solution was determined using a calibration curve showing the relationship between absorbance and metal ion concentration (*viz.* Appendix C.2).

3.5 Adsorption kinetics and equilibrium isotherms

3.5.1 Assessing adsorption kinetics

Adsorption was initiated by the addition of the biosorbent to the ion solution. For this experiment a 5% and 25% (w/w) metal loading was used on all supports. To accurately observe adsorption onto the bacteria, samples were taken from the reaction vessel over an extended 60 minute biosorption period at 30°C without agitation. Over the one hour period, samples were taken every 5 minutes for the first 30 minutes and then approximately every 10 minutes thereafter. The collected samples were centrifuged at 13000 rpm for 2 minutes at 4°C to separate the pellet and supernatant in a Eppendorf 5418R microcentrifuge. The supernatant was thereafter decanted and stored at 4°C. In the absence of an electron donor, removal of the pellet at low temperatures (4°C) limited any influence that promoted reduction of the residual metal ions in the stored sample solution.

3.5.2 Assessing adsorption at equilibrium

Adsorption at equilibrium provides an essential understanding of the maximum capacity of the various supports and provides insight into the mechanism of adsorption of metals such as Pd and Au. A similar reaction system setup to the kinetic experiments was used to assess adsorption at equilibrium (Section 3.5.1). However, for this investigation the initial metal ion concentration was varied from 1 mM, 2 mM, 5 mM, 7 mM and 10 mM. The effect of varying this initial ion concentration on biosorption was observed by taking samples from the reaction vessel after the fourth day to validate equilibrium. As with the samples extracted during the kinetics experiments, the samples were centrifuged after which the liquid was extracted and stored at 4°C. The residual metal ion concentration of the samples were analysed using either the stannous chloride (Pd) or thiamine-phloxine (Au) colorimetric assays.

3.6 Characterisation techniques

Biofabricated catalysts using the techniques outlined in Section 3-1-3.5 were developed on *E. coli* DH5α, *E. coli* ATCC25922 and *E. coli* BL21DE3 supports using multiple metals (Pd and Au), electron donors (sodium formate and hydrogen) and metal loadings (5% - 25% w/w) as outlined in Table 3-2.

Table 3-2 Summary of all possible catalyst made under various metals, metal loadings, microorganisms and electron donors

Metal	Metal loading (w/w)	Microorganisms	Electron donor
Pd	5%	*E. coli* DH5α	Sodium formate
Pd	5%	*E. coli* DH5α	Hydrogen
Pd	5%	*E. coli ATCC25922*	Sodium formate
Pd	5%	*E. coli* ATCC25922	Hydrogen
Pd	5%	*E. coli* BL21DE3	Sodium formate
Pd	5%	*E. coli* BL21DE3	Hydrogen
Pd	25%	*E. coli* DH5α	Sodium formate
Pd	25%	*E. coli* DH5α	Hydrogen
Pd	25%	*E. coli* ATCC25922	Sodium formate
Pd	25%	*E. coli* ATCC25922	Hydrogen
Pd	25%	*E. coli* BL21DE3	Sodium formate
Pd	25%	*E. coli* BL21DE3	Hydrogen
Au	5%	*E. coli* DH5α	Sodium formate
Au	5%	*E. coli* DH5α	Hydrogen
Au	5%	*E. coli* ATCC25922	Sodium formate
Au	5%	*E. coli* ATCC25922	Hydrogen
Au	5%	*E. coli* BL21DE3	Sodium formate
Au	5%	*E. coli* BL21DE3	Hydrogen
Au	25%	*E. coli* ATCC25922	Hydrogen

These nanoparticle catalysts were characterised according to their particle size, distribution and morphology using multiple analytical techniques. These included Transition Electron Microscopy (TEM), Scanning Electron Microscopy (SEM), Fourier Transform Infrared Radiation (FTIR) and Inductively Coupled Plasma (ICP) analyses.

3.6.1 TEM analysis and preparation

TEM analysis provides a cross-sectional view of the samples and was used to determine the size, distribution and the morphology of the nanoparticles and the support. Energy dispersive X-ray (EDX), often used in conjunction with TEM, was used to confirm the elemental composition of the nanoparticles present within the support.

Preparing biofabricated catalysts for TEM analysis is challenging as bacterial cells are composed of 20% solids with the remainder made up of water contained within a permeable membrane (Feijó Delgado et al., 2013). Consequently, vacuum conditions applied during

analysis rupture the cell, negatively affecting the results (Kiruthika, n.d.; National diagnostics, n.d.). To prevent this from occurring the cells need to be turgid with all water removed. A further challenge of TEM analysis included the vast difference in the composition between the biological support and the metallic component. As the cell is carbon-based, it has a lighter atomic weight compared to the metal nanoparticles. This results in the support being less defined under electron microscopy. Dye staining is therefore required to adequately define the support structure (Kiruthika, n.d.; National diagnostics, n.d.). TEM sample preparation therefore included (1) fixing the biologically supported catalysts to ensure turgidity of the cell walls or proteins, (2) dehydration of the cell, (3) incorporating the sample into a resin and (4) sectioning of the sample into thin segments.

Fixing of the biofabricated catalyst support

Before washing and drying the catalyst, 0.1-0.2 ml samples of the suspended nanoparticles were extracted into 2 ml Eppendorf tubes. These samples were washed two to three times in deionized water, and then in a fixative solution composed of 2.5% (w/v) glutaraldehyde solution in phosphate-buffered saline (PBS) buffer. The catalyst-buffer solution was left at rest to incorporate overnight at 4^{o}C. During this period the cell structure was stabilised by the cross-linking of proteins, promoted by the fixative. After the stabilization period, the mixture was centrifuged under ambient temperatures for 2 minutes at 13000 rpm to remove the fixative. The solid catalyst sample was then washed with pre-made PBS buffer. Thereafter, the pellet was re-suspended in approximately 0.5 ml of PBS buffer and an equal volume of 1% (w/v) osmium tetraoxide (OsO_4) fixative solution. This fixative solution was left to incorporate for one hour after which the osmium tetraoxide mixture was centrifuged to separate the suspended particles from the liquid phase at 13000 rpm for 2 minutes at ambient temperature. The remaining pellet was washed twice in PBS buffer and then in deionised water to remove any excess osmium and PBS present.

Dehydration and resin incorporation

Once the cell was fixed, dehydration of the cell was performed serially using increasing concentrations of ethanol (at 30%, 50%, 70%, 80%, 90%, 95%, 100% v/v) followed by a final wash in 100% (v/v) acetone. Gradual dehydration was performed to ensure the cells were not shocked by the immediate introduction of high ethanol concentrations that may contribute to the disruption of the cell structure. Serial dehydration followed a repeated procedure of resuspending the cells in a small volume of ethanol that sufficiently covered the pellet. The suspended cells were then left to stand, at rest, for 5 min at ambient temperature after which the mixture was centrifuged at 13000 rpm to separate out the ethanol supernatant for 2 minutes at ambient temperatures. This process was repeated for each of the increasing ethanol concentrations up to 95% (v/v). For the 100% (v/v) ethanol and 100% (v/v) acetone solutions the aforementioned procedure was repeated twice.

After the final acetone wash, the pellet was gradually introduced to the resin by resuspending the dehydrated pellet in a mixture of equal volume of Spurr's resin and 100% (v/v) acetone

and placed on a roller at room temperature. The concentration of the resin was gradually increased to 100% (v/v) resin over 2-3 days allowing the steady incorporation of the resin into the cells. After incorporating the resin within the cells, labelled plastic tubes were used to create resin moulds of the sample. A drop of approximately 0.1 ml of 100% (v/v) resin was placed at the bottom of each plastic tube ensuring that no air bubbles were formed. Any air bubbles present were removed with the aid of a hypodermic needle and syringe. Once all air bubbles were removed, approximately 5-10 mg of the resin-incorporated catalyst was added to the mould. The mould was then filled to the brim with resin and left overnight in an oven at 60^{o}C, to harden. Each catalyst sample was prepared in duplicate.

Staining and sectioning of samples

In preparation for TEM analysis the hardened catalyst-resin moulds were cut to provide a cross-section through the catalyst. A trapezium 1.0 x 0.75 μm in size containing catalyst was cut out of the tip of the mould and sectioned using a diamond knife. The diamond knife is used as it is a robust material which is resistant to micro-scratches and thus ensures precise and smooth images. The thin trapezium sections were then placed on a copper grid for viewing under TEM. For the purpose of viewing the cell structure, sample sections were stained with 1% (v/v) osmium tetraoxide. As staining impairs the visibility of smaller nanoparticles (< 5 nm) on the cell (Torgeman, 2017), duplicate sections of the samples that were not stained were prepared. The unstained sample sections were used for particle size distribution analyses

All analysis was performed with the assistance of Mr. Mohamed Jaffer, at the Electron Microscope Unit, University of Cape Town. The analysis was conducted on either the FEI F20 CYRO FEGTEM or FEI F20 TEM.

3.6.2 SEM analysis and preparation

SEM analysis was used to image the exterior surfaces of the biofabricated nanoparticle catalysts. Images using this technique are generated as a result of an incident electron beam interacting with the catalyst sample (Nebraska Center for Materials and Nanoscience, n.d.). This produces secondary as well as a backscattering of electrons (BSE). The BSE allows for the classification of elements based on their atomic number with higher atomic number elements showing up as brighter regions on the final image (Nebraska Center for Materials and Nanoscience, n.d.).

If any particles were noted on the exterior of the cell during TEM imaging, the sample was then sent for SEM analysis. Following drying with acetone during catalyst formation, the samples were then spread onto graphite tape to dry further until all visible moisture was absent. Any non-conductive materials such as the microbial cells, were coated with graphite to improve instrument detection. Energy Dispersive Spectrometry (EDS) is often complimentary to SEM analysis. Each periodic element has a specific layer of electrons that act uniquely when the electrons are excited allowing the elemental composition of the metals present to be identified the sample (Nebraska Center for Materials and Nanoscience, n.d.).

3.6.3 Assessing support functional groups using FTIR

Hydroxyl, amine and thiol functional groups present on the microorganisms are considered to play a vital role in the adsorption of metals onto the cell (Bunge et al., 2010; Deplanche, 2008; Rotaru et al., 2012). The abundance of functional groups could vary depending on the strain and is essential to quantify. Molecules and functional groups can exhibit vibrations, rotational changes and jumps in electron energy once they have been subjected to electromagnetic radiation at a specific frequency (Reusch, 2013; Soderberg, 2020). Infrared radiation excite the electrons, to promote vibrational energy changes. Each functional group has a specific wavelength under which stretching and bending are observed. These vibrational changes present as strong sharp or broad bands with varying intensity on the FTIR spectrum (University of California Department of Chemistry, n.d.; University Of Missouri–St. Louis, 1997). Stretching of particular functional groups appear at known wavelengths that are easily identified using the available databases.

Functional groups associated with different support strains were assessed using crushed catalyst for powder FTIR-ATR with the assistance of Associate Professor Greg Smith, Department of Chemistry, University of Cape Town. For this analysis, the catalyst was streaked onto a glass plate and left to dry in acetone at 37^{o}C prior to the catalyst being ground to a fine powder using a pestle and mortar (Deplanche et al., 2011a; Torgeman, 2017; Zhu, 2014). Approximately 5 mg sample of each of the catalysts was used for analysis for each of the *E. coli* strains (BL21DE3, DH5α, ATCC25922) considered.

3.6.4 Assessing metal loading using ICP

Confirmation of the composition of the metal present on the support was required to ensure that the intended concentration of metal was reduced and maintained on the bacteria. ICP analysis was preformed using the Varian 730 ES ICP-Optical Emission Spectrophotometer. The samples were analyzed by S. Klink, S. Nyimbinya and R. Geland in the Analytical Laboratory in the Department of Chemical Engineering at the University of Cape Town. Initially 10 mg of the crushed catalyst in McCartney bottles was dissolved using 4-5 drops HNO_3 (0.1M) and suspended in 20 ml of deionized water. As 0.1 M HNO_3 was not strong enough to leach the metal, a stronger acid was used. The samples in the McCartney bottles were resuspended in a new vessel using 5 ml of Aqua Regia. An additional 10 ml of Aqua Regia was added to the new vessel with the sample. The solution (15 ml in total) was boiled down on a hot plate to decrease the volume and until the solid samples could not be visually detected. The sample was filtered using a 0.2 µm filter and 2.5 ml of the sample was then added to a 25 ml volumetric flask. The remaining volume in the flask was made up using a 2% (by weight) HNO_3 solution. A similar method was used to prepare standards of the metal ion at 0.2, 0.5, 1, 2, 5 and 10 ppm.

3.7 Catalyst activity tests

Once the various catalysts had been effectively characterized, activity tests were conducted. The activity tests were done to assess the performance and applicability of the catalyst to an industry relevant reaction. This activity was defined by the ability of the catalyst to promote the conversion of the alcohol to the corresponding aldehyde with high selectivity.

3.7.1 Radley reactor activity testing

After inactivity of the catalyst in the Amber vial system at ambient conditions, the Radley reactor was used to determine the activity of the catalyst. This reactor system had a maximum pressure rating of 1 psi (0.069 bar). Unlike the amber vials, direct supply of the oxidant to the reagents could be achieved in these reactors. The Radley reactor system consisted of several glass reaction vessels, a temperature probe, a carousel reactor with a hot plate as well as a cooling system and gas inlet port (Figure 3-5)

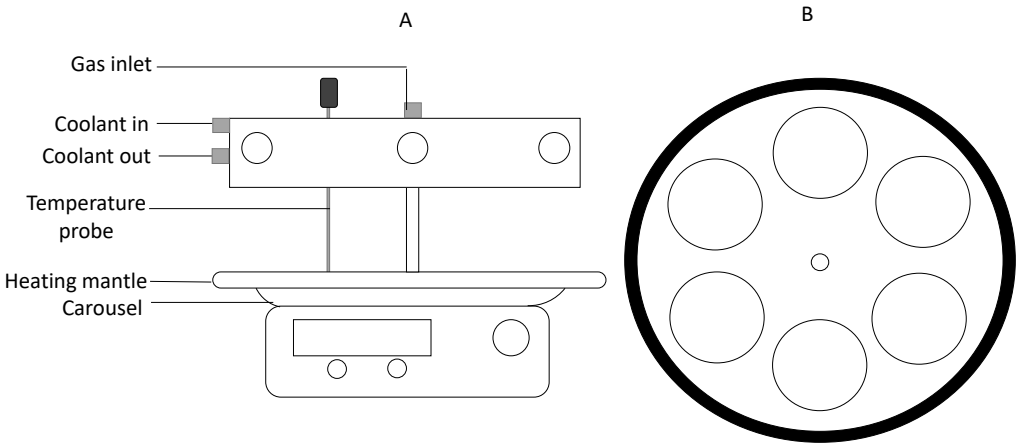

Figure 3-5 Schematic of the front view of the reactor setup (A) and the top view of the carousel with six reactor vessel slots (B)

To perform the reaction, each reactor vessel was assigned a specific role in all experiments. The vessels were set up to ensure each catalyst was analysed in duplicate with two additional vessels allocated as a negative control and a control for monitoring the operating temperature of the reaction solution (Figure 3-5.B). The negative control was operated in the absence of the catalyst, containing only the reactant. This eliminated the potential for any catalytically promoted product being formed. The temperature control vessel was filled halfway with water to monitor the operating temperature and to ensure it was maintained at the specified reaction conditions throughout the experiment. Within the Radley reactor, activity testing conditions were performed by loading the catalyst in 10 ml of substrate, either benzyl alcohol or 1-octanol (see Appendix D.2 for reagent details). Benzyl alcohol, unlike the aliphatic alcohol, was selected as the control reaction as it has been well established in literature and can serve as a way to compare the activity of the biofabricated catalyst to other catalyst systems. However, as previous investigations considered n-octane as the model compound for the bio-catalytic activation of alkanes the resulting 1-octanol product would be the ideal feed for an integrated tandem valorization approach. To ensure the most active catalyst was selected, the control

reaction was used as a screening method whereby the most active catalyst was chosen for the oxidation of 1-octanol.

Each reaction was performed at 90°C and 250 rpm with a continuous supply of air over a 6 hour period at 1 bar. At the higher metal loading the volume of reagent was reduced to 4 ml to keep the percentage catalyst loading constant.

3.7.2 Reaction sampling for product analysis

After the completion of each reaction, approximately 1 ml of sample was extracted from each reactor vessel into an Eppendorf tube to identify the products formed. The Eppendorf tube was kept on ice to halt the reaction and limit the loss of any volatile products. To extract the liquid product, the catalyst-liquid mixture was centrifuged to separate the supernatant from the catalyst pellet. Once separated, the supernatant was decanted into a fresh Eppendorf tube. The supernatant sample was centrifuged once more to ensure settling of any catalyst still present. All centrifugation was performed at 13000 rpm for 5 min at 4°C. After the liquid component was decanted into a new Eppendorf tube, the sample was kept on ice to be analysed by gas chromatography (GC).

3.7.3 Liquid phase gas chromatography

GC analysis was used to determine the products formed during activity testing. The Varian 3900 CP-8410 equipped with a flame ionization detector (FID) was used for the quantification of these products. The Agilent J & W column (VF-5 ms, Part number CP8961) was found to be suitable for detecting hydrocarbons. The dimensions of the column were set at 60 m x 0.32 mm x 0.25 μm (L x W x D). For this analysis the column consisted of a 5% phenyl-methylpolysiloxane stationary phase while nitrogen gas was used as the mobile phase. To ensure an accurate analysis and identification of any products, samples were prepared as illustrated in Figure 3-6.

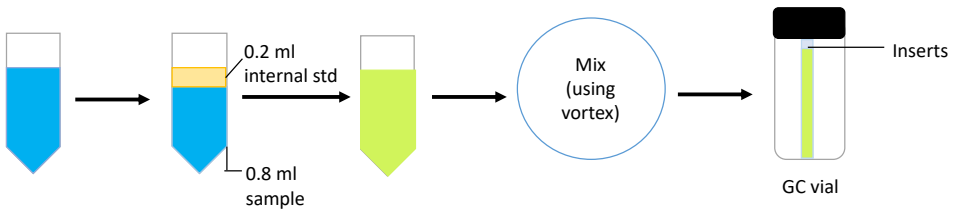

Figure 3-6 Schematic of the preparation process for GC analysis of reaction samples

For the preparation of samples for analyses, 0.8 ml of the stored supernatant sample was added to an eppendorf tube together with ~~an~~ 0.2 ml of internal standard consisting of 2 mM of 1-decanol in ethyl acetate (Figure 3-6). The 1-decanol compound (of a known retention time) was selected as the internal standard. The sample, internal standard and solvent were mixed for approximately 10 seconds using the vortex. Lastly, 200 μl of this mixture was extracted

into GC inserts within vials and sealed for analysis. The GC program used for the analysis of alkanes and other hydrocarbons is provided in Table 8-8 (see Appendix D.1).

Standard curves were generated for all of the products identified and are presented in Appendix D.3. This was done using the same preparation and GC protocols used for the reaction samples From the conversion of benzyl alcohol and 1-octanol various products were detected each with a specific retention times (Table 8-9 in Appendix D.2). The products described in Table 8-9, were identified by injection of the near pure compound into the GC and comparing the retention achieved to those produced in reaction sample chromatograms.

Chapter 4

4 Biosorption of Pd and Au on *E. coli*

4.1 Chapter Overview

In this chapter biosorption characteristics of Pd(II) and Au(III) onto *E. coli* DH5α, *E. coli* ATCC25922 and *E. coli* BL21DE3 were investigated to determine the most suitable strain to biofabricate nanoparticle catalysts. Predictive models were used to further understand the mechanism of ion adsorption and to establish parameters that best describe metal adsorption under varying conditions, such as precursor concentration, and support type. The kinetic and equilibrium adsorption characteristics of the selected *E. coli* strains for Pd(II) and Au(III) ions were also considered.

4.2 Adsorption of Pd onto *E. coli* scaffolds

4.2.1 Adsorption kinetics and equilibrium isotherm analysis

The adsorption of metals by bacteria can occur primarily via bioaccumulation to be used within the cell or for the detoxification of the cell environment. The manner in which metals interact with the bacteria depend on the type of microorganism and strain (De Vargas et al., 2004; Deplanche et al., 2014). In this study, the degree to which the bacteria can accumulate metal ions was assessed for three different *E. coli* strains, namely *E. coli* DH5α, *E. coli* ATCC25922 and *E. coli* BL21DE3. Using the protocols outlined in Chapter 3, kinetic experiments were performed anaerobically at 30^{o}C with a starting solution pH of 5.6. Aliquots of approximately 0.5 ml were extracted every 5 minutes for the first 30 minutes and every 10 minutes thereafter. These samples were then analysed using the $SnCl_2$ assay to determine the Pd(II) concentration (Section 3.4.1). The amount of metal adsorbed was normalized on a dry cell mass (g) basis, ensuring comparison across different absorbates (Figure 4-1, Figure 4-2).

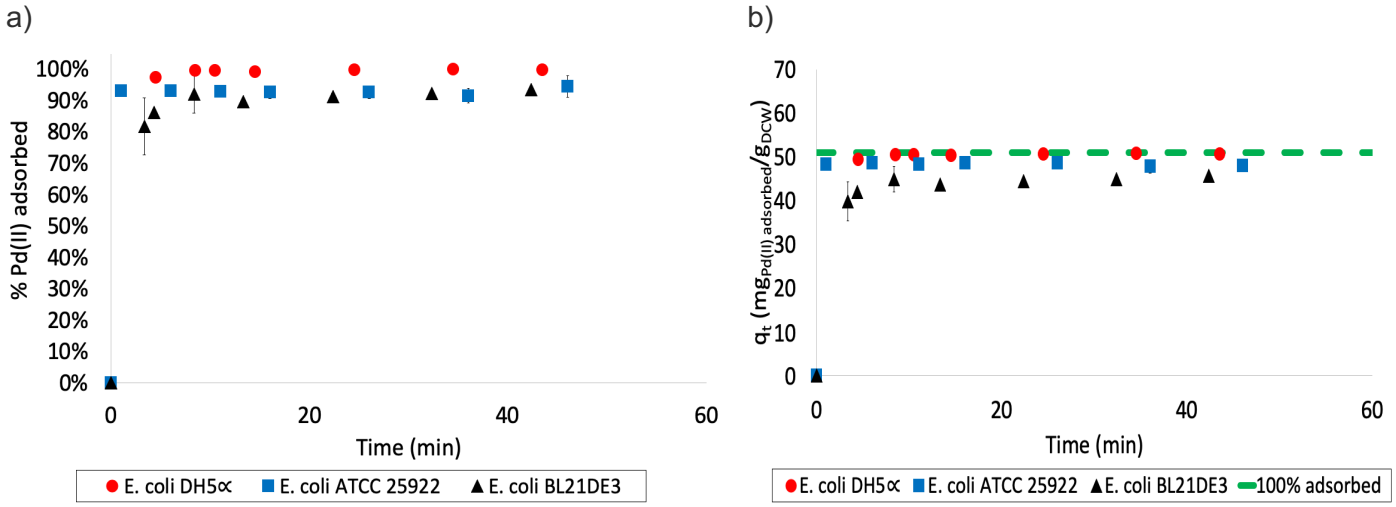

Figure 4-1 Adsorption of Pd(II) on *E. coli* DH5α (●), *E. coli* ATCC25922 (■) and *E. coli* BL21DE3 (▲) performed at 30°C and 120 rpm. Where a) is the percentage of Pd ions adsorbed over time and b) is the adsorption capacity qt ($mg_{Pd(II)\ adsorbed}/g_{DCW}$) with time. A 2 mM sodium tetrachloropalladate solution (pH2.3) was used as the metal precursor. A constant dry cell weight (DCW) of 0.2 g was maintained at the 5% (w/w) Pd loading

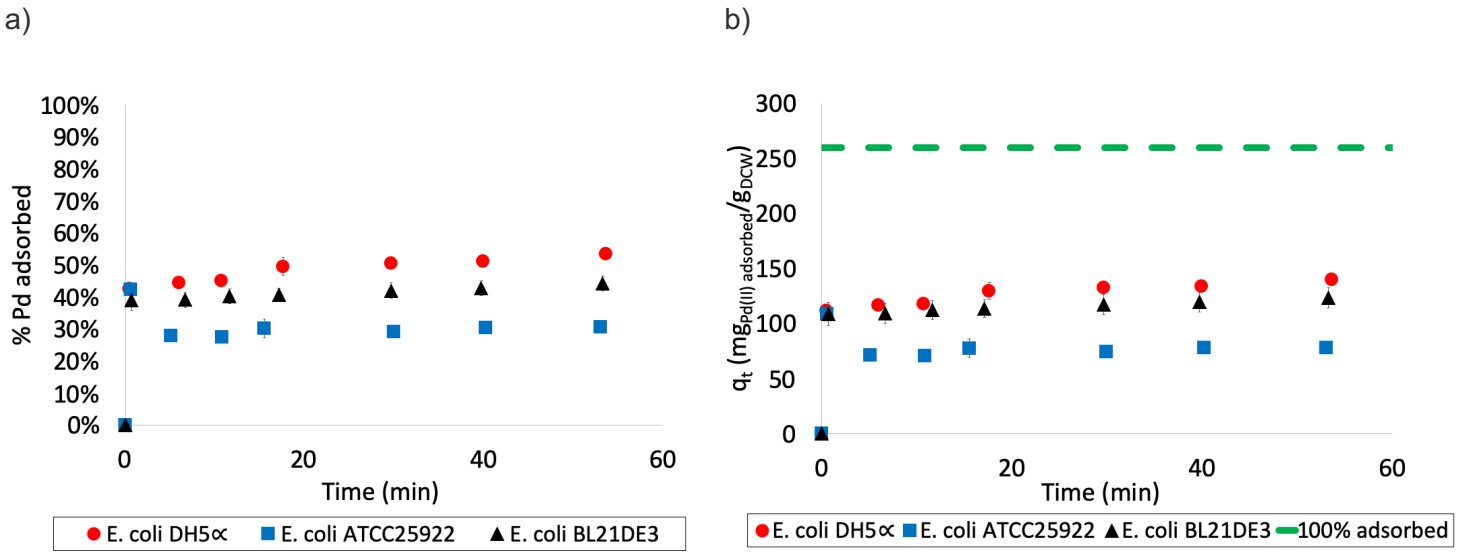

Figure 4-2 Adsorption of Pd(II) onto *E. coli* DH5α (●), *E. coli* ATCC25922 (■) and *E. coli* BL21DE3 (▲) was performed at 30°C and 120 rpm. Where a) is the percentage of Pd ions adsorbed over time and b) is the adsorption capacity qt (mgPd(II) adsorbed/gDCW) with time. A 2 mM sodium tetrachloropalladate solution (pH 2.3) was used as the metal precursor. A constant dry cell weight (DCW) of 0.07 g was maintained at the 25% (w/w) Pd loading

Similar Pd(II) ion adsorption characteristics were observed for the three *E. coli* strains (Figure 4-1). A rapid initial adsorption of the adsorbate occurred within the first 5 minutes of exposure followed by a plateau. This plateau was indicative of an equilibrium being reached between adsorption and desorption of the metal ions at the surface of the adsorbent. For all microbial strains, near-complete adsorption of Pd(II) was achieved, with *E. coli* DH5α accumulating *ca.* 99.7% of the metal ions from solution while *E. coli* ATCC25922 and *E. coli* BL21DE3 adsorbed 94.4% and 93.4% of the Pd ions, respectively (Figure 4-1a). A maximum capacity between 45.6 to 50.6 $mg_{Pd(II)\ adsorbed}/g_{DCW}$ was achieved across all microbial strains.

To further assess the adsorption capabilities of the three microbial strains, a higher metal loading was considered. The higher metal loading ensures a greater driving force for adsorption. However, depending on the metal (and its use within the bacterial cell) a higher

loading could impair the metabolic state and may influence the adsorptive properties of the bacterial cells. To determine the influence of a higher metal loading on the adsorption kinetics of *E. coli* DH5α, *E. coli* ATCC25922 and *E. coli* BL21DE3 the amount of Pd was increased from 5% (w/w) to 25% (w/w). The kinetics of the system was observed under similar conditions to those used previously at the 5% (w/w) metal loading (Figure 4-2).

Table 4-1 The initial rate of adsorption on *E. coli* DH5α, *E. coli* ATCC25922 and *E. coli* BL21DE3 at a 25% (w/w) Pd loading

Microbial strain	Initial rate of adsorption ($mg_{Pd(II)\ adsorbed}/g_{DCW}.min$)
E. coli DH5α	222.8
E. coli ATCC25922	177.8
E. coli BL21DE3	162.5

At a 25% (w/w) loading of Pd(II) all three *E. coli* strains experienced similar rapid adsorption within the first 0-2 minutes of metal exposure (Figure 4-2 and Table 4-1). The fast uptake noted across both Pd loadings indicated that all microbial strains exhibited a strong affinity for the metal. *E. coli* ATCC25922 and *E. coli* BL21DE3 had similar rates of adsorption (170.1 ± 10.8 $mg_{Pd(II)\ adsorbed}/g_{DCW}.min$) while the rate of adsorption by *E. coli* DH5α was 1.3 times faster than the aforementioned strains (Table 4-1). Unlike the 5% (w/w) loading (Figure 4-1) where equilibrium was achieved on all strains after the initial rapid accumulation of metal ions, a plateau in the amount of Pd(II) ions adsorbed was not noted on *E. coli* DH5α and *E. coli* BL21DE3 at the higher loading (Figure 4-2). *E. coli* DH5α and *E. coli* BL21DE3 reached a maximum capacity of 133.4 $mg_{Pd(II)\ adsorbed}/g_{DCW}$ and 140.0 $mg_{Pd(II)\ adsorbed}/g_{DCW}$ after the biosorption period. The capacity of the two strains was approximately 2.6-2.8 times higher than what was noted at the lower metal loading. However, at the 25% (w/w) loading the amount of Pd ion adsorbed on *E. coli* DH5α and *E. coli* BL21DE3 was approximately halved (to 44.4% and 53.5% respectively) from the near complete adsorption at the 5% (w/w) loading (Figure 4-1, Figure 4-2).

Although the initial capacities of all the microbial strains were similar (112.5 ± 4.4 $mg_{Pd(II)\ adsorbed}/g_{DCW}$), the capacity of *E. coli* ATCC25922 dropped by 14.5% after initial exposure to the metal, lowering the percentage of Pd adsorbed to 27.9% from 42.4% over 5 minutes (Figure 4-2.a). The decrease in capacity was indicative of desorption of the Pd(II) ion from the microbial support and was likely due to the activation of detoxification pathways within the bacterial cells to maintain metabolic activity. This rapid decline in capacity was not noted at the 5% (w/w) Pd loading on *E. coli* ATCC25922 where the strain achieved 94.4% adsorption of the Pd ion. After the desorption of Pd(II) ions from *E. coli* ATCC25922 an equilibrium was reached that corresponded to a maximum capacity of 78.3 $mgPd_{(II)\ adsorbed}/g_{DCW}$. This capacity was only 1.6 times greater than at the 5% (w/w) loading. The limitation in the amount of Pd adsorbed at the 25 % (w/w) loading indicated that the active sites available on the cells were over saturated.

To quantify the maximum capacity and tolerance of each of the *E. coli* strains for Pd(II), the adsorption of Pd(II) at equilibrium was investigated. In generating these equilibrium isotherms, biosorption protocols in Section 3.3.2 were followed. The initial metal ion precursor was varied between 1 mM and 10 mM (1 mM, 2 mM, 5 mM, 7 mM and 10 mM) maintaining a constant volume-to-mass ratio of the metal ions in solution and the cell mass. The resulting microbe-metal complexes were incubated under anoxic conditions at 30°C and 120 rpm. Initial equilibrium was established within 5-10 minutes, after which point a slight shift in equilibrium capacity was still possible. Previous investigations of similar adsorption environments showed that stabilization of the ion adsorbed only occurred after 4 days (De Vargas et al., 2004). As such, biosorption was extended over the same period to ensure that the system achieved a stable equilibrium point. This is referred to as the true equilibrium (De Vargas et al., 2004). After this period samples were extracted and the residual metal ions in solution were determined using the $SnCl_2$ assay. From this, the relationship between the Pd(II) adsorbed onto the support and the residual metal ion concentration in solution at equilibrium was established (Figure 4-3).

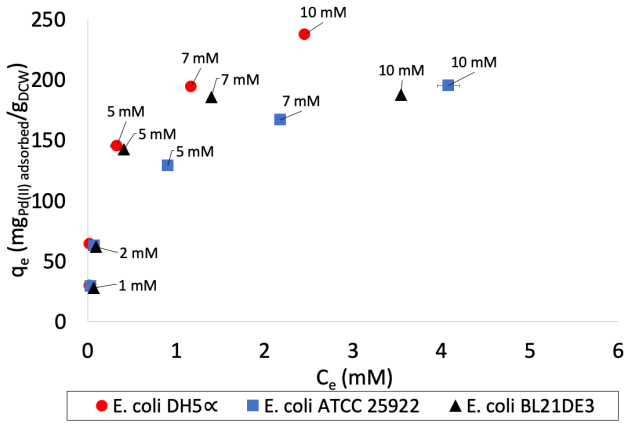

Figure 4-3 Equilibrium adsorption of Pd(II) on *E. coli* DH5α (●), *E. coli* ATCC25922 (■) and *E. coli* BL21DE3 (▲). The initial Pd ion concentration was varied from 1 mM, 2 mM, 5 mM, 7 mM, 10 mM (pH 2.3) as indicated. The dry cell weight (DCW) was kept constant (0.028 g) across all concentrations. The residual metal ion concentration was determined after a 4 day incubation period at 30oC and 120 rpm.

Upon analysing the biosorption characteristics of each of the microbial strains *E. coli* ATCC*2592* appeared to be the least efficient at accumulating Pd(II) ions in solution at the 5 mM and 7 mM concentrations. *E. coli* BL21DE3 had the lowest capacity at the 10 mM concentration (187.5 $mg_{Pd(II)\ adsorbed}/g_{DCW}$, Figure 4-3). In comparison, at an initial metal ion concentration of 10 mM Pd(II), *E. coli* ATCC25922 and *E. coli* DH5α strains had a maximum capacity of 192.4 $mg_{Pd(II)\ adsorbed}/g_{DCW}$ and 237.5 $mg_{Pd(II)\ adsorbed}/g_{DCW}$, respectively. These two microbial strains did not reach a stable plateau when exposed to similar concentrations of ion precursor. This indicated that these two scaffolds potentially had capacity to further adsorb metal cations from solution. In a similar study, De Vargas et al. (2004) noted that *D. desulfuricans* was the most effective strain in both capacity and efficiency of adsorption than any of the other *Desulfovibrio* strains investigated. *D. desulfuricans* was able to adsorb 90% of Pd(II) in less than 15 minutes to reach a maximum capacity of 160 $mg_{Pd(II)\ adsorbed}/g_{DCW}$. Although similar to the efficiency and rapid adsorption noted on the strains investigated in Figure 4-3, the *E. coli* scaffolds in this study surpassed what was previously achieved by De Vargas et al. (2004). This establishes *E. coli* as a more effective bacterial scaffold. Of the three

microbial strains *E. coli* DH5α had the greatest affinity for the Pd ion. In the context of bioremediation this strain would be the most efficient as it can remove more metals from solution per gram of cells.

4.2.2 Model fitting for Pd adsorption on *E. coli*

Predictive adsorption models are related to the mass transfer of the adsorbate onto the adsorbent (Section 2.5). Common kinetic models include the Pseudo-first order, Pseudo-second order, Elovich and Intra-particle diffusion (IPD) models. These are typical L-shape models that are used mainly to determine the rate of removal of pollutants from waste streams. Langmuir, Freundlich, Temkin and Dubinin-Radushkevich (D-R) are predictive models that define adsorption at equilibrium and further consider the type of interactions that occur between the adsorbate and adsorbent. These models are often described using the general linear form given in Equation 4-1 and are summarized by the equations in Table 4-2.

$$Y = mX + c \qquad \text{Equation 4-1}$$

where Y is the dependent variable and X the independent variable.

Table 4-2 Summary of predictive kinetic and equilibrium model equations that describe adsorption. All model constants (q_t, k1, k2, qe(exp), β, α, f, c, qmax, *b*, kf, n, bt, BT, at/AT,β_{D-R} qD) are defined in the glossary

Model	Equation
Pseudo-first order	$q_t = q_e(1 - e^{-k_1 t})$
Pseudo-second order	$q_t = \frac{k_2 {q_e}^2 t}{1 + k_2 q_e t}$
Elovich	$\ln(q_t) = \frac{1}{\beta}\ln(\alpha\beta) + \frac{1}{\beta}\ln(t)$
Intra-particle diffusion	$q_t = f t^{0.5} + c$
Langmuir	$q_e = \frac{b q_{max} C_e}{1 + bC_e}$ $\quad R_L = \frac{1}{1 + bC_o}$
Freundlich	$q_e = k_F {C_e}^{\frac{1}{n}}$
Temkin	$q_e = B_T(lnA_T + lnC_e)$ $\quad B_T = \frac{RT}{b_t}; A_T = a_t$
Dubinin-Radushkevich	$\ln(q_e) = \ln(q_D - \beta_{D-R}\varepsilon^2)$ $\quad \varepsilon = RTln\left(1 + \frac{1}{C_e}\right)$ $\quad E = \frac{1}{(2\beta_{D-R})^{0.5}}$

These models may be used to predict the influence of altering reaction environments on adsorption as well as provide an insight into the mechanism of adsorption; and the suitability of the selected strain as a support for the biofabrication of nanoparticles. The affinity of Pd to the different *E. coli* strains was determined based on the capacity of the cells and the rate at which the metal absorbed to the cells. This provided a common reference for comparison

across the various supports. In this investigation, the difference between the predictive model and the observed results was quantified by the sum of squared errors (SSE; Equation 4-2). The SSE is used to measure the goodness of fit of the model output. Similarly, the model parameters were determined by minimising the difference between the experimental and modelled data points using non-linear least square regression. The Chi-squared test, a normalization of Equation 4-2, was further used to determine statistical significant difference between the observed results and the predictive model (Equation 4-3)

$$SSE = \sum_{i=0}^{i=n} (Y_{exp} - Y_{model})^2 \quad \text{Equation 4-2}$$

$$\chi^2 = \sum_{i=0}^{i=n} \frac{(Y_{exp} - Y_{model})^2}{Y_{model}} \quad \text{Equation 4-3}$$

In Equation 4-2 and Equation 4-3 Y_{model} is defined as the dependent variable in the model equation (Table 4-2) and Y_{exp} is the corresponding value obtained after experimental analysis. Once regression was performed, the fit of the model was assessed according to the co-efficient of determination (R^2, Equation 4-4) and the average absolute relative deviation (AARD, Equation 4-5)

$$R^2 = 1 - \frac{\sum(Y_{exp} - Y_{model})^2}{\sum(Y_{exp} - Y_{avg})^2} \quad \text{Equation 4-4}$$

$$(AARD) = \frac{100}{n} \left| \frac{Y_{model} - Y_{exp}}{Y_{exp}} \right| \quad \text{Equation 4-5}$$

where R^2 is the variation in the regressed values from the experimental data points and *n* is the number of data points obtained during the experiments. The AARD assesses the dispersion of experimental data providing an indication of variability. These factors also provided a measure of the effectiveness of the model at predicting the applied case.

Using this regression technique, the kinetic data was analyzed and a suitable model was selected to describe adsorption of Pd(II), for both metal loadings, on all *E. coli* strains (Table 4-3, Table 4-4, Table 4-5). With coefficients of determination R^2 close to 1.0, a minimized Chi-squared and AARD, the Elovich, Pseudo-first and Pseudo-second order models were all good fits and therefore appropriately representative of the type of adsorption that occurred across all strains at the 5% (w/w) Pd loading (Table 4-3). These three models were similarly representative of the adsorption that occurred at higher Pd(II) concentrations (25% w/w loading, Table 4-4). However, the randomness in the residuals for the non-linear Elovich model indicated that this model was more suitable in describing the adsorption of the metal ion onto the different supports. A pitfall of this model is that it cannot predict adsorption at the initial time point, (t = 0). However, of the three models, it was the only model that adequately

described the desorption of Pd that was observed with *E. coli* ATCC25922 at the 25% (w/w) loading (Figure 4-7).

The Elovich, Pseudo-first and Pseudo-second order models are inherently similar in that each model has the underlying assumption that chemisorption of the adsorbate occurs onto the heterogenous adsorbent surface. According to Bunge et al. (2010) and Rotaru et al. (2012), the Pd ions passively adsorb on amine and hydroxyl functional groups on the cell surface. Consequently, the availability of binding sites for each of the microbial strains was assessed using FTIR to determine whether there was any significant difference in accessible functional groups (Figure 4-4).

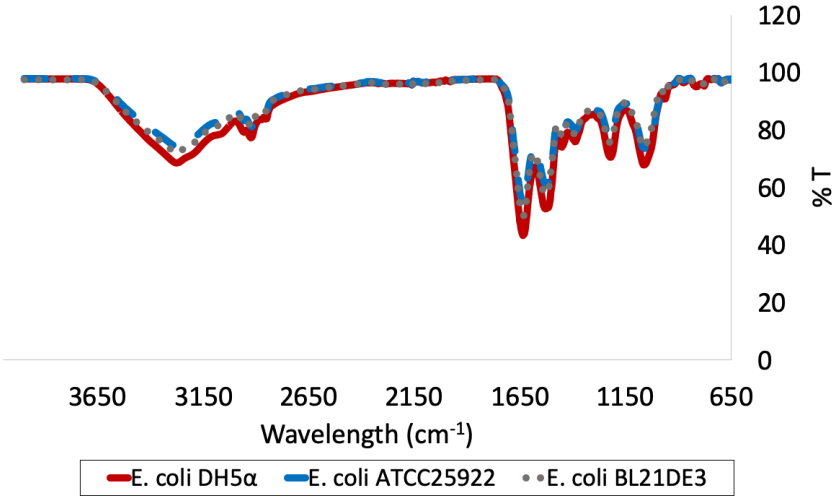

Figure 4-4 FTIR analysis of the microbial strains *E. coli* DH5α (—), *E. coli* ATCC25922 (— —) and *E. coli* BL21DE3 (• • •)

FTIR analysis on the *E. coli* showed similar profiles across each of the strains indicating that the functional groups on the cell surfaces are similarly distributed. A stretch between 3500 – 3000 cm^{-1} on the FTIR spectrum confirmed that hydroxyl and amine groups are prevalent on *E. coli* (Figure 4-4). As the intensity of the peaks is a function of type and volume of binding sites that exist across the microbial strains, all microbial scaffolds have similar composition and volume of function groups. As a consequence, all the microbial strains investigated had similar adsorption capacities at the 5% (w/w) metal loading that likely occurred via chemisorption (Figure 4-1).

From the adsorption isotherm models considered, it was clear that adsorption of Pd(II) on *E. coli* DH5α, *E. coli* ATCC25922, and *E. coli BL21DE3* at equilibrium was best described by the Temkin model (Table 4-6). This model accounts for any interactions between adjacently adsorbed metal ions and assumes that the heat of adsorption, B_T, increases or decreases linearly with surface coverage. For Pd on *E. coli* DH5α, *E. coli* ATCC25922, and *E. coli* BL21DE3, B_T was positive therefore the heat of adsorption increased with coverage on the support (Table 4-6). Although both the Langmuir and the Freundlich models reasonably fit the data, these were not applicable as these models do not account for any potential interactions that may occur between adsorbed molecules.

Table 4-3 Kinetic model fit to the experimental adsorption of Pd(II) at a 5% (w/w) loading onto the various *E. coli* strains. Where model constants k_1, k_2, $q_{e\,(exp)}$, β , α, f and c were determined by non-linear regression

	Pseudo-first order						Pseudo-second order					
	k_1 (min^{-1})	$q_{e\,(exp)}$ (mg/g)	Residual pattern	χ^2	R^2	AARD	k_2	$q_{e\,(exp)}$ (mg/g)	Residual pattern	χ^2	R^2	AARD
E. coli DH5α	0.7	51.0	Uncertain	$7.7x10^{-4}$	1.0	0.9%	0.3	51.0	Uncertain	$5.1x10^{-4}$	1.0	0.6%
E. coli ATCC25922	3.6	50.0	No	$7.4x10^{-3}$	1.0	2.7%	0.4	50.0	No	$6.4x10^{-3}$	1.0	2.6%
E. coli BL21DE3	0.7	46.0	Yes	$5.8x10^{-3}$	1.0	2.4%	0.1	46.0	Uncertain	$1.7x10^{-3}$	1.0	1.2%
	Elovich model (@ Boundary conditions)						Intra-particle diffusion					
	β (g/mg)	α (mg/g.min)	Residual pattern	χ^2	R^2	AARD	f ($mg/g.min^{0.5}$)	C	Residual pattern	χ^2	R^2	AARD
E. coli DH5α	2.2	$3.7x10^{46}$	No	$1.9x10^{-4}$	1.0	0.4%	5.7	23.6	Yes	0.7	0.5	13.7%
E. coli ATCC25922	2.3	$3.7x10^{46}$	Uncertain	$1.5x10^{-3}$	1.0	1.1%	4.2	27.3	Yes	0.9	0.4	13.5%
E. coli BL21DE3	0.6	$1.0\ x10^{11}$	No	$3.3x10^{-3}$	1.0	1.2%	4.0	23.8	Yes	0.7	0.5	11.8%

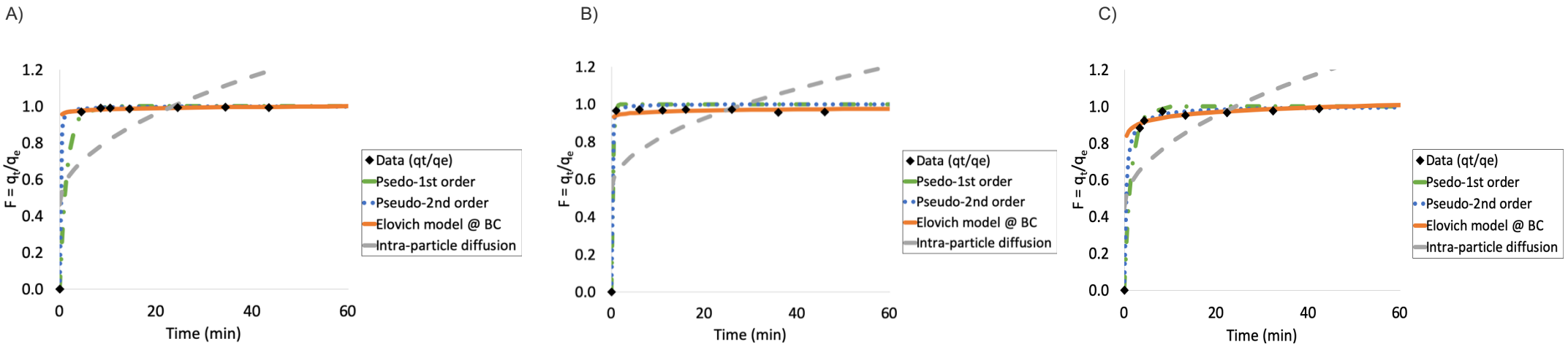

Figure 4-5 Fit of Pseudo-first order (—●—), Pseudo-second order (● ● ● ●) Elovich (——) and the Intra-particle diffusion (- - - -) kinetic models to experimentally determined adsorption of Pd ions (♦) at a 5% (w/w) loading onto A) *E. coli* DH5α , B) *E. coli* ATCC25922 C) *E. coli* BL21DE3 scaffolds. The fit of the model was achieved by using the model parameters obtained after non-linear regression analysis.

Table 4-4 Kinetic model fit to the experimental adsorption of Pd(II) ions at a 25% (w/w) loading onto the various *E. coli* strains. Where the model constants k_1, k_2, $q_{e\,(exp)}$, β , α, *f* and *c* were determined by non-linear regression

	Pseudo-first order						Pseudo-second order					
	k_1 (min^{-1})	$q_{e\,(exp)}$ (mg/g)	Residual pattern	χ^2	R^2	AARD	k_2	$q_{e\,(exp)}$ (mg/g)	Residual pattern	χ^2	R^2	AARD
E. coli DH5α	3.2	140.0	Yes	0.1	0.9	7.1%	0.05	140.0	Yes	0.1	0.9	6.8%
E. coli ATCC25922	8.9	109.0	Uncertain	0.2	0.8	6.7%	40.0	109.0	Uncertain	0.2	0.8	6.7%
E. coli BL21DE3	3.0	124.0	Yes	$3.4x10^{-2}$	1.0	5.5%	0.05	124.0	Yes	$2.9x10^{-2}$	1.0	5.4%
	Elovich model (@ Boundary conditions)						Intra-particle diffusion					
	β (g/mg)	α (mg/g.min)	Residual pattern	χ^2	R^2	AARD	f ($mg/g.min^{0.5}$)	C	Residual pattern	χ^2	R^2	AARD
E. coli DH5α	0.9	$1.9 x10^{48}$	Yes	$2.8x10^{-2}$	1.0	5.5%	12.5	64.9	Yes	0.2	0.6	11.4%
E. coli ATCC25922	1.4	$3.7 x10^{50}$	Uncertain	$2.1x10^{-1}$	0.8	13.6%	3.4	59.7	Uncertain	0.5	0.1	8.9%
E. coli BL21DE3	0.5	$2.0 x10^{26}$	Yes	$5.0x10^{-2}$	1.0	7.7%	10.4	62.4	Yes	0.2	0.5	11.7%

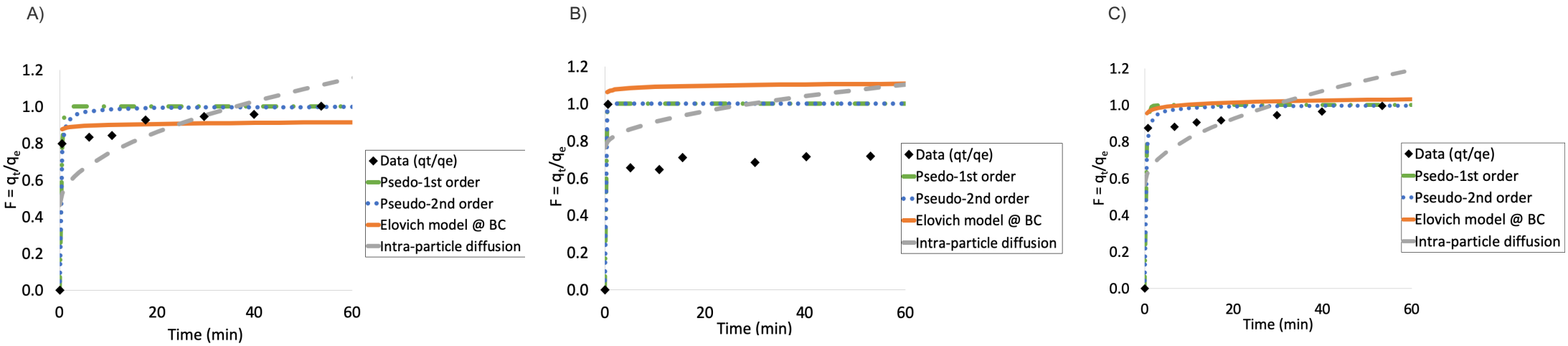

Figure 4-6 Fit of Pseudo-first order (—••—), Pseudo-second order (••••) Elovich (—) and the Intra-particle diffusion (- - - -) kinetic models to experimentally determined adsorption of Pd ions (♦) at a 25% (w/w) loading onto A) E. coli DH5α , B) E. coli ATCC25922 C) E. coli BL21DE3 scaffolds. The fit of the model was achieved by using the model parameters obtained after non-linear regression analysis.

4-5 Kinetic model fit to the experimental adsorption of Pd(II) ions at a 25% (w/w) loading onto the *E. coli* ATCC25922. Where the model constants k_1, k_2, $q_{e\,(exp)}$, β , α, f and c were determined by non-linear regression

	Pseudo-first order						Pseudo-second order					
	k_1 (min^{-1})	$q_{e\,(exp)}$ (mg/g)	Residual pattern	χ^2	R^2	AARD	k_2	$q_{e\,(exp)}$ (mg/g)	Residual pattern	χ^2	R^2	AARD
L1	91.7	109.0	-	-	1.0	-	40.0	109.0	-	-	1.0	-
L2	6.0	109.0	-	0.1	0.6	26.9%	-0.5	109.0	-	0.1	0.04	28.0%
L3	0.05	109.0	-	1.1	-0.5	31.3%	0.02	78.0	-	0.5	0.0	40.6%
Overall			Yes	1.2	0.5	30.2%			Uncertain	0.6	0.5	37.5%
	Elovich model (@ Boundary conditions)						Intra-particle diffusion					
	β (g/mg)	α (mg/g.min)	Residual pattern	χ^2	R^2	AARD	f ($mg/g.min^{0.5}$)	C	Residual pattern	χ^2	R^2	AARD
L1	0.1	3.7×10^{6}	-	-0.1	1.0	-	109.0	4.0	-	-0.1	1.0	-
L2	-0.1	-6.4×10^{-2}	-	1.5×10^{-2}	1.0	4,8%	-29.8	138.0	-	1.5×10^{-2}	1.0	0,6%
L3	0.3	4.5×10^{9}	-	6.5×10^{-3}	0.7	1,8%	1.4	68.5	-	6.5×10^{-3}	0.6	2,0%
Overall			No	2.2×10^{-2}	1.0	2,6%			No	2.2×10^{-2}	1.0	2,1%

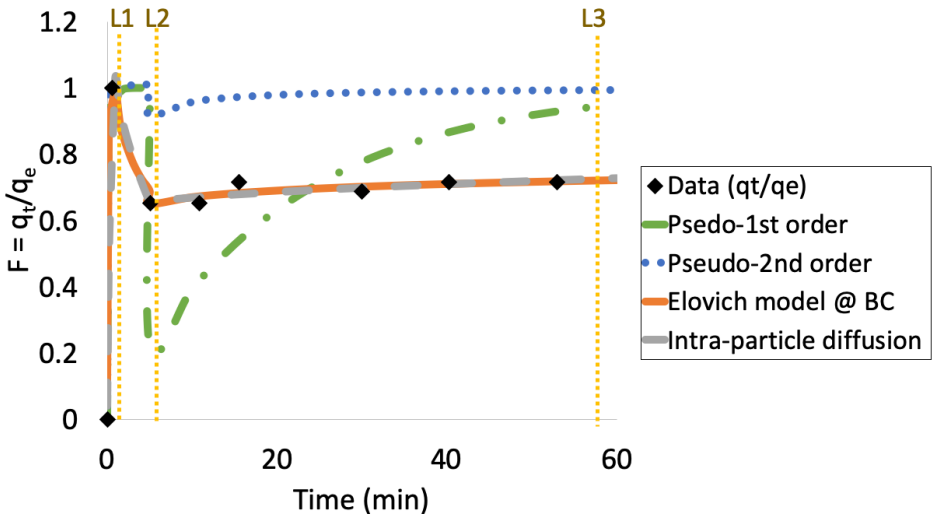

Figure 4-7 Fit of Pseudo-first order (— • —), Pseudo-second order (• • • •) Elovich (——) and the Intra-particle diffusion (- - - -) kinetic models to experimentally determined adsorption of Pd ions (♦) at a 25% (w/w) loading onto E. coli ATCC25922. The fit of the model was achieved by using the model parameters obtained after non-linear regression analysis. The kinetic trend was sectioned in regions L1, L2 and L3

Table 4-6 Isotherm model fit to the experimental adsorption of Pd(II) at equilibrium. Where the model constants q_{max}, b, k_f, n, b_t B_T, a_t/A_T, β and q_D were determined by non-linear regression

	Langmuir						Freundlich					
	b (L/mg)	q_{max} (mg/g)	Residual pattern	χ^2	R^2	AARD	n	k_f	Residual pattern	χ^2	R^2	AARD
E. coli DH5α	5.6	245	Yes	87.3	0.9	24.0%	3.3	187.1	Yes	13.5	1.0	21.6%
E. coli ATCC25922	3.2	202	Yes	29.2	0.9	21.7%	3.1	127.1	Yes	4.8	1.0	12.3%
E. coli BL21DE3	4.7	203	Yes	9.88	1.0	17.9%	3.0	143.0	Yes	36.9	0.8	33.7%
	Temkin						Dubinin-Radushkevich					
	B_T (J/mol)	A_T/a_t	Residual pattern	χ^2	R^2	AARD	β (mol²/J²)	q_D (mg/g)	Residual pattern	χ^2	R^2	AARD
E. coli DH5α	36.8	198.2	Uncertain	11.6	1.0	16.8%	$1.5x10^{-8}$	206.1	Uncertain	22.5	0.9	20.1%
E. coli ATCC25922	31.9	87.4	Uncertain	1.3	1.0	3.9%	$2.2x10^{-8}$	167.3	Uncertain	9.6	0.9	9.6%
E. coli BL21DE3	41.0	46.2	Uncertain	15.0	0.9	21.2%	$3.4x10^{-8}$	200.0	Uncertain	4.9	1.0	11.7%

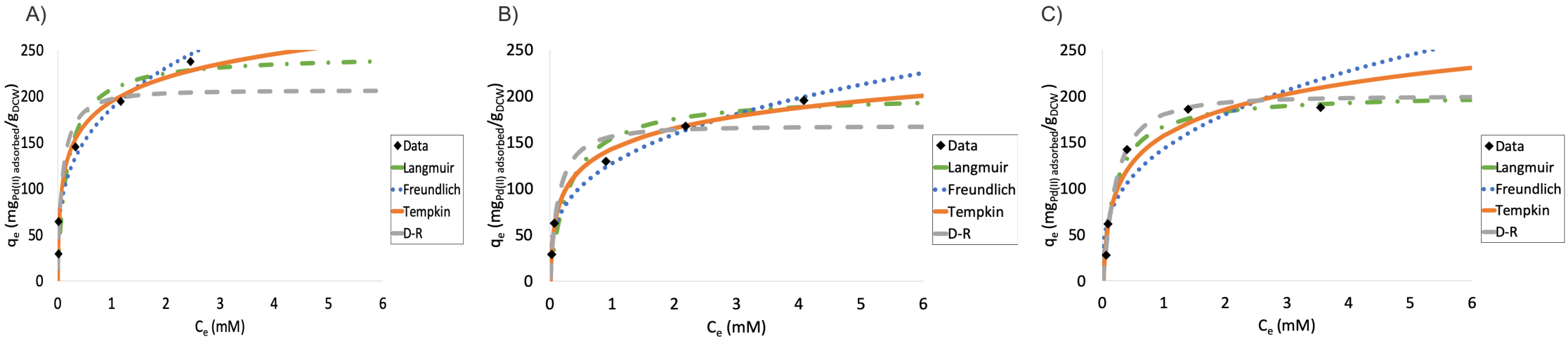

Figure 4-8 Fit of Langmuir (—••—), Freundlich (••••) Temkin (——) and the Dubinin-Radushkaveich (- - - -) isotherm models to experimentally determined adsorption of Pd ions (♦) onto A) *E. coli* DH5α , B) *E. coli* ATCC25922 C) *E. coli* BL21DE3 scaffolds. The fit of the model was achieved by using the model parameters obtained after non-linear regression analysis.

4.3 Adsorption of Au on *E. coli* scaffolds

4.3.1 Adsorption kinetics and equilibrium isotherm analysis

The affinity of *E. coli* strains for Au(III) was also investigated by observing the kinetics and maximum capacity of the microbial strains for this cation. Au(III) adsorption was initiated by the addition of a constant mass of cells to a predetermined volume of Au(III) ion precursor in accordance with methods outlined in Section 3.3.2. During the incubation period, 0.5 ml aliquots were extracted and analyzed using a colorimetric thiamine-phloxine B assay to quantify the residual metal ion concentration in solution. From these analyses the amount of Au(III) adsorbed by each of the microbial strains was determined over time (Figure 4-9, Figure 4-10).

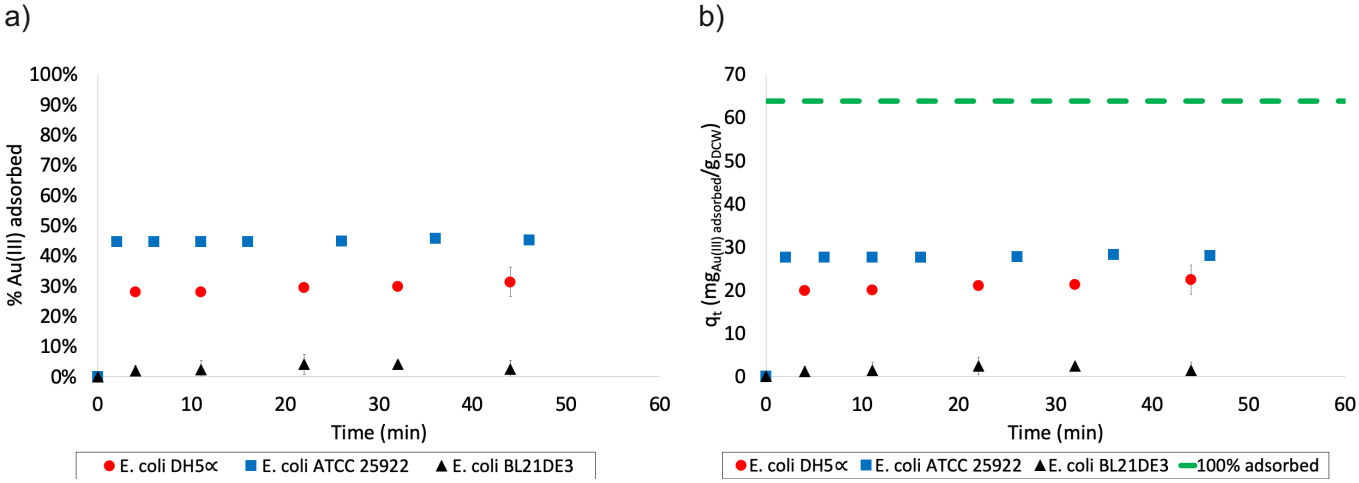

Figure 4-9 Adsorption of Au(III) on *E. coli* DH5α (●), *E. coli* ATCC25922 (■) and *E. coli* BL21DE3 (▲) was performed at 30°C and 120 rpm. Where a) is the percentage of Au(III) ions adsorbed over time and b) is the adsorption capacity qt ($mg_{Au(III)\ adsorbed}/g_{DCW}$) with time. A 1 mM gold(III) tetrachloroaurate trihydrate solution (pH 2.3) was used as the metal precursor. A constant dry cell weight (DCW) of 0.14 g was maintained at a 5% (w/w) Au loading,

From Figure 4-9, it was clear that the adsorption of Au(III) ions at the lower loading onto the various *E. coli* strains occurred within 2-4 minutes of exposure after which a maximum capacity was reached as the adsorption approached a plateau. For each of the strains considered, the adsorption capacity did not exceed more than half of the total ions in solution (Figure 4-9.a). *E. coli* ACC25922 showed the greatest affinity for Au(III) by adsorbing ca. 45.6% of the cations from solution with a maximum capacity of 28.2 mgAu(III) adsorbed/gDCW. This was followed by *E. coli* DH5α, with a maximum adsorption capacity of 22.3 $mg_{Au(III)\ adsorbed}/g_{DCW}$, which was equivalent to 31.1% of Au(III) in solution. In contrast to these two scaffolds, only ca. 4.0% of Au(III) was adsorbed by *E. coli* BL21DE3, which achieved the lowest capacity of 2.4 $mg_{Au(III)\ adsorbed}/g_{DCW}$.

An investigation by Nakajima (2003) similarly noted kinetic and equilibrium adsorption parameters for Au(III) on *E. coli* IAM 1264. In comparison to the current study, *E. coli* IAM 1264 achieved a maximum capacity of 64 $mg_{Au(III)\ adsorbed}/g_{DCW}$, more than twice as much as what was achieved by *E. coli* ATCC25922 at the corresponding metal loading. From these results, it was evident that the selected cell strain for the adsorption of Au(III) had a direct

impact on the adsorption efficiency and capacity. The results showed that *E. coli* BL21DE3 has a very low affinity for Au(III), indicating that at this loading the microbial strain would not be suitable as a scaffold for the biofabrication of Au nanocatalysts. However, the low affinity noted across each of the *E. coli* strains for this metal may have also been likely as a result of the low Au loading, which limits the driving force for mass transfer of the ions to the support.

To determine the influence of a higher Au(III) loading on the adsorption capabilities of the three microbial strains, the metal loading was increased to 25% (w/w) (Figure 4-10).

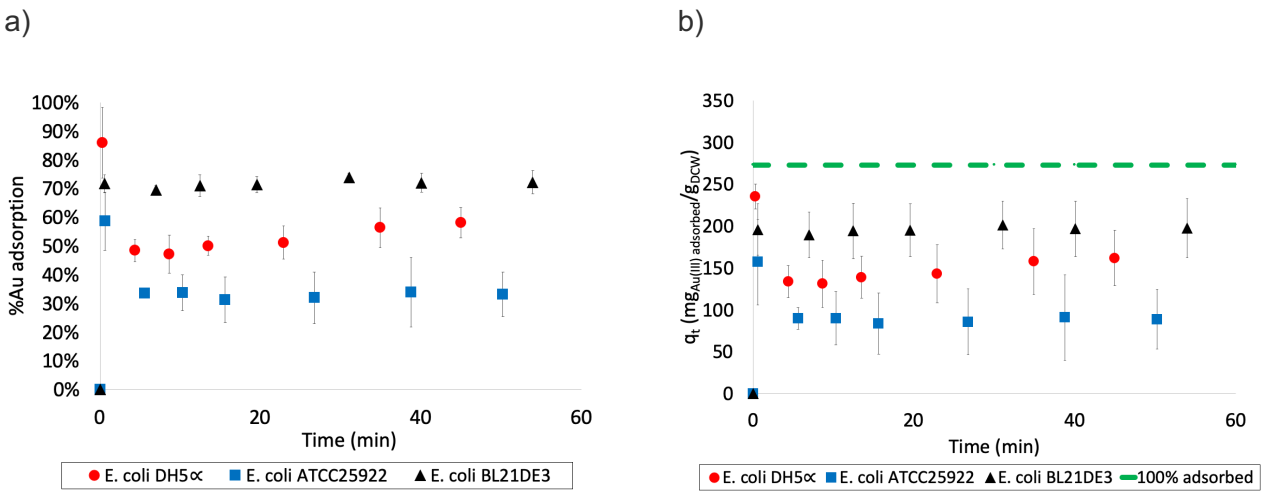

Figure 4-10 Adsorption of Au(III) on *E. coli* DH5α (●), *E. coli* ATCC25922 (■) and *E. coli* BL21DE3 (▲) was performed at 30°C and 120 rpm. Where a) is the percentage of Au(III) adsorbed over time and b) is the adsorption capacity qt ($mgAu_{(III)\ adsorbed}/g_{DCW}$) with time. A 1 mM gold tetrachloroaurate solution (pH 2.3) was used as the metal precursor. A constant dry cell weight (DCW) of 0.07 g was maintained at a 25% (w/w) Au loading

As with the 5% (w/w) metal loading, a rapid initial adsorption was also noted at the 25% (w/w) loading for Au(III) on *E. coli* DH5α, *E. coli* ATCC25922 and *E. coli* BL21DE3 between 0-2 minutes (Figure 4-10). During this time, *E. coli* DH5α achieved a rate that was almost 2.3-3.3 times faster than the other microbial strains (Table 4-7). However, a sudden release of the precursor back into solution was observed following the initial adsorption from the *E. coli* DH5α and *E. coli* ATCC25922 strains. This desorption of Au decreased the amount of the metal adsorbed onto *E. coli* DH5α from 85.9% to 48.4% and from 63.7% to 33.7% on *E. coli* ATCC25922 (Figure 4-10.a). This final amount adsorbed was only approximately 10% higher than the Au ion absorbed at the 5% (w/w) loading. The maximum capacities for *E. coli* DH5α and *E. coli* ATCC25922 were therefore limited to 161.7 $mg_{Au(III)\ adsorbed}/g_{DCW}$ and 88.6 $mg_{Au(III)\ adsorbed}/g_{DCW}$, respectively (Figure 4-10.b).

Elevated concentrations of the Au metal ion in solution appears to trigger a detoxification response in *E. coli* DH5α and *E. coli* ATCC25922. This expulsion of the ion is to avert any compromise in metabolic activity. In comparison, *E. coli* BL21DE3 retained the majority of the Au(III) at the 25% (w/w) metal loading, adsorbing 72.1% of the metal ion while maintaining a capacity of 197.4 $mg_{Au(III)\ adsorbed}/g_{DCW}$. The capacity was nearly 82 times greater than the capacity at the 5% (w/w) Au loading for this strain (Figure 4-9).

Table 4-7 The initial rate of adsorption on *E. coli* DH5α *E. coli* ATCC25922 and *E. coli* BL21DE3 at a 25% (w/w) Au loading

Microbial strain	Initial rate of adsorption ($mg_{Au(III)\ adsorbed}/g_{DCW}.min$)
E. coli DH5α	783.6
E. coli ATCC25922	235.7
E. coli BL21DE3	335.6

At lower loadings preferential adsorption of Pd(II) onto *E. coli* occurs by active bacterial cells that mistakenly absorb Pd in place of similarly structured Ni cations commonly used during protein synthesis (Torgeman, 2017). In contrast, a vastly different adsorption mechanism for the Au metal is observed. Establishing a potential mechanism as well as the tolerance of microbial strains to Au(III) was therefore investigated by varying the initial precursor concentration between 1-10 mM (1, 2, 5, 7 and 10 mM). From this the residual metal ion concentration at equilibrium was assessed (Figure 4-11).

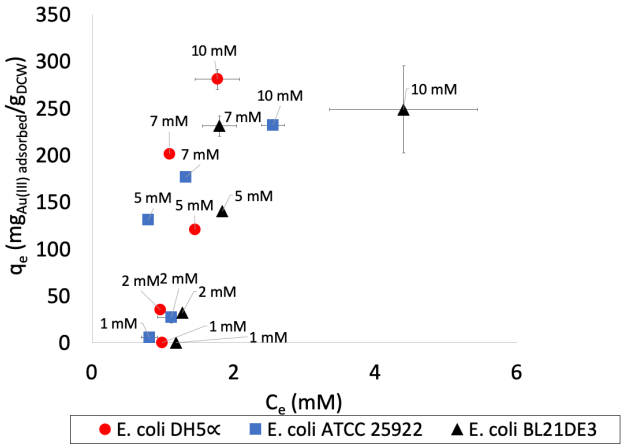

Figure 4-11 Equilibrium adsorption of Au (III) on *E. coli* DH5α (●), *E. coli* ATCC25922 (■) and *E. coli* BL21DE3 (▲). The initial Au (III) ion concentrations was varied from 1 mM, 2 mM, 5 mM, 7 mM, 10 mM (pH 2.3). The dry cell weight (DCW) was kept constant (0.028 g) across all concentrations. The residual metal ion concentration was determined after 4 days of incubation at 30°C and 120 rpm.

From Figure 4-11 it was evident that, apart from the 1 mM and 5 mM concentrations, *E. coli* DH5α had the highest capacity for Au(III) for all metal precursor concentrations. It was expected that Au adsorption isotherms would exhibit similar characteristics to those observed for Pd. However, in comparison to Pd(II), where L-shaped adsorptive behaviour for each of the strains was observed, S-shaped isotherms were noted for Au(III). This indicated that the mechanism for the adsorption of Au(III) differed from that of Pd(II) (Figure 4-3, Figure 4-11). Corresponding to findings by Nakajima (2003), the Au(III) concentration range clearly impacted adsorption. As the metal ion concentration was increased a sigmoidal isotherm similarly evolved in this study with the maximum capacity for Au(III) appearing to continuously increase with increasing ion concentration (Giles et al., 1922; Kumar et al., 2011; Limousin et al., 2007; Nakajima, 2003). This S-shaped trend was presumed to be a product of co-operative adsorption. In an attempt to model this non-uniform behaviour of the Au ions onto the biological supports, the four kinetic and isotherm models used to describe the affinity of Pd to the

microorganism surfaces was similarly applied to determine the kinetic parameters for Au (Figure 4-9, Figure 4-10, Figure 4-11)

4.3.2 Model fitting for Au adsorption on *E. coli*

Predictive models were used to gain insight into the underlying mechanisms regulating the adsorption of the Au(III) ions onto the *E. coli* scaffolds. Through the process of non-linear regression, kinetic model fits were assessed by comparing the R^2, AARD, Chi-squared and residuals for the Pseudo-first order, Pseudo-second order, Elovich and IPD models (Table 4-8, Table 4-9, Table 8-10, Table 8-11).

At the higher metal loading, multiple areas of linearity observed upon adsorption onto *E. coli* ATCC25922 and *E. coli* DH5α (Figure 4-14 a and b), indicated that adsorption was governed by different stages of mass transfer to and from the support. As such, the observed adsorption trends were segmented into three regions L_1, L_2, and L_3 to gain clearer understanding of this non-uniform behaviour (see Figure 4-12 and Appendix E:). Thereafter, kinetic models were applied over each region. Of the four kinetic models, the Elovich model was found to be the most appropriate for predicting the adsorption of Au(III) onto *E. coli* DH5α and *E. coli* ACC25922 at both loadings (Figure 4-12, Table 4-8, Table 4-9, Table 8-10, Table 8-11). In comparison to *E. coli* ATCC25922 and *E. coli* DH5α, none of the investigated models were suitable in describing the adsorption of Au(III) onto *E. coli* BL21DE3 at the lower metal loading. This was likely due to the negligible amount of Au(III) adsorbed onto this microbial strain (Figure 4-10). As noted with Pd adsorption, although the Elovich model appropriately described adsorption onto *E. coli* DH5α and *E. coli* ACC25922, the model could not effectively predict the instantaneous adsorption observed near time zero.

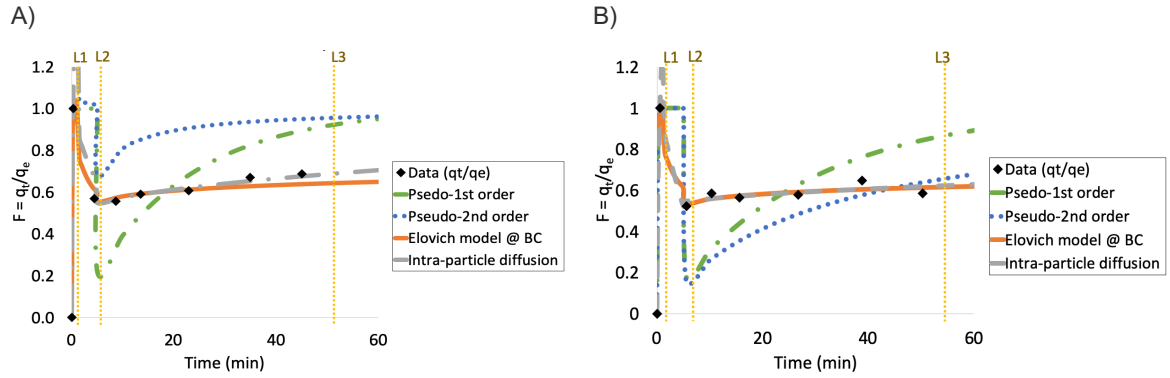

Figure 4-12 Fit of Pseudo-first order (—•—), Pseudo-second order (• • • •) Elovich (—) and the Intra-particle diffusion (- - - -) kinetic models to experimentally determined adsorption of Au ions (♦) at a 25% (w/w) loading onto A) *E. coli* DH5α , B) *E. coli* ATCC25922 scaffolds. The fit of the model was achieved by using the model parameters obtained after non-linear regression. The kinetic trend was sectioned in regions L1, L2 and L3.

With an R^2 close to 1, and a minimized AARD and Chi-squared, the Pseudo-First order and Pseudo-Second order models also achieved a representative fit for the adsorption of Au(III) onto *E. coli* ACC25922 and *E. coli* DH5α at the lower loading, and similarly for *E.coli* BL21DE3 at the higher loading (Table 4-8, Figure 4-13 a and b). Given that Au(III) adsorption followed the Elovich, Pseudo-First order and Pseudo-Second order kinetics, a common assumption

across these models is that chemisorption was likely the governing mechanism of adsorption onto these scaffolds. Au(III) ions are known to coordinate to functional groups such as thiol which are abundant in the cell (De Vargas et al., 2004; Rotaru et al., 2012). Upon assessment of the model fits at the higher metal loading (Figure 4-9), the pseudo second order model equation was not able to adequately predict desorption of Au(III) from *E. coli* ACC25922 and *E. coli* DH5α (Figure 4-14. a and b). Despite the challenges in modeling adsorption near t=0, the Elovich model was still effective in describing adsorption after this time point as well as desorption at the higher Au loading (Figure 4-14). However, none of the models considered, including the Elovich model was universally applicable at either precursor loading. A better understanding of the mechanism of adsorption of Au can be obtained at equilibrium (Table 4-10, Figure 4-15)

Table 4-8 Kinetic model fit to the experimental adsorption of Au(III) ions at a 5% (w/w) loading onto the various *E. coli* strains. Where the model constants k_1, k_2, $q_{e\,(exp)}$, β , α, f and c were determined by non-linear regression

	Pseudo-first order						Pseudo-second order					
	k_1 (min^{-1})	$q_{e\,(exp)}$ (mg/g)	Residual pattern	χ^2	R^2	AARD	k_2	$q_{e\,(exp)}$ (mg/g)	Residual pattern	χ^2	R^2	AARD
E. coli DH5α	0.5	23.0	No	$4.4x10^{-2}$	1.0	5.3%	0.05	23.0	No	$2.1x10^{-2}$	1.0	3.4%
E. coli ATCC25922	1.5	29.0	No	$1.2x10^{-2}$	1.0	3.4%	0.1	29.0	No	$9.6x10^{-3}$	1.0	2.9%
E. coli BL21DE3	0.1	2.5	Yes	0.4	0.5	29.2%	0.07	2.5	Yes	0.3	0.6	25.5%
	Elovich model (@ BC)						Intra-particle diffusion					
	β (g/mg)	α (mg/g.min)	Residual pattern	χ^2	R^2	AARD	f ($mg/g.min^{0.5}$)	C	Residual pattern	χ^2	R^2	AARD
E. coli DH5α	0.2	35.6	No	0.1	0.9	8.0%	2.7	6.9	Yes	0.6	0.6	11.5%
E. coli ATCC25922	2.3	$1.5 x10^{26}$	Uncertain	$1.4x10^{-3}$	1.0	0.9%	1.0	24.0	Yes	0.9	0.2	4.6%
E. coli BL21DE3	4.0	10.2	No	0.4	0.7	22.6%	0.2	0.5	Yes	0.7	0.4	26.9%

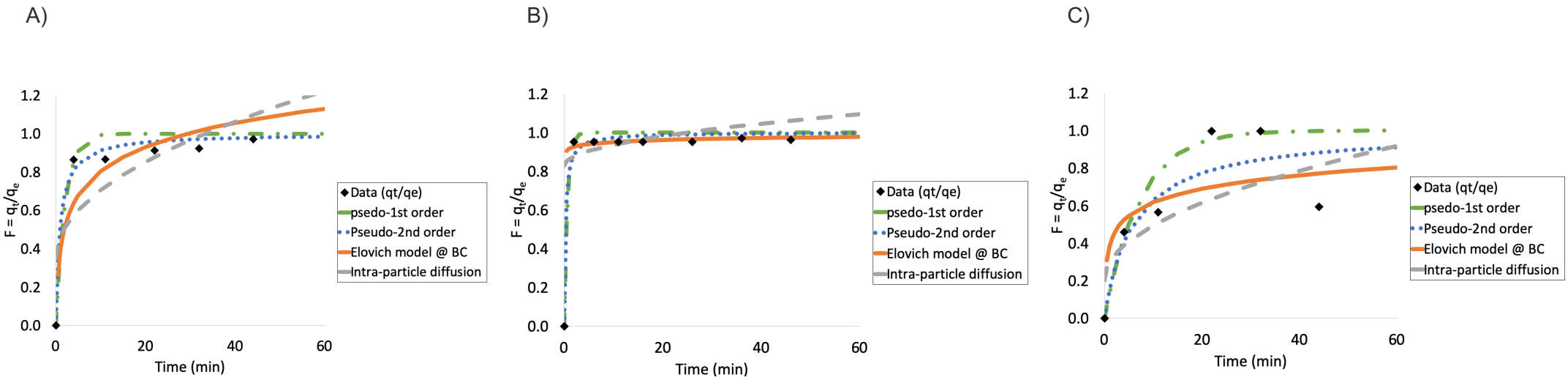

Figure 4-13 Fit of Pseudo-first order (▬ • ▬), Pseudo-second order (• • • •) Elovich (▬) and the Intra-particle diffusion (▪ ▪ ▪ ▪) kinetic models to experimentally determined adsorption of Au ions (♦) at a 5% (w/w) loading onto A) *E. coli* DH5α , B) *E. coli* ATCC25922 C) *E. coli* BL21DE3 scaffolds. The fit of the model was achieved by using the model parameters obtained after non-linear regression analysis.

Table 4-9 Kinetic model fit to the experimental adsorption of Au(III) ions at a 25% (w/w) loading onto the various *E. coli* strains. Where the model constants k1, k2, qe (exp), β , α, f and c were determined by non-linear regression

	Pseudo-first order						Pseudo-second order					
	k_1 (min^{-1})	$q_{e\ (exp)}$ (mg/g)	Residual pattern	χ^2	R^2	AARD	k_2	$q_{e\ (exp)}$ (mg/g)	Residual pattern	χ^2	R^2	AARD
E. coli DH5α	200.1	235.0	Yes	0.9	0.3	47.9%	10.0	235.0	Yes	0.9	0.2	47.9%
E. coli ATCC25922	100.0	157.0	Yes	1.1	0.2	58.9%	40.0	157.0	Yes	1.1	0.2	58.9%
E. coli BL21DE3	6.6	201.0	No	$6.2x10^{-3}$	1.0	2.2%	0.2	201.0	No	$5.8x10^{-3}$	1.0	2.2%
	Elovich model (@ Boundary conditions)						Intra-particle diffusion					
	β (g/mg)	α (mg/g.min)	Residual pattern	χ^2	R2	AARD	f (mg/g.min0.5)	C	Residual pattern	χ^2	R2	AARD
E. coli DH5α	0.6	$5.0\ x10^{50}$	Yes	0.3	0.7	25.7%	2.8	180.2	Yes	1.2	0.7	28.3%
E. coli ATCC25922	1.5	$3.3\ x10^{62}$	Yes	0.3	0.7	13.7%	0.6	96.2	Yes	0.9	0.7	14.2%
E. coli BL21DE3	0.1	$7.9\ x10^{11}$	No	$1.7x10^{-2}$	1.0	2.9%	0.1	195.1	No	1..0	1.0	1.1%

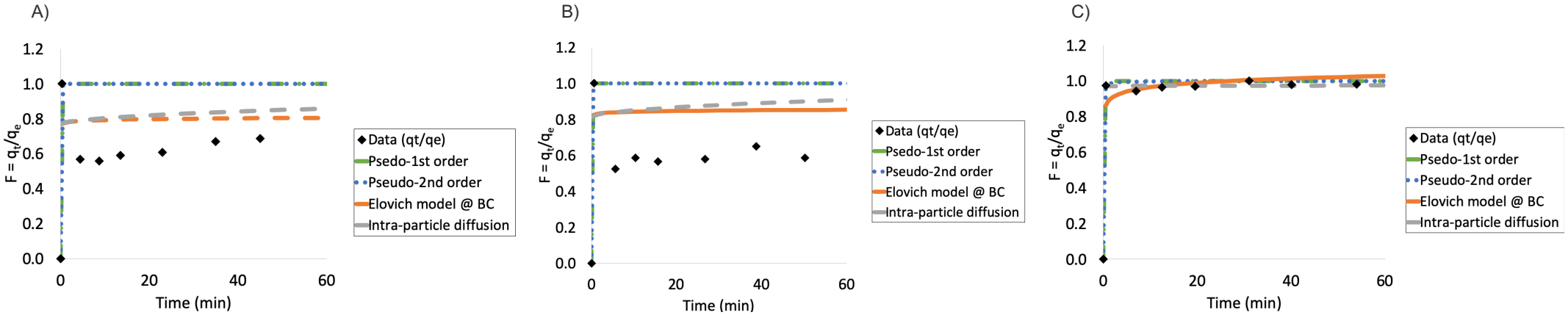

Figure 4-14 Fit of Pseudo-first order (—•—), , Pseudo-second order (• • • •) Elovich (—) and the Intra-particle diffusion (- - - -) kinetic models to experimentally determined adsorption of Au ions (♦) at a 25% (w/w) loading onto A) *E. coli* DH5α , B) *E. coli* ATCC25922 C) *E. coli* BL21DE3 scaffolds. The fit of the model was achieved by using the model parameters obtained after non-linear regression analysis.

Table 4-10 Isotherm model fit to the experimental adsorption of Au (III) at equilibrium. Where the model constants q_{max}, b, k_f, n, b_t B_T, a_t/A_T, β and q_D was determined by non-linear regression analysis

	Langmuir						Freundlich					
Support	**b (L/mg)**	**q_{max} (mg/g)**	**Residual pattern**	**χ^2**	**R^2**	**AARD**	**n**	**k_f**	**Residual pattern**	**χ^2**	**R^2**	**AARD**
E. coli DH5α	0.6	314.6	No	-360.0	0.2	67.4%	0.4	55.0	No	299.6	0.6	27.7%
E. coli ATCC25922	0.8	232.0	Uncertain	222.7	0.3	372.9%	0.5	31.8	No	886.4	0.4	93.4%
E. coli BL21DE3	0.3	427.0	Yes	218.4	0.7	57.1%	0.6	24.2	Yes	548.2	0.6	30.2%
	Temkin						**Dubinin-Radushkevich**					
Support	**B_T (J/mol)**	**a_t**	**Residual pattern**	**χ^2**	**R^2**	**AARD**	**β (mol²/J²)**	**q_D(mg/g)**	**Residual pattern**	**χ^2**	**R^2**	**AARD**
E. coli DH5α	7.7	1.2	No	214.1	0.6	32.0%	8.1×10^{-7}	732.4	No	245.4	0.6	33.2%
E. coli ATCC25922	17.3	1.8	No	224.3	0.6	251.1%	5.5×10^{-7}	334.3	No	384.8	0.5	161.1%
E. coli BL21DE3	14.0	1.1	Yes	159.6	0.8	32.3%	6.9×10^{-7}	315.0	Yes	153.4	0.8	34.7%

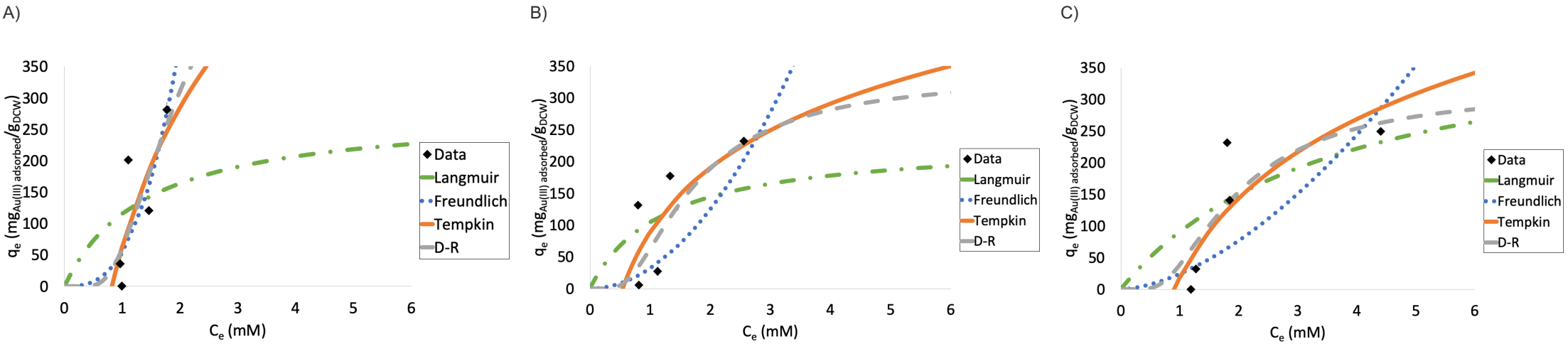

Figure 4-15 Fit of Langmuir (—•—),, Freundlich(• • • •), Temkin (——) and the Dubinin-Radushkaveich (- - - -) isotherm equilibrium models to experimentally determined adsorption of Au ions (♦) onto A) *E. coli* DH5α , B) *E. coli* ATCC25922 C) *E. coli* BL21DE3 scaffolds. The fit of the model was achieved by using the model parameters obtained after non-linear regression analysis.

From Table 4-10, it is apparent that none of the isotherm models considered are adequate to model the adsorption of Au onto any of the microbial scaffolds at equilibrium (Figure 4-15). As an S-class isotherm was noted on all strains, none of the models account for what is likely co-operative adsorption of Au. Consequently, an alternative model, such as, the Fowler-Guggenheim model that considers interactions between adsorbate molecules was applied.

The Fowler-Guggenheim model was first developed by Fowler and Guggenheim (1956) and incorporates the lateral interaction of adsorbed molecules on the support (Beltrán-Heredia and Sánchez-Martín, 2009; Hamdaoui and Naffrechoux, 2007). The model describes the concentration of the adsorbate at equilibrium (C_e) as a function of coverage of the adsorbate in relation to the heat of adsorption (Equation 4-6 and Equation 4-7).

$$\ln\left(\frac{\theta}{C_e(1-\theta)}\right) = \ln(k_{FG}) - \frac{2w}{RT}\theta \qquad \text{Equation 4-6}$$

and

$$\theta = \frac{q_e}{q_{max}} \qquad \text{Equation 4-7}$$

where k_{FG} (L/mg) is the model equilibrium constant, *w* (kJ/mol) is the interaction energy between adsorbed molecules, R (kJ/mol.K) the universal gas constant and T (K) is the temperature of adsorption. In this model θ is dimensionless and defined as the coverage of the adsorbate on the support (Equation 4-6). The coverage is as a function of the fraction of the total amount adsorbed at equilibrium q_e relative to the maximum adsorption capacity q_{max} (Equation 4-7). Since *w* determines the interaction between absorbed species, a positive value indicates attractive interactions whereas a negative value indicates repulsive interaction between the adsorbed molecules. If the *w* value is zero the model reduces to the Langmuir model where no lateral interactions between molecules are assumed to occur (Ayawei et al., 2017; Beltrán-Heredia and Sánchez-Martín, 2009; Hamdaoui and Naffrechoux, 2007).

By incorporating lateral interactions between adsorbed Au(III) molecules, the Fowler-Guggenheim model was able to achieve a reasonable fit to the experimental data across all microbial strains (Table 4-11).

Table 4-11 Fowler-Guggenheim isotherm model fit to the experimental adsorption of Au(III) at equilibrium. Where θ, q_e, q_{max}, C_e, k_{FG}, *w*, *R* and *T* are defined after non-linear regression analysis

	Fowler-Guggenheim						
Support	**k_{FG} (L/mg)**	**w (kJ/mol)**	**q_{max}**	**Residuals**	**χ^2**	**R^2**	**AARD**
E. coli DH5α	0.07	-6.3	302.2	No	0.02	1.0	6.3%
***E. coli* ATCC25922**	0.03	-8.0	237.6	No	1.1	1.0	35.2%
E. coli BL21DE3	0.04	-6.6	257.5	Uncertain	-0.1	1.0	10.7%

As the interaction energy *w* was negative for each of the strains, repulsive lateral interactions were likely observed between the adsorbed molecules. The equilibrium constants k_{FG} in all cases were low and within the same magnitude. The low equilibrium constant in this model

and the limited capacities observed for this metal (Figure 4-9, Figure 4-10), indicated that these microbial strains have a low affinity for Au ions in solution.

In summary, it was shown that Pd and Au adsorption on all microbial strains occurred almost instantaneous as the cells were exposed to the precursors. *E. coli ACC25922* had the greatest capacity for both Pd and Au at the 5% (w/w) loading. However this strain seemed to be least tolerant to higher metal loadings as rapid desorption of both metals occurred on this microbial strain. Kinetic modelling indicated that adsorption of the metals to the various *E. coli* cells was mostly likely by chemisorption onto functional groups of the cells' organic matrix. Isotherm modelling also indicated that interactions between adsorbate molecules have an impact on the mechanism. The decline in the amount of Pd adsorbed from the 5% (w/w) to the 25% (w/w) loading (Figure 4-1, Figure 4-2) indicated that the bacterial cells were over saturated. Conversely, a greater affinity for adsorption was noted for the Au ions at the higher metal loading. Unlike Pd adsorption at equilibrium, a plateau was not reached for this noble metal. Rather a S-shaped isotherm was noted for Au adsorption. This indicated that the mechanism of adsorption was influenced by lateral interaction between the absorbed ion molecules thereby limiting efficient adsorption of this metal to each of the *E. coli* strains investigated.

Chapter 5

5 Bioreduction and characterization

5.1 Chapter Overview

Several studies have considered the effect of electron donor as well as the influence of the variation of functional groups and hydrogenase activity on reduction across a range of microorganisms (Deplanche et al., 2014; Deplanche and Macaskie, 2008; Kashefi et al., 2001; Yong et al., 2002a). It was noted that these factors impact reduction timeframes, influence the size and morphology of nanoparticles formed as well as the distribution of nanoparticles across the cell surface.

Chemical and gaseous electron donors such as lactate, formate, and hydrogen are commonly used in the biofabrication of nanoparticles (Liamleam and Annachhatre, 2007). Hydrogen is the preferred electron donor in acidic metal ion solutions, such as metal-rich waste leachates, as it is closely associated with the maintenance of hydrogenase activity in acidic environments (Yong et al., 2002a). The choice of microorganism or microbial strain dictates the availability of crucial electron shuttle enzymes required for reduction. These include hydrogenase and nitrogenase proteins. The significance of hydrogenase is noted during the reduction of Pd(II) ions on hydrogenase-deficient microorganisms. A deficiency of these proteins results in the slower reduction timeframes, an irregular distribution of nanoparticles, and larger metal agglomerate formation (Deplanche et al., 2010; Mikheenko et al., 2008; Torgeman, 2017). The impact of the interaction of the electron donor with the microbial strain on reduction can, however, be specific to the metal considered. For example, the reduction of Au ions tends to be more successful in the presence of gaseous electron donors as compared to chemical based forms (Kashefi et al., 2001; Konishi et al., 2006). Previous investigations show the formation of 5 nm spherical Pd nanoparticles as compared to biofabricated Au nanoparticles that range from 20 – 50 nm in size that are often irregularly shaped (Deplanche et al., 2008; Du et al., 2007). High catalyst activity is often observed when nanoparticles are morphologically uniform, mono-dispersed and have an approximate size range of less than 5 nm (Deplanche et al., 2010). Considering the impact of these factors, the influence of electron donor, metal loading, and microbial strain on the shape, size and distribution of biofabricated nanoparticles during metal reduction are explored.

5.2 5% (w/w) metal loading

5.2.1 Formation of monometallic Pd nanoparticles

The formation of Pd nanocatalysts following biosorption was initiated by a chemical (HCOONa) or gaseous (H_2) electron donor (Section 3.3.1). Reduction of the metal-cell pellet complex was performed at 30°C and confirmed by a colour change of the solution from yellow to black (Figure 5-1).

A) B)

Figure 5-1 Image of observed colour change in solution upon successful Pd(0) formation. Where A) is the initial Pd ion solution before reduction B) is the final solution after donor addition and bioreduction at 30°C

Although this change was observed on all microbial strains and electron donors, varying reduction timeframes were noted across the two donors. Hydrogen-assisted reduction on *E. coli* exhibited a colour change within 20 to 30 minutes of sparging. Comparatively, sodium formate-induced reduction was only detected after overnight incubation. Negative controls, without any of the microbial strains present were incubated under similar conditions. After electron donor addition, the control similarly exhibited a colour change from yellow to clear with a black precipitate. Some of this black participate was suspended in solution while heavier aggregates settled to the bottom of the vessel. Similar colloidal aggregate formation in the control was observed by Torgeman (2017), who attributed the precipitation to the presence of the MOPS-NaOH buffer. It is likely this interaction of buffer and metal ion also occurs in the presence of the bacterial cell. However, as the cell is abundant in functional groups like amine, these groups act as stabilizers for particle growth and allow for the regular distribution of colloids onto a support (Monai et al., 2018). Ultimately, these colloids bind to the cell to further act as seeds for further Pd(0) formation.

Although a colour change signalled the formation of Pd(0), it was important to verify the formation of nanoparticles on, or within, the *E. coli* scaffolds. Analytical techniques, such as ICP, TEM, EDX and SEM, were used to confirm the composition, metal loading as well as to define the size, shape and distribution of the nanoparticles on the microbial scaffolds (Section 3.6). Using these findings, a comparison of the physical and chemical characteristics of the nanoparticles was made to determine the most suitable electron donor and microbial strain for monometallic Pd(0) production.

Influence of electron donor and microbial strain

TEM imaging was used to assess the size, shape, distribution as well as the interactions between the nanoparticles and the microbial cells. Samples were prepared for TEM by embedding the biofabricated Pd catalysts in resin and thereafter sectioning the samples (Section 3.6.1). These sectioned samples were subsequently stained to highlight the structure of the cell. Analysis of the resulting stained images provided further indication of how microbial strains were affected upon exposure to the metal. Cell stress was noted by morphological changes such as lysing, large vacuoles or outer membrane vesicles (OMV). TEM image processing software was used to generate a representative average particle size distribution, with error, for all samples (Figure 5-2 to Figure 5-4).

E. coli DH5α

E. coli ATCC25922

E. coli BL21DE3

A)

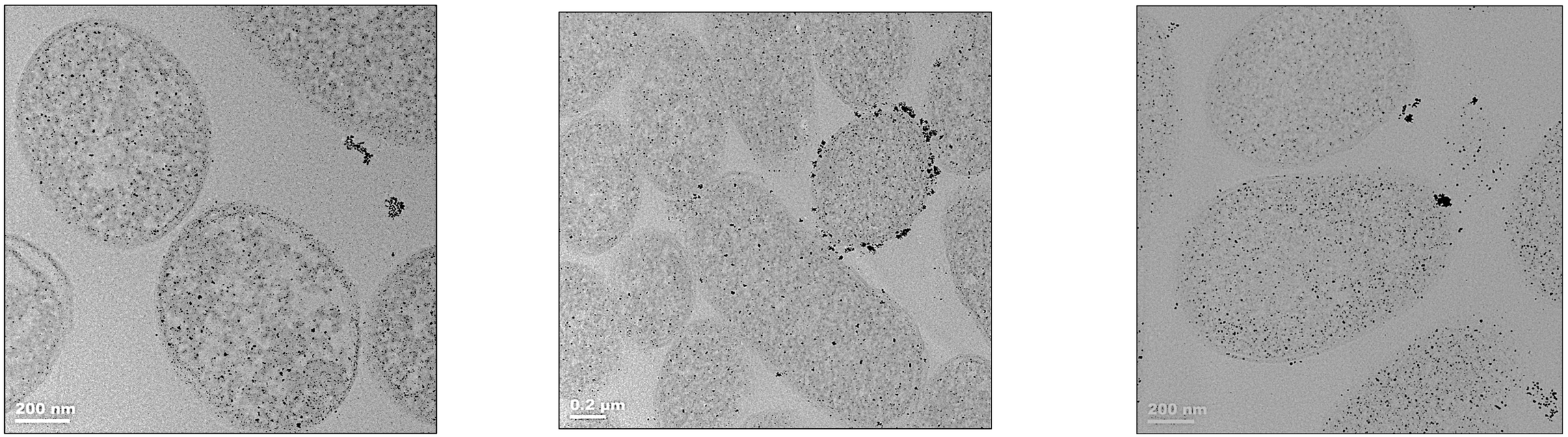

B)

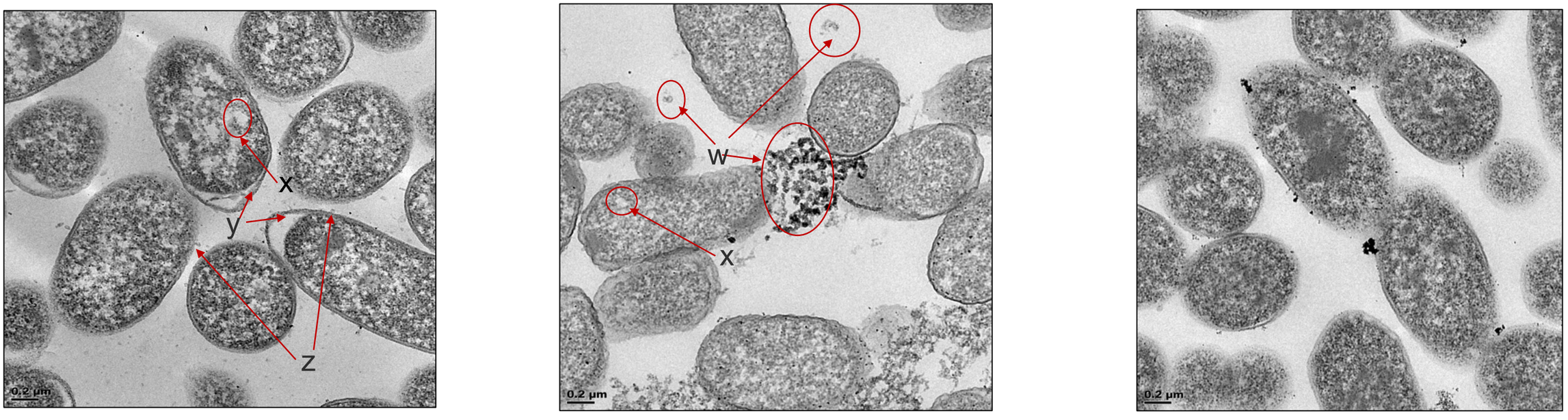

Figure 5-2 TEM imaging of 5% (w/w) Pd catalysts on the three *E. coli* strains using sodium formate as the electron donor. Biofabricated catalysts were washed in water and 2.5 % (w/v) glutaraldehyde (in PBS) and fixed with 1% (w/v) osmium tetraoxide (OsO_4) solution and thereafter dried in ethanol, fixed in epoxy resin and then sectioned. Row A) are the unstained biofabricated Pd samples that were used to determine particle size distribution B) the biofabricated Pd samples that were stained with 1% (w/v) OsO_4 and used for quantifying cell structure. Where lysed cells, cell vacuoles, distended or disrupted cell walls and blebbing or OMV's are denoted by *w, x, y* and *z*, respectively. Note that 200 nm = 0.2 μm.

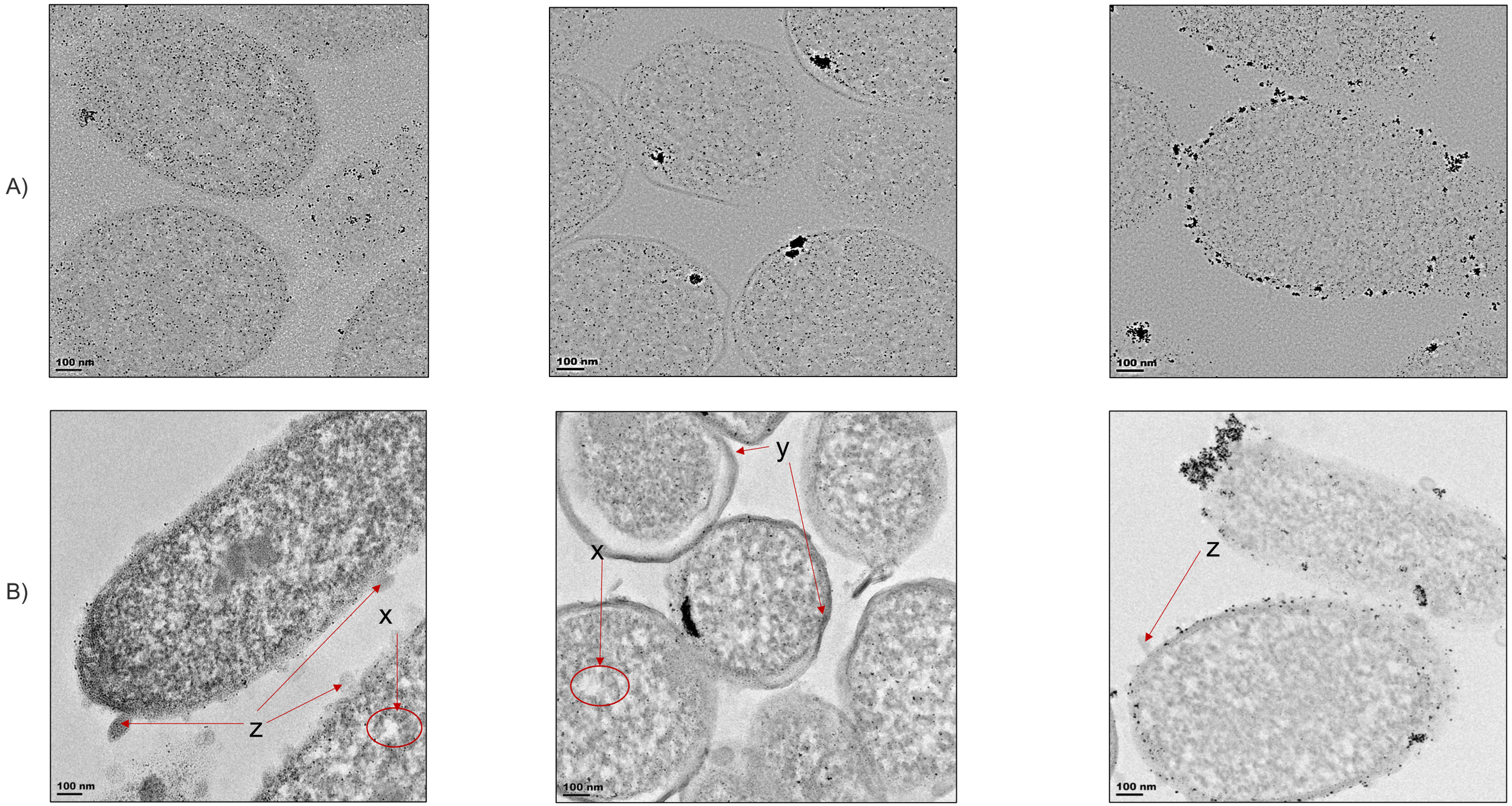

Figure 5-3 TEM imaging of 5% (w/w) Pd catalyst on the three *E. coli* strains using hydrogen as the electron donor. Biofabricated catalysts were washed in water and 2.5 % (w/v) glutaraldehyde (in PBS) and fixed with 1% (w/v) osmium tetraoxide (OsO_4) solution and thereafter dried in ethanol, fixed in epoxy resin and then sectioned. Row A) are the unstained biofabricated Pd samples that were used to determine particle size distribution B) the biofabricated Pd samples that were stained with 1% (w/v) OsO_4 and used for quantifying cell structure. Where cell vacuoles, distended or disrupted cell walls and blebbing or OMV's are denotated by x, y and z, respectively

A)

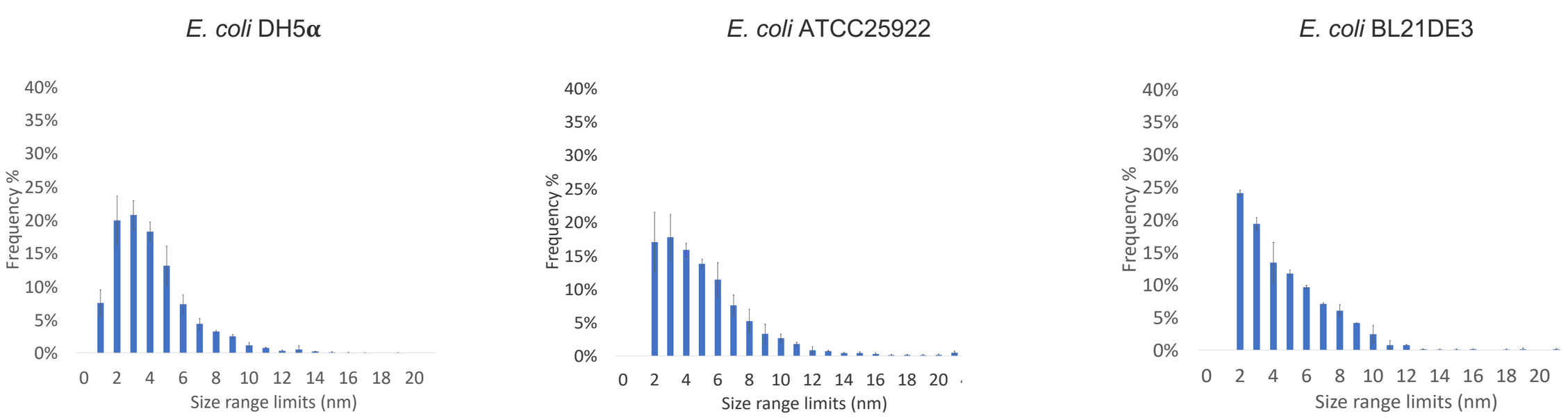

B)

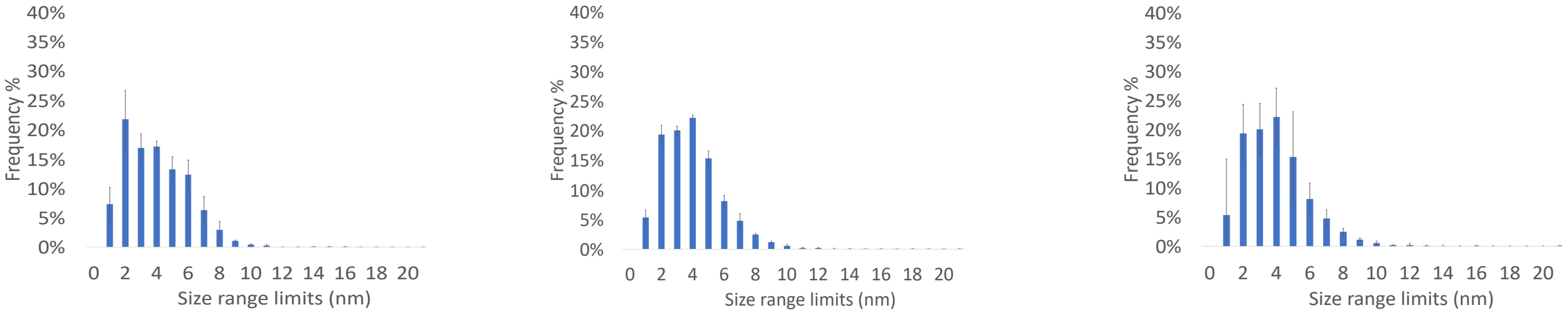

Figure 5-4 Average particle size distribution of 5% (w/w) Pd nanoparticles on the three *E. coli* strains when using A) sodium formate and B) hydrogen as the electron donor

From image analysis, it was clear that Pd nanoparticles bind to all microbial strains irrespective of the reducing agent (Figure 5-2 and Figure 5-3). The resulting nanoparticles had a near-spherical shape with an average circularity factor ranging between 0.9-1 (1 indicates complete circularity) (Figure 5-3). For each microbial strain, the nanoparticles were mainly located within the cytoplasm with clustering only evident in the periplasm of *E. coli* ATCC25922 and *E. coli* BL21DE3. Agglomeration was likely caused by the autocatalytic adsorption and reduction of residual Pd(II) ions in solution that resulted in concentrated Pd(0) seeds being formed on these strains.

Clusters within the periplasm of *E. coli* ATCC25922 have been further attributed to Hyd-1 and Hyd-2 or other such membrane-bound proteins. These proteins are abundant in amine functional groups (Figure 4-4) that stimulate electron transfer and thus may promote agglomeration at specific cell locations (Lukey et al., 2010; Pinske et al., 2011a). Clustering of particles less that 50 nm in size were also sporadically noted along the periplasm of *E. coli* BL21DE3 (Figure 5-2 and Figure 5-3). As this *E. coli* strain is deficient in these periplasmic hydrogenase (Pinske et al., 2011a), it is likely that other key electron transport enzymes also assist in reduction.

Average particle size was used as an indicator of reductive potential and the prominence of aggregation. Using the TEM images and size distribution analysis of nanoparticles formed on *E. coli* DH5α, *E. coli* ATCC25922 and *E. coli* BL21DE3 (Figure 5-4), the average particle size was determined (Table 5-1)

Table 5-1 Average size of the 5% (w/w) Pd(0) nanoparticles formed across the various *E. coli* strains and electron donors

	Average particle size (nm)	
***E. coli* strain**	**Sodium formate**	**Hydrogen**
E. coli DH5α	3.6 ± 0.4	3.5 ± 0.5
E. coli ATCC25922	4.7 ± 0.7	3.5 ± 0.3
E. coli BL21DE3	4.1 ± 0.3	3.0 ± 0.6

Nanoparticles produced in the presence of sodium formate on each of the *E. coli* strains resulted in particles with a mean size between ca. 3.5 – 5.0 nm (Table 5-1). In comparison, hydrogen induced reduction resulted in well-distributed, uniform Pd nanoparticles between 3.0 - 3.5 nm in diameter across all microbial strains within 30 minutes of electron donor addition (Table 5-1 and Figure 5-4). This observation indicated that hydrogen is more efficient over sodium formate as an electron donor for effective nanoparticle formation within the desired particle size range (<5 nm) to produce nanocatalysts with high activity. When comparing the reduction across the selected *E. coli* strains, *E. coli* DH5α outperformed *E. coli* ATCC25922 and *E. coli* BL21DE3 by generating well-distributed, uniform particles across the scaffold. This strain appeared to be more robust over its counterparts as this level of consistency across the support is often difficult to achieve (Figure 5-2 and Figure 5-3).

Agglomeration on *E. coli* ATCC25922 and *E. coli* BL21DE3, hinders the potential of these *E. coli* as ideal supports. However, as seen in Table 5-1 the resulting agglomeration noted in Figure 5-2 and Figure 5-3 does not greatly influence the average nanoparticle size for either of these strains. Consequently, either of these strains may potentially be used as an alternative

scaffold to *E. coli* DH5α for the biofabrication of nanoparticles. Reduction on previously studied hydrogenase-deficient microorganisms, like *E. coli* BL21DE3, were described to be slow, promoting a poor distribution of nanoparticles with a high degree of agglomeration on the exterior cell surface (Deplanche et al., 2010; Mikheenko et al., 2008). In contrast to these findings, most of the nanoparticles formed within *E. coli* BL21DE3 in this study were indistinguishable in size and shape compared to those observed on *E. coli* ATCC25922 and *E. coli* DH5α. The similarity between the nanoparticles suggests a secondary mechanism for reduction, potentially through other active electron shuttle pathways, with hydrogenase playing a less prominent role than suspected (Torgeman, 2017).

Bacterial cell morphology

Even though strain type had little impact on the nanoparticle structure, the metal did have an effect on the morphology of the microorganisms (Figure 5-2.B and Figure 5-3.B).. Microbial cells in the presence of metal ions respond to the stress by either bioaccumulation or detoxification of the ions from its environment (Deplanche, 2008; Lloyd et al., 1997; Torgeman, 2017).

The presence of large vacuoles, elongated and lysed cell walls, the formation of blebbing and OMVs were indicative that the bacterial cells were indeed under stress once exposed to the metals ions in solution (*viz*. stained TEM images in Figure 5-2.B and Figure 5-3.B). OMVs formed as a result of leaking of cell contents through perforated microbial cell walls. Such perforations were likely due to an accumulation and the active transport of metal ion particulates within the cells. Large vacuole formation was prominent across all three microbial strains, regardless of the electron donor. In the case of *E. coli* DH5α, the formation of nanoparticles resulted in a slight distention of the cell wall. OMV development was prominently noted in the presence of hydrogen. Similarly upon Pd reduction on *E. coli* ATCC25922, distention of the cell walls, and in some cases perforations, were detected leading to leaking of internal cell contents. For this microbial strain, production of OMVs were minimized with hydrogen reduction, however these artefacts were still evident. In this case it is postulated that rapid adsorption and nanoparticle formation using hydrogen, as compared to slower reduction using sodium formate, leads to the greater degree of perforation. The slower reduction with sodium formate is in part due to the cell needing to convert this molecule to hydrogen before contributing to the electron pool used for ion reduction. The enzyme deficient *E. coli* BL21DE3 strain showed the least signs of lysis, cell wall distention or OMV formation compared to the other microbial strains, indicating that the cell was the most tolerant to the Pd(II) ions.

5.2.2 Formation of monometallic Au nanoparticles

As with Pd(II), Au(III) reduction was initiated by incubating the metal ion precursor with the various *E. coli* strains overnight at 30°C in the presence of the selected electron donors. Successful reduction of the Au(III) ions to Au(0) was verified by a colour change of the solution from a pale yellow to a bright purple-pink – typically indicative of nanoparticle synthesis (Figure 5-5) (Deplanche and Macaskie, 2008; Kashefi et al., 2001; Konishi et al., 2006; Liz-Marzán, 2004).

A) B)

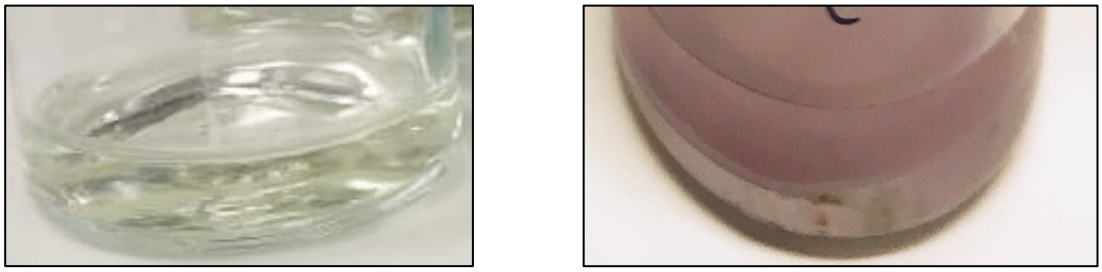

Figure 5-5 Image of the expected colour change in solution upon successful Au(0) formation. Where A) is the initial Au ion solution before reduction and B) is the final solution after donor addition and bioreduction overnight at 30°C

This distinctive colour change was only noted on *E. coli* ATCC25922 when the ion solution complex was pre-saturated and incubated overnight with hydrogen (Figure 5-5). A slight colour change to grey-purple in solutions containing either *E. coli* BL21DE3 or *E. coli* DH5α was noted under similar reduction conditions. However, these changes were only evident after extending the incubation period by a further four to five days. A similar colour change was not noted upon addition of the sodium formate electron donor, even when extending the reduction period over four to five days. Negative controls, without any of the microbial strains present, also exhibited a change in solution colour from yellow to clear with a red precipitate. Some of the resulting particles remained suspended in solution while heavier aggregates settled to the bottom of the vessel. Similar to the Pd ion controls, this reduction was induced in the presence of the buffer.

Influence of electron donor and microbial strain

TEM imaging analyses of approximately 0.1 ml of biofabricated Au catalyst (5% w/w) samples were used to assess the physical characteristics of the nanoparticles and microbial strains. Using the same procedures outlined for monometallic Pd nanoparticles, these samples were fixed, dried in an epoxy resin and then cut into thin sections, providing a cross-sectional view of the samples (Figure 5-6).

E. coli DH5α

E. coli ATCC25922

E. coli BL21DE3

A)

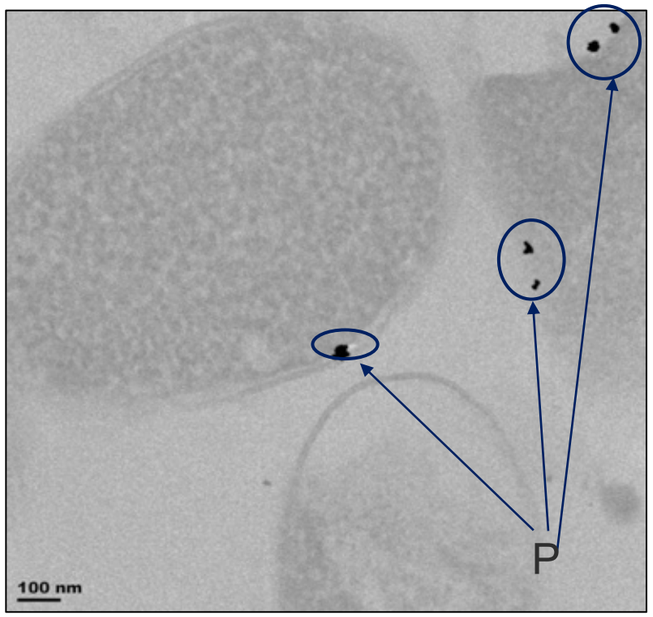

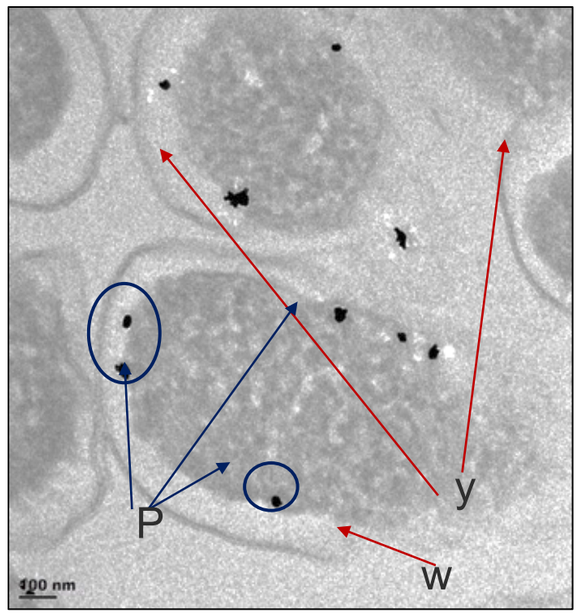

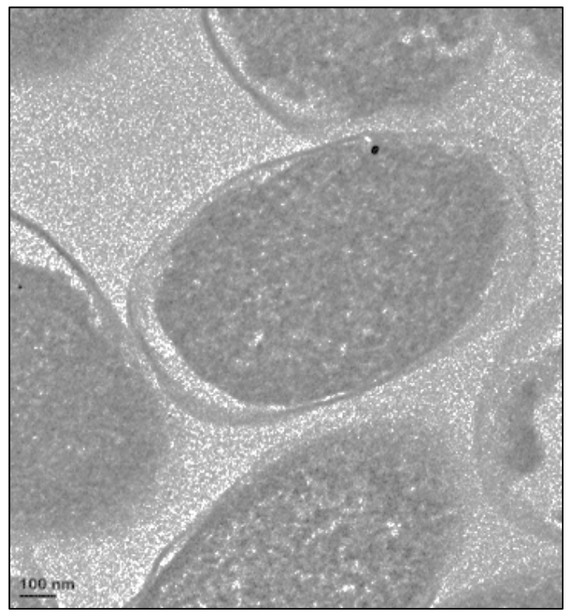

B)

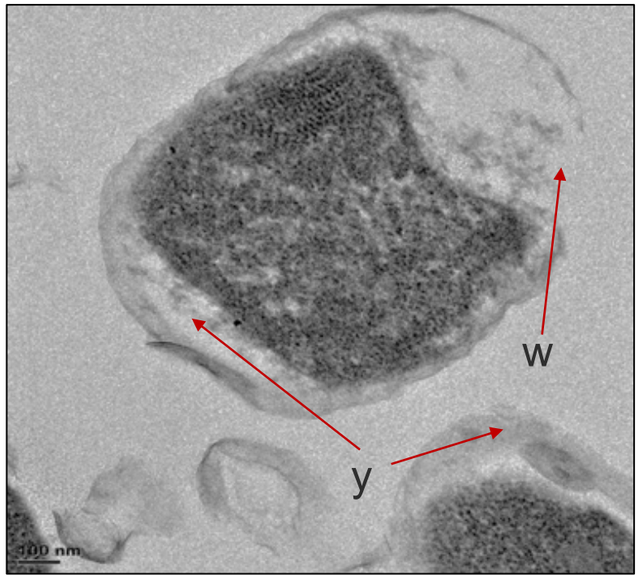

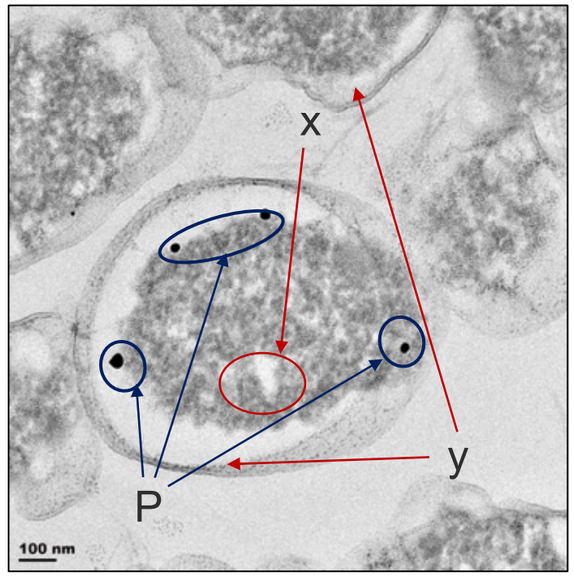

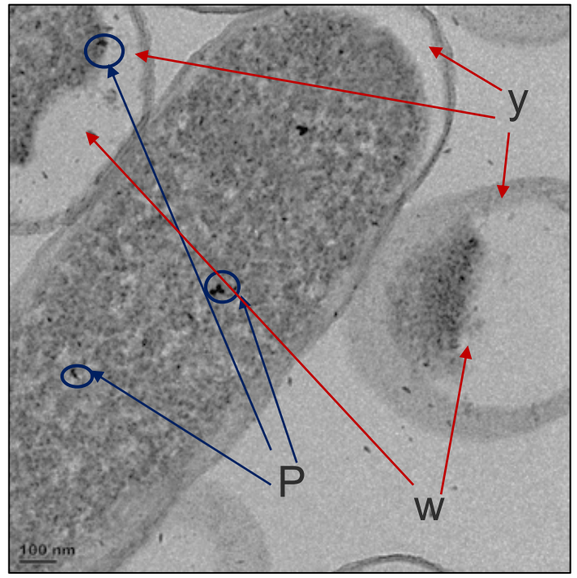

Figure 5-6 TEM imaging of 5% (w/w) Au catalyst on the three *E. coli* strains using hydrogen as the electron donor. Biofabricated catalysts were washed in water and 2.5 % (w/v) glutaraldehyde (in PBS) and fixed with 1% (w/v) osmium tetraoxide (OsO_4) solution and thereafter dried in ethanol, fixed in epoxy resin and then sectioned. Row A) are the unstained biofabricated Au samples that were used to determine particle size distribution B) the biofabricated Au samples that were stained with 1% (w/v) OsO_4 and used for quantifying cell structure. Where lysed cell, cell vacuoles, distended or disrupted cell walls and nanoparticle clusters are denotated by w, x, y and P, respectively.

Analysis of the TEM images indicated that biofabricated Au(0) nanoparticles were formed on all microbial strains when the metal ion precursor was saturated with hydrogen (Figure 5-6). However, as noted earlier, this was not observed when sodium formate was used as the electron donor. Large clusters of irregularly shaped Au(0) nanoparticles, with an average circularity factor between 0.6-0.8, were evident on the interior membrane of the periplasm of *E. coli* DH5α and *E. coli* ATCC25922 when using hydrogen. On these microbial strains an average of 3-6 nanoparticles between 20 - 40 nm in size were noted sporadically across the cells, which was consistent with findings by Deplanche and Macaskie (2008), Liz-Marzán (2004) and Torgeman (2017). These agglomerates were not detected on every cell and were not uniformly distributed along the scaffolds. As such, the distribution of nanoparticles across cells were not reproducible with the size deviating from ideal catalyst characteristics (Liu and Corma, 2018). Slight clustering of the reduced Au(0) nanoparticles was also detected within the cytoplasm of *E. coli* BL21DE3 ranging between 20 - 40 nm in size. On closer inspection of this microbial strain additional finer particles (< 5 nm) were distributed throughout the cell cytoplasm (Figure 5-7).

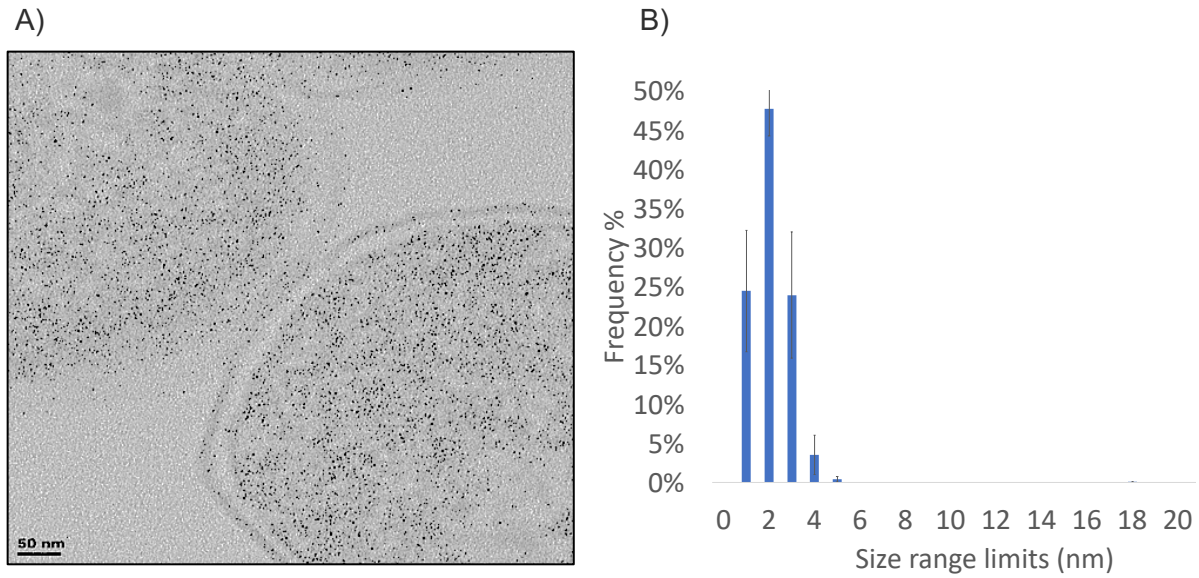

Figure 5-7 TEM imaging of the 5% (w/w) Au nanocatalyst on *E. coli* BL21DE3 using hydrogen as the electron donor. Biofabricated Au samples were fixed in 2.5 % (w/v) glutaraldehyde (in PBS) and 1% (w/v) osmium tetraoxide (OsO_4) solution and thereafter dried in ethanol, fixed in epoxy resin and left to dry before sectioning using an ultramicrometre. The unstained biofabricated Au samples in figure A) were used for particle size distribution analysis of biofabricated Au nanoparticles as shown in figure B).

A size distribution analysis on the TEM images indicated that the cytoplasmic nanoparticles had an average size of 1.6 $\pm$ 0.2 nm (Figure 5-7). Particles of this size were not noted within the *E. coli* DH5α and *E. coli* ATCC25922 strains. A similar variation in adsorption capacity of Au across the microbial strains was also observed (Section 4.3). This suggested that the mechanism for Au nanoparticle formation is dictated by a biological factor that differs across these microbial strains. Previous studies on reduction of Au indicate that the mechanism for nanoparticle formation is a product of enzymes involved in the cell's electron transport chain (Ali et al., 2019; Deplanche et al., 2008; Gahlawat and Choudhury, 2019; Kashefi et al., 2001). Electron transport enzymes such as nitrate reductase, redox mediators (such as NADH) and cytochrome c proteins are known to facilitate the bioreduction process (Ahmed et al., 2016;

Brayner et al., 2007; Rotaru et al., 2012; Torgeman, 2017). These enzymes are produced during cell growth under conditions, such as oxygen limitation, that induce oxidative stress (Kadenbach et al., 2004). In an oxygen limited environment these proteins normally assist in the shuttling of electrons to generate energy and maintain the cell's metabolism. In this study, growth of *E. coli* BL21DE3 was poor under such anoxic conditions which is attributed to a lack of the *FNR* gene that governs the production of key electron shuttle enzymes like hydrogenase and nitrate reductase (Pinske et al., 2011b). Small nanoparticles in the cytoplasm of *E. coli* BL21DE3 were similarly observed by Gahlawat and Choudhury (2019) for microorganisms lacking the cytochrome c protein. As a consequence, it was postulated that the deficiency of key Au reductase enzymes in *E. coli* BL21DE3 resulted in poor active site availability for adsorption resulting in a low-density distribution of circular nanoparticles (shape factor of 0.9-1) with reduced size and limited impact on the cell integrity.

Oxidative stress may also be induced upon exposure of cells to high concentrations of metals, thus promoting the production of enzymes necessary for Au(0) formation. However, excessive levels of cytochrome c can induce cell death. The degree of cell death depends on the tolerance of the microorganism to Au ions in solution (Ali et al., 2019; Chah et al., 2005; Gahlawat and Choudhury, 2019). Torgeman (2017) found that for *E. coli* MC4100, Au(III) concentrations greater than 0.7 mM resulted in complete cell death. It is evident that regardless of metal reductase availability, the excessive ion concentration for this particular metal brings about similar apoptosis in the cells (Figure 5-6). Where fine nanoparticles were detected, *E. coli* BL21DE3 cells were shielded from complete rupturing. A consequence of the minimal uptake of Au(III) ions (ca. 2.4% w/w) noted for this strain.

Bacterial cell morphology

Analysis of TEM images in Figure 5-6 showed that the clustering of Au(0) nanoparticles were prevalent on the inner-periplasmic membrane of the microbial strains as well as within the cytoplasm of *E. coli* BL21DE3 (*P* in Figure 5-6). These agglomerations were associated with the distinctive distending of the cell walls (*y* in Figure 5-6). In some cases, the cells were completely ruptured or lysed (*w* in Figure 5-6). These artifacts were considered to be a result of the interaction of larger Au(0) nanoparticles with the cell cytoplasm that caused severe morphological alterations. Under the stress of metal toxicity, microorganisms often respond by undergoing apoptosis. One way of bringing about such apoptosis is by the production of reactive oxygen species (ROS) in cells. The presence of ROS, such as intracellular hydrogen peroxide produced through the autooxidation of redox enzymes, leads to increased levels of cytochrome c that then initiates degradation and pit formation of the cell wall (Kadenbach et al., 2004; Shah et al., 2016; Wang et al., 2017). Although this enzyme is required for metal reduction, high levels of cytochrome c can promote complete rupturing and leakage of the cell's metabolic content (Shah et al., 2016; Wang et al., 2017). This disintegration was noted across all strains and indicated that cell viability was compromised upon exposure to Au. Cell death resulted in deactivation of key enzymes, resulting in slow reduction as well as

agglomeration of Au(0) nanoparticles with poor uniformity and distribution across on the biological scaffolds (Figure 5-6).

5.3 25% (w/w) metal loading

TEM images at the lower metal loading showed that Pd(0) nanoparticles were present within the cytoplasm and on the exterior surface of *E. coli* ATCC25922 and *E. coli* BL21DE3. Such Pd(0) nanoparticles were identified by several researchers in similar locations using *E. coli* MC4100 as supports (Deplanche and Macaskie, 2008; Macaskie et al., 2012; Penfold et al., 2003; Torgeman, 2017; Zhu, 2014). In contrast to these findings, extracellular Pd(0) nanoparticles were not noted on *E. coli* DH5α in this study. Nanoparticles on this microbial strain were mono-dispersed and evenly distributed displaying attributes of an ideal catalyst support for Pd and potentially for the development of bimetallic catalysts (Figure 5-2.A and Figure 5-3.A). Although these properties were predominant at lower metal loadings, it was necessary to demonstrate whether these characteristics would be persistent at higher metal loadings when reduced with the identified electron donors (Figure 5-8 to Figure 5-10).

A) B)

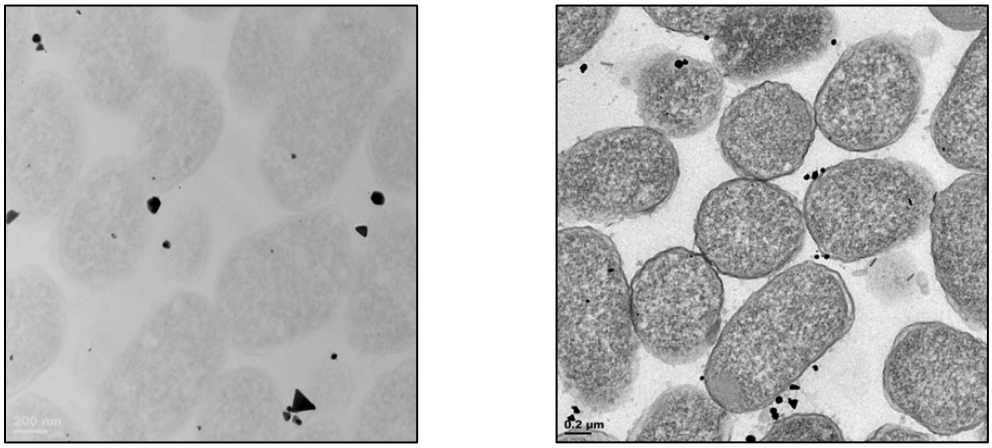

C)

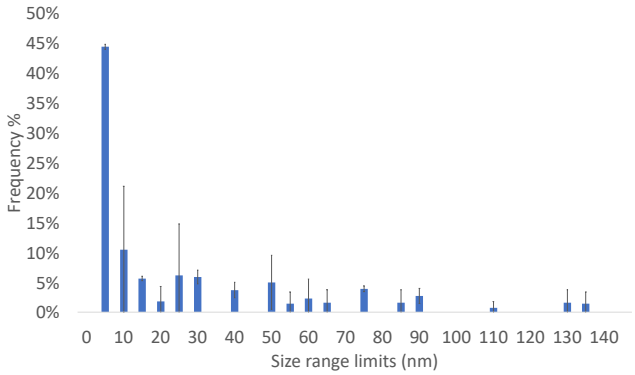

Figure 5-8 TEM images of 25% (w/w) Au on *E. coli* ATCC25922 using hydrogen as the electron donor. Biofabricated Au samples were extracted and fixed in 2.5 % (w/v) glutaraldehyde (in PBS) and 1% (w/v) osmium tetraoxide (OsO_4) solution and thereafter dried in ethanol, fixed in epoxy resin and left to dry before sectioning using an ultramicrometre. Where A) is the unstained biofabricated Au samples used to determine the particle size distribution B) the biofabricated Au sectioned samples that were stained with OsO_4 and used for quantifying cell morphology and C) the average size distribution of Au nanoparticles.

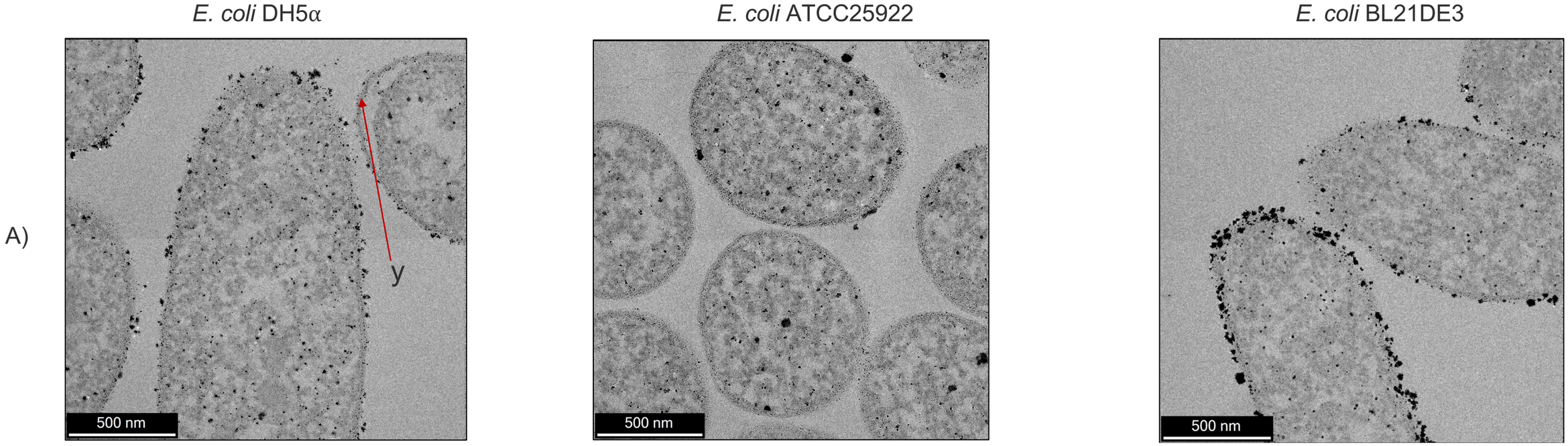

Figure 5-9 TEM imaging of 25% (w/w) Pd catalyst on the three *E. coli* strains using sodium formate as the electron donor. Biofabricated catalysts were washed in water and 2.5 % (w/v) glutaraldehyde (in PBS) and fixed with 1% (w/v) osmium tetraoxide (OsO_4) solution and thereafter dried in ethanol, fixed in epoxy resin and then sectioned. Row A) are the unstained biofabricated Pd samples that were used to determine particle size distribution B) the biofabricated Pd samples that were stained with 1% (w/v) OsO_4 and used for quantifying cell structure. Where lysed cells, cell vacuoles, distended or disrupted cell walls and blebbing or OMV's are denotated by w, x, y and z, respectively

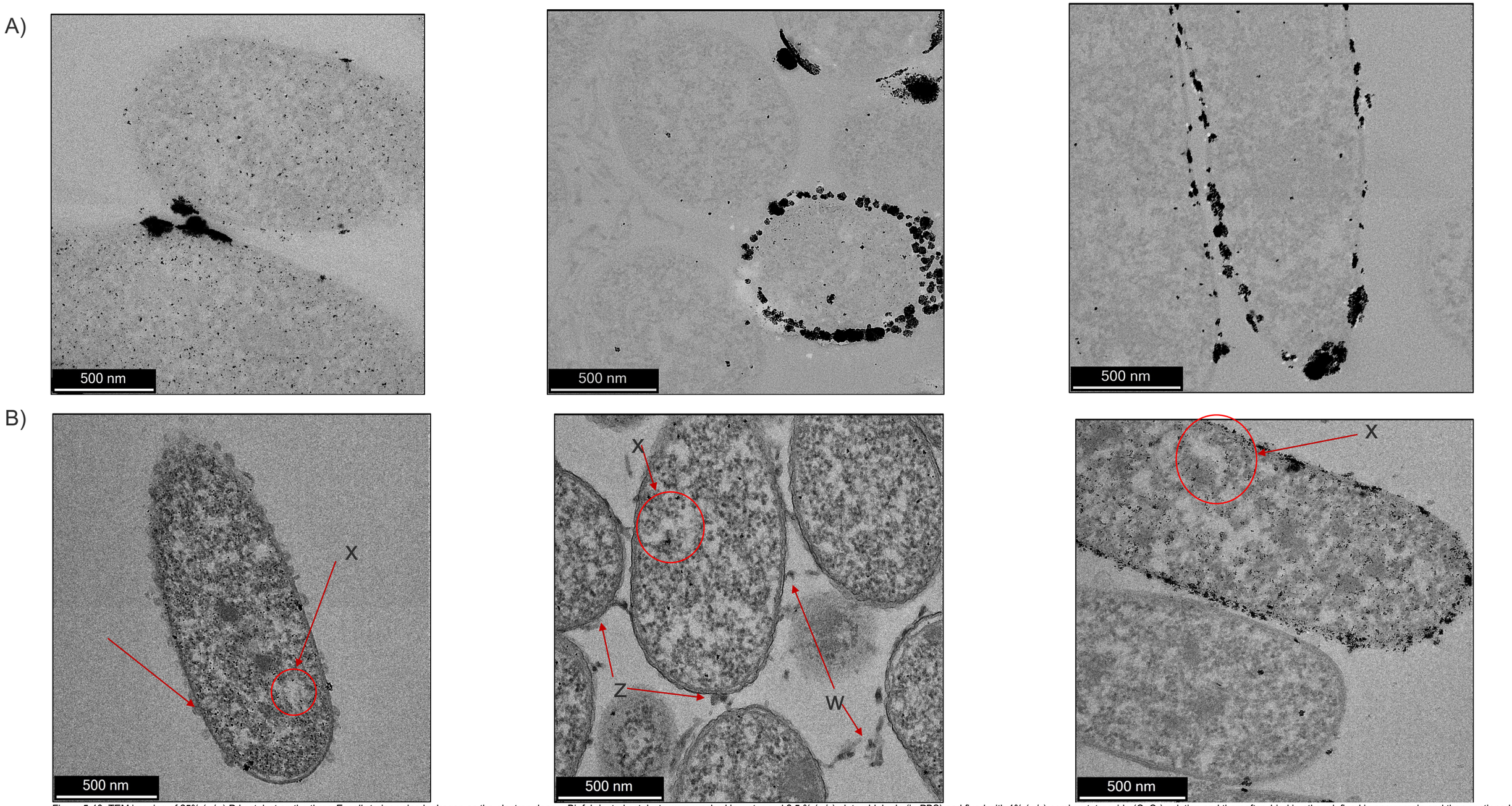

Figure 5-10 TEM imaging of 25% (w/w) Pd catalyst on the three *E. coli* strains using hydrogen as the electron donor. Biofabricated catalysts were washed in water and 2.5 % (w/v) glutaraldehyde (in PBS) and fixed with 1% (w/v) osmium tetraoxide (OsO_4) solution and thereafter dried in ethanol, fixed in epoxy resin and then sectioned. Row A) are the unstained biofabricated Pd samples that were used to determine particle size distribution B) the biofabricated Pd samples that were stained with 1% (w/v) OsO_4 and used for quantifying cell structure. Where lysed cells, cell vacuoles and blebbing or OMV's are denotated by w, x and z, respectively

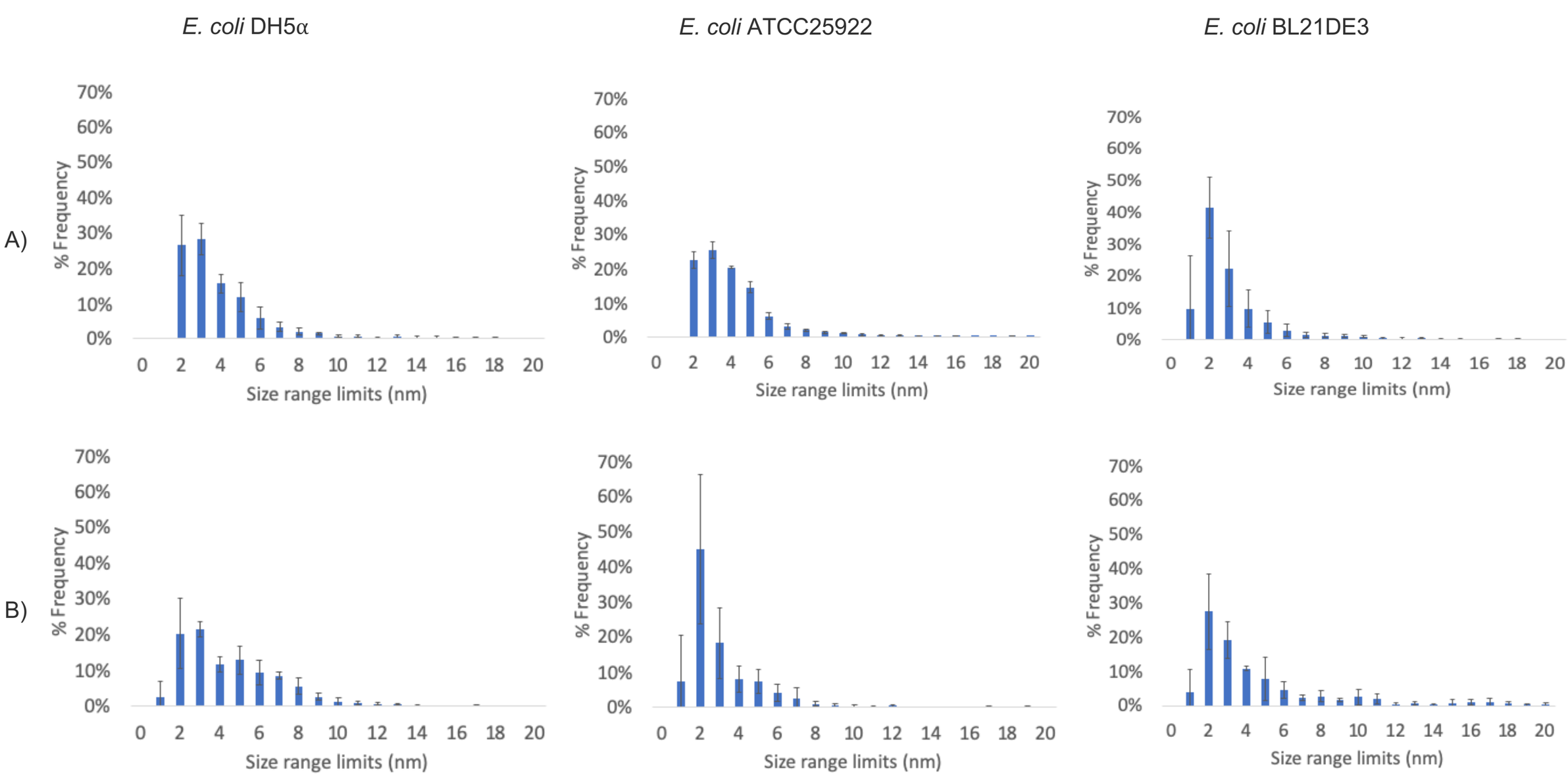

Figure 5-11 Average particle size distribution of 25% (w/w) Pd nanoparticles on the three *E. coli* strains when using A) sodium formate and B) hydrogen as the electron donor

The impact of the higher metal loading was established by analysing TEM images of the biofabricated catalysts (Figure 5-9, Figure 5-10). Similar to the 5% (w/w) Pd-loaded catalyst, nanoparticles predominantly formed in the cytoplasm of the cells with instances of agglomeration on the exterior cell surface when the Pd loading was increased to 25% (w/w). The limited clustering noted upon all three strains (Figure 5-9) when using sodium formate was attributed to the extended overnight reduction. The longer reduction period promoted the gradual absorption of the metal ions with 50-70 % (w/w) of the Pd ions remaining in solution (Section 4.2). In comparison to the chemical donor, the use of the hydrogen gas induced Pd ion reduction within 20-30 minutes across all three microbial strains. This rapid reduction did not allow for the absorption of the remaining Pd ions into the cell but rather rapid reduction of the ions remaining in solution and then the autocatalytic growth of the nanoparticles on the cell. This self-organizing growth of the metal particle was induced through further reduction of ions in solution onto Pd(0) seeds resulting in larger nanoparticle formation as prominently noted on *E. coli* ATCC25922 and *E. coli* BL21DE3 (Figure 5-10). These clusters often ranged in size between 20-200 nm, were irregularly shaped (shape factor of 0.7-0.8), and mainly formed within the periplasmic space and on the exterior cell surface. More uniformly shaped (shape factor of 0.9-1.0), well distributed nanoparticles were evident in the cytoplasm of the cells (Table 5-2).

Table 5-2 Average size of the 25% (w/w) Pd(0) nanoparticles formed across the various *E. coli* strains and electron donors

	Average particle size (nm)	
***E. coli* strain**	**Sodium formate**	**Hydrogen**
E. coli DH5α.	3.9 ± 0.9 nm	4.8 ± 1.0 nm
E. coli ATCC25922	3.6 ± 0.3 nm	3.9 ± 2.1 nm
E. coli BL21DE3	2.9 ± 0.8 nm	9.3 ± 4.2 nm

From TEM Imaging the size distribution as well as the average particle size was determined (Table 5-2, Figure 5-11). Nanoparticles identified within the cytoplasm, on average, ranged between 3.9-4.8 nm on *E. coli* DH5α. and *E. coli* ATCC25922 when using hydrogen as the donor. A similar size distribution was observed within the cytoplasm of *E. coli* BL21DE3, however, clustering on the cell surface skewed the average particle size to larger fractions. The standard deviation in the Pd(0) nanoparticle size on *E. coli* ATCC25922, and more so on the *E. coli* BL21DE3 microbial support, was an indication of the variation in the nanoparticles that formed. In comparison to the gaseous donor, the sodium formate induced nanoparticles achieved a similar particle size to those at the 5% (w/w) metal loading and maintained a smaller average size (2.9-3.9 nm) than the hydrogen-induced nanoparticles (Table 5-2).

5.3.1 Elemental analysis

With the similarity in morphology (shape factor of 0.9-1.0) between the 5% (w/w) and the 25% (w/w) nanoparticles noted upon TEM analysis (Figure 5-9, Figure 5-10), it was necessary to confirm if the intended metal loading was achieved on the microbial strains following reduction (Table 5-3, Table 5-4).

Table 5-3 ICP-OES analysis of the composition of the expected 5% (w/w) Pd(0) and 5% (w/w) Au(0) nanoparticles on the three *E. coli* strains using either hydrogen or sodium formate as the electron donors

	% (w/w) Palladium		% (w/w) Gold	
***E. coli* Strain**	Sodium Formate	Hydrogen	Sodium Formate	Hydrogen
E. coli DH5∝	4.8%	3.1%	-	-
E. coli ATCC25922	6.1%	4.6%	-	2.5%
E. coli BL21DE3	5.9%	5.0%	-	-

Table 5-4 ICP-OES analysis of the composition of the expected 25% (w/w) Pd(0) and 25% (w/w) Au(0) nanoparticles on the three E. coli strains using either hydrogen or sodium formate as the electron donors

	% (w/w) Palladium		% (w/w) Gold	
***E. coli* Strain**	Sodium Formate	Hydrogen	Sodium Formate	Hydrogen
E. coli DH5∝	16.2%	18.7%	-	-
E. coli ATCC25922	24.0%	26.7%	-	12.4%
E. coli BL21DE3	21.8%	22.9%	-	-

With the exception of *E. coli* DH5∝, the expected 5% (w/w) and 25% (w/w) Pd loadings were reached when performing reduction with either electron donor (Table 5-3, Table 5-4). However, the calculated metal loadings for *E. coli* ATCC25922 and *E. coli* BL21DE3 were slightly higher with an average of 22.4-25.4% (w/w) across the two donors. For either of these strains, clustering was prevalent upon reduction (Figure 5-9, Figure 5-10). In contrast, *E. coli* DH5α achieved a loading lower than the expected 5% (w/w) and 25% (w/w) Pd with either electron donor. The difference between the expected and calculated metal loading (between 0.2-2.8% w/w) was attributed to the loss of nanoparticles during the washing of the catalyst. During the harvesting of the biofabricated catalysts, the wash liquid was grey/black in colour which was indicative of Pd(0) in solution. As detached nanoparticles were noted in solution and a loss of mass was detected via ICP, it was apparent that *E. coli* DH5α could not strongly bind Pd(0) nanoparticles. Potentially a blockage or inaccessibility of amine functional groups, upon which Pd ions coordinate, resulted in nanoparticle detachment with this strain (De Vargas et al., 2004; Rotaru et al., 2012).

The ICP-OES analysis of the Au nanoparticles formed overnight in the presence of hydrogen on *E. coli* ATCC25922, confirmed the presence of the metal (Table 5-3, Table 5-4). At both the expected 5% (w/w) and 25% (w/w) loadings the donor and microbial strain used was only able to reduce half of the initial metal ion present. This suggested that the reduction mechanism for these two metals on the cells were more amenable to Pd ions than Au ions.

5.4 Selection of a suitable catalyst scaffold

In an effort to determine the most appropriate scaffold for the biofabrication of nanocatalysts, the morphology of the nanoparticles and microbial supports were compared across the two donors for either of the metals (Table 5-5).

Table 5-5 Summary of the characteristics of Pd(0) and Au(0) nanoparticles formed on the three *E. coli* strains when using either sodium formate or hydrogen as the electron donors.

Support	Metal	Character	Electron donor	
			Sodium formate	Hydrogen
-	Pd	**Reduction**	Overnight	20-30 minutes
E. coli DH5α	5% (w/w) Pd	**Average size**	3.6 ± 0.4 nm	3.5 ± 0.5 nm
		Shape	0.96, circular	0.95, circular
		Location	Cytoplasm, Periplasm	Cytoplasm, Periplasm
		Agglomeration (% of total particles)	Present, Low quantity (1-3%)	Present, Low quantity (1-3%)
		% Reduced metal (w/w)	4.8%	3.1%
		Cell integrity	Moderate damage	Moderate damage
	25% (w/w) Pd	**Average size**	3.9 ± 0.9 nm	4.8 ± 1.0 nm
		Shape	0.95, circular	0.8-9, circular
		Location	Cytoplasm, Periplasm	Cytoplasm, Periplasm, protruding on cell wall
		Agglomeration (% of total particles)	Present, Low quantity (1.2%)	Present, Low quantity (0.8%)
		% Reduced metal (w/w)	16.2%	18.7%
		Cell integrity	Low damage	Low damage
E. coli ATCC25922	5% (w/w) Pd	**Average size**	4.7 ± 0.7 nm	3.5 ± 0.3 nm
		Shape	0.95, circular	0.95, circular
		Location	Cytoplasm, Periplasm, exterior cell wall	Cytoplasm, Periplasm
		Agglomeration (% of total particles)	Present, low levels, localized to exterior cell wall (1-3%)	Present, moderate levels, localized to particular region of periplasm (1-3%)
		% Reduced metal (w/w)	6.1%	4.6%
		Cell integrity	Moderate damage	Moderate damage
	25% (w/w) Pd	**Average size**	3.6 ± 0.3 nm	3.9 ± 2.1 nm
		Shape	0.93, circular	0.92, circular
		Location	Cytoplasm, Periplasm	Cytoplasm, Periplasm exterior cell wall
		Agglomeration (% of total particles)	Present, low levels, localized to cytoplasm (0.7%)	Present, moderate levels, localized to particular regions around the cell surface and periplasm (3.4%)
		% Reduced metal (w/w)	24.0%	26.7%
		Cell integrity	Low damage	Low damage

Support	Metal	Character	Electron donor	
			Sodium formate	Hydrogen
-	Au	**Reduction**	-	Overnight
E. coli ATCC25922	5% (w/w) Au	**Average size**	-	31.0 ± 5.2 nm
		Shape	-	0.75, Irregular
		Location	-	Periplasm, cytoplasm
		Agglomeration (% of total particles)	-	Present, moderate levels
		% Reduced metal (w/w)	-	2.5%
		Cell integrity	-	Extensive damage
	25% (w/w) Au	**Average size**	-	22.0 ± 0.8 nm
		Shape	-	0.6-0.8, Irregular, triangular
		Location	-	Extra cellular
		Agglomeration (% of total particles)	-	Present, excess levels
		% Reduced metal (w/w)	-	12.4%
		Cell integrity	-	Minimal damage
E. coli BL21DE3	5% (w/w) Pd	**Average size**	4.1 ± 0.3 nm	3.0 ± 0.6 nm
		Shape	0.94, circular	0.94, circular
		Location	Cytoplasm, periplasm, exterior cell wall	Cytoplasm, periplasm, exterior cell wall
		Agglomeration (% of total particles)	Present, low levels, localized to exterior cell wall (1-3%)	Present, low to moderate levels, localized to periplasm and exterior cell wall (1-3%)
		% Reduced metal (w/w)	5.9%	5.0%
		Cell integrity	Low damage	Low damage
	25% (w/w) Pd	**Size**	2.9 ± 0.8 nm	9.3 ± 4.2 nm
		Shape	0.92, circular	0.81, circular
		Location	Cytoplasm, periplasm, exterior cell wall	Cytoplasm, periplasm, exterior cell wall
		Agglomeration (% of total particles)	Present, low levels, localized to exterior cell wall (0.8%)	Present, low to moderate levels, localized to periplasm and exterior cell wall (8.7%)
		% Reduced metal (w/w)	21.8%	22.9%
		Cell integrity	Low damage	Low damage

InTable 5-5 cell integrity was related to structural artefacts in the bacterial cell that resulted from metal reduction. The degree of damage to the cell was determined by a combination of the morphological changes (cell lysis, large vacuoles, distended cell walls, OMVs) on the *E. coli* support. Minimal to low damage was assumed when ≤ 1 of the morphological changes

were identified. Moderate damage was defined when 2 morphological changes occurred and extensive damage was noted when 3-4 morphological changes were identified.

Nanoparticles with the required Pd composition, regular distribution and morphology, with a particle size less than 5 nm were predominant in the cytoplasm of *E. coli* ATCC25922. Although there was visible clustering of the nanoparticles on this strain, agglomeration was localised to specific areas of the cells. From the TEM images in Figure 5-3 and Figure 5-10 it was noted that at a 5% (w/w) and 25% (w/w) metal loading, hydrogen induced reduction resulted Pd(0) nanoparticle agglomeration, to some degree, on the exterior surfaces of *E coli* ATCC25922. Clusters ranged between 20 - 400 nm in size with an average nanoparticle size of 3.5 $\pm$ 0.3 nm and 3.9 $\pm$ 2.1 nm at both loadings; with some nanoparticles also detected within the cytoplasm. However, for either electron donor the cells were noticeably stressed with clear distending and lysis when exposed to the metal.

Similar to the 5% (w/w) metal loading, Au(III) reduction was only noted in the case of *E coli* ATCC25922 with an intensified colour change in solution when the Au metal loading was increased to 25% (w/w). Au nanoparticles formed at these loadings were mainly located within the extracellular spaces between cells. Even though similar large clusters were observed at the 5% (w/w) Au loadings, most clusters at the higher loadings were not bound to the cells (Figure 5-8). Triangular, spherical as well as irregular shaped clusters (circularity factor 0.6-0.8 nm) were detected within this environment with an average size of approximately 22.4 $\pm$ 0.8 nm. Although the Au nanoparticles formed extracellularly, vacuoles and OMV's were still visible within the cells (Figure 5-8.C). However, lysing and disruption noted at the 5% (w/w) Au loading of the cells was limited at the 25% (w/w) loading. Maintenance of the cell integrity at these elevated gold concentrations was not expected. This was likely due to the limited interaction between the microbial support and the extracellularly produced nanoparticles.

In summary (Table 5-5), the imaging analyses of the 5% (w/w) and 25% (w/w) metal-loaded catalysts showed that nanoparticles were bound to the cell. Uniform Pd(0) formation was noted on all strains and donors with minimal instances of agglomeration on the surface of *E. coli* ATCC25922 and *E. coli* BL21DE3. *E. coli* DH5α, although initially considered to be ideal in terms of size and distribution, exhibited a loss between 0.2-2.8% (w/w) of Pd(0) after reduction. This loss of active metal sites could bring about lower activity when applied in oxidation reactions. Unlike Pd(II), Au(III) reduction was only detected when using hydrogen as an electron donor on *E. coli* ATCC25922. Upon characterization, it was evident that rather than a uniform morphology and distribution of particles, aggregates ranging between 20-50 nm in size were formed mainly on the cell surface. This irregular morphology and poor distribution decreased the exposed active surface area of the Au catalyst, which could hinder the oxidation reactions. Cytoplasmic particles were evident on some cells and were often accompanied by instances of cell rupture. This metal ion had a more disruptive effect on the bacteria, regardless of the strain. However, upon closer inspection of *E. coli* BL21DE3, fine (2.8 ± 0.3 nm), near spherical nanoparticles were noted in the cytoplasm of some cells due to a limited Au(III) ion uptake over a longer reduction period.

The fact that *E. coli* BL21DE3 was able to produce Pd(0) nanoparticles similar to *E. coli* ATCC25922 and *E. coli* DH5α indicated that in spite of the deficiency in hydrogenase, reduction of the Pd(II) ion was still occured within the cell cytoplasm and within the periplasm. Rather than the large Pd agglomerates expected on hydrogenase-deficient strains, fairly uniform, spherical well distributed nanoparticles were detected on *E. coli* BL21DE3 (Deplanche et al., 2010; Mikheenko et al., 2008; Torgeman, 2017). This suggested that although hydrogenase may play an active role in reduction it is likely that an additional mechanism assists in reduction. As reduction of the metals was still observed in spite of deficiency alternate electron shuttling proteins like nitrogenase/nitrate reductase, cytochrome c as well as the NADPH cofactors are proposed to induce reduction. In comparison, Au reduction was only possible in the presence of hydrogen and was limited on the hydrogenase deficient *E. coli* BL21DE3. This indicates that for this metal, hydrogenase plays a more active role in this reduction mechanism.

E. coli ATCC25922 was the most effective support for the formation of Pd(0) nanoparticles and the only microbial strain that produced Au(0) nanoparticles. This microbial strain had the highest cell concentration under anoxic growth conditions (0.8 g/L). In comparison, *E. coli* BL21DE3, which was deficient in the key genes necessary for oxygen-limited growth, had a final cell concentration of 0.21 g/L. Thus, for *E. coli* ATCC25922, a greater mass of the microbial support can be generated for the same culture volume while still successfully generating Au(0) nanoparticles. The Pd(0) nanoparticles produced on this strain were favourably uniform in size and shape, with minimal agglomeration and adequately distributed throughout the support. The *E. coli* ATCC25922 strain showed the most promise as an alternative to synthetic supports for the manufacture of Pd and Au nanocatalysts. The biological support offers a means of producing nanocatalysts without the use of toxic stabilizers and capping agents.

Chapter 6

6 Catalyst activity

6.1 Chapter overview

In chapters 4 and 5, multiple microbial strains and electron donors were compared relative to the adsorption capacity and reductive capabilities of the scaffolds as well as the nanoparticles size, shape and distribution. These factors were used to identify an appropriate biofabricated Pd and Au catalyst for the oxidation of alcohols. Both metals were previously used for the oxidation of alcohols due to their unique catalytic properties in the nanoparticle form.

Of the three microbial strains studied *E. coli* ATCC25922 had a good affinity for both metal ions at the lower metal loading. However, at a higher Pd loading the adsorption ability of the *E. coli* strain was reduced by 50% and in the case of Au(III) the microbial strain achieved 11.9% lower adsorption. At the 5% (w/w) and 25% (w/w) metal loadings on *E. coli* ATCC25922 reduction of Pd was achieved using either donor. The nanoparticles that formed were within 5 nm, with minimal clustering of Pd(0) as well as a good distribution, limited mass loss and a uniform shape. Nanoparticles formed using sodium formate were the most consistent in terms of particle size (< 5 nm) with agglomeration prevalent after hydrogen reduction. Clustering was most evident on *E. coli* BL21DE3 at the higher metal loading. *E. coli* ATCC25922 was the only microbial strain where Au reduction was evident upon overnight incubation in a hydrogen-rich environment. However, the Au nanoparticles were not uniformly distributed and tended to agglomerate, resulting in particle sizes ranging between 20 - 40 nm on the cell surface.

Nanoparticle morphology and metal type have a significant influence on catalyst activity (Bennett et al., 2010; Dimitratos et al., 2006; Liz-Marzán, 2004). Smaller, uniform particles allow for a greater active surface area, while the metal type can dictate the limiting stage in the activation of catalytic sites (Dimitratos et al., 2006; Meenakshisundaram et al., 2010; Villa et al., 2009). Consequently, the effect of these characters and the applicability of the catalysts on selected *E. coli* supports were further investigated in this Chapter via the oxidation of alcohols to higher value aldehydes.

Efficacy of the biofabricated catalysts in this study for the oxidation of alcohols was established through the conversion of benzyl alcohol to benzaldehyde. This well-established reaction ensured consistent comparison to literature (Deplanche et al., 2011a; Enache et al., 2006; Miedziak et al., 2011a). The most efficient catalyst for aromatic alcohol oxidation was then selected for activity testing with 1-octanol. With the intent of integrating the bio-catalytic alkane activation and the chemo-catalytic oxidation process into a one-pot tandem system, the oxidation reaction was performed at mild conditions. These reaction conditions were used in an effort to ensure catalyst compatibility in a tandem bio-chemo catalytic system.

6.1.1 Dehydrogenation of alcohols

After confirming that metal nanoparticles were bound to each of the selected biological supports, it was essential to test the activity of these catalysts. Activity of the monometallic catalysts was determined via the oxidation of alcohols, namely, benzyl alcohol and 1-octanol to the corresponding aldehyde. The catalytic cycle for the activation of such alcohols to the aldehyde is governed by an established dehydrogenation mechanism (Figure 6-1).

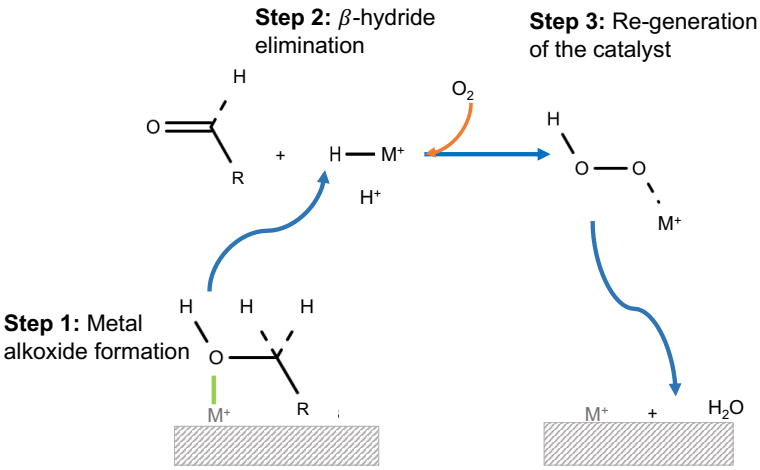

Figure 6-1 Catalytic cycle for the oxidation of alcohols to aldehyde using a metal catalyst (Davis et al., 2013; Nagy et al., 2019; Yamaguchi and Mizuno, 2002)

The catalytic conversion of alcohols to aldehydes follows three main stages (Figure 6-1). During the first stage the alcohol binds to the metal catalyst surface to produce the metal alkoxide. The alkoxide compound then undergoes β-hydride elimination to give rise to a metal hydride complex (*M-H*) and a carbonyl molecule (the aldehyde) intermediate. In the final stage of the dehydrogenation mechanism, reforming of the catalyst surface occurs in the presence of oxygen. As oxygen is introduced, the metal hydride forms an unstable ionic intermediate that then regenerates the active metal site to its initial state (Davis et al., 2013; Nagy et al., 2019; Yamaguchi and Mizuno, 2002). The β-hydride abstraction step is considered to be rate limiting in this catalytic cycle (Villa et al., 2009). However, some studies have shown that this limiting step is influenced by the catalyst metal (Dimitratos et al., 2006; Meenakshisundaram et al., 2010). In the case of Au, a base (such as NaOH) is often used to improve rate limiting H atom abstraction from the metal alkoxide. Whereas for the Pd catalyst cycle, the regeneration of the active site is limited by the removal of the H atom from the metal hydride complex (Villa et al., 2009).

6.2 Oxidation of benzyl alcohol

6.2.1 Catalyst activity in comparison to literature

Biofabricated Pd(0) on whole cell *E. coli* MC4100, were shown by Deplanche et al. (2011a) to be active on benzyl alcohol at 90°C, 1 bar air, 250 rpm and 0.36% (w/v) catalyst loading. In this study, activity tests were performed at the same reaction conditions as Deplanche et al.

(2011a) to establish the efficacy of the novel biofabricated catalysts. From these activity tests, no measurable activity was noted on the whole cell supported catalysts. Unlike the biofabricated catalysts studied by Deplanche et al. (2011a), nanoparticles were not predominant on the cell surface of the *E. coli* strains investigated in this study, but rather enclosed within the cell membrane (Deplanche et al., 2012, 2011a; Torgeman, 2017). This limited the exposure of the active sites to the reagent in these experiments. To maximise the active specific area, the biofabricated catalysts were subsequently crushed prior to testing to improve the contact of the catalyst with the reactants to facilitate the oxidation of alcohols (Table 6-1, Table 6-2). Activity was evident on all biofabricated Pd catalysts. However, there was difficulty when attempting to maintain the carbon balance over the reaction, particularly at the higher metal loading. This discrepancy in the mass balance was most evident when comparing the conversion by substrate and the conversion based on products formed ($X_{Substrate}$ and $X_{Product}$) (Table 6-1, Table 6-2). Possible alternate oxidative products, apart from the carboxylic acid, were not identified upon GC analysis. To allow for a consistent comparison to the literature, the conversion discussed hereafter will relate to the amount of substrate converted upon reaction ($X_{Substrate}$).

Monometallic 5% (w/w) and 25% (w/w) Au catalysts in this investigation did not show any activity towards the conversion of benzyl alcohol to benzaldehyde (Table 6-3). This was similar to observations by Deplanche et al. (2011a), Sun et al. (2017) and Wang et al. (2015) who noted low activity on Au catalysts under mild, solvent free conditions (Table 6-3) Sun et al. (2017) and Wang et al. (2015) had near insignificant conversions while Deplanche et al. (2011a), who studied similar biofabricated Au catalysts on *E. coli* MC4100, noted 2% (mol/mol) conversion of the alcohol with 98% (mol/mol) selectivity to the aldehyde (Table 6-3). Limitations in activity noted by Deplanche et al. (2011a), Sun et al. (2017) and Wang et al. (2015) were expected when Au catalysed reactions are performed without a base, as H^+ abstraction was hindered (Prati and Rossi, 1998). However, Enache et al. (2006), who investigated similar synthetic Au catalysts on titanium oxide (TiO_2) at slightly more aggressive reaction conditions (100°C, 1 bar oxygen, 1500 rpm, 0.02% w/v catalyst loading over 22 hours), observed higher conversions (10% mol/mol) but lower selectivity to the aldehyde (67% mol/mol) over a six hour period. Activity experiments performed with these synthetically supported Au catalysts were conducted at higher temperatures and at extended reaction periods (Table 6-3). This ensured enough energy and time to exceed the energy threshold for hydride abstraction as compared to the biofabricated Au catalyst studies, thus showing more aggressive conditions are necessary to assist the reaction in the absence of a base.

v

Table 6-1 The activity for the oxidation of benzyl alcohol to benzaldehyde using 5% (w/w) Pd on various *E. coli* supports (*E. coli* DH5∝, *E. coli* ATCC25922, *E. coli* BL21DE3). Activity was not noted on the 5% (w/w) Au catalyst and thus is not shown. These catalysts were manufactured with either hydrogen or sodium formate as indicated. Conditions for all catalytic reactions were performed at 90°C, 250 rpm, 0.36% (w/v) catalyst loading and at 1 bar of air in the Radley reactor. In the table, X is defined as conversion, Y is defined as yield and was based on change in the substrate, S is defined as the selectivity and was based on the amount of product formed.

Metal loading (% w/w)	Metal	Electron donor	Support	Benzyl alcohol volume (ml)	$X_{Substrate}$ (%mol/mol)	$X_{Product}$ (%mol/mol)	Y Benzaldehyde (%mol/mol)	Y Toluene (%mol/mol)	Y Benzoic acid (%mol/mol)	S Benzaldehyde (%mol/mol)	S Toluene (%mol/mol)	S Benzoic acid (%mol/mol)
5%	Pd	Hydrogen	*E. coli* DH5∝	10ml	3.5%	5.6%	113.1%	2.0%	0%	98.3%	1.7%	0%
5%	Pd	Hydrogen	*E. coli* ATCC25922	10ml	2.9%	3.3%	69.8%	1.4%	0%	98.0%	2.0%	0%
5%	Pd	Hydrogen	*E. coli* BL21DE3	10ml	5.4%	5.6%	75.5%	1.8%	0%	97.6%	2.4%	0%
5%	Pd	Sodium formate	*E. coli* DH5∝	10ml	4.7%	8.1%	76.3%	0.1%	0.1%	99.1%	0.6%	0.4%
5%	Pd	Sodium formate	*E. coli* ATCC25922	10ml	8.5%	7.1%	46.4%	0.1%	0.0%	99.3%	0.6%	0.2%
5%	Pd	Sodium formate	*E. coli* BL21DE3	10ml	7.0%	7.4%	53.3%	0.2%	0.1%	97.7%	1.8%	0.5%

Table 6-2 The activity for the oxidation of benzyl alcohol to benzaldehyde using 25% (w/w) Pd on various *E. coli* supports (*E. coli* DH5∝, *E. coli* ATCC25922, *E. coli* BL21DE3). Activity was not noted on the 25% (w/w) Au catalyst and thus is not shown. These catalysts were manufactured with either hydrogen or sodium formate as indicated. Conditions for all catalytic reactions were performed at 90°C, 250 rpm, 0.36% (w/v) catalyst loading and 1 bar of air in the Radley reactor. In the table, X is defined as conversion, Y is defined as yield and was based on change in the substrate, S is defined as the selectivity and was based on the amount of product formed.

Metal loading (% w/w)	Metal	Electron donor	Support	Benzyl alcohol volume (ml)	$X_{Substrate}$ (%mol/mol)	$X_{Product}$ (%mol/mol)	Y Benzaldehyde (%mol/mol)	Y Toluene (%mol/mol)	Y Benzoic acid (%mol/mol)	S Benzaldehyde (%mol/mol)	S Toluene (%mol/mol)	S Benzoic acid (%mol/mol)
25%	Pd	Hydrogen	*E. coli* DH5∝	5ml	29.7%	23.0%	67.5%	2.9%	0.4%	95.4%	4.1%	0.4%
25%	Pd	Hydrogen	*E. coli* ATCC25922	5ml	34.5%	10.3%	25.0%	2.5%	0.1%	90.9%	8.8%	0.3%
25%	Pd	Hydrogen	*E. coli* BL21DE3	5ml	34.3%	5.9%	16.4%	0.5%	0.2%	96.0%	3.0%	1.0%
25%	Pd	Sodium formate	*E. coli* DH5∝	5ml	5.6%	11.4%	150.5%	3.2%	1.8%	96.3%	2.7%	1.1%
25%	Pd	Sodium formate	*E. coli* ATCC25922	5ml	1.8%	9.0%	257.8%	11.7%	4.4%	93.2%	5.3%	1.4%
25%	Pd	Sodium formate	*E. coli* BL21DE3	5ml	2.9%	5.6%	216.4%	2.3%	3.4%	93.5%	5.5%	1.0%

Table 6-3 Comparison of the activity of Au(0) catalysts in the current study relative to similarly synthesized catalysts on synthetic and biological scaffolds as reported in the literature (Deplanche et al., 2011a, 2012; Enache et al., 2006; Ma et al., 2009; Pritchard et al., 2010; Sun et al., 2017; Wang et al., 2015). Catalyst activity is reported over the full reaction period as well as over 6 hours in the presence of either air or oxygen as the oxidant. In the table, X is defined as conversion, S is defined as the selectivity and was based on the amount of product formed.

Paper	Stirring (rpm)	T (°C)	P (bar)	Oxidant	Solvent	Base	Catalyst loading (w/v)	Metal loading (% w/w)	Support	Reaction time (h)	X_{full_time} (%mol/mol)	S_{full_time} (%mol/mol)	$X_{(6)}$ (%mol/mol)	$S_{(6h)}$ (%mol/mol
Biological support														
This study	250	90	1	Air	-	-	0.36%	5%	*E. coli* DH5α	6	0%	0%	0%	0%
This study	250	90	1	Air	-	-	0.36%	5%	*E. coli* ATCC25922	6	0%	0%	0%	0%
This study	250	90	1	Air	-	-	0.36%	5%	*E. coli* BL21DE3	6	0%	0%	0%	0%
Deplanche et al. (2011)	250	90	1	Air	-	-	0.50%	5%	*E. coli* MC4100	6	2%	88%	2%	88%
Synthetic support														
Enache et al. (2006)	1500	100	1	Oxygen	-	-	0.02%	5%	TiO_2	22	62%	89%	10%	67%
Ma et al. (2009)	800	80	1.013	Air	-	Na_2CO_3	40.00%	4%	SBA-15 (IMAuS)	8	1.3%	98%	1%	98%
Ma et al. (2009)	800	80	1.013	Air	-	Na_2CO_3	40.00%	4%	SBA-15 (DAuS-1)	8	1.4%	98%	2%	98%
Ma et al. (2009)	800	80	1.013	Air	-	Na_2CO_3	40.00%	4%	SBA-15 (DAuS)	8	6.4%	97%	7%	97%
Sun et al.(2017)		90	1.013	Oxygen	-	-	0.40%	0.9%	TiO_2	6	0%	0%	0%	0%
Wang et al. (2015)	1250	90	1.013	Oxygen	-	-	0.50%	1%	TiO_2	6	0%	0%	0%	0%
Pritchard et al. (2010)	F1500	120	10	Oxygen	-	-	0.13%	1%	$C_{(SI)}$	6	6.6%	63.9%	6.6%	63.9%

Table 6-4 Comparison of the activity of Pd(0) catalysts in the current study relative to similarly synthesized catalysts on synthetic and biological scaffolds as reported in the literature (Deplanche et al., 2011a, 2012; Enache et al., 2006; Ma et al., 2009; Pritchard et al., 2010; Sun et al., 2017; Wang et al., 2015). Catalyst activity is reported over the full reaction period as well as over 6 hours in the presence of either air or oxygen as the oxidant. In the table, X is defined as conversion, S is defined as the selectivity and was based on the amount of product formed. Hi

Paper	Stirring (rpm)	T (°C)	P (bar)	Oxidant	Solvent	Base	Catalyst loading (w/v)	Metal loading (% w/w)	Support	Reaction time (h)	X_{full_time} (%mol/mol)	S_{full_time} (%mol/mol)	$X_{(6h)}$ (%mol/mol)	$S_{(6h)}$ (%mol/mol)
Biological support														
This study	250	90	1	Air	-	-	0.36%	5%	*E. coli* DH5α	6	3.5%	98.3%	3.5%	98.3%
This study	250	90	1	Air	-	-	0.36%	5%	*E. coli* ATCC25922	6	2.9%	98.0%	2.9%	98.0%
This study	250	90	1	Air	-	-	0.36%	5%	*E. coli* BL21DE3	6	5.4%	97.6%	5.4%	97.6%
Deplanche et al. (2011)	250	90	1	Air	-	-	0.50%	5%	*E. coli* MC4100	7	6.0%	96.0%	5%	96%
Synthetic support														
Enache et al. (2006)	1500	100	1	Oxygen	-	-	0.02%	5%	TiO2	6	67.0%	35.0%	67%	35%
Ma et al. (2009j	800	80	1.013	Air	-	Na2CO3	40.0%	4%	SBA-15 (DPdS)	8	0.3%	99.0%	0.3%	99.0%
Sun et al. (2017)		90	1.013	Oxygen	-	-	0.4%	0.05%	TiO2	6	7.0%	85.7%	7.0%	85.7%
Wang et al. (2015)	1250	90	1.013	Oxygen	-	-	0.5%	1.0%	SiO2-8c	6	0.0%	0.0%	0.0%	0.0%
Pritchard et al. (2010)	1500	120	10	Oxygen	-	-	0.1%	1.0%	C(SI)	6	59.3%	74.7%	59.3%	74.7%

Unlike the Au catalyst, the monometallic Pd catalysts synthesised using either of the electron donors explored in this study exhibited higher activity for the oxidation of benzyl alcohol for each of the selected microbial strains (Table 6-4). An average conversion across the three microbial strains of 3.9%±1.3% (mol/mol) and 6.7%±1.9 (mol/mol) was achieved with the biofabricated Pd nanocatalysts produced using either hydrogen or sodium formate, respectively (Table 6-1). Correspondingly, the average selectivity towards benzaldehyde was 98.0%±0.4% (mol/mol) and 98.7%±0.9 (mol/mol). Overall these Pd nanocatalysts had an average particle size less than 5 nm and a fairly circular shape. At the 5% (w/w) loading the sodium formate induced Pd(0) nanoparticles maintained a smaller particle size promoting a greater amount of available active sites. The increased availability of active sites led to a higher activity on the chemical catalysts over the hydrogen induced catalysts at this loading.

Deplanche et al. (2011a), observed similar conversions of 5% (mol/mol) and selectivities above 96% (mol/mol) of benzyl alcohol to benzaldehyde for the hydrogen-induced biofabricated Pd nanoparticle catalysts on *E. coli* MC4100 under the same reaction conditions (Table 6-4). In comparison, however, synthetic Pd catalysts used by Enache et al. (2006) exhibited conversions 11-12 times higher than with the biofabricated catalysts (Table 6-4). The higher overall conversion achieved with the synthetic catalysts for both Pd and Au are attributed to the use of pure oxygen and a lower catalyst loading. This ensured adequate access to the oxidant and sufficient oxygen promoted rapid regeneration of the active metal sites on the synthetic supports. This availability, however, allowed for alternate side reactions such as the disproportionation of alcohol to toluene to proceed unhindered. As a consequence, the oxygen rich environment induced by Enache et al. (2006) led to reduced benzaldehyde selectivity after six hours between 35% (mol/mol) and 67% (mol/mol) for the synthetic Pd and Au catalysts, respectively (Table 6-3 and Table 6-4). Sun et al. (2017) who investigated the same synthetic catalyst at less intense conditions (90^{o}C, 1 bar oxygen at a 0.4% w/v catalyst loading and 0.05% w/w metal loading) noted higher selectivity (85.7% mol/mol) to the aldehyde. This increase in selectivity and decreased conversion (7.0% mol/mol) of benzyl alcohol was a result of limited active metal sites available to the oxidant, hindering over oxidation.

6.2.2 Reactor and mass transfer limitations

It is evident by comparing the synthetic catalyst reaction system to the reaction conditions used in this study that the oxidation reactions with the biofabricated catalyst was prone to oxygen limitations. This was apparent by the improvements in activity noted by Enache et al. (2006) at 1 bar oxygen when using 0.02% (w/v) loading of the synthetic catalyst. The oxygen-environment promoted greater conversion of the alcohol (67% mol/mol) but also allowed for over oxidation, as seen by the reduced selectivity to the aldehyde (ca. 35% mol/mol in Table 6-4). This was in contrast to results obtained by Deplanche et al. (2011; 2012) where conversions of ca. 5% (mol/mol) and selectivity of 96% (mol/mol) were noted when air was introduced as oxidant and in the presence of 18 times the catalyst loading used by Enache et al. (2006). Air is a desirable oxidant as it is inexpensive, environmentally green and a safer

alternative to pure oxygen. However, when using air as the main oxidant in a biofabricated catalyst system, the driving force for gaseous diffusion to the active site was reduced, limiting the regeneration of the metal active sites (Step 3 Figure 6-1). This reduction in the gaseous oxidant transfer is therefore likely due to the dilution of oxygen in air, as oxygen only makes up ca. 21% (v/v) of the total gas volume.

Limitation in the oxidant supply may be compounded by the low pressure of the air as well as the use of a high catalyst loading (Miedziak et al., 2011a; Zhu, 2014). Zhu (2014) showed for 5% (w/w) biofabricated Au-Pd catalysts operating at 110^{o}C, 5 bar air, with no base or solvent and at 0.02% (w/v) catalyst loading, oxygen in air was consumed within the first 3 hours. Although initially fast, the rapid consumption of the oxidant in the initial stages slowed down the reaction considerably, limiting the conversion of the alcohol to less than 2% (mol/mol). Without any replenishment of the oxidant once consumed, an inert head space resulted in the reactor, decreasing the oxygen partial pressure considerably in the system, thus stalling the reaction (Zhu, 2014).

The total pressure of the gaseous oxidant was also a contributing factor to oxygen availability. Miedziak et al (2011a) showed that by operating at pressures above 1 bar the driving force, and therefore conversion, of the oxidant was significantly improved. A consequence that was limited in the present study. Although fresh air was continuously introduced into the reaction environment at a constant rate to replenish any depleted oxygen over time, the glass reaction vessel limited the maximum operating pressure to 1 bar. Working at such low pressure imposed further mass transfer, and hence, activity limitations in the present study.

The concentration of the catalyst used can also directly influence oxygen availability. It is known that increasing the catalyst loading in a reaction increases the number of active sites available for reaction. However, if the catalyst loading exceeds a critical limit, then the rate at which oxygen is consumed is greater than what is being supplied and activity is subsequently hindered (Zhu, 2014). A lower catalyst loading like the 0.02% (w/v) used in Enache et al. (2006) and Zhu (2014), led to slower consumption of the oxidant allowing for sufficient time for regeneration of the surface and greater conversions.

6.2.3 Catalyst activity at the higher metal loading

In Chapters 4 and 5 a 25% (w/w) metal loading was applied to determine the tolerance of the microbial supports. After reduction a uniform mono-dispersed spread of the nanoparticles was observed across the microbial supports and electron donors (viz. TEM images in Figure 5-2, Figure 5-3, Figure 5-9 and Figure 5-10). The impact of the morphology and distribution of the particles was determined by analysing the activity of these 25% (w/w) metal loaded nanocatalysts. These results were subsequently compared to the activity of the 5% (w/w) Pd loaded nanocatalysts (Table 6-2).

Screening of the 25% (w/w) Pd catalysts on benzyl alcohol indicated that, similar to the activity results of the 5% (w/w) Pd catalyst, the sodium formate generated catalysts achieved conversions between 1.8%-5.6% (mol/mol) with selectivity ranging from 93.2%-96.3%

(mol/mol) across the microbial strains (Table 6-2). Unlike the chemical electron donor, the hydrogen generated catalysts resulted in an average alcohol conversion of 32.8%± 2.7% (mol/mol) across the microbial strains, which was considerably higher than achieved with the 5% (w/w) metal loaded counterparts (3.9%±1.3% mol/mol in Table 6-1). These catalysts were able to maintain similar selectivity of 94.1%±2.8% (mol/mol), on average, to the aldehyde across the same three microbial supports. At the higher metal loading, apart from minimal clustering on *E. coli* ATCC25922 and *E. coli* BL21DE3, the particles that formed were within 5 nm and maintained circularity. A greater concentration of active sites would be available at the 25% (w/w) loading, thus greater activity would be expected. However, sodium formate catalyst activity was similar at both metal loadings and across microbial strains. The ineffectiveness of these catalysts can potentially be a result of CO catalyst poisoning, formed when the chemical donor was broken down. Due to these attributes at the 25% (w/w) loading, the hydrogen-induced catalysts had better activity than the chemical electron donor.

The improved activity when hydrogen was used as the donor across all strains at the 25% (w/w) Pd loading could be attributed to the increased availability of active metal sites. The hydrogen-induced catalysts on *E. coli* DH5∝, *E. coli* ATCC25922, *E. coli* BL21DE3 was therefore selected to test the activity of these catalyst in the presence of 1-octanol.

6.3 Oxidation of 1-octanol

Alkanes are known to be difficult to activate due to their stable nature. This has been one of the foremost challenges in the chemical industry (Bergman, 2007; Bordeaux et al., 2012; Labinger and Bercaw, 2002). Recent advances in catalysis has shown promising results for terminal C-H bond activation. In bio-catalysis, research has focused on the oxyfunctionalization of the alkanes to higher value products using more sustainable, less energy intensive activation methods (Ayala and Torres, 2004; Gudiminchi et al., 2012; Meissner, 2013). Previous studies on n-octane activation using CYP P450 enzymes, such as CYP153A6, have resulted in the generation of small volumes of a low value alcohol (1-octanol) as the major product (Olaofe, 2013).

The low volumes of 1-octanol generated together with the inexpensive price (R 814/kg) of this chemical indicate that this bio-catalytic process is not feasible. However, in industry the alcohol product does serve as a good platform chemical to higher value products (such as octanal which is valued at R1330/kg). Further activation of the alcohol intermediate through a tandem catalytic approach ensures the valorisation of the bio-catalytically activated alkane. It is known that long chained, linear alcohols, such as 1-octanol, are difficult to oxidize further and often requires the presence of an aqueous solvent to promote the reaction (Dimitratos et al., 2006).

Of the metals considered Pd is thought to be generally more effective for the activation of aromatic alcohols while Pt is favoured for aliphatic molecules (Anderson et al., 2002; Griffin et al., 2002). This was shown by He et al (2015). The authors noted that Pt was the preferred catalyst for the oxidation of 1-octanol after reaching an iso-conversion of 10% (mol/mol) in 3 hours; 5 times faster than the Pd catalyst. However, within 6 hours of reaction, the conversion

increased to ca. 20% (mol/mol) while the selectivity of the Pt-based catalyst dropped dramatically to 49% (mol/mol). In comparison, the Pd-based catalysts maintained selectivity to the aldehyde (between 80-85% mol/mol) over the 3-6 hour time period. Although Pt was initially more effective for substrate conversion, the catalyst was less selective for the aldehyde over extended periods of time under mild conditions. The Pd catalyst is preferred for linear alcohol oxidation reactions. When compared to Pt this Pd catalyst is a cheaper alternative and is able to maintain activity with good selectivity to the aldehyde over longer reaction periods (Enache et al., 2007; Griffin et al., 2002).

The low conversions noted upon benzyl alcohol oxidation were a result of limitations in oxidant availability. When migrating to linear alcohol systems, it was expected that similar difficulties in activation as experienced in the benzyl alcohol system would be further compounded by the known complexity of converting 1-octanol to its corresponding aldehyde (Dimitratos et al., 2006; Griffin et al., 2002). With the addition of a higher metal loading, mass transfer limitations in these systems may be counteracted through the exposure of a greater concentration of active sites.

To improve activity towards aliphatic compounds, the oxidation of 1-octanol to its corresponding aldehyde was performed at the same conditions used for the benzyl alcohol system using 25% (w/w) Pd catalysts. Given that the hydrogen-induced 25% (w/w) loaded Pd nanocatalysts appeared to be more active during the oxidation of the aromatic alcohol, preliminary screening on 1-octanol was performed using these catalysts (Table 6-5).

Table 6-5 The oxidation of 1-octanol to octanal using hydrogen induced 25% (w/w) Pd nanocatalysts on various *E. coli* supports (*E. coli* DH5∝, *E. coli* ATCC25922, *E. coli* BL21DE3). All catalytic reactions were performed at 90°C, 250 rpm, 0.36% (w/v) catalyst loading and at 1 bar of air in the Radley reaction system. All solvents were added in a ratio of 1:4 water to alcohol. Where X is the conversion, Y is the yield relative to the substrate, and S is the selectivity of the product formed.

Metal loading (%w/w)	**Metal**	***E.coli* support**	**Solvent**	**octanol volume (ml)**	**$X_{Substrate}$** (%mol/mol)	**$X_{Product}$** (%mol/mol)	**Y Octanal** (%mol/mol)	**Y Octanoic acid** (%mol/mol)	**S Octanal** (%mol/mol)	**S Octanoic acid** (%mol/mol)
25%	Pd	DH5∝	None	5ml	2.9%	1.3%	27.9%	11.9%	70.9%	29.1%
25%	Pd	ATCC25922	None	5ml	2.4%	0.9%	32.0%	6.1%	82.7%	17.3%
25%	Pd	BL21DE3	None	5ml	3.0%	1.6%	41.6%	15.2%	72.1%	27.9%
25%	Pd	DH5∝	Water	4ml	5.1%	1.4%	18.1%	5.3%	75.3%	24.7%
25%	Pd	ATCC25922	Water	4ml	9.6%	0.7%	8.6%	0.1%	99.4%	0.6%
25%	Pd	BL21DE3	Water	4ml	5.6%	1.5%	14.8%	6.2%	70.4%	29.6%

In each of the oxidation reactions with 1-octanol, similar conversions ($X_{DH5\alpha}$ =2.9% mol/mol and $X_{BL21DE3}$=3.0% mol/mol) and selectivity to the aldehyde ($S_{DH5\alpha}$=70.9% mol/mol and $S_{BL21DE3}$=72.1% mol/mol respectively) were achieved with the 25% (w/w) Pd loaded *E. coli* DH5∝ and *E. coli* BL21DE3 nanocatalysts in the absence of a solvent. Although the *E. coli* ATCC25922 biofabricated nanocatalysts also achieved a 2.4% (mol/mol) conversion, a significantly higher selectivity towards the aldehyde (82.7% mol/mol) was noted (Table 6-5).

Dimitratos et al. (2006) noted that the use of water as a solvent may improve activity within alcohol reaction systems. Upon addition of water to the 1-octanol system, an improvement in conversion (ca. 4% mol/mol) was noted across the microbial strains (Table 6-5). Selectivity to the aldehyde increased by 4.4% (mol/mol) for the *E. coli* DH5∝ nanocatalysts but no further improvement in activity was noted for the *E. coli* BL21DE3 supported nanocatalysts. Upon addition of water to the 25% (w/w) Pd catalyst on *E. coli* ATCC25922, conversion increased by a factor of 4 (to 9.6% mol/mol) while the selectivity to the aldehyde increased to 99.4% mol/mol (Table 6-5). He et al. (2015) investigated similar solvent free conditions for 1-octanol oxidation using a monometallic Pd catalyst supported on magnesium-aluminium hydrotalcite. Oxidation performed using a 1% (w/w) Pd loaded synthetic catalyst at 100°C and 3 bar of oxygen, resulted in a similar conversion of 9% (mol/mol) and poorer selectivity (a difference of 19.4%) to the aldehyde (80% mol/mol) as compared to the 25% (w/w) Pd catalyst on *E. coli* ATCC25922 (Table 6-5).

Apart from hydrogen-induced Pd on *E. coli* ATCC25922 the over-oxidised product, namely the octanoic acid, accounted for 27.9%-29.1% (mol/mol) of the total reaction product (Table 6-5). The low conversion noted for the oxidation of this alcohol using the biofabricated catalysts was therefore likely a combination of mass transfer limitations as well as the increased presence of octanoic acid. As a result of the increased concentration of carboxylic acid within the reaction environment, more of these molecules were available to occupy the active catalytic sites thereby limiting the interaction of the alcohol with the catalyst and thus hindering the conversion of the substrate (Sankar et al., 2014).

From these preliminary experiments, it was clear that the biofabricated catalysts exhibited sufficient activity to facilitate the oxidation of 1-octanol to octanal. As expected, 1-octanol conversions were relatively low. The selectivity to the primary product in the presence of the Pd biofabricated nanocatalysts was similar to what has been previously reported for the synthetically supported counterparts (He et al., 2015). The presence of octanoic acid appeared to hinder conversion. However, as noted by Dimitratos et al. (2006) the addition of water as a solvent to the hydrogen-induced 25% (w/w) Pd catalyst on *E. coli* ATCC25922 improved the conversion of the alcohol to the aldehyde.

Considering the successful activity for both aromatic and linear alcohols to the desired aldehyde when using hydrogen-synthesized Pd(0) nanoparticles, *E. coli* ATCC25922 would be the preferred biological support for further studies. The activity on this strain was comparable to previously investigated catalysts under similar conditions. The use of hydrogen promoted rapid reduction and limited catalyst poisoning. At the higher Pd loading, activity on this particular catalyst support was a result of good uniformity in nanoparticle shape and size, with well distributed particles throughout the support. Clustering and loss of Pd was limited on *E. coli* ATCC25922 allowing for ample available active sites.

Activity on the hydrogen induced Pd catalyst supported on *E. coli* ATCC25922 was greatly improved when water was added as a solvent. This ensured the suppression of over-oxidative reaction pathways and selectivity to the preferred, high-value, aldehyde product.

Chapter 7

7 Conclusions and Recommendations

7.1 Conclusions

The potential of microorganisms, in particular gram-negative bacteria such as *E. coli*, to function as supports for metal nanoparticles as catalysts was investigated. The natural affinity of these bacteria to acquire certain metal ions can be utilized for remediation or, as in this study, as a 'green' method for nanocatalyst synthesis (Deplanche et al., 2011a; Lesmana et al., 2009; Lovley, 1993; Mabbett et al., 2006; Pantidos and Horsfall, 2014; Yong et al., 2002b). This study focused on the chemo-catalytic oxidation of alcohols following the bio-catalytic activation of n-octane to 1-octanol (Ayala and Torres, 2004; Gudiminchi et al., 2012; Meissner, 2013; Olaofe et al., 2013; Pennec et al., 2014). In this system, the biofabricated catalysts were considered a viable alternative to chemically synthesized nanocatalysts to successfully valorise low value alkanes in a single reactor (one-pot) tandem bio-chemo catalytic process. Biologically synthesised Pd and Au nanoparticles were considered due to their unique catalytic properties and known synergy. Although, previous investigations successfully demonstrated *E. coli* as the most effective gram-negative scaffold (Deplanche et al., 2014), comparative studies investigating the efficacy of different *E. coli* strains as catalyst supports are not available. As such, this study aimed to determine the most suitable *E. co*li strain to biofabricate nanoparticles that would successfully catalyse the oxidation of alcohols to higher value aldehydes. Catalyst activity was assessed under mild conditions to ensure compatibility with biotransformation of alkanes in the tandem system.

All microbial strains tested in this study showed potential as biological scaffolds for the biofabrication of nanoparticle catalyst to some degree. In the biosorption test, these gram-negative bacteria rapidly adsorbed both Pd(II) and Au(III) ions upon exposure. However, the hydrogenase deficient *E. coli* BL21DE3 was less effective at absorbing Au(III) ions at the 5% (w/w) loading, while the affinity of *E. coli* ATCC25922 decreased significantly (by 66.5 % for Pd and 11.9% for Au) as the metal loading was increased to 25% (w/w). Given that main mechanism for adsorption of the metal ions to the bacteria was found to be via chemisorption, this reduced affinity was likely a circumstance of the cell available active sites becoming over saturated. This was further supported by FTIR analysis. All microbial strains were composed of amine and hydroxyl groups that are known to coordinate Pd ions, and therefore were similarly absorbed by all microbial scaffolds. Au(III) coordinating thiol groups; however, were less visible using FTIR, and thus potentially existing at lower concentrations than the hydroxyls and amines.

Even though both gaseous and chemical electron donors successfully reduced the absorbed metal species on all *E. coli* strains, hydrogen was clearly the preferred electron donor. Reduction occurred within the first half hour with this gas in comparison to overnight incubation

with sodium formate. In either instance, near circular Pd(0) nanoparticles were formed that were less than 5 nm in size. A characteristic for an ideal nanocatalyst was to achieve uniform, mono-dispersed particles across the support. Achieving these particle characteristics would ensure more available active surface area for the reaction to occur. Given the near-ideal characteristics of the Pd(0) nanoparticles observed on all microbial strains, activity for the oxidation of benzyl alcohol was evident and aligned with published results for biofabricated *E. coli* MC4100 5% (w/w) Pd nanocatalysts using air as an oxidant (Deplanche et al., 2011a).

Although agglomeration of the nanoparticles was prevalent at higher Pd loadings on *E. coli* ATCC25922 and *E. coli* BL21DE3, the nanoparticle morphology and size of the 25% (w/w) Pd loaded *E. coli* ATCC25922 nanocatalysts were unaffected. However, the size of hydrogen-induced 25% (w/w) Pd(0) nanoparticles on *E. coli* BL21DE3 deviated from the ideal size range exceeding 5 nm (*ca.* 9.3 nm) potentially highlighting the importance of hydrogenase during reduction. A more successful reduction was evident on *E. coli* DH5α, where uniform, mono-dispersed Pd(0) nanoparticles with minimal agglomeration were noted. However, regardless of the donor used, Pd(0) loaded on this support was lost after harvesting of the catalyst, potentially due to weak binding sites. This higher degree of agglomeration and the loss of Pd noted on *E. coli* BL21DE3 and *E. coli* DH5α, respectively, limited active surface area and led to lower activity in the 1-octanol reaction. For *E. coli* ATCC25922 uniformity in particle size and shape, the limited clustering and loss of Pd(0) nanoparticles maximized the active surface area for reaction making this strain the frontrunner for biofabricating nanocatalysts.

Catalyst activity clearly improved with increasing metal loading on *E. coli* ATCC25922. At the 25% (w/w) Pd loading the conversion of benzyl alcohol increased by 31.6% (mol/mol) relative to the 5% (w/w) Pd loaded catalysts. Despite the observed nanoparticle agglomeration with the 25% (w/w) hydrogen-induced Pd biofabricated catalysts the selectivity towards benzaldehyde in the control reaction remained high at *ca.* 90.9% (mol/mol). Of all the hydrogen-induced 25% (w/w) Pd nanoparticles, the *E. coli* ATCC25922 supported nanocatalyst achieved comparable conversion of 1-octanol to the other strains but provided the greatest selectivity to octanal (82.7% mol/mol). The addition of water as a solvent counteracted potential byproduct poisoning of the active sites, increasing conversion and selectivity to the aldehyde on *E. coli* ATCC25922 to 9.6% (mol/mol) and 99.4% (mol/mol), respectively.

Reduction of Au(III) to Au(0) was only evident on *E. coli* ATCC25922 within 24 hours when hydrogen was used as the electron donor. Unlike Pd(0), the Au(0) nanoparticles exhibited poor uniformity, extensive agglomeration with irregularly shaped particles distributed sporadically. With the absence of an alkaline reagent to promote H abstraction coupled with oxidant limitations in the reactor, activity on benzyl alcohol for Au catalysts under mild reaction conditions was undetectable.

In conclusion the nanoparticles that formed on the microbial strains were similar in size and location to those particles identified on *E. coli* MC4100 in previous studies. The nanoparticles that formed were observed near the cytoplasmic and periplasmic hydrogenases. Of the three

strains, *E. coli* ATCC25922 achieved the best growth under anoxic conditions (0.8 g/L) and was capable of adsorbing both Pd(II) and Au(III) metal ions. The ability of this microbial strain to grow well under oxygen-limited conditions ensures the activation of pathways (involving enzymes like hydrogenase) that assist in generating a large electron pool. When hydrogen is used as the electron donor, these same pathways are favoured leading to the rapid generation of electrons for bioreduction. In the case of Au, *E. coli* ATCC25922 was the only strain capable of supporting the successful manufacture Au(0) nanoparticles in the presence of hydrogen. Reduction in the presence of hydrogen indicates that for this microbial strain it was likely that high levels of hydrogenase were available to catalyze the reduction of Au(III). Further, this microbial strain ensured stable attachment of uniform, mono-dispersed Pd(0) nanoparticles. Noting these characteristics along with the greater degree of agglomeration on *E. coli* BL21DE3 and loss of metal mass on *E. coli* DH5α, *E. coli* ATCC25922 was the most suitable strain for nanoparticle formation. Such characteristics of the Pd(0) nanoparticles and the greater availability of active surface area of the hydrogen-induced 25% (w/w) Pd catalysts on *E. coli* ATCC25922 resulted in the best activity for 1-octanol oxidation. For this particular biofabricated catalyst the resulting activity exceeded what was evident in literature, achieving near complete selectivity to the aldehyde.

7.2 Recommendations

During kinetic experiments an accurate determination of the amount of ions adsorbed onto the bacteria within the first minutes was difficult to acquire. Aliquot extraction and separation of the liquid-pellet were not instantaneous, making it difficult to determine the adsorption profile in the initial stages. To improve the accuracy and sample frequency during this period it is recommended that an online, rapid response sampling and detection method be implemented (redox or online modified ICP-OES analysis). Upon analysis of adsorption isotherms, it was observed that the maximum Pd capacity of *E. coli* ATCC25922 and *E. coli* DH5α was not yet confirmed. Using a higher ion precursor solution concentration (> 10 mM) would further establish the maximum capacity of each microbial strain and the accuracy of the predictive models. Observing adsorption of the metal ions at different temperatures can provide further understanding on the mechanism of adsorption. To understand the role of the microorganisms in mechanisms of adsorption and reduction, quantification of enzyme activity, specifically hydrogenase, would elucidate the function of these enzymes in reduction.

Before activity testing can continue, further optimization of the reactor and reaction conditions are necessary to ensure that the right amount of oxygen is supplied during reaction. This optimization of the reactor conditions can, in part, improve activity of the catalysts on 1-octanol. As this study identified *E. coli* ATCC25922 as the most suitable support for conversion of alcohol to the aldehyde, bimetallic Au-Pd catalyst manufacture on this support should be considered. The synergy of the two metals can be determined by altering ratios of Pd to Au and applying to the oxidation of alcohols.

Reference List

Ahmed, S., Annu, Ikram, S., Yudha, S., 2016. Biosynthesis of gold nanoparticles: A green approach. J. Photochem. Photobiol. B Biol. https://doi.org/10.1016/j.jphotobiol.2016.04.034

Ali, J., Ali, N., Wang, L., Waseem, H., Pan, G., 2019. Revisiting the mechanistic pathways for bacterial mediated synthesis of noble metal nanoparticles. J. Microbiol. Methods 159, 18–25. https://doi.org/10.1016/j.mimet.2019.02.010

Aljeboree, A.M., Alshirifi, A.N., Alkaim, A.F., 2017. Kinetics and equilibrium study for the adsorption of textile dyes on coconut shell activated carbon. Arab. J. Chem. 10, S3381–S3393. https://doi.org/10.1016/j.arabjc.2014.01.020

Allen, S.J., Mckay, G., Porter, J.F., 2004. Adsorption isotherm models for basic dye adsorption by peat in single and binary component systems. J. Colloid Interface Sci. 280, 322–333. https://doi.org/10.1016/j.jcis.2004.08.078

Ambili, V.K., 2011. Studies on catalysis by ordered Mesoporous SBA 15 materials modified with transition metals. Cochin University of Science and Technology.

Ananikov, V.P., 2015. Nickel : The " Spirited Horse " of Transition Metal Catalysis. https://doi.org/10.1021/acscatal.5b00072

Anastas, P., Eghbali, N., 2009. Green Chemistry: Principles and Practice. Chem. Soc. Rev. 39, 301–312. https://doi.org/10.1039/b918763b

Anderson, R., Griffin, K., Johnston, P., Alsters, P.L., 2002. Selective Oxidation of Alcohols to Carbonyl Compounds and Carboxylic Acids with Platinum Group Metal Catalysts.

Ashraf, M.A., Peng, W., Zare, Y., Rhee, K.Y., 2018. Effects of Size and Aggregation/Agglomeration of Nanoparticles on the Interfacial/Interphase Properties and Tensile Strength of Polymer Nanocomposites. Nanoscale Res. Lett. https://doi.org/10.1186/s11671-018-2624-0

Astruc, D., Lu, F., Aranzaes, J.R., 2005. Nanoparticles as Recyclable Catalysts : The Frontier between Homogeneous and Heterogeneous Catalysis. Angew. Chemie Int. Ed. 44, 7852–7872. https://doi.org/10.1002/anie.200500766

Ayala, M., Torres, E., 2004. Enzymatic activation of alkanes: Constraints and prospective. Appl. Catal. A Gen. 272, 1–13. https://doi.org/10.1016/j.apcata.2004.05.046

Ayawei, N., Ebelegi, A.N., Wankasi, D., 2017. Modelling and Interpretation of Adsorption Isotherms. J. Chem. https://doi.org/10.1155/2017/3039817

Ayres, G.H., Alsop, J.H., 1959. Spectrophotometric Determination of Palladium(II) with Tin(II). Anal. Chem. 31, 1135–1138. https://doi.org/10.1021/ac60151a019

Azizian, S., 2004. Kinetic models of sorption: A theoretical analysis. J. Colloid Interface Sci. 276, 47–52. https://doi.org/10.1016/j.jcis.2004.03.048

Beltrán-Heredia, J., Sánchez-Martín, J., 2009. Removal of sodium lauryl sulphate by coagulation/flocculation with Moringa oleifera seed extract. J. Hazard. Mater. 164, 713–719. https://doi.org/10.1016/J.JHAZMAT.2008.08.053

Bennett, J.A., Creamer, N.J., Deplanche, K., Macaskie, L.E., Shannon, I.J., Wood, J., 2010. Palladium supported on bacterial biomass as a novel heterogeneous catalyst: A comparison of Pd/Al2O3 and bio-Pd in the hydrogenation of 2-pentyne. Chem. Eng. Sci.

65, 282–290. https://doi.org/10.1016/j.ces.2009.06.069

Bennett, J.A., Mikheenko, I.P., Deplanche, K., Shannon, I.J., Wood, J., Macaskie, L.E., 2013. Nanoparticles of palladium supported on bacterial biomass: New re-usable heterogeneous catalyst with comparable activity to homogeneous colloidal Pd in the Heck reaction. Appl. Catal. B Environ. 140–141, 700–707. https://doi.org/10.1016/j.apcatb.2013.04.022

Bennett, J.A., Wilson, K., Lee, A.F., 2016. Catalytic applications of waste derived materials. J. Mater. Chem. A 4, 3617–3637. https://doi.org/10.1039/C5TA09613H

Bergman, R.G., 2007. Organometallic chemistry: C-H activation. Nature 446, 391–393.

Bernardotto, G., Menegazzo, F., Pinna, F., Signoretto, M., Cruciani, G., Strukul, G., Saragat, V., 2009. Applied Catalysis A : General New Pd – Pt and Pd – Au catalysts for an efficient synthesis of H 2 O 2 from H 2 and O 2 under very mild conditions. Appl. Catal. A Gen. 358, 129–135. https://doi.org/10.1016/j.apcata.2009.02.010

Besson, M., Gallezot, P., 2000. Selective oxidation of alcohols and aldehydes on metal catalysts, Catalysis Today.

Bhati, N., Sarma, K., Goswami, A., 2008. Expedient method for oxidation of alcohol by hydrogen peroxide in the presence of amberlite IRA 400 resin (basic) as phase-transfer catalyst. Synth. Commun. https://doi.org/10.1080/00397910801916090

Bhattarai, N., Casillas, G., Khanal, S., Salazar, J.J.V., Ponce, A., Jose-Yacaman, M., 2013. Origin and shape evolution of core-shell nanoparticles in Au-Pd: From few atoms to high Miller index facets. J. Nanoparticle Res. 15. https://doi.org/10.1007/s11051-013-1660-z

Bordeaux, M., Galarneau, A., Drone, J., 2012. Catalytic, mild, and selective oxyfunctionalization of linear alkanes: Current challenges. Angew. Chemie Int. Ed. 51, 10712–10723. https://doi.org/10.1002/anie.201203280

Brayner, R., Barberousse, H., Hemadi, M., Djedjat, C., Yéprémian, C., Coradin, T., Livage, J., Fiévet, F., Couté, A., 2007. Cyanobacteria as bioreactors for the synthesis of Au, Ag, Pd, and Pt nanoparticles via an enzyme-mediated route. J. Nanosci. Nanotechnol. 7, 2696–2708. https://doi.org/10.1166/jnn.2007.600

Bricout, H., Carpentier, J.-F., Mortreux, A., 1998. Nickel vs. palladium catalysts for coupling reactions of allyl alcohol with soft nucleophiles: activities and deactivation processes. J. Mol. Catal. A Chem. 136, 243–251. https://doi.org/10.1016/S1381-1169(98)00067-3

Brummund, J., Sonke, T., Muller, M., 2015. Process Development for Biocatalytic Oxidations Applying Alcohol Dehydrogenases. Org. Process Res. Dev. 19, 1590–1595. https://doi.org/10.1021/op500307e

Bühler, B., Bollhalder, I., Hauer, B., Witholt, B., Schmid, A., 2003. Use of the two-liquid phase concept to exploit kinetically controlled multistep biocatalysis. Biotechnol. Bioeng. 81, 683–694. https://doi.org/10.1002/bit.10512

Bunge, M., Søbjerg, L.S., Rotaru, A.E., Gauthier, D., Lindhardt, A.T., Hause, G., Finster, K., Kingshott, P., Skrydstrup, T., Meyer, R.L., 2010. Formation of Palladium(0) Nanoparticles at Microbial Surfaces. Biotechnol. Bioeng. 107, 206–215. https://doi.org/10.1002/bit.22801

Carter, J.H., Althahban, S., Nowicka, E., Freakley, S.J., Morgan, D.J., Shah, P.M., Golunski, S., Kiely, C.J., Hutchings, G.J., 2016. Synergy and Anti-Synergy between Palladium and Gold in Nanoparticles Dispersed on a Reducible Support. ACS Catal. 6, 6623–6633. https://doi.org/10.1021/acscatal.6b01275

Chah, S., Hammond, M.R., Zare, R.N., 2005. Gold nanoparticles as a colorimetric sensor for protein conformational changes. Chem. Biol. 12, 323–328. https://doi.org/10.1016/j.chembiol.2005.01.013

Chen, B.Y., Chen, C.Y., Guo, W.Q., Chang, H.W., Chen, W.M., Lee, D.J., Huang, C.C., Ren, N.Q., Chang, J.S., 2014. Fixed-bed biosorption of cadmium using immobilized Scenedesmus obliquus CNW-N cells on loofa (Luffa cylindrica) sponge. Bioresour. Technol. 160, 175–181. https://doi.org/10.1016/j.biortech.2014.02.006

Chen, M., Kumar, D., Yi, C.-W., Goodman, D.W., 2005. The Promotional Effect of Gold in Catalysis by Palladium-Gold. Science 310, 291–293. https://doi.org/10.1126/science.1115800

Ciriminna, R., Albanese, L., Meneguzzo, F., Pagliaro, M., 2016. Hydrogen Peroxide: A Key Chemical for Today's Sustainable Development. ChemSusChem. https://doi.org/10.1002/cssc.201600895

Ciriminna, R., Pagliaro, M., 2013. Green Chemistry in the Fine Chemicals and Pharmaceutical Industries. Org. Process Res. Dev. 17, 1479–1484. https://doi.org/10.1021/op400258a

Ciriminna, R., Pandarus, V., Béland, F., Xu, Y.J., Pagliaro, M., 2015. Heterogeneously Catalyzed Alcohol Oxidation for the Fine Chemical Industry. Org. Process Res. Dev. https://doi.org/10.1021/acs.oprd.5b00204

Coleman, M.L., Hedrick, D.B., Lovley, D.R., White, D.C., Pye, K., 1993. Reduction of Fe(III) in sediments by sulphate-reducing bacteria. Nature 361, 436–438. https://doi.org/10.1038/361436a0

Creamer, N.J., Mikheenko, I.P., Yong, P., Deplanche, K., Sanyahumbi, D., Wood, J., Pollmann, K., Merroun, M., Selenska-Pobell, S., Macaskie, L.E., 2007. Novel supported Pd hydrogenation bionanocatalyst for hybrid homogeneous/heterogeneous catalysis. Catal. Today 128, 80–87. https://doi.org/10.1016/j.cattod.2007.04.014

Dada, A.O., Olalekan, A.P., Olatunya, A.M., Dada, 2012. Langmuir, Freundlich, Temkin and Dubinin-Radushkevich Isotherms Studies of Equilibrium Sorption of Zn 2+ Unto Phosphoric Acid Modified Rice Husk. IOSR J. Appl. Chem. 3, 38–45.

Davis, S.E., Ide, M.S., Davis, R.J., 2013. Selective oxidation of alcohols and aldehydes over supported metal nanoparticles. Green Chem. 15, 17–45. https://doi.org/10.1039/C2GC36441G

De Corte, S., Hennebel, T., Fitts, J.P., Sabbe, T., Bliznuk, V., Verschuere, S., Van Der Lelie, D., Verstraete, W., Boon, N., 2011a. Biosupported bimetallic Pd-Au nanocatalysts for dechlorination of environmental contaminants. Environ. Sci. Technol. 45, 8506–8513. https://doi.org/10.1021/es2019324

De Corte, S., Hennebel, T., Verschuere, S., Cuvelier, C., Verstraete, W., Boon, N., 2011b. Gold nanoparticle formation using Shewanella oneidensis: A fast biosorption and slow reduction process. J. Chem. Technol. Biotechnol. 86, 547–553. https://doi.org/10.1002/jctb.2549

De Klerk, A., 2008. Fischer-Tropsch Refining.

De Vargas, I., Macaskie, L.E., Guibal, E., 2004. Biosorption of palladium and platinum by sulfate-reducing bacteria. J. Chem. Technol. Biotechnol. 79, 49–56. https://doi.org/10.1002/jctb.928

De Windt, W., Aelterman, P., Verstraete, W., 2005. Bioreductive deposition of palladium (0) nanoparticles on Shewanella oneidensis with catalytic activity towards reductive dechlorination of polychlorinated biphenyls. Environ. Microbiol. 7, 314–325.

https://doi.org/10.1111/j.1462-2920.2004.00696.x

Denard, C., Hartwig, J., Zhao, H., 2013. Multistep One-Pot Reactions Combining Biocatalysts and Chemical Catalysts for Asymmetric Synthesis. ACS Catal. 3, 2856–2864. https://doi.org/10.3390/catal6120194

Deplanche, K., 2008. Kevin Deplanche.

Deplanche, K., Bennett, J.A., Mikheenko, I.P., Omajali, J., Wells, A.S., Meadows, R.E., Wood, J., Macaskie, L.E., 2014. Catalytic activity of biomass-supported Pd nanoparticles: Influence of the biological component in catalytic efficacy and potential application in 'green' synthesis of fine chemicals and pharmaceuticals. Appl. Catal. B Environ. 147, 651–665. https://doi.org/10.1016/J.APCATB.2013.09.045

Deplanche, K., Caldelari, I., Mikheenko, I.P., Sargent, F., Macaskie, L.E., 2010. Involvement of hydrogenases in the formation of highly catalytic Pd(0) nanoparticles by bioreduction of Pd(II) using Escherichia coli mutant strains. Microbiology 156, 2630–2640. https://doi.org/10.1099/mic.0.036681-0

Deplanche, K., Macaskie, L.E., 2008. Biorecovery of gold by Escherichia coli and Desulfovibrio desulfuricans. Biotechnol. Bioeng. 99, 1055–1064. https://doi.org/10.1002/bit.21688

Deplanche, K., Merroun, M.L., Casadesus, M., Tran, D.T., Mikheenko, I.P., Bennett, J.A., Zhu, J., Jones, I.P., Attard, G.A., Wood, J., Selenska-Pobell, S., Macaskie, L.E., 2012. Microbial synthesis of core/shell gold/palladium nanoparticles for applications in green chemistry. J. R. Soc. Interface 9, 1705–1712. https://doi.org/10.1098/rsif.2012.0003

Deplanche, K., Mikheenko, I.P., Bennett, J.A., Merroun, M., Mounzer, H., Wood, J., MacAskie, L.E., 2011a. Selective oxidation of benzyl-alcohol over biomass-supported Au/Pd bioinorganic catalysts. Top. Catal. 54, 1110–1114. https://doi.org/10.1007/s11244-011-9691-0

Deplanche, K., Murray, A., Mennan, C., Taylor, S., Macaskie, L., 2011b. Biorecycling of Precious Metals and Rare Earth Elements, in: Rahman, M. (Ed.), Nanomaterials. InTech, pp. 279–314.

Deplanche, K., Woods, R.D., Mikheenko, I.P., Sockett, R.E., Macaskie, L.E., 2008. Manufacture of stable palladium and gold nanoparticles on native and genetically engineered flagella scaffolds. Biotechnol. Bioeng. 101, 873–880. https://doi.org/10.1002/bit.21966

Dimitratos, N., Villa, A., Wang, D., Porta, F., Su, D., Prati, L., 2006. Pd and Pt catalysts modified by alloying with Au in the selective oxidation of alcohols. J. Catal. 244, 113–121. https://doi.org/10.1016/j.jcat.2006.08.019

Ding, Y., Fan, F., Tian, Z., Wang, Z., 2010. Atomic structure of Au− Pd bimetallic alloyed nanoparticles. J. Am. Chem. Soc. 12480–12486.

Dong, J., Fernández-Fueyo, E., Hollmann, F., Paul, C.E., Pesic, M., Schmidt, S., Wang, Y., Younes, S., Zhang, W., 2018. Biocatalytic Oxidation Reactions: A Chemist's Perspective. Angew. Chemie Int. Ed. 57, 9238–9261. https://doi.org/10.1002/anie.201800343

Du, L., Jiang, H., Liu, X., Wang, E., 2007. Biosynthesis of gold nanoparticles assisted by Escherichia coli DH5α and its application on direct electrochemistry of hemoglobin. Electrochem. commun. 9, 1165–1170. https://doi.org/10.1016/j.elecom.2007.01.007

Ehrlich, H.L., 1997. Microbes and metals. Appl. Microbiol. Biotechnol. 48, 687–692. https://doi.org/10.1007/s002530051116

Enache, D.I., Barker, D., Edwards, J.K., Taylor, S.H., Knight, D.W., Carley, A.F., Hutchings,

G.J., 2007. Solvent-free oxidation of benzyl alcohol using titania-supported gold-palladium catalysts: Effect of Au-Pd ratio on catalytic performance. Catal. Today 122, 407–411. https://doi.org/10.1016/j.cattod.2007.01.003

Enache, D.I., Edwards, J.K., Landon, P., Solsona-Espriu, B., Carley, A.F., Herzing, A.A., Watanabe, M., Kiely, C.J., Knight, D.W., Hutchings, G.J., 2006. Solvent-Free Oxidation of Primary Alcohols to Aldehydes Using Au-Pd/TiO2 Catalysts. Science (80-.). 311, 362–366. https://doi.org/10.1126/science.1120560

Feijó Delgado, F., Cermak, N., Hecht, V.C., Son, S., Li, Y., Knudsen, S.M., Olcum, S., Higgins, J.M., Chen, J., Grover, W.H., Manalis, S.R., 2013. Intracellular Water Exchange for Measuring the Dry Mass, Water Mass and Changes in Chemical Composition of Living Cells. PLoS One 8. https://doi.org/10.1371/journal.pone.0067590

Ferrando, R., Jellinek, J., Johnston, R.L., 2008. Nanoalloys: From theory to applications of alloy clusters and nanoparticles. Chem. Rev. 108, 845–910. https://doi.org/10.1021/cr040090g

Flint, D., 2017. Why Are Transition Metals Good Catalysts? [WWW Document]. URL https://sciencing.com/why-are-transition-metals-good-catalysts-12342816.html (accessed 1.18.18).

Fowler, R., Guggenheim, E.A., 1956. Staatistical Thermodynamics: A version of Statistical Mechanics for Students of Physics and Chemistry, in: Staatistical Thermodynamics: A Version of Statistical Mechanics for Students of Physics and Chemistry.

Fujita, Y., Mori, I., Matsuo, T., 1999. Spectrophotometric determination of gold (III) by an association complex formation between gold-thiamine and phloxine. Anal. Sci. 15, 1009–1012.

Fujiwara, K., Ramesh, A., Maki, T., Hasegawa, H., Ueda, K., 2007. Adsorption of platinum (IV), palladium (II) and gold (III) from aqueous solutions onto l-lysine modified crosslinked chitosan resin. J. Hazard. Mater. 146, 39–50. https://doi.org/10.1016/j.jhazmat.2006.11.049

Gahlawat, G., Choudhury, A.R., 2019. A review on the biosynthesis of metal and metal salt nanoparticles by microbes. RSC Adv. 9, 12944–12967. https://doi.org/10.1039/c8ra10483b

Gandolfi, R., Ferrara, N., Molinari, F., 2001. An easy and efficient method for the production of carboxylic acids and aldehydes by microbial oxidation of primary alcohols, TETRAHEDRON LETTERS.

Gao, F., Goodman, D.W., 2012. Pd-Au bimetallic catalysts: understanding alloy effects from planar models and (supported) nanoparticles. Chem Soc Rev 41, 8009–8020. https://doi.org/10.1039/c2cs35160a

Gavriilidis, A., Constantinou, A., Hellgardt, K., Hii, K.K.M., Hutchings, G.J., Brett, G.L., Kuhn, S., Marsden, S.P., 2016. Aerobic oxidations in flow: Opportunities for the fine chemicals and pharmaceuticals industries. React. Chem. Eng. https://doi.org/10.1039/c6re00155f

Gawande, M.B., Goswami, A., Asefa, T., Guo, H., Biradar, A. V, Peng, D., Zboril, R., Varma, R.S., 2015. Core-shell nanoparticles: synthesis and applications in catalysis and electrocatalysis. Chem. Soc. Rev. 44, 7540–7590. https://doi.org/10.1039/C5CS00343A

Giles, C.H., Macewan, T.H., Nakhwa, S.N., Smith, D., 1922. Solution Adsorption Isotherms, and its Use in Diagnosis of Adsorption Mechanisms and in Measurement of Specific Surface Areas of Solids.

Govender, M., 2021. Data set [WWW Document]. https://doi.org/10.25375/uct.c.5338196

Griffin, K.G., Johnston, P., Bennett, S., Kaliq, S., 2002. Use of platinum group metal catalysts for the selective oxidation of alcohols to carbonyls in the liquid phase. pp. 169–178.

Gröger, H., Hummel, W., 2014. Combining the “two worlds” of chemocatalysis and biocatalysis towards multi-step one-pot processes in aqueous media. Curr. Opin. Chem. Biol. 19, 171–179. https://doi.org/10.1016/j.cbpa.2014.03.002

Gudiminchi, R.K., Randall, C., Opperman, D.J., Olaofe, O.A., Harrison, S.T.L., Albertyn, J., Smit, M.S., 2012. Whole-cell hydroxylation of n-octane by Escherichia coli strains expressing the CYP153A6 operon. Appl. Microbiol. Biotechnol. 96, 1507–1516. https://doi.org/10.1007/s00253-012-3984-5

Hamdaoui, O., Naffrechoux, E., 2007. Modeling of adsorption isotherms of phenol and chlorophenols onto granular activated carbon. Part I. Two-parameter models and equations allowing determination of thermodynamic parameters. J. Hazard. Mater. 147, 381–394. https://doi.org/10.1016/j.jhazmat.2007.01.021

Hartings, M., 2012. Reactions coupled to palladium. Nat. Chem. 4, 764. https://doi.org/10.1038/nchem.1437

Haruta, M., 2003. When Gold Is Not Noble: Catalysis by Nanoparticles. Chem. Rec. 3, 75–87. https://doi.org/10.1002/tcr.10053

Haruta, M., Yamada, N., Kobayashi, T., Iijima, S., 1989. Gold catalysts prepared by coprecipitation for low-temperature oxidation of hydrogen and of carbon monoxide. J. Catal. https://doi.org/10.1016/0021-9517(89)90034-1

He, J., Ichinose, I., Kunitake, T., Nakao, A., Shiraishi, Y., Toshima, N., 2003. Facile fabrication of Ag-Pd bimetallic nanoparticles in ultrathin TiO2-gel films: Nanoparticle morphology and catalytic activity. J. Am. Chem. Soc. 125, 11034–11040. https://doi.org/10.1021/ja035970b

He, Y., Feng, J., Brett, G.L., Iu, Y., Miedziak, P.J., Edwards, J.K., Knight, D.W., Li, D., Hutchings, G.J., 2015. Oxidation of Aliphatic Alcohols by Using Precious Metals Supported on Hydrotalcite under Solvent-and Base-Free Conditions.

Ho, Y.S., 2006. Review of second-order models for adsorption systems. J. Hazard. Mater. 136, 681–689. https://doi.org/10.1016/j.jhazmat.2005.12.043

Ho, Y.S., McKay, G., 1998a. Sorption of dye from aqueous solution by peat. Chem. Eng. J. 70, 115–124. https://doi.org/10.1016/S1385-8947(98)00076-X

Ho, Y.S., McKay, G., 1998b. A Comparison of Chemisorption Kinetic Models Applied to Pollutant Removal on Various Sorbents. Process Saf. Environ. Prot. 76, 332–340. https://doi.org/10.1205/095758298529696

Hoeldericht, W.F., Kollmer, F., 2000. Oxidation reactions in the synthesis of fine and intermediate chemicals using environmentally benign oxidants and the right reactor system, in: Pure and Applied Chemistry. https://doi.org/10.1351/pac200072071273

Hosseinkhani, B., Søbjerg, L.S., Rotaru, A., Emtiazi, G., Skrydstrup, T., Meyer, R.L., 2012. Microbially Supported Synthesis of Catalytically Active Bimetallic Pd-Au Nanoparticles 109, 45–52. https://doi.org/10.1002/bit.23293

Husseiny, M.I., El-Aziz, M.A., Badr, Y., Mahmoud, M.A., 2007. Biosynthesis of gold nanoparticles using Pseudomonas aeruginosa. Spectrochim. Acta - Part A Mol. Biomol. Spectrosc. 67, 1003–1006. https://doi.org/10.1016/j.saa.2006.09.028

Hutchings, G.J., 2007. A golden future for green chemistry. Catal. Today 122, 196–200. https://doi.org/10.1016/j.cattod.2007.01.018

Hutchings, G.J., 1985. Vapor phase hydrochlorination of acetylene: Correlation of catalytic activity of supported metal chloride catalysts. J. Catal. https://doi.org/10.1016/0021-9517(85)90383-5

Hutchings, G.J., Haruta, M., 2005. A golden age of catalysis: A perspective. Appl. Catal. A Gen. 291, 2–5. https://doi.org/10.1016/J.APCATA.2005.05.044

Imlay, J.A., Linn, S., 1987. Mutagenesis and Stress Responses Induced in Escherichia coli by Hydrogen Peroxide. J. Bacteriol. 169, 2967–2976.

Inam, E., Etim, U.J., Akpabio, E.G., Umoren, S.A., 2017. Process optimization for the application of carbon from plantain peels in dye abstraction. J. Taibah Univ. Sci. 11, 173–185. https://doi.org/10.1016/j.jtusci.2016.01.003

Inyinbor, A.A., Adekola, F.A., Olatunji, G.A., 2016. Kinetics, isotherms and thermodynamic modeling of liquid phase adsorption of Rhodamine B dye onto Raphia hookerie fruit epicarp. Water Resour. Ind. 15, 14–27. https://doi.org/10.1016/j.wri.2016.06.001

Iravani, S., 2014. Bacteria in Nanoparticle Synthesis: Current Status and Future Prospects. Int. Sch. Res. Not. 2014, 1–18. https://doi.org/10.1155/2014/359316

Ishida, T., Ogihara, Y., Ohashi, H., Akita, T., Honma, T., Oji, H., Haruta, M., 2012. Base-free direct oxidation of 1-octanol to octanoic acid and its octyl ester over supported gold catalysts. ChemSusChem 5, 2243–2248. https://doi.org/10.1002/cssc.201200324

Johnson and Matthey, 2019. Market data tables [WWW Document]. URL http://www.platinum.matthey.com/services/market-research/market-data-tables (accessed 2.27.19).

Johnson and Matthey, 2017. PGM Market Report.

Julsing, M.K., Cornelissen, S., Bühler, B., Schmid, A., 2008. Heme-iron oxygenases: powerful industrial biocatalysts? Curr. Opin. Chem. Biol. 12, 177–186. https://doi.org/10.1016/j.cbpa.2008.01.029

Kadenbach, B., Arnold, S., Lee, I., Hüttemann, M., 2004. The possible role of cytochrome c oxidase in stress-induced apoptosis and degenerative diseases. Biochim. Biophys. Acta - Bioenerg. https://doi.org/10.1016/j.bbabio.2003.06.005

Kashefi, K., Tor, J.M., Nevin, K.P., Lovley, D.R., 2001. Reductive Precipitation of Gold by Dissimilatory Fe(III)-Reducing Bacteria and Archaea. Appl. Environ. Microbiol. 67, 3275–3279. https://doi.org/10.1128/AEM.67.7.3275-3279.2001

Kiruthika, S., n.d. Sample Preparation Techniques in Light Microscopy [WWW Document]. URL https://www.biologydiscussion.com/microbiology-2/microscopy/sample-preparation-techniques-in-light-microscopy-microbiology/84715 (accessed 8.26.20).

Kitco, 2015. Technical Gold Charts and Data [WWW Document]. URL https://www.kitco.com/charts/CPM_charts.html (accessed 2.27.19).

Koch, D.J., Arnold, F.H., 2013. REGIOSELECTIVE ALKANE Hydroxylation with a mutant CYP153A6 Enzyme.

Konishi, Y., Tsukiyama, T., Ohno, K., Saitoh, N., Nomura, T., Nagamine, S., 2006. Intracellular recovery of gold by microbial reduction of AuCl 4- ions using the anaerobic bacterium Shewanella algae. Hydrometallurgy 81, 24–29. https://doi.org/10.1016/j.hydromet.2005.09.006

Kumar, R., Bhatia, D., Singh, R., Rani, S., Bishnoi, N.R., 2011. Sorption of heavy metals from electroplating effluent using immobilized biomass Trichoderma viride in a continuous packed-bed column. Int. Biodeterior. Biodegrad. 65, 1133–1139.

https://doi.org/10.1016/j.ibiod.2011.09.003

Labinger, J.A., Bercaw, J.E., 2002. Understanding and exploiting C-H bond activation. Nature 417, 507–514.

Lam, C.H., 2011. Organic Seminar Recent Advances in Ni Catalyzed Suzuki Coupling: Toward Green, Cheap and Environmentally Friendly Catalysis.

Langmuir, I., 1918. The adsorption of glass on plane surfaces of glass, mica and platinum 345. https://doi.org/10.1021/ja02242a004

Largitte, L., Pasquier, R., 2016. A review of the kinetics adsorption models and their application to the adsorption of lead by an activated carbon. Chem. Eng. Res. Des. 109, 495–504. https://doi.org/10.1016/j.cherd.2016.02.006

Latham, J., Henry, J.M., Sharif, H.H., Menon, B.R.K., Shepherd, S.A., Greaney, M.F., Micklefield, J., 2016. Integrated catalysis opens new arylation pathways via regiodivergent enzymatic C-H activation. Nat. Commun. 7, 1–8. https://doi.org/10.1038/ncomms11873

Lesmana, S.O., Febriana, N., Soetaredjo, F.E., Sunarso, J., Ismadji, S., 2009. Studies on potential applications of biomass for the separation of heavy metals from water and wastewater. Biochem. Eng. J. 44, 19–41. https://doi.org/10.1016/j.bej.2008.12.009

Li, X., Xu, H., Chen, Z.S., Chen, G., 2011. Biosynthesis of nanoparticles by microorganisms and their applications. J. Nanomater. https://doi.org/10.1155/2011/270974

Liamleam, W., Annachhatre, A.P., 2007. Electron donors for biological sulfate reduction. Biotechnol. Adv. 25, 452–463. https://doi.org/10.1016/j.biotechadv.2007.05.002

Limousin, G., Gaudet, J.P., Charlet, L., Szenknect, S., Barthès, V., Krimissa, M., 2007. Sorption isotherms: A review on physical bases, modeling and measurement. Appl. Geochemistry. https://doi.org/10.1016/j.apgeochem.2006.09.010

Lin, B.-L., Liu, L., Fu, Y., Luo, S.-W., Chen, Q., Guo, Q.-X., 2004. Comparing Nickel-and Palladium-Catalyzed Heck Reactions. https://doi.org/10.1021/om034067h

Liu, L., Corma, A., 2018. Metal Catalysts for Heterogeneous Catalysis: From Single Atoms to Nanoclusters and Nanoparticles. Chem. Rev. https://doi.org/10.1021/acs.chemrev.7b00776

Liz-Marzán, L.M., 2004. Nanometals: formation and color. Mater. Today 3, 26–31.

Lloyd, J.R., Cole, J.A., Macaskie, L.E., 1997. Reduction and Removal of Heptavalent Technetium from Solution by Escherichia coli, JOURNAL OF BACTERIOLOGY.

Lloyd, J.R., Yong, P., Macaskie, L.E., 1998. Enzymatic recovery of elemental palladium by using sulfate-reducing bacteria. Appl. Environ. Microbiol. 64, 4607–4609.

Lok, C.M., 2015. Structure and Performance of Selective Hydrogenation Catalysts.

Lovley, D.R., 1993. Dissimilatory Metal Reduction. Annu. Rev. Microbiol. 47, 263–290.

Lovley, D.R., Phillips, E.J.P., 1988. Novel Mode of Microbial Energy Metabolism: Organic Carbon Oxidation Coupled to Dissimilatory Reduction of Iron or Manganese. Appl. Environ. Microbiol. 54, 1472–1480. https://doi.org/10.1103/PhysRevLett.50.1998

Lukey, M.J., Parkin, A., Roessler, M.M., Murphy, B.J., Harmer, J., Palmer, T., Sargent, F., Armstrong, F.A., 2010. How Escherichia coli Is Equipped to Oxidize Hydrogen under Different Redox Conditions. J. Biol. Chem. 285, 3928–3938. https://doi.org/10.1074/jbc.M109.067751

Ma, C.Y., Dou, B.J., Li, J.J., Cheng, J., Hu, Q., Hao, Z.P., Qiao, S.Z., 2009. Catalytic oxidation of benzyl alcohol on Au or Au-Pd nanoparticles confined in mesoporous silica. Appl. Catal. B Environ. 92, 202–208. https://doi.org/10.1016/j.apcatb.2009.07.007

Mabbett, A.N., Sanyahumbi, D., Yong, P., Macaskie, L.E., 2006. Biorecovered precious metals from industrial wastes: Single-step conversion of a mixed metal liquid waste to a bioinorganic catalyst with environmental application. Environ. Sci. Technol. 40, 1015–1021. https://doi.org/10.1021/es0509836

Macaskie, L.E., Humphries, A.C., Mikheenko, I.P., Baxter-Plant, V.S., Deplanche, K., Redwood, M.D., Bennett, J.A., Wood, J., 2012. Use of Desulfovibrio and Escherichia coli Pd-nanocatalysts in reduction of Cr(VI) and hydrogenolytic dehalogenation of polychlorinated biphenyls and used transformer oil. J. Chem. Technol. Biotechnol. 87, 1430–1435. https://doi.org/10.1002/jctb.3763

Maitlis, P.M., Klerk, A. de., 2013. Greener Fischer-Tropsch processes for fuels and feedstocks. Wiley-VCH.

Mallat, T., Baiker, A., 2004. Oxidation of alcohols with molecular oxygen on solid catalysts. Chem. Rev. 104, 3037–3058. https://doi.org/10.1021/cr0200116

Meenakshisundaram, S., Nowicka, E., Miedziak, P.J., Brett, G.L., Jenkins, R.L., Dimitratos, N., Taylor, S.H., Knight, D.W., Bethell, D., Hutchings, G.J., 2010. Oxidation of alcohols using supported gold and gold–palladium nanoparticles. Faraday Discuss. 145, 341–356. https://doi.org/10.1039/b920917b

Mehrabadi, B., Eskandari, S., Khan, U., Catalysis, R.W.-… in, 2017, U., 2017. A review of preparation methods for supported metal catalysts. Elsevier Advances i.

Meissner, M.P., 2013. Reactor Design for The Hydroxylation of n-Octane Using a CYP153A6-based Biocatalytic System Expressed in Escherichia coli. 1–165.

Miedziak, P.J., He, Q., Edwards, J.K., Taylor, S.H., Knight, D.W., Tarbit, B., Kiely, C.J., Hutchings, G.J., 2011a. Oxidation of benzyl alcohol using supported gold-palladium nanoparticles. Catal. Today 163, 47–54. https://doi.org/10.1016/j.cattod.2010.02.051

Miedziak, P.J., Sankar, M., Dimitratos, N., Lopez-sanchez, J.A., Carley, A.F., Knight, D.W., Taylor, S.H., Kiely, C.J., Hutchings, G.J., 2011b. Oxidation of benzyl alcohol using supported gold – palladium nanoparticles. Catal. Today 164, 315–319. https://doi.org/10.1016/j.cattod.2010.10.028

Mikheenko, I.P., Rousset, M., Dementin, S., Macaskie, L.E., 2008. Bioaccumulation of palladium by Desulfovibrio fructosivorans wild-type and hydrogenase-deficient strains. Appl. Environ. Microbiol. 74, 6144–6146. https://doi.org/10.1128/AEM.02538-07

Mobley, J.K., Crocker, M., 2015. Catalytic oxidation of alcohols to carbonyl compounds over hydrotalcite and hydrotalcite-supported catalysts. RSC Adv. https://doi.org/10.1039/c5ra11254k

Monai, M., Melchionna, M., Fornasiero, P., 2018. From metal to metal-free catalysts: Routes to sustainable chemistry 63, 1–73. https://doi.org/10.1016/BS.ACAT.2018.10.001

Mulvaney, P., 1996. Surface plasmon spectroscopy of nanosized metal particles. Langmuir 12, 788–800. https://doi.org/10.1021/la9502711

Murzin, D., 2013. Engineering catalysis. Walter de Gruyter GmbH, Berlin.

Nagy, G., Beck, A., Sáfrán, G., Schay, Z., Liu, S., Li, T., Qiao, B., Wang, J., Lázár, K., 2019. Nanodisperse gold catalysts in oxidation of benzyl alcohol: comparison of various supports under different conditions. React. Kinet. Mech. Catal. 128, 71–95.

https://doi.org/10.1007/s11144-019-01615-8

Nakajima, A., 2003. Accumulation of gold by microorganisms. World J. Microbiol. Biotechnol. 19, 369–374. https://doi.org/10.1023/A:1023944905364

Namasivayam, C., Kavitha, D., 2007. Adsorption of Methylene Blue From Water Onto Activated Carbon Prepared From Coir Pith, an Agricultural Solid Waste 54, 339–343. https://doi.org/10.1142/9789812704320_0059

Narayanan, K.B., Sakthivel, N., 2010. Biological synthesis of metal nanoparticles by microbes. Adv. Colloid Interface Sci. 156, 1–13. https://doi.org/10.1016/j.cis.2010.02.001

National diagnostics, n.d. Fixing Tissue for Electron Microscopy [WWW Document]. URL https://www.nationaldiagnostics.com/histology/article/fixing-tissue-electron-microscopy (accessed 8.26.20).

Nebraska Center for Materials and Nanoscience, n.d. Specimen Interaction [WWW Document]. URL https://ncmn.unl.edu/enif/microscopy/interact.shtml (accessed 8.26.20).

Ng, C., Losso, J.N., Marshall, W.E., Rao, R.M., 2002. Freundlich adsorption isotherms of agricultural by-product-based powdered activated carbons in a geosmin-water system. Bioresour. Technol. 85, 131–135. https://doi.org/10.1016/S0960-8524(02)00093-7

Okazaki, K., Ichikawa, S., Maeda, Y., Haruta, M., Kohyama, M., 2005. Electronic structures of Au supported on TiO2. Appl. Catal. A Gen. 291, 45–54. https://doi.org/10.1016/j.apcata.2005.02.047

Olaofe, O. a, Fenner, C.J., Gudiminchi, R.K., Smit, M.S., Harrison, S.T.L., 2013. The influence of microbial physiology on biocatalyst activity and efficiency in the terminal hydroxylation of n-octane using Escherichia coli expressing the alkane hydroxylase, CYP153A6. Microb. Cell Fact. 12, 1–12. https://doi.org/10.1186/1475-2859-12-8

Olaofe, O.A., 2013. A bioprocess approach for enhanced biocatalytic activity and efficiency of whole cell Escherichia coli expressing alkane hydroxylase CYP153A6 for terminal hydroxylation of n-octane. University of cape Town.

Omajali, J.B., Hart, A., Walker, M., Wood, J., Macaskie, L.E., 2017. In-situ catalytic upgrading of heavy oil using dispersed bionanoparticles supported on gram-positive and gram-negative bacteria. Appl. Catal. B Environ. 203, 807–819. https://doi.org/10.1016/j.apcatb.2016.10.074

Osma, J.F., Saravia, V., Toca-Herrera, J.L., Couto, S.R., 2007. Sunflower seed shells: A novel and effective low-cost adsorbent for the removal of the diazo dye Reactive Black 5 from aqueous solutions. J. Hazard. Mater. 147, 900–905. https://doi.org/10.1016/j.jhazmat.2007.01.112

Overbury, S.H., Ortiz-Soto, L., Zhu, H., Lee, B., Amiridis, M.D., Dai, S., 2004. Comparison of Au catalysts supported on mesoporous titania and silica: Investigation of Au particle size effects and metal-support interactions. Catal. Letters 95, 99–106. https://doi.org/10.1023/B:CATL.0000027281.96719.42

Özcan, A.S., Erdem, B., Özcan, A., 2005. Adsorption of Acid Blue 193 from aqueous solutions onto BTMA-bentonite. Colloids Surfaces A Physicochem. Eng. Asp. 266, 73–81. https://doi.org/10.1016/j.colsurfa.2005.06.001

Padmesh, T.V.N., Vijayaraghavan, K., Sekaran, G., Velan, M., 2006. Application of two- and three-parameter isotherm models: Biosorption of acid red 88 onto Azolla microphylla. Bioremediat. J. 10, 37–44. https://doi.org/10.1080/10889860600842746

Pantidos, N., Horsfall, L.E., 2014. Biological Synthesis of Metallic Nanoparticles by Bacteria, Fungi and Plants. Nanomedicine Nanotechnol. Pantidos Horsfall 5. https://doi.org/10.4172/2157-7439.1000233

Peck, H.D., Gest, H., 1955. A New Procedure for Assay of Bacterial Hydrogenase 71, 70–80.

Peköz, R., Oymak, H., 2014. Binary Alloy Clusters : Structures and Electronic Properties Binary Alloy Clusters : Structures and Electronic Properties. https://doi.org/10.1166/rits.2014.1026

Penfold, D.W., Forster, C.F., Macaskie, L.E., 2003. Increased hydrogen production by Escherichia coli strain HD701 in comparison with the wild-type parent strain MC4100. Enzyme Microb. Technol. 33, 185–189. https://doi.org/10.1016/S0141-0229(03)00115-7

Pennec, A., Jacobs, C.L., Opperman, D.J., Smit, M.S., 2014. Revisiting cytochrome P450-mediated oxyfunctionalization of linear and cyclic alkanes. Adv. Synth. Catal. 357, 118–130. https://doi.org/10.1002/adsc.201400410

Pinske, C., Bönn, M., Krüger, S., Lindenstrauß, U., Sawers, R.G., 2011a. Metabolic deficiences revealed in the biotechnologically important model bacterium Escherichia coli BL21(DE3). PLoS One 6. https://doi.org/10.1371/journal.pone.0022830

Pinske, C., Krüger, S., Soboh, B., Ihling, C., Kuhns, M., Braussemann, M., Jaroschinsky, M., Sauer, C., Sargent, F., Sinz, A., Sawers, R.G., 2011b. Efficient electron transfer from hydrogen to benzyl viologen by the [NiFe]-hydrogenases of Escherichia coli is dependent on the coexpression of the iron-sulfur cluster-containing small subunit. Arch. Microbiol. 193, 893–903. https://doi.org/10.1007/s00203-011-0726-5

Pittaway, F., Paz-Borbon, L.O., Johnston, R.L., Arslan, H., Ferrando, R., Mottet, C., Barcaro, G., Fortunelli, A., 2009. Theoretical Studies of Palladium−Gold Nanoclusters: Pd−Au Clusters with up to 50 Atom. J. Phys. Chem. C 113, 9141–9152. https://doi.org/doi:10.1021/jp9006075

Prati, L., Rossi, M., 1998. Gold on carbon as a new catalyst for selective liquid phase oxidation of diols. J. Catal. 176, 552–560. https://doi.org/DOI 10.1006/jcat.1998.2078

Pritchard, J., Kesavan, L., Piccinini, M., He, Q., Tiruvalam, R., Dimitratos, N., Lopez-Sanchez, J.A., Carley, A.F., Edwards, J.K., Kiely, C.J., Hutchings, G.J., 2010. Direct synthesis of hydrogen peroxide and benzyl alcohol oxidation using Au-Pd catalysts prepared by sol immobilization. Langmuir. https://doi.org/10.1021/la101597q

Qiu, H., Lv, L., Pan, B., Zhang, Q., Zhang, W., Zhang, Q., 2009. Critical review in adsorption kinetic models. J. Zhejiang Univ. A 10, 716–724. https://doi.org/10.1631/jzus.a0820524

Ramachandran, A., Vairamuthu, R., Ponnusamy, S., 2011. Adsorption Isotherms, Kinetics, Thermodynamics and Desorption Studies of Reactive Orange16 on Activated Carbon Derived from Ananas comosus (L.) Carbon. ARPN J. Eng. Appl. Sci. 6, 15–26.

Reusch, W., 2013. Infrared Spectroscopy [WWW Document]. URL https://www2.chemistry.msu.edu/faculty/reusch/VirtTxtJml/Spectrpy/InfraRed/infrared.htm (accessed 8.26.20).

Rodriguez, J.A., Rodriguex, J.A., 1996. Physical and chemical properties of bimetallic surfaces. Surf. Sci. Rep. 24, 223. https://doi.org/10.1016/0167-5729(96)00004-0

Roginsky, S., Zeldovich, Y.., 1934. The catalytic oxidation of carbon monoxide on manganese dioxide. Acta Phys. Chem. 554. https://doi.org/10.1088/1742-6596/1173/1/012007

Rotaru, A.E., Jiang, W., Finster, K., Skrydstrup, T., Meyer, R.L., 2012. Non-enzymatic palladium recovery on microbial and synthetic surfaces. Biotechnol. Bioeng. 109, 1889–

1897. https://doi.org/10.1002/bit.24500

Rudroff, F., Mihovilovic, M.D., Gröger, H., Snajdrova, R., Iding, H., Bornscheuer, U.T., 2018. Opportunities and challenges for combining chemo- and biocatalysis. Nat. Catal. 1, 12–22. https://doi.org/10.1038/s41929-017-0010-4

Rushdi, A.I., Simoneit, B.R.T., 2001. Lipid formation by aqueous Fischer-Tropsch type synthesis over a temperature range of 100 to 400 ◦C. Orig. Life Evol. Biosph. 31, 103–118. https://doi.org/10.1023/A:1006702503954

Sádaba, I., López Granados, M., Riisager, A., Taarning, E., 2015. Deactivation of solid catalysts in liquid media: the case of leaching of active sites in biomass conversion reactions. Green Chem. https://doi.org/10.1039/c5gc00804b

Sadri, F., Ramazani, A., Massoudi, A., Khoobi, M., Tarasi, R., Shafiee, A., Azizkhani, V., Dolatyari, L., Joo, S.W., 2014. Green oxidation of alcohols by using hydrogen peroxide in water in the presence of magnetic Fe3O4 nanoparticles as recoverable catalyst. Green Chem. Lett. Rev. https://doi.org/10.1080/17518253.2014.939721

Sakata, Y., Tamaura, Y., Imamura, H., Watanabe, M., 2006. Preparation of a new type of CaSiO3 with high surface area and property as a catalyst support, in: Studies in Surface Science and Catalysis. https://doi.org/10.1016/S0167-2991(06)80924-9

Sankar, M., Nowicka, E., Carter, E., Murphy, D.M., Knight, D.W., Bethell, D., Hutchings, G.J., 2014. The benzaldehyde oxidation paradox explained by the interception of peroxy radical by benzyl alcohol. Nat. Commun. 5. https://doi.org/10.1038/ncomms4332

Senthil Kumar, P., Vincent, C., Kirthika, K., Sathish Kumar, K., 2010. Kinetics and equilibrium studies of Pb2+ ion removal from aqueous solutions by use of nano-silversol-coated activated carbon. Brazilian J. Chem. Eng. https://doi.org/10.1590/s0104-66322010000200012

Sezonov, G., Joseleau-Petit, D., D'Ari, R., 2007. Escherichia coli physiology in Luria-Bertani broth. J. Bacteriol. 189, 8746–8749. https://doi.org/10.1128/JB.01368-07

Shah, M.M.R., Liang, Y., Cheng, J.J., Daroch, M., 2016. Astaxanthin-Producing Green Microalga Haematococcus pluvialis: From Single Cell to High Value Commercial Products. Front. Plant Sci. 7, 531. https://doi.org/10.3389/fpls.2016.00531

Sheldon, R.A., Arends, I., Hanefeld, U., 2007. Green chemistry and catalysis. Wiley-VCH.

Sinfelt, J.H., 1977. Catalysis by Alloys and Bimetallic Clusters. Bimetallic Clust. Catal. 10, 15–20.

Sobjerg, L.S., Lindhardt, A.T., Skrydstrup, T., Finster, K., Meyer, R.L., 2011. Size control and catalytic activity of bio-supported palladium nanoparticles. Colloids Surfaces B Biointerfaces 85, 373–378. https://doi.org/10.1016/j.colsurfb.2011.03.014

Soderberg, T., 2020. Vibrations and Rotations of Molecules: Infrared and Microwave Spectroscopy - Chemistry LibreTexts [WWW Document]. URL https://chem.libretexts.org/Bookshelves/General_Chemistry/Map%3A_Principles_of_Modern_Chemistry_(Oxtoby_et_al.)/UNIT_5%3A_RATES_OF_CHEMICAL_AND_PHYSICAL_PROCESSES/20%3A_Molecular_Spectroscopy_and_Photochemistry/20.2%3A_Vibrations_and_Rotations_of_Molecule (accessed 8.26.20).

Solsona, B.E., Edwards, J.K., Landon, P., Carley, A.F., Herzing, A., Kiely, C.J., Hutchings, G.J., 2006. Direct Synthesis of Hydrogen Peroxide from H2 and O2 Using Al2O3 Supported Au−Pd Catalysts. Chem. Mater. 18, 2689–2695. https://doi.org/10.1021/cm052633o

Stoyanov, J. V., Browns, N.L., 2003. The Escherichia coli copper-responsive copA promoter is activated by gold. J. Biol. Chem. 278, 1407–1410. https://doi.org/10.1074/jbc.C200580200

Sudiro, M., Bertucco, A., 2009. Production of synthetic gasoline and diesel fuel by alternative processes using natural gas and coal: Process simulation and optimization. Energy.

Sun, J., Han, Y., Fu, H., Qu, X., Xu, Z., Zheng, S., 2017. Au-Pd/TiO2 with atomically dispersed Pd as highly active catalyst for solvent-free aerobic oxidation of benzyl alcohol. Chem. Eng. J. 313, 1–9. https://doi.org/10.1016/j.cej.2016.12.024

Tan, K.L., Hameed, B.H., 2017. Insight into the adsorption kinetics models for the removal of contaminants from aqueous solutions. J. Taiwan Inst. Chem. Eng. 74, 25–48. https://doi.org/10.1016/j.jtice.2017.01.024

Tasker, S.Z., Standley, E.A., Jamison, T.F., 2014. Recent Advances in Nickel Catalysis. Nature 509, 299–309. https://doi.org/10.1038/nature13274

Tavakoli, A., Sohrabi, M., Kargari, A., 2007. A Review of Methods for Synthesis of Nanostructured Metals with Emphasis on Iron Compounds. Chem. Pap 61, 151–170. https://doi.org/10.2478/s11696-007-0014-7

Tempkin, M.I., Pyzhev, V., 1940. Kinetics of ammonia synthesis on promoted iron catalyst. Acta Phys. Chim 12, 327–356. https://doi.org/10.1021/ie50402a012

Ten Brink, G.J., Arends, I.W.C.E., Sheldon, R.A., 2000. Green, catalytic oxidation of alcohols in water. Science (80-.). https://doi.org/10.1126/science.287.5458.1636

Thakkar, K.N., Mhatre, S.S., Parikh, R.Y., 2010. Biological synthesis of metallic nanoparticles. Nanomedicine Nanotechnology, Biol. Med. 6, 257–262. https://doi.org/10.1016/j.nano.2009.07.002

Torgeman, E., 2017. Biosynthesis of gold and palladium nanoparticles via bacteria.

U.S. Department of the Interior, 2017. U.S. Geological Survey Mineral Commodities Summaries. Virginia. https://doi.org/http://dx.doi.org/10.3133/70140094.

University of California Department of Chemistry, n.d. Introduction to IR Spectra [WWW Document]. URL https://webspectra.chem.ucla.edu/irintro.html (accessed 8.26.20).

University Of Missouri–St. Louis, 1997. Infrared Spectroscopy [WWW Document]. URL http://www.umsl.edu/~orglab/documents/IR/IR2.html (accessed 8.26.20).

van der Pol, A.J.H.P., van Hooff, J.H.C., 1993. Oxidation of linear alcohols with hydrogen peroxide over titanium silicalite 1. Appl. Catal. A Gen. 106, 97–113. https://doi.org/10.1016/0926-860X(93)80158-M

Villa, A., Dimitratos, N., Chan-Thaw, C.E., Hammond, C., Prati, L., Hutchings, G.J., 2015. Glycerol oxidation using gold-containing catalysts. Acc. Chem. Res. 48. https://doi.org/10.1021/ar500426g

Villa, A., Janjic, N., Spontoni, P., Wang, D., Su, D.S., Prati, L., 2009. Au-Pd/AC as catalysts for alcohol oxidation: Effect of reaction parameters on catalytic activity and selectivity. Appl. Catal. A Gen. 364, 221–228. https://doi.org/10.1016/j.apcata.2009.05.059

Wang, H., Wang, C., Yan, H., Yi, H., Lu, J., 2015. Precisely-controlled synthesis of Au-Pd core-shell bimetallic catalyst via atomic layer deposition for selective oxidation of benzyl alcohol. J. Catal. 324, 59–68. https://doi.org/10.1016/j.jcat.2015.01.019

Wang, L., Hu, C., Shao, L., 2017. The antimicrobial activity of nanoparticles: Present situation and prospects for the future. Int. J. Nanomedicine. https://doi.org/10.2147/IJN.S121956

Wang, Y., Zhao, H., Ren, H., 2018. Expanding the Boundary of Biocatalysis: Design and Optimization of in vitro Tandem Catalytic Reactions for Biochemical Production 115–129. https://doi.org/10.1080/10409238.2018.1431201

Wells, A.S., Meadows, R.E., Wood, J., Macaskie, L.E., 2014. Catalytic activity of biomass-supported Pd nanoparticles: Influence of the biological component in catalytic efficacy and potential application in “green” synthesis of fine chemicals and pharmaceuticals. Appl. Catal. B Environ. 147, 651–665. https://doi.org/10.1016/j.apcatb.2013.09.045

Will, W.R., 2015. What would be the proper volume of LB media in a flask for optimal aeration and thus growth of E.coli? [WWW Document]. URL https://www.researchgate.net/post/What_would_be_the_proper_volume_of_LB_media_in_a_flask_for_optimal_aeration_and_thus_growth_of_Ecoli (accessed 8.26.20).

World Gold Council, 2019. How Much Gold Has Been Mined? [WWW Document]. URL https://www.gold.org/about-gold/gold-supply/gold-mining/how-much-gold (accessed 9.25.19).

Xu, Z., Zhang, W., Pan, B., Hong, C., Lv, L., Zhang, Q., Pan, B., Zhang, Q., 2008. Application of the Polanyi potential theory to phthalates adsorption from aqueous solution with hyper-cross-linked polymer resins. J. Colloid Interface Sci. 319, 392–397. https://doi.org/10.1016/j.jcis.2007.12.015

Yamaguchi, K., Mizuno, N., 2002. Supported Ruthenium Catalyst for the Heterogeneous Oxidation of Alcohols with Molecular Oxygen. Angew. Chemie Int. Ed. 41, 4538–4542.

Yong, P., Macaskie, L.E., Rowson, N.A., Farr, J.P.G., Harris, L.R., 2003. A novel electrobiotechnology for the recovery of precious metals from spent automotive catalysts. Environ. Technol. (United Kingdom) 24, 289–297. https://doi.org/10.1080/09593330309385561

Yong, P., Rowson, N.A., Farr, J.P.G., Harris, I.R., Macaskie, L.E., 2002a. Bioreduction and biocrystallization of palladium by Desulfovibrio desulfuricans NCIMB 8307. Biotechnol. Bioeng. 80, 369–379. https://doi.org/10.1002/bit.10369

Yong, P., Rowson, N.A., Farr, J.P.G., Harris, I.R., Macaskie, L.E., 2002b. Bioaccumulation of palladium by Desulfovibrio desulfuricans. J. Chem. Technol. Biotechnol. 77, 593–601. https://doi.org/10.1002/jctb.606

Yu, W.-Y., Mullen, G.M., Mullins, C.B., 2013. Hydrogen Adsorption and Absorption with Pd−Au Bimetallic Surfaces. J. Phys. Chem. https://doi.org/10.1021/jp406736b

Zhang, H., Lu, B., You, X., Ma, F., Zhao, J., Cai, Q., 2015. Mixed Oxides FeVOx for Selective Oxidation of Octanol to Octanal under Solvent-free Condition. J. Chinese Chem. Soc. 62, 722–727. https://doi.org/10.1002/jccs.201400167

Zhu, J.U., 2014. Synthesis of Precious Metal Nanoparticles Supported on Bacterial Biomass for Catalytic Applications in Chemical Transformations School of Chemical Engineering.

8 Appendices

Appendix A: Culture growth

The data set linked to this thesis can be located in Zivahub using the link in the reference list - unpublished as of submission (Govender, 2021)

A.1 Growth media preparation

The cell culture was grown on standard LB medium

Table 8-1 Standard LB media formula for cell growth

Chemical	Concentration
Tryptone	10 g/L
Yeast Extract	5 g/L
Sodium Chloride	5 g/L

Table 8-2 Adjusted LB media formula for cell growth

Chemical	Concentration
Tryptone	10 g/L
Yeast Extract	5 g/L
Sodium Chloride	5 g/L
Sodium fumarate dibasic	0.4 % (w/v)
Glycerol (100%)	0.5 % (v/v)

For the purpose of this study growth media for the *E. coli* strains was described by Table 8-1 and Table 8-2 and was used for aerobic preculture and anaerobic culture growth, respectively

A.2 Dry cell weight and OD correlation

OD versus dry cell weight correlations for the three *E. oli* strains were considered in this study and are provided in Table 8-3.

Table 8-3 Dry cell weight and OD600 correlation growth co-efficient. Growth of cells observed at 37°C in a modified LB media

Strain	DCW (g/L) at OD_{600} of 1
E. coli DH5α	0.49
E. coli ATCC25922	0.75
E. coli BL21DE3	0.53

To obtain these correlations the culture was grown as indicated in Section 3.1. The 1 L culture was harvested and diluted once more in fresh media creating a concentrated cell suspension. A serial dilution was then performed on the concentrated culture. The OD at 600nm of these cultures was assessed (by extracting 3 ml of sample to measure using the spectrophotometer). The cells mass in each dilution were harvested via centrifugation (7000 rpm, 10 minutes, 4°C). The wet cells were transferred to pre-dried, weighed Eppendorf tubes and then washed (twice) with deionised water. The cells were dried over 2 days in an 80°C oven. Once dry the Eppendorf tubes were place in a desiccator for at least 1 hour to ensure the samples cooled down to room temperature and no moisture formed in the tubes. The weight of the dry cell mass was then correlated to their respective OD values to obtain correlation coefficients (Table 8-3).

Appendix B: Preparation for bioreduction

B.1 Preparation of cell buffer

The cell buffer was necessary to maintain cell activity outside the growth media

Table 8-4 Composition of 40 mM MOPS buffer stock solution

Chemical	Concentration (mM)	Molar mass(g/mol)
MOPS	40	209.3
EDTA (disodium dihydrate)	10	372.24
Sodium acetate (trihydrate)	1	136.08

A 40 mM stock MOPS buffer solution was prepared (Table 8-4). A sample calculation of the reagents used can be noted below;

For a 40 mM MOPS stock solution with a 1 L final volume;

$$\frac{40\ mmol}{L} \times 1L \times \frac{209.3\ mg}{mmol} \times \frac{1\ g}{1000\ mg} = 8.37\ g\ of\ MOPS$$

$$\frac{10\ mmol}{L} \times 1L \times \frac{372.24\ mg}{mmol} \times \frac{1\ g}{1000\ mg} = 3.72\ g\ of\ EDTA$$

$$\frac{1\ mmol}{L} \times 1L \times \frac{136.08\ mg}{mmol} \times \frac{1\ g}{1000\ mg} = 0.14\ g\ Sodium\ acetate\ trihydrate$$

Once the stock solution is made, it is diluted by a factor of 2 (resulting in a 20 mM MOPS solution). The pH is adjusted to 7 using 10M NaOH. The buffer must be degassed before use. The MOPS-NaOH buffer can be stored at room temperature until use. It was noted that the buffer solution is sensitive to light. When exposed to light over an extended period, the solution tends to turn from clear to yellow. If the yellow-coloured buffer was used, the cells were affected such that no reduction was noted under these conditions. To prevent deactivation form occurring, once the buffer was made the container was completely covered.

B.2 Metal ion solution preparation

Table 8-5 Salt precursor solution requirements and constants

Chemical	Concentration (mM)	Molar mass(g/mol)
Sodium tetrachloropalladate	2	294.20
Gold chloride trihydrate	1	398.93

From Table 8-5 above the mass of metal salt to be dissolved in acidified water (pH 2.3) can be derived. For a 100 ml batch solution the following reagent is required;

$$\frac{2\ mmol}{L} \times\ 0.1L \times \frac{294.20\ mg}{mmol} \times \frac{1\ g}{1000\ mg} = 0.0588\ g\ of\ Na2PdCl4$$

$$\frac{1\ mmol}{L} \times\ 0.1L \times \frac{398.93\ mg}{mmol} \times \frac{1\ g}{1000\ mg} = 0.0399\ g\ of\ HAuC4$$

B.3 Cell culture preparation

To assess the mass of cells/adsorbate obtained after growth and the mass to be added to the reduction system, OD and DCW correlations were necessary (see Appendix A.2).

For a 1L growth culture after 14-18 hours growth, the following OD is achieved;

Table 8-6 Example of the observed OD after bulk anoxic cell growth

Strain	OD (600 nm) [measured at 14-18 h]	CDW (g/L) @ OD = 1
E. coli DH5α	1	0.49
E. coli ATCC25922	1.1	0.75
E. coli BL21DE3	0.4	0.53

From this the mass of cells present at this time point can be derived from the measured OD . Once know the total cell mass of cell is to be resuspended in the degassed MOPS-NaOH buffer

B.4 Metal reduction onto support: sample calculation

The following example calculation is used to achieve the required 5% (w/w) metal loading on *E. coli* DH5α upon bioreduction

$$m\ cells\ total = \frac{0.49g}{L} \times 1L \times 1 = 0.49\ g$$

The factor of the total biomass used in the serum bottle is set at 0.43 for this strain

$$m\ cells = 0.49\ g \times 0.43 = 0.211\ g$$

The metal loading is set at 5% (w/w) which means a ratio of 1:19 (mass Pd to mass dry cell) is used. Therefore for 0.211 g of cells 0.011 g of Pd is required.

$$n\ Pd = 0.011\ g \times \frac{mol}{106.42\ g} \times \frac{1000\ mmol}{mol} = 0.104\ mmol\ Pd\ (0.104\ mmol\ Na2PdCl4)$$

The total cells harvested were resuspended in a certain volume of buffer, calculated below;

$$1000\ ml \times \frac{1}{50} = 20\ ml$$

$$Conc\ cell - buffer\ suspension = \frac{0.49\ g}{20\ ml} = \frac{0.025g}{ml}$$

$$Volume\ cell - buffer\ suspension\ (added\ to\ serum\ bottle) = \frac{ml}{0.025\ g} \times 0.211\ g = 8.6\ ml$$

From the equation below one can use the fact that 2 mM Pd(II) ion solution remains constant to determine the volume of metal precursor to add the mass of cells .

$$\frac{n1}{V1} = \frac{n2}{V2}$$

$$\frac{2\ mmol}{1L} = \frac{0.104\ mmol}{V2}$$

$$V2 = \left(\frac{1L}{2\ mmol}\right)(0.104) = 0.0521\ L\ (52.1\ ml)$$

If required, a certain amount of sodium formate needs to be added as an electron donor;

A stock solution of sodium formate 50 mM sodium formate is made by dissolving a particular mass of reagent in deionized water;

$$m = \frac{50\ mmol}{L} \times 1L \times \frac{68.01\ mg}{mmol} \times \frac{g}{1000\ mg} = 3.4005\ g$$

To ensure that 20 mM of the electron donor is added to manufacture 5%(w/w) Pd on *E. coli* DH5α, the following calculation was used;

$$V\ sodium\ formate = \frac{20\ mM}{50\ mM} \times (Vcell - buffer + Vmetal\ salt)$$

$$V\ sodium\ formate = \frac{20\ mM}{50\ mM} \times (8.6\ ml + 52.1) = 24.3\ ml$$

Appendix C: The residual metal assays

C.1 Stannous chloride assay for Pd

C.1.1 $SnCl_2$ assay standard curve

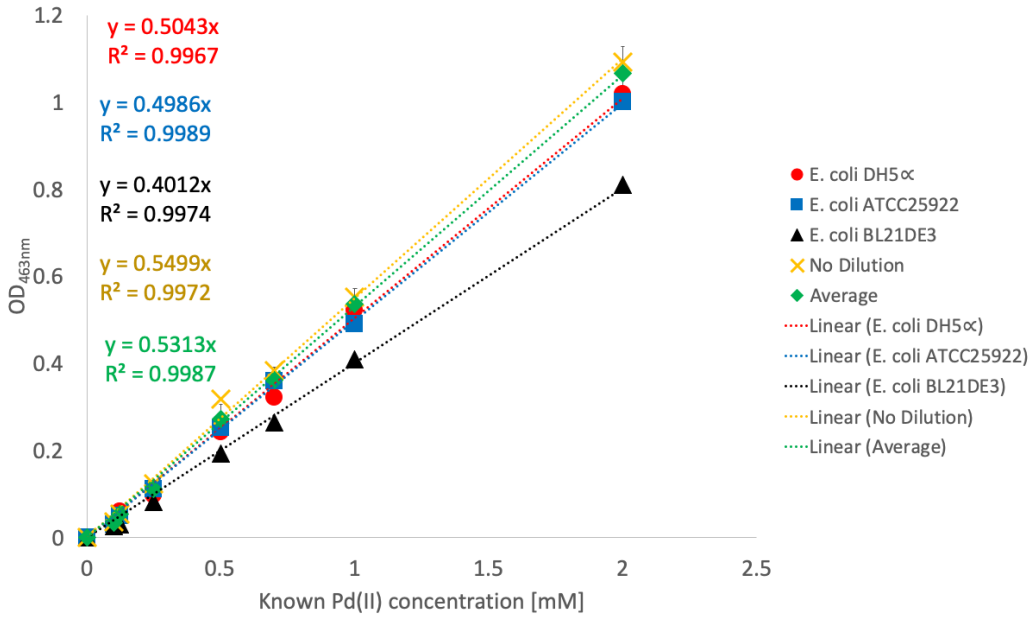

Figure 8-1 $SnCl_2$ assay standard curve for 5% (w/w) Pd adsorption onto the *E. coli* strains

C.2 Thiamine-phloxine assay for Au

C.2.1 Reagent preparation

Various reagents are needed to perform the Au assay as indicated in the methodology, the composition of these soltions are indicated in Table 8-7;

Table 8-7 Thiamine-phloxine assay rreagent composition

Chemical	Amount	Molar Mass (g/mol)
Methyl cellulose	0.5% (w/v)	-
Thiamine nitrate	0.1 M (100 mM)	327.36
Phloxine B	0.01 M (10 mM)	829.63
EDTA (trisodium, anhyd)	0.05 M	358.19
Citric acid	0.1 M	192.12

To prepare the methylcellulose, a third of the water to be used was heated to a temperature greater than 80°C. The required amount of methylcellulose powder was then added, and the mixture agitated. This agitation continued until the powder was well-dispersed and wet. The remaining two-thirds of the water was then added as ice/cold water. This lowers the temperature of the solution until the correct temperature was reached. This temperature was determined by the viscosity of the methylcellulose solution. For this study the chemical purchased had a viscosity of 25 cp which correlated to a temp of 41°C. The solution was cooled down further to between 0 °C to 5°C and the mixture was agitated for a further 30 minutes.

A sample calculation of the stock solution preparation is given below

$$Methylcellulose = \frac{0.5\ g}{100\ ml} \times 100 = 0.5\%$$

The thiamine nitrate and phloxine B solutions are prepared to a volume of 100 ml. The EDTA-citrate buffer was prepared to a 200 ml volume.

$$m\ Thiamine\ nitrate = \frac{0.1\ mol}{L} \times 0.1L \times \frac{327.36\ g}{mol} = 3.27\ g$$

$$m\ Phloxine.B = \frac{0.01\ mol}{L} \times 0.1L \times \frac{829.63\ g}{mol} = 0.83\ g$$

$$m\ EDTA(3Na) = \frac{0.05\ mol}{L} \times 0.2L \times \frac{358.19\ g}{mol} = 3.58\ g$$

$$m\ citric\ acid = \frac{0.1\ mol}{L} \times 0.2L \times \frac{192.19\ g}{mol} = 3.84\ g$$

C.2.2 Thiamine-phloxine assay standard curve

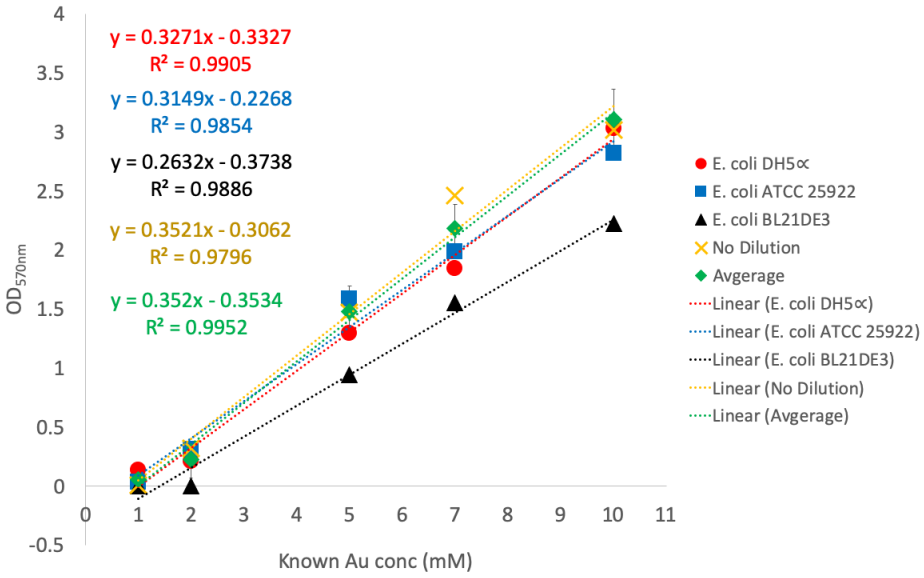

Figure 8-2 Thiamine-Phloxine assay standard curve for 5% (w/w) Au adsorption on the *E. coli* strains

Appendix D: Oxidation reaction analysis

Table 8-8 Method protocol used to run the Varian 3900. The parameters were set in Galaxie Workstation software

Autosampler	
Syringe volume	10 μl
Injection mode	Split
Injector	
Heater	Yes
Setpoint	240°C
Initial split ratio	80
Oven	
Stabilization time	1 minute
Heater	On
Ramp	
Rate	30°C/min
Step initial	60°C
Time initial	3 minutes
Step final	180°C
Time final	7 minutes
Total time final	**14 minutes**
Column pneumatics	
Isobaric/constant flow	Constant flow
Flow rate	1 ml/min
Detector	
Heater	On
Setpoint	280°C
FID	
Range initial	12
Autozero	Yes
Gas flow	
Nitrogen	30 ml/min
Hydrogen	30 ml/min
Air	300 ml/min

D.1 GC method protocol

The above method in Table 8-8 was used by the GC software to allow for the detection of the products generated upon the oxidation of the alcohols in the presence of the biofabricated catalysts.

D.2 GC compound identification

From knowledge of the reaction system certain predictable assumptions can be made about the reaction products generated after oxidation. The following reagents were examined (Table 8-9);

Table 8-9 Retention times for reagents and products detected via GC analysis

Chemicals	Purchased/Obtained from	Grade/Purity %	Retention time (minutes)
Benzyl alcohol	UCT Catalysis/Sigma	99-100	9.8 to 10
Benzaldehyde	Sigma	99	9.2
Benzoic acid	UCT Catalysis/Sigma	≥ 99.5	10.8
Toluene	Merek	≥ 99..9	7.2
1-Octanol	Merek	>99	10.1
Octanal	Sigma	(Analytical standard)	9.42
Octanoic acid	UCT Catalysis/Sigma	99.5	10,8
Ethyl acetate	Merek	≥ 99.5	6.06
1-Decanol	Sigma	>98	11.8

From injection of a small known quantity of sample into the GC the retention time of the product versus the known chemical are compared to verify the presence of the compound in the reaction vessel

D.3 GC analysis: standard curves

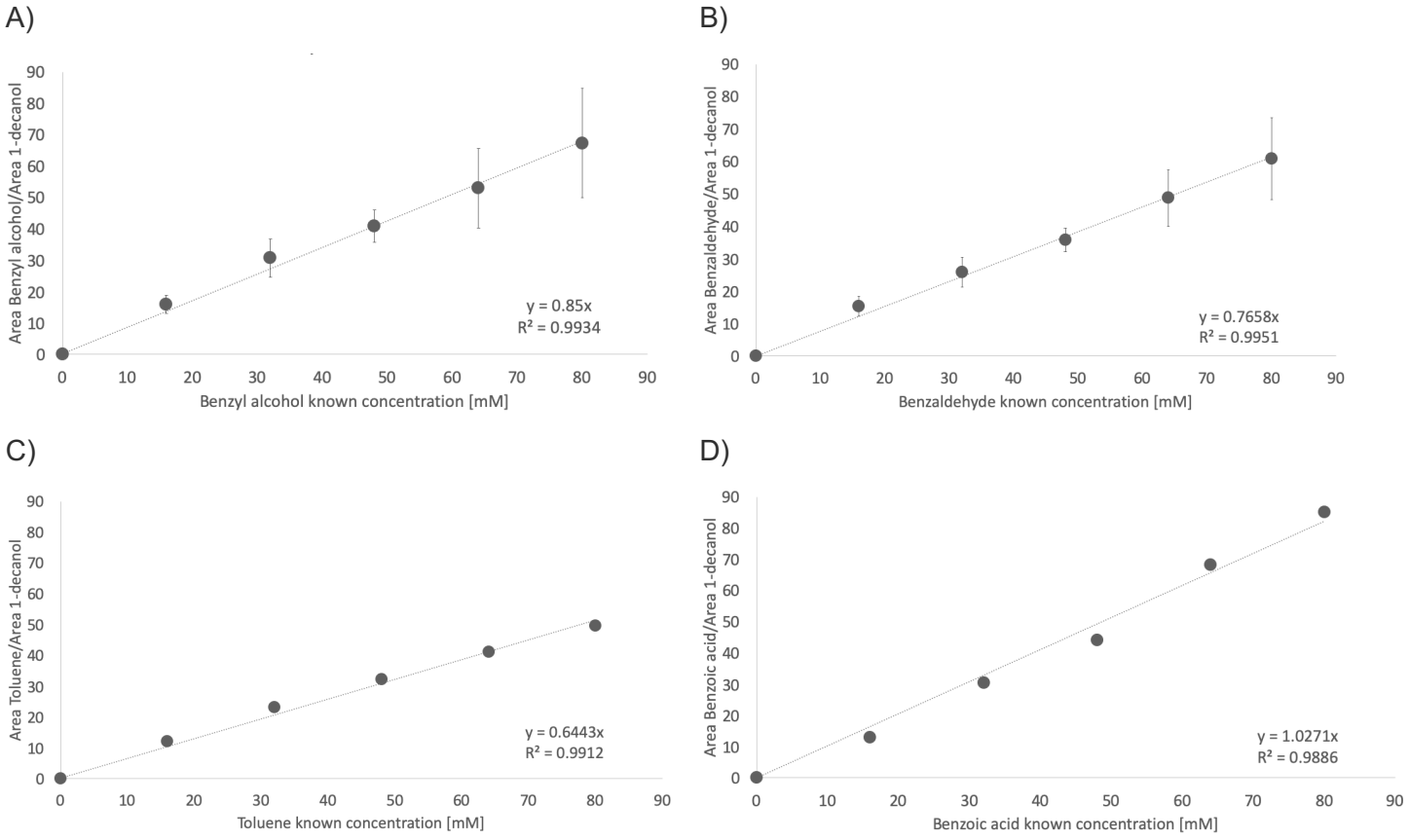

Figure 8-3 Standard curve for reagents and products identified via GC analysis after the oxidation of aromatic alcohol. Where A) is benzyl alcohol B) benzaldehyde C) toluene and D) benzoic acid

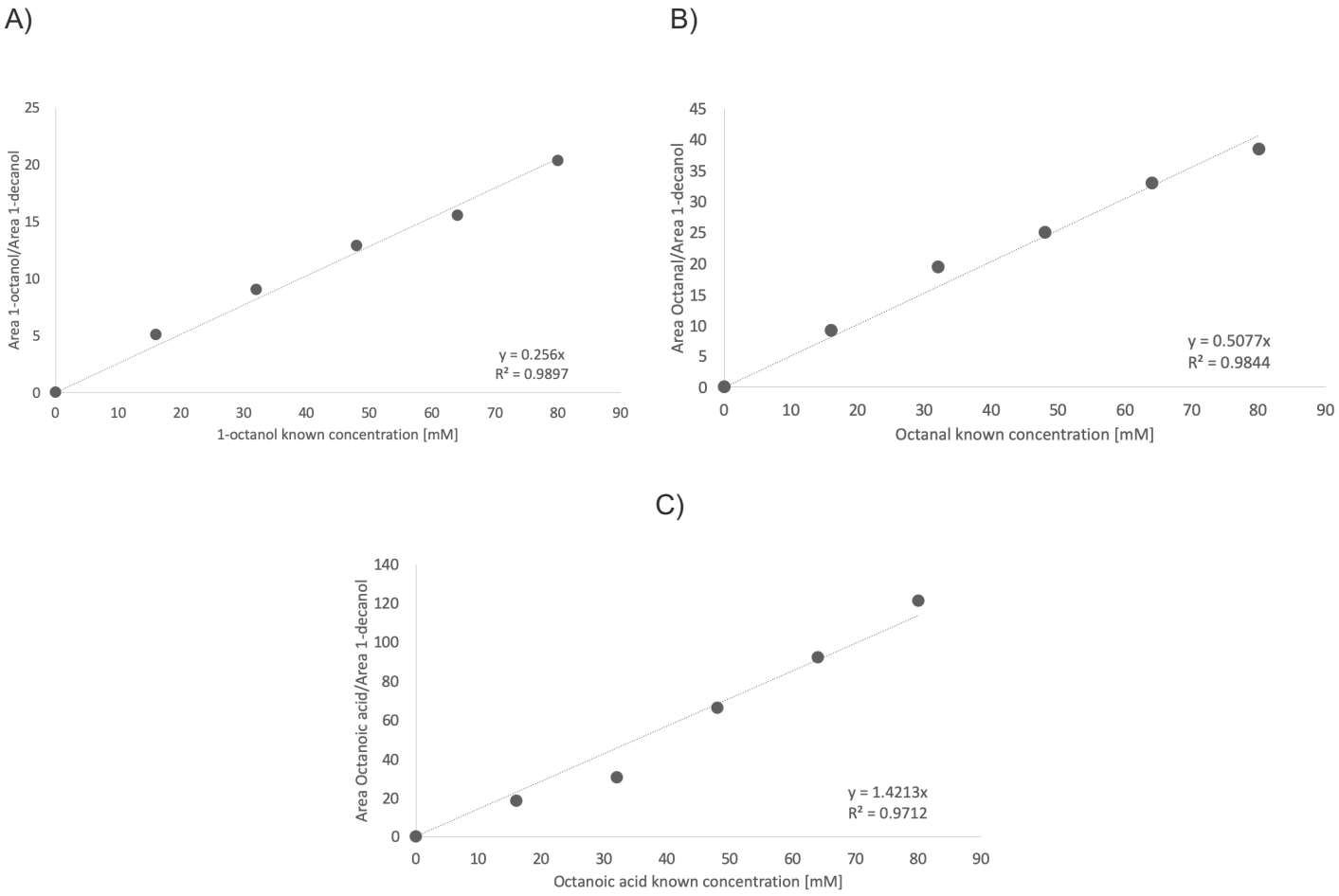

Figure 8-4 Standard curve for reagents and products identified via GC analysis after the oxidation of aromatic alcohol. Where A) is 1-octanol B) octanal C) and octanoic acid

Appendix E: Model fitting at a higher loading

In an effort to describe adsorption at the higher metal loading where desorption of the solid ion is evident , the trend was divided to three sections. The fit of the various models was assessed to establish the most beneficial overall fit (Table 8-10 and Table 8-11)

Table 8-10 Kinetic model fit to the experimental adsorption of Au(III) ions at a 25% (w/w) loading onto *E. coli* ATCC25922. Where the model constants k1, k2, qe (exp), β , α, f and c were defined upon non-linear regression analysis. The region L1 is defined as the initial adsorption stage, L2 is defined as desorption stage and L3 is the defined as point at which equilibrium is reached.

	Pseudo-first order						Pseudo-second order					
	k_1 (min^{-1})	$q_{e\ (exp)}$ (mg/g)	Residual pattern	χ^2	R^2	AARD	k_2	$q_{e\ (exp)}$ (mg/g)	Residual pattern	χ^2	R^2	AARD
L1	8.0	185.0	-	-	1.0	-	0.4	185.0	-	-	1.0	-
L2	13.7	185.0	-	0.2	0.1	45.5%	-9.0×10^{9}	185.0	-	0.2	0.0	45.5%
L3	0.04	185.0	-	1.0	-4.5	33.8%	0.0	185.0	-	1.3	-0.7	32.9%
Overall fit			Yes	1.2	0.4	36.8%			Yes	1.6	0.4	36.3%
	Elovich model (@ Boundary conditions)						Intra-particle diffusion					
	β (g/mg)	α (mg/g.min)	Residual pattern	χ^2	R^2	AARD	f ($mg/g.min^{0.5}$)	C	Residual pattern	χ^2	R^2	AARD
L1	0.1	8.9×10^{5}	-	-0.1	1.0	-	240.7	3.0	-	$1.7X10^{-2}$	1.0	-
L2	-0.04	-8.57×10^{-2}	-	$1.5X10^{-2}$	0.9	10.6%	-64.9	242.1	-	$5.6X10^{-3}$	1.0	6.2%
L3	0.2	7.82×10^{6}	-	$6.5X10^{-3}$	0.5	3.8%	2.8	94.5	-	$7.3X10^{-3}$	0.5	4.0%
Overall fit			No	$2.2X10^{-2}$	1.0	5.7%			No	$1.4X10^{-2}$	1.0	4.8%

Table 8-11 Kinetic model fit to the experimental adsorption of Au(III) ions at a 25% (w/w) loading onto E. coli DH5α. Where the model constants k1, k2, qe (exp), β , α, f and c were defined upon non-linear regression analysis. The region L1 is defined as the intial adsorption stage, L2 is defined as desorption stage and L3 is the defined as point at which equilibrium is reached

	Pseudo-first order						Pseudo-second order					
	k_1 (min^{-1})	$q_{e\ (exp)}$ (mg/g)	Residual pattern	χ^2	R^2	AARD	k_2	$q_{e\ (exp)}$ (mg/g)	Residual pattern	χ^2	R^2	AARD
L1	12.0	235.1	-	-	1.0	-	2.0	235.1	-	-	1.0	-
L2	50.0	235.1	-	0.2	-0.4	51.7%	-0.1	235.1	-	0.3	0.2	63.5%
L3	0.1	235.1	-	0.4	-0.2	23.9%	0.0	235.1	-	0.6	0.0	42.4%
Overall fit			Yes	0.6	0.4	-			Uncertain	0.9	0.4	-
	Elovich model (@ Boundary conditions)						Intra-particle diffusion					
	β (g/mg)	α (mg/g.min)	Residual pattern	χ^2	R^2	AARD	f ($mg/g.min^{0.5}$)	C	Residual pattern	χ^2	R^2	AARD
L1	0.05	4.0×10^{6}	-	0.1	1.0	-	438.0	0.0	-	-	1.0	-
L2	-0.03	-1.0×10^{-1}	-	0.0	1.0	5.1%	-50.0	264.0	-	0.0	0.9	10.0%
L3	0.11	3.0×10^{6}	-	0.01	0.7	3.5%	6.7	114	-	0.0	0.9	1.7%
Overall fit			No	0.0	1.0	-			No	0.0	1.0	-